Injector Characterisation Measurement Technology for a Production Environment

By Stefan Stojanovic





Oxford Brookes University

Department of Mechanical Engineering and Mathematical Sciences

In collaboration with

Delphi Technologies, Stonehouse

Test Development Integration Department

A thesis submitted in partial fulfilment of the requirements of the award of Doctor of Philosophy

Oct 2020

ABSTRACT

The performance of Heavy-Duty common rail injectors is directly responsible for the power, efficiency, and emission levels of diesel engines. The variance in injector measurements, negatively impact performance and emissions characteristics of engines in real world applications. The main objectives of this work were to identify sources of injection measurement variance in a rate tube injection meter, and to gain insight into how to characterise high pressure multiple injection events for near future applications.

Experimental schemes were developed using existing production injector test equipment to investigate sources of injector performance measurement variance. The investigations were carried out using standard production measurement equipment. This research identified sources of variance in a rate tube meter, as: zero value baseline variance originating from pressure wave activity in the fluid medium, high frequency cavitation activity in the injection event, accuracy of the temperature to speed of sound transfer function, cumulative signal offset driven by fluid dependant properties during the injection event, and artefacts in the characteristic injection rate profile after the end of the injection event.

A 1D hydraulic model of a rate tube was constructed to identify the source of the experimental observations. The knowledge gained from the analysis of the model informed the design of a three-month trial under production conditions, to improve the accuracy of the temperature to speed of sound transfer function using large datasets. Results from the experimental schemes were used to construct normalised datasets for feature selection using data mining and correlation analysis. This led to the discovery of a source of previously unknown injector performance variance caused by high pressure supply resonant wave activity.

Major contributions to the field of automotive fuel injector performance characterisation from the research included an optimised hydraulic design approach that eliminates previously unknown low frequency resonant zero value variance, a unique data set on high frequency resonance spectrograms of an unfiltered rate tube signal, and demonstration that post injection rate distortion is a product of fluid friction from the tube walls before the sensor port. Additional contributions of this work included a 1D rate tube model, novel cepstrum signal noise and fluid properties analysis, distortion free injection rate signal processing, improved accuracy of temperature to speed of sound signal magnitude calibration, identification of the criteria for the repeatability of thermal signal offsets, and automated feature selection algorithms that reveal novel sources of variance. This knowledge transferred to the production environment in 2018, enabling reduced cycle times and an order-of-magnitude improvement in consecutive mass measurement repeatability, leading to a 10% increase in Overall Equipment Effectiveness.

ACKNOWLEDGEMENTS

The financial and technical support provided by Delphi Technologies Stonehouse is acknowledged.

I would like to thank the members of the Delphi Technologies Stonehouse Manufacturing Engineering team, in particular the members of the Test Development and Integration Team for their technical support throughout the study. I would like to also thank the members of the Stonehouse Operations Team for continually supporting the implementation of commercial outcomes of this work.

Thank you to my mentors Bill Kaighin and David Jewel for believing in me, generously offering this opportunity to explore new possibilities.

I would further like to thank Dr Stephen Samuel and Professor John Durodola for their support throughout my studies. Offering sage advice during difficult times, ensuring the work remained academically grounded.

Lastly I would like to thank Stacey Stojanovic whose support was continuous throughout.

TABLE OF CONTENTS

1 INTRODUCTION 20

1.1 DELPHI INJECTOR DESIGN HISTORY UP TO EU5 EMISSIONS LEVELS 21
1.2 THE IMPACT OF EU6 DIESEL EMISSIONS STANDARDS 23
1.2.1 Heavy duty vs Light duty emissions testing 24
1.2.2 EU5 commercial vehicle emissions test regime 25
1.2.3 EU6 CV emissions test regime 26
1.2.4 Delphi EU6 common rail injector design 29
1.2.5 Diesel fuel system calibration trim strategy 30
1.3 OBJECTIVES 33
1.4 COMMERCIAL MOTIVATIONS FOR RESEARCH 34
1.5 ENVIRONMENTAL MOTIVATIONS FOR RESEARCH 35
1.6 HUMAN WELFARE MOTIVATIONS FOR RESEARCH 36
1.7 RESEARCH APPROACH 37
1.8 THESIS ORGANISATION 39

2 LITERATURE REVIEW 40

2.1 NEAR FUTURE COMMERCIAL VEHICLE EMISSIONS 40
2.1.1 Tighter production tolerances 41
2.1.2 Increased injection pressure 41
2.1.3 Close coupled multiple injection 42
2.1.4 Injection rate shape characterisation 43
2.2 REVIEW OF INJECTOR CHARACTERISATION TECHNOLOGY 43
2.2.1 Continuous flow meters 44
2.2.2 Shot-to-shot injection rate meters 44
2.2.3 Piston-displacement 45
2.2.4 Zeuch chamber 46
2.2.5 Rate tube 47
2.2.6 Zero value baseline 52
2.2.7 High frequency 53
2.2.8 Speed of sound (SOS) 55
2.2.9 Rate float 56
2.2.10 End of injection bump 58
2.3 SOURCES OF INJECTOR PERFORMANCE VARIANCE 59
2.4 SUMMARY 60

3 EXPERIMENTAL METHODOLOGY 62

3.1 THE INJECTOR 62
3.2 RATE TUBE PRODUCTION MEASUREMENT SYSTEM 63
3.3 PRODUCTION MEASUREMENT SYSTEM PLATFORMS 64
3.3.1 Test machine engine emulation 67
3.4 SCHEME OF EXPERIMENTS 69
3.4.1 Experimental scheme hardware strategies 70
3.4.2 Common parameters 72
3.4.3 Production hardware 72
3.4.4 Simulation space 74
3.4.5 Coriolis mass meter production trial 75
3.4.6 Custom hardware 76
3.5 DIVISION OF RESPONSIBILITIES 78

4 THE EFFECT OF ENVIROMENTAL VARIABLES 79

4.1 INTRODUCTION TO SOURCES OF MEASUREMENT VARIANCE IDENTIFIED 79
4.1.1 Zero Value variance 80
4.1.2 High frequency variance 80
4.1.3 Rate height 81
4.1.4 End of injection: Bump 81
4.1.5 End of injection: Rate float 82
4.1.6 End of injection: Closing Delay 82

5 ZERO VALUE VARIANCE 83

5.1 INFLUENCE OF HYDRAULIC CONFIGURATION 84
5.1.1 Quiescence target 85
5.1.2 Changes in rate tube geometry 85
5.1.3 Position of the backpressure regulator 89
5.1.4 Internal bore of the following hose 92
5.1.5 Flow restriction before the regulator 94
5.1.6 Increased backpressure 100
5.2 MODEL SPACE HYDRAULIC CHARACTERISATION 103
5.2.1 Hydraulic Modelling 104
5.2.2 Hydraulic Component Modelling 111
5.2.3 Rate tube system model 112
5.2.4 Initial settings 112
5.2.5 Rate tube system sub models 113
5.2.6 Critical model parameter tuning 118
5.2.7 Reflected wave height 124
5.2.8 30bar Regulated Coriolis meter system model 125
5.2.9 Following hose diameter 129
5.2.10 Following hose length 132
5.2.11 Hose length and coriolis flow measurement 135
5.2.12 Regulator leakage 136
5.3 ZERO VALUE VARIANCE TEMPERATURE SENSITIVITY 137
5.4 OPTIMISED HYDRAULIC CONFIGURATION 140
5.4.1 Following hose length 142
5.4.2 T-pipe resonant damper 144
5.4.3 Multiple orifice diaphragm regulator 146
5.4.4 First following hose accumulator 149
5.4.5 Second rate tube accumulator 153
5.4.6 Optimised hydraulic design vs experimental scheme 3 155

6 HIGH FREQUENCY VARIANCE 158

6.1 CHARACTERISATION OF HYDRAULIC SOURCES OF HIGH FREQUENCY VARIANCE 160
6.1.1 High frequency content of the injection event 163
6.1.2 Rate sensor natural frequency excitation 164
6.1.3 Rate sensor port natural frequency excitation 164
6.2 CHARACTERISATION OF ELECTRONIC SOURCES OF HIGH FREQUENCY VARIANCE 169
6.2.1 Effect of signal amplifier on high frequency variance 169
6.2.2 Cepstrum for periodic high frequency signal noise identification 172

7 RATE HEIGHT 183

7.1 AUTOMATING CORIOLIS MASS MEASUREMENT 184
7.2 MASS CALIBRATION CURVE FITTING 186

8 END OF INJECTION VARIANCE 190

8.1 INFLUENCE OF INJECTION RATE OBSERVATION POSITION 191
8.2 RATE FLOAT 194
8.2.1 Characterisation of rate float 195
8.3 ADVANCED DATA MINING METHODS 198
8.4 RAIL PRESSURE INFLUENCE ON CLOSING DELAY 200

9 CONCLUSIONS 203

9.1 COMMERCIAL OBJECTIVE: IMPROVE OVERALL EQUIPMENT EFFECTIVENESS (OEE) 207
9.1.1 Secondary commercial objective: EU7 knowledge transfer 208
9.2 LIMITATIONS OF THIS PRESENT WORK 208
9.3 DIRECTIONS FOR FUTURE RESEARCH 208

10 REFERENCES 210

11 APPENDICIES 220

11.1 ADDITIONAL PHOTOS OF EXPERIMENTAL HARDWARE USED FOR SCHEMES ONE, THREE AND FOUR. 220
11.1.1 Experimental scheme one 'science mobile' data logger. 220
11.1.2 Experimental scheme three coriolis mass flow meter installation. 221
11.1.3 Experimental scheme four custom work area. 222
11.2 INJECTOR CALIBRATION TRIM VARIANCE WHEN USING AN ARO REGULATOR 223
11.3 PRODUCTION APPLICATION SPECIFIC CAVITATION FREQUENCY INTENSITY STUDIES 224
11.3.1 Rate tube bore surface finish 224
11.3.2 Effect of injection pressure and system backpressure 227
11.4 PRODUCTION APPLICATION SPECIFIC END OF INJECTION RATE VARIANCE STUDIES 230
11.4.1 Influence of additional connected volumes 230
11.5 APPLICATION SPECIFIC TRANSIENT TEST CONDITIONS INFLUENCE ON RATE FLOAT 236
11.5.1 Rate float implications for multiple injection event measurement 239
11.6 AMESIM MODEL DETAILS 240
11.6.1 Flexible hose model 240
11.6.2 Regulator poppet model 247
11.6.3 Regulator moving mass model 251
11.6.4 Regulator setting spring model 257

LIST OF FIGURES

Figure 1.1: Section view of E3 EUI installed in an engine block. 21

Figure 1.2: Section view of the Nozzle Control Valve operation, holding or releasing pressure in the Piston Spring Guide chamber to control nozzle opening timing. 22

Figure 1.3: E3 EUI EU5 internal valve schematics. Sourced from Lillington, Chetwynd and Jones (2015) 23

Figure 1.4: Engine dynamometer emissions test bay for heavy-duty diesel engines, sourced from (AVL, 2013) 24

Figure 1.5: Left: Light Duty NEDC drive cycle sourced from (Kurt, 2015). 24

Figure 1.6: Heavy-Duty EU5 Emissions test regime. Adapted from (Delphi, 2016) 25

Figure 1.7: Heavy-Duty EU6 Emissions test regime. Adapted from (Delphi, 2016). Top Left: World Heavy Duty Cycle (WHTC) Top Right: World Heavy Duty Steady-State Cycle (WHSC) Bottom Left: Off Cycles Emissions randomised testing (OCE) Bottom Right: WHSC load points represented by engine map position. 27

Figure 1.8: Delphi Technologies EU5 EUI and EU6 common rail fuel system product family. F2 system used in this work highlighted in dashed red. 29

Figure 1.9: Injector Opening Delay (OD) injection timing trim calculation. 31

Figure 1.10: Fuel consumption trends of Class 8 commercial vehicles. Sourced from (T&E, 2015) 35

Figure 1.11: Total NOx emissions from heavy-duty vehicles across London, showing the savings brought about from implementing EU6 emissions stand London-wide. Sourced from (TfL, 2016). 36

Figure 2.1: Pulsed injection rate shaping possible on DFI21 EU7 injectors. 42

Figure 2.2: Example of start of injection rate profiles for different EU6 F2 injector applications. Sourced from (Meek et al., 2014). 43

Figure 2.3: Schematic diagram of a piston displacement injection rate meter. 45

Figure 2.4: Schematic of a typical Zeuch chamber method rate of injection meter. 46

Figure 2.5: Effect of low pass filter cut of thresholds on observed signal distortion from a Zeuch chamber injection rate measurement system. 47

Figure 2.6: Principle of operation of a rate tube injection meter. Left: Generalised rate tube schematic. Right: Integration of area under the pressure wave to derive total injected fuel mass. 47

Figure 2.7: Injection rate signal for a rate tube injection meter. 50

Figure 2.8: Comparison of original unfiltered injection rate waveforms from:..... 51

Figure 2.9: Illustration of injection rate float / the cumulative offset correction algorithm and the signal thresholds required to implement it. 57

Figure 2.10: Simulation of the influences of fluid friction, pressure dependent and temperature dependent fuel properties on injection rate float. Sourced from (van Bebber and Reuter, 2017). 57

Figure 2.11: End of injection Bump artefact illustrated. Taken at Peak power engine condition for the F2 injector on existing production measurement equipment. 58

Figure 2.12: Images of EOI wetting and overspill known to occur after end injection when injecting into gaseous volume. A potential source of the bump artefact on the signal of a rate tube meter. Sourced from (Sykes et al., 2019). 59

Figure 3.1: Delphi Heavy Duty F2 EU6 injector. 62

Figure 3.2: The Bosch fuel rate indicator, Sourced from (Lillington, Chetwynd and Jones, 2015). 63

Figure 3.3: Original Delphi Technologies EU6 rate tube production measurement system design schematic (not to scale)..... 64

Figure 3.4: Front view of the original EU6 prototype development injector calibration test machine fitted with a single rate tube measurement system. Retired from series production and required refit. 65

Figure 3.5: Front view of an EU6 production injector calibration machine fitted with 4 synchronised identical rate tube measurement systems..... 65

Figure 3.6: 3D CAD assembly of the four parallel reciprocating stainless steel tube configuration used in series production injector calibration test machines. 66

Figure 3.7: Front view of an EU6 production injector calibration machine with front enclosure removed and a single reciprocating rate tube measurement system annotated. 66

Figure 3.8: Engine environment emulation system schematic. Comprising of the injector drive, high pressure supply, and acquisition sub-systems. 67

Figure 3.9: Top down schematic view of the EU6 production injector calibration test machine used for experimental scheme one 73

Figure 3.10: Top down schematic view of the EU6 production injector calibration test machine used for experimental scheme one, with Coriolis mass flow meter backpressure circuit retrofit that was used for experimental scheme three. 75

Figure 3.11: Top down schematic view of the upgraded EU6 prototype development, injector calibration test machine used for experimental scheme four. 77

Figure 4.1: Sources of variance identified for an injection rate measurement device 80

Figure 4.2: End of injection 'bump' artefact magnified view 81

Figure 5.1: Schematic diagram of the method of action of zero value variance..... 83

Figure 5.2: Injection rate pressure signal observation point in the production measurement system..... 85

Figure 5.3: Left: Tube termination block cross Section diagram. 86

Figure 5.4: Illustration of non-constant cross Section prior to the orifice, caused by the geometry of the production standard rate tube termination block. 87

Figure 5.5: Illustration of 6.35mm constant diameter cross Section prior to the orifice achieved by modifying the standard rate tube termination block to allow use of a custom orifice plate. 88

Figure 5.6: Modified constant cross section orifice inlet vs standard drilled BSP blank rate tube termination orifices. 89

Figure 5.7: Gyson Gromelle R4000 series 2bar non-return valves. 90

Figure 5.8: Check valve backpressure regulator position at the start vs the end of the following hose. 91

Figure 5.9: Effect on observed pressure wave of moving the check valve from the start to the end of the following hose. 2400bar pressure 2300µs duration injection condition. ... 92

Figure 5.10: : Modified 2bar production measurement system with check valve after the following hose, with the following hose to be modified highlighted. 93

Figure 5.11: Influence on observed pressure wave of different following hose ID..... 93

Figure 5.12: Left: Modified 2bar system with check valve after the following hose. 94

Figure 5.13: Effect on observed pressure wave of adding a fuel chiller and Coriolis meter at end of the following hose. 2400bar pressure 2300µs duration injection condition. 95

Figure 5.14: Left: Modified production 2bar system with check valve after the following hose. 96

Figure 5.15: Power Spectrum DFT analysis of adding a fuel chiller and Coriolis meter at the end of the following hose. 2400bar pressure 2300µs duration injection condition. .. 97

Figure 5.16: Delphi Technologies bespoke fuel chiller with narrow flow area. 99

Figure 5.17: Left: 2bar measurement system, Coriolis chiller circuit after following hose. 101

Figure 5.18: Effect on observed pressure wave of adding 30bar ARO® regulator before the Coriolis mass meter chiller. 2400bar pressure 2300µs duration injection condition. 101

Figure 5.19: DFT Power spectrum of the effect on the observed pressure frequencies of adding a 30bar ARO® regulator before the Coriolis mass meter chiller restriction. 2400bar pressure 2300µs duration injection condition. 102

Figure 5.20: Internal state variables of line lumped model. 108

Figure 5.21: Viscoelastic behaviour of a hose wall, ... 109

Figure 5.22: Mean flow rate profile used to simulate the 2400bar pressure 2300µs duration injection condition. 110

Figure 5.23: Final model iteration for standard 2bar production measurement system. 112

Figure 5.24: Initial vs final nozzle tooling geometry represented in the model. 115

Figure 5.25: Rate tube termination orifice model description. Left: Picture of Section view of the 0.8mm tube termination orifice. Right: Amesim orifice sub model. 116

Figure 5.26: 2bar check valve dynamic model description. Left: Picture of Section view of the 2bar check valve. Right: Final Amesim check valve model..... 117

Figure 5.26: 2bar model simulated injection rate for different air contents. 119

Figure 5.27: 2bar model simulated SOS at the observation point for different air contents..... 120

Figure 5.30: Simulated injection rate for different fluid temperatures in the rate tube vs experimental result from experimental scheme one. 122

Figure 5.31: Final tuned 2bar model simulated injection rate vs experimental result from experimental scheme one..... 123

Figure 5.32: Simulated injection rate with superimposed wave activity at the standard observation point and separated wave activity at the middle point of the rate tube. ... 124

Figure 5.33: Illustration of pressure waves in the following hose dissipating to atmosphere in the standard 2bar system. Also, the location of trapped pressure wave activity in the following hose in the 30bar system from experimental scheme one. 126

Figure 5.34: Final model iteration for standard 30bar regulator measurement system. 127

Figure 5.35: Additional model elements to construct 30bar system model. 127

Figure 5.36: Simulated and experimentally observed pressure at chiller inlet for the 30bar system model and experimental scheme one. Average of the dynamic simulated result shown in dash-dot blue line. 129

Figure 5.37: Comparison of pressure at the injection rate observation point for 1/4" and 3/16" BSP bore flexible hoses fitted to the 30bar system model..... 130

Figure 5.38: Comparison of pressure at the following hose inlet for 1/4" and 3/16" BSP bore flexible hoses fitted to the 30bar system model. 131

Figure 5.39: Simulated pressure at the following hose inlet with 3/16" bore diameter and 1m, 1.75m, 3m hose lengths. 133

Figure 5.40: FFT showing the frequencies and magnitude of the simulated pressure wave activity at the following hose inlet with 3/16" bore diameter and 1m, 1.75m, 3m hose lengths. 133

Figure 5.41: Restricted and unrestricted ARO® backpressure regulator poppet lift for the baseline 30bar system model. 136

Figure 5.42: Simulated pressure at the injection rate observation point for restricted and unrestricted ARO® backpressure regulator poppet lift for the baseline 30bar system model..... 137

Figure 5.43: Full 15hz period injection rate for different system temperatures on experimental scheme three. 2400bar pressure 2300µs duration injection condition. ... 138

Figure 5.44: Amplitude spectrum of full 15hz period injection rate for different system temperatures on experimental scheme three. 2400bar pressure 2300µs duration injection condition. 139

Figure 5.45: Additional pressure sensor instrumentation layout for..... 141

Figure 5.46: Optimised rate tube termination hydraulic design that minimises zero value variance..... 142

Figure 5.47: Following hose optimisation. 143

Figure 5.48: T-pipe installation and working principle schematic 144

Figure 5.49: T-pipe optimisation. 145

Figure 5.50: Single vs multiple flow orifice regulator comparison. 147

Figure 5.51: Equilibar© research series backpressure regulator principle of operation. 148

Figure 5.52: Schematic diagram of accumulator placement in system. 149

Figure 5.53: Effect of placing an 0.07L accumulator at the following hose inlet. 150

Figure 5.54: Effect of placing a 0.7mm orifice inlet restricted 0.07L accumulator at the following hose inlet. 152

Figure 5.55: Schematic of second accumulator at the rate tube termination orifice inlet. 154

Figure 5.56: Effect of placing a 0.5mm orifice inlet restricted 0.07L accumulator at the rate tube termination orifice inlet. Blue: Experimental scheme three fitted with backpressure system design optimisations and 0.5mm inlet restricted accumulator at the rate tube termination orifice inlet. Red: Experimental scheme three fitted with backpressure system design optimisations and no accumulator in the rate tube volume. 155

Figure 5.57: Result of all hydraulic design optimisations combined. Blue: Optimised hydraulic design. Red: Experimental scheme three baseline 156

Figure 6.1: The injected mass flow rate measurement window period. 158

Figure 6.2: RAW original injection rate signal illustrated. 2400bar pressure 2300μs duration injection condition. ±1 standard deviation bounds in red for 5 separate events. 159

Figure 6.3: High frequency analysis of baseline 2bar production measurement system. Top: Spectrogram of injection rate signal. 162

Figure 6.4: Section view of the (left) quarter wave cylinder and (right) Helmholtz chamber sensor port geometries. 165

Figure 6.5: Spectrogram of frequency intensity vs time for the injection event measurement window with the resonance identified for the quarter wave cylinder port configuration. 166

Figure 6.6: Spectrogram of frequency intensity vs time for the injection event measurement window with the resonance identified for the Helmholtz port configuration. 166

Figure 6.7: Ratio between primary and secondary Helmholtz frequencies across three pressure levels. 167

Figure 6.8: Injection pressure vs power spectral density for both port configurations. 168

Figure 6.9: Quarter wave resonance vs normalised frequency at the three lowest pressure levels observed and predicted using relative SOS changes derived from the reflection period in the tube. 169

Figure 6.10: Comparison of 2400bar pressure 2300μs duration injection rate signals. 170

Figure 6.11: Comparison of injection rate signals for the different amplifiers. 171

Figure 6.12: Injection rate signal for a full 15Hz period 173

Figure 6.13: Injection rate real amplitude cepstrum on experimental scheme one. 174

Figure 6.14: Full 15Hz period injection rate signal for 4, 6 and 12 minutes after beginning at ambient temperatures. 175

Figure 6.15: First reflected wave in rate signal at different temperatures 176

Figure 6.16: Zoomed view of the first cepstral peak with different tube temperatures. 176

Figure 6.17: Location of second cepstral peak with pump driveshaft rotation..... 177

Figure 6.18: Alternative charge amplifier signal routing (highlighted in yellow). 179

Figure 6.19: Difference in full cepstrum for alternative charge amplifiers. 179

Figure 6.20: Zoom of low quefrency range of the cepstrum for alternative charge amplifiers to highlight thin cepstral peaks..... 180

Figure 6.21: Schematic diagram detailing the ground loop source of measured injection rate signal noise identified using cepstrum. 181

Figure 6.22: Schematic diagram detailing the ground loop source of measured injection rate signal noise identified using cepstrum. 182

Figure 7.1: Existing manually operated weighing scales SOS to mass calibration technique. 184

Figure 7.2: Newly developed automatic test cycle coriolis flow meter SOS to mass calibration technique. 185

Figure 7.3: View of the Matlab curve fitting toolbox for 1 of the 4 datasets polynomial fit. uncalibrated fuel/RAWbits = Raw pressure signal at observation point; RateGuageTemp = Temperature of the thermocouple at the observation point; coriolisFuel = Average coriolis mass flow per second divided by the firing rate. Top: Surface map of polynomial fit. Bottom: Residual errors for the polynomial fit. 186

Figure 7.4: View of the Matlab neural network fitting app training epoch output for simple single layer network trained using 85%/15% training/validation dataset split and Levenberg technique for the 1000 data points. 187

Figure 7.5: Root Mean Square Error of SOS to temperature compensation using different techniques. 188

Figure 8.1: Sources of variance identified for an injection rate measurement device with the three sources of end of injection event variance highlighted in dashed box. 190

Figure 8.2: Post end of injection rate shape distortion in the form of a bump artefact. 191

Figure 8.3: Original and closer pressure sensor position in the injector nozzle tooling fixture. 191

Figure 8.4: 2400bar pressure 2300µs duration injection rate shape comparison for the two pressure sensor positions. 192

Figure 8.5: Effect of pipe friction on pressure gradient within a pipe. As demonstrated for a gas injector using the Bosch rate tube method by ARAKI et al. (2007). 193

Figure 8.6: Illustration describing the Rate float / signal cumulative phenomenon effect 2300bar pressure 2300µs duration injection event..... 194

Figure 8.7: Photographic images of test machine console injection rate display for first 60 seconds after a cold start. 196

Figure 8.8: Temperature at the injection rate sensor during warmup from a cold start. 2400bar pressure 2300µs duration injection condition. 197

Figure 8.9: Temperature at the outer surface of the nozzle tooling during warmup from ambient temperatures. 197

Figure 8.10: Stepwise feature selection with a ReliefF feature ranking layer applied to the result at the transient 2400bar pressure 745µs duration injection condition. Deviation in measured fuel value between injector test cycles as the target. CD and Supply pressure droop provide a combined predictor rank of 99% suggesting a strong relationship to fuel variance. 199

Figure 8.11: First two principal components for the 2400bar pressure 745µs duration injection condition with a strong positive correlation between CD and the Assumed fuel delta. 200

Figure 8.12: Illustration of the fluid hammer location in the high pressure supply pipe configuration of experimental scheme four..... 202

Figure 11.1: Picture of experimental scheme one 'science mobile' portable 1MHz four channels oscilloscope data logger. 220

Figure 11.2: Experimental scheme 3 coriolis mass meter installation on production equipment to enable 3 months of mass flow data collection in parallel with existing measurements. 221

Figure 11.3: Experimental scheme 4 custom work area and experimental apparatus. 222

Figure 11.4: Increase in 1 standard deviation for the production test injector drive logic timing correction conditions as measured for a population of 18 injectors..... 223

Figure 11.5: Location of nozzle 'Donut' seal carrier fixture..... 225

Figure 11.6: Spectrograms illustrating the effect of tooling erosion on frequency intensity. 226

Figure 11.7: Effect of increasing pressure on frequency intensities. 228

Figure 11.8: Measured fuel value drift caused by inception of seal degradation at wear level 2. A subtle fuel value drift of 0.6% (2-3mg) gradually trends over three hours, stabilising at a miss-calibrated position. 230

Figure 11.9: Injector nozzle seal 6 month dataset and wear scale devised. Left: Histogram of sear wear level categories over the six month period. Right: Visual scale for seal wear weekly inspection implemented in 2016. 231

Figure 11.10: Injection rate shape comparison between seal wear condition levels 2, 3 and no seal compared to a new seal baseline. Top: New seal baseline vs seal condition 2. Middle: New seal baseline vs seal condition 3. Bottom: New seal baseline vs no seal present in holder..... 232

Figure 11.11: Illustration of additional accumulator volume behind the nozzle seal and the relief channel that removes it. 234

Figure 11.12: Start of calibration test high pressure injection duration sweep. Rate float shown for descending injection durations at 2400 bar injection pressure. High to low (right to left) duration as the test sequence..... 236

Figure 11.13: Negative rate float observed after pressure level step down from 2400 to 1625 bar injection pressure. Rate float shown for descending injection durations at 1625 bar injection pressure. High to low (right to left) duration as the test sequence. 237

Figure 11.14: Difference in rate float magnitude between a fast transient production injector test cycle and a slow steady state temperature stabilised cycle for the 2400 bar 2300 µs test condition. 238

Figure 11.15: 2700 bar injection pressure, 3 x 750 µs duration with 500 µs separation between the injection events. Cumulative rate float magnitude increased highlighted in the time between injection events. 239

LIST OF TABLES

Table 2.1: Developing injector control trends, adapted from (Lillington, Chetwynd and Jones, 2015) 41

Table 3.1: Scheme of experiments 71

Table 3.2: Time required for experimental plan 71

Table 3.3: Summary of parameters common to all schemes 72

Table 5.1: Rate tube harmonic frequencies 97

Table 5.2: Relative roughness values for the tube lengths in the model. 113

Table 5.3: Rate tube resonance frequency orders observed within the following hose.. 134

Table 6.1: Location of second cepstral peak with pump driveshaft rotation 178

Table 8.1: Injection pressure level in the transient production injector test and the corresponding injection duration at which peak closing delay variance is observed..... 201

Table 11.1: Difference in fuel calibration trim standard deviation in microseconds for the standard vs ARO® backpressure circuit configurations for a population of 18 injectors. 223

LIST OF SYMBOLS AND ABBREVIATIONS

ASME	The American Society of Mechanical Engineers
AVL	UK emissions testing company
BSP	British Standard Pipe size specification
CAD	Computer Aided Design
CD	Closing Delay
CDI	Common-rail Direct Injection
CO	Carbon Monoxide
CO_x	Carbon Oxides
CV	Commercial Vehicles
DFI	EURO 7 Delphi injector designation
DfT	Department for transport
DFT	Digital Fourier Transform
DPCRS	BOSCH Dual Pressure Common Rail System
EC	European Community
ECE	United Nations Economic Commission for Europe
ECU	Engine Control Unit
EEC	European Economic Community
EGR	Exhaust Gas Recirculation
ELR	European Load Response test cycle
EOI	End Of Injection timing
ESA	Environmental Services Association
ESC	European Stationary Cycle
ETC	European Transient Cycle
EU	European Union
EU3	EURO 3 emissions standard
EU4	EURO 4 emissions standard
EU5	EURO 5 emissions standard
EU6	EURO 6 emissions standard
EU7	EURO 7 emissions standard
EUI	Electronic Unit Injector
EURO	Europe
FFT	Fast-Fourier-Transform
FIE	Fuel Injection Equipment
F2	Heavy Duty EURO 6 diesel injector made by Delphi Technologies
GDI	Gasoline Direct Injection
GEM	Sensor Brand
GRPE	Working Party on Pollution and Energy
HDA	Bosch-Moehwald Zeuch chamber rate measurement device

IAV	Injection Analyser rate tube measurement device
ICAM	Kistler industrial piezoelectric amplifier
ICCT	International Council on Clean Transportation
ID	Internal Diameter
IEEE	Institute of Electrical and Electronics Engineers
ISO	International Standard
LOWFLOW	Manufacturer of precision low flow rate regulators
LVDT	Linear Variable Differential Transformer
MATLAB	Scientific data visualisation programming enviroment
MDP	Minimum Drive Pulse
MH	MegaHertz frequency unit
MTC	Manufacturing Technology Centre
NCV	Nozzle Control Valve
NEDC	New European Drive Cycle
NI	National Instruments signal acquisition hardware manufacturer
NO_x	Nitrogen Oxides
NTE	Not To Exceed emissions limits
OCE	Off Cycle Emissions testing
OD	Opening Delay
OEE	Overall Equipment Effectiveness
OEM	Original Equipment Manufacturer
OMV	Outlet Metering Valve
PCA	Principal Component Space
PEM	Portable Emissions Equipment
PLC	Programmable Logic Controller
PLM	Product Life Cycle Management
PM	Particulate Matter emissions
PTFE	Polytetrafluoroethylene
PWC	Pressure Wave Compensation
RAW	Original unfiltered signal
RDE	Real Driving Emissions
RSME	Root Mean Square Error
SAE	Society of Automotive Engineers
SCP	Kistler amplifier rackmount system
SCR	Selective Catalytic Reduction
SCV	Spill Control Valve
SD	Standard Deviation
SOS	Speed Of Sound
SQL	Database software
TBD	To Be Determined
TC	Turbo Compound
ULEV	Ultra Low Emissions Zone
UN	United Nations

US	United States
VNL	Volvo class 8 truck model
WHDC	World-wide harmonized Heavy-Duty Certification
WHSC	World-wide harmonized Steady State Certification
WHTC	World-wide harmonized Transient Certification

1 INTRODUCTION

Decades of innovation in commercial vehicle engine design has been driven by the need to reduce localised air pollution and greenhouse gas emissions from combustion devices. This has resulted in the introduction of stringent emissions level targets for localised air pollutants harmful to human health, such as Oxides of Nitrogen (NO_x), Carbon Monoxide (CO) and soot. Recent legislation has also set targets for the release of greenhouse gasses called Carbon Oxides (CO_x), to reduce their cumulative effect on global warming.

Improving combustion quality and reducing emissions levels are directly linked to the fuel delivery into the combustion chamber. Factors such as the size of the fuel droplets, evaporation characteristics, and penetration of the fuel into the cylinder must be carefully optimised to minimise the levels of pollutants released in engine exhaust gases. The precise timing, quantity, and pressure of the fuel injection into the engine cylinder plays a major role in controlling these factors. Commercial vehicle diesel fuel injector design has been continually developed over the years to optimise these factors.

Early diesel fuel injection systems comprised a sprung loaded fuel delivery nozzle in each cylinder of an engine, and a fuel pump. When the fuel supply pressure generated by the pump surpassed the spring force, then the nozzle would open, and fuel delivery was achieved. This meant that the timing of the injection was tied to the mechanical movement of the fuel pump and its corresponding pressure rise characteristic. This method, whilst reliable and simple to implement, did not allow for high injection pressures, due to issues with supply pressure pulsation in the connection lines to the injectors. It also meant that the injection timing was fixed to engine operating speed for different parts of the engine map. Without this facility to change injection timing, engine calibration engineers could not meet the increasingly stringent emission targets they faced. To meet this need, the design of fuel injection systems have become increasingly more sophisticated.

The performance of each injection fuel system must be measured when it is manufactured, to guarantee the precise injection timing and quantity on engine applications. Each new generation of commercial vehicle diesel fuel injection systems has improved the ability of engine calibration engineers to control precisely the timing and quantity of injection.

Consequently, there has been a need to improve the precision of the corresponding measurement equipment used to characterise the fuel system performance in production. The primary focus of this work is to meet the requirements for injection timing and quantity measurement presented by the current and future generations of commercial vehicle diesel fuel injector designs. This work enables future reductions in commercial vehicle emissions levels, both

locally and globally, by improving the measurement technology used to characterise advanced fuel system designs in a production environment.

To better understand the motivations for the present research, this Section will describe the evolution of diesel injector design over time, examine the difference between light and heavy duty testing cycles, detail the impact of EURO 5 (EU5) vs EURO 6 (EU6) CV emission testing on diesel fuel system design and characterisation, and highlight the limitations of the existing system as the motivation for the present study.

1.1 Delphi Injector design history up to EU5 emissions levels

To overcome the lack of timing control available with the previously discussed mechanically limited systems, fast acting, electromechanically actuated, hydraulic solenoid valves were introduced into the injector design. This allowed for the timing of the pressure rise and fall inside the injector to be electronically controlled by an Engine Control Unit (ECU). This innovation resulted in the E1 Electronic Unit Injector (EUI), featuring an integrated fuel pump to simplify fuel system design. Designed by Delphi Technologies to achieve EURO 3 (EU3) commercial vehicle diesel emissions levels, the engine installation of the EUI design is shown in Figure 1.1.

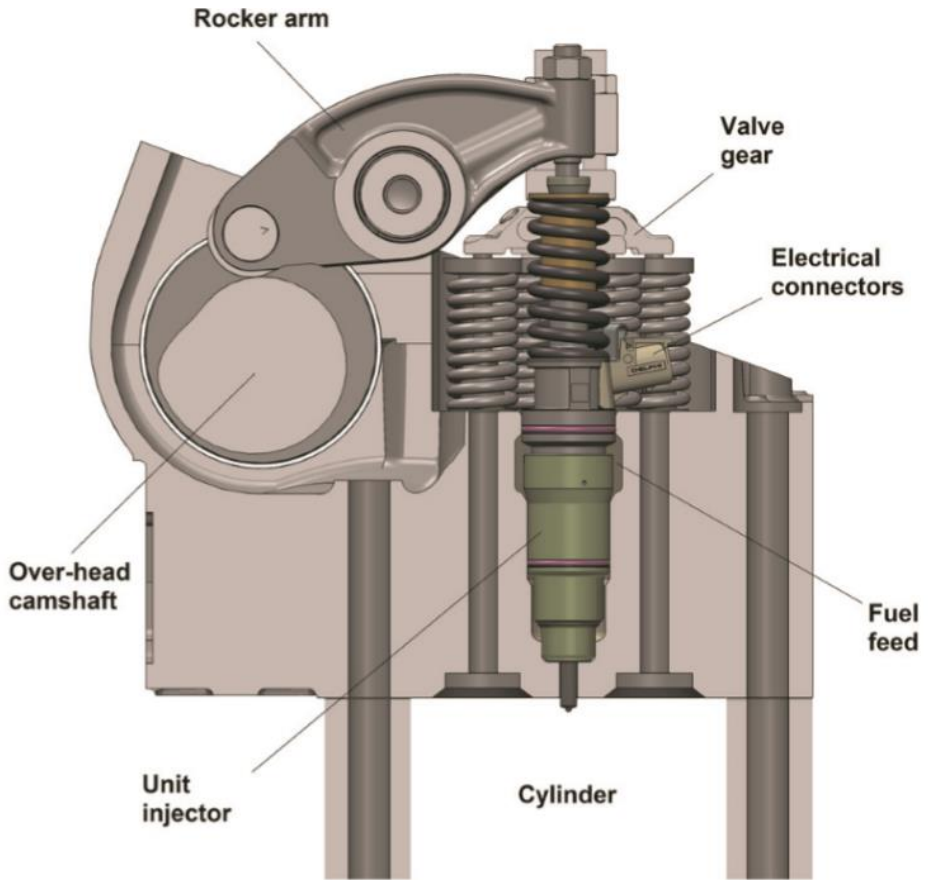


Figure 1.1: Section view of E3 EUI installed in an engine block.

It enabled engine calibration engineers to dictate when the pressure behind the nozzle rose, and subsequently, the time it would take to overcome the spring force holding it closed, starting the injection event. By spilling the pressure during injection, the pressure behind the nozzle will collapse, allowing the nozzle spring to force it closed, ending the injection event.

This design relied on nozzle spring force setting to control when the nozzle opened. This limited the injection pressures that could be achieved inside the injector, because of mechanical constraints. It was discovered that the high injection pressure drives cavitation activity in the injected spray, enhancing air entrainment and reducing emissions through a more complete combustion of the injected fuel, as demonstrated by Dembinski, Angstrom and Winklhofer (2014).

Higher injection pressures were sought to enable greater use of Exhaust Gas Recirculation (EGR) technology, that redirects exhaust gases back into the air intake, significantly reducing engine emissions levels such as NO_x. When using this technology, greater injection pressure is required to penetrate the fuel spray through the more dense exhaust gases re-entering the cylinder. To enable higher injection pressures, a solution was sought that would also allow for control of pressure rise inside the nozzle, independently to the nozzle spring force that had previously dictated it.

This was achieved using a device called the Nozzle Control Valve (NCV). The previous valve used is called the Spill Control Valve (SCV) which controls the rise of pressure within the injector. With the addition of the NCV, this pressure could be redirected to act on the nozzle needle to force it to remain closed, regardless of the pressure inside the injector. When the desired pressure has been achieved within the injector, the NCV releases the pressure that is forcing the nozzle needle closed, allowing it to open rapidly and deliver fuel at a higher starting injection pressure. A Section view to illustrate how the NCV achieves this control is provided in Figure 1.2.

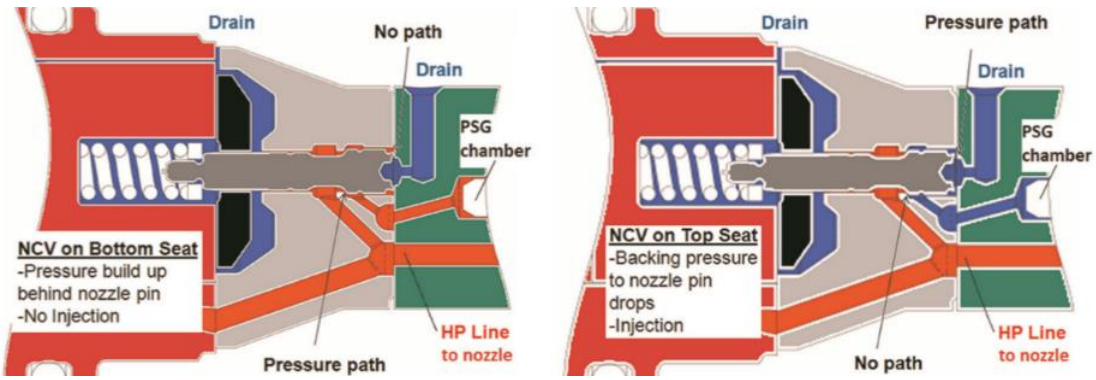


Figure 1.2: Section view of the Nozzle Control Valve operation, holding or releasing pressure in the Piston Spring Guide chamber to control nozzle opening timing. Left: NCV operation to hold nozzle closed, Right: NCV operation to open nozzle and start injection. Adapted from Lillington, Chetwynd and Jones (2015).

The NCV technology achieves higher levels of spray penetration, enabling the use of EGR heavy engine applications. This implementation was called the E3 EUI, as shown in Figure 1.3.

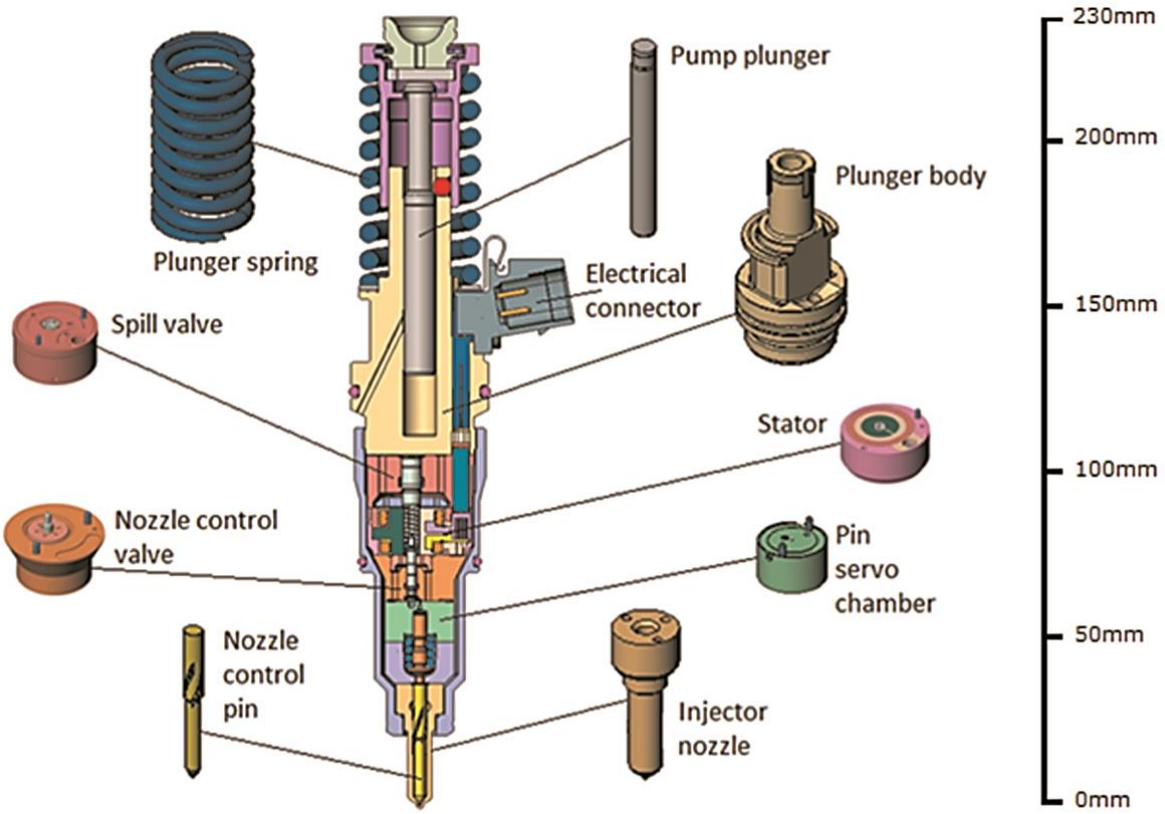


Figure 1.3: E3 EUI EU5 internal valve schematics. Sourced from Lillington, Chetwynd and Jones (2015)

Whilst the rise and release of pressure could be controlled by the SCV and NCV, the rate of this rise was still influenced by the speed of rotation of the cam that drives the pumping element of a unit injector. Therefore, up to EU5, the rise of pressure within the injector was influenced and limited by the engine cam timings at different engine speeds. For example, at low engine revolutions per minute (rpm), it is impossible to generate higher pressures due to the slow rate of pressure rise within the injector.

1.2 The impact of EU6 diesel emissions standards

The EUI E3 injectors were used in engines around the world to achieve high injection pressures up to 2700bar and EU5 emissions levels. However, when EU6 emissions were introduced in 2013 (Regulation, 2005) for commercial vehicles, the nature of the emissions testing regime forced a technological leap in injector design. To understand the change in the fuel system strategy adopted, we must first examine how the emissions test regime enforced new requirements on engine calibration engineers, and hence fuel system OEMs through the years.

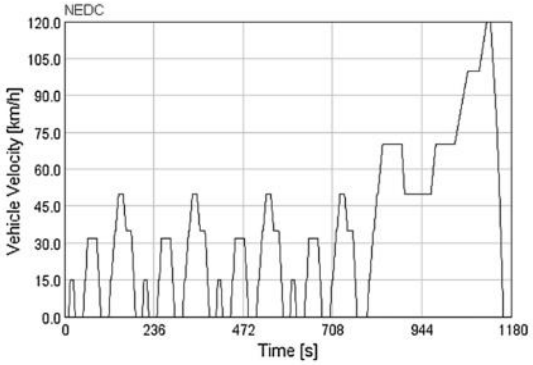
1.2.1 Heavy duty vs Light duty emissions testing

There are separate rules for governing the emissions testing of Commercial Vehicles than for light and medium duty passenger vehicles. The tests carried out and the overall methodology are significantly different, to reflect the different use cases and environmental implications. The primary difference is that light and medium duty vehicles are tested with the whole vehicle on a rolling road dynamometer. However, heavy duty emissions testing is carried out as an engine out test, with the engine and emissions system directly mounted to a dynamometer, as shown in Figure 1.4.

Figure 1.4 has been removed from this version of the thesis due to copyright restrictions

Figure 1.4: Engine dynamometer emissions test bay for heavy-duty diesel engines, sourced from (AVL, 2013)

At the time of EU6, light duty testing was still being carried out using the New European Drive Cycle, on a whole vehicle dynamometer as shown in Figure 1.5.



A photograph has been removed from this version of the thesis due to copyright restrictions

Figure 1.5: Left: Light Duty NEDC drive cycle sourced from (Kurt, 2015). Right: Light duty whole vehicle dynamometer sourced from (AVL, 2013).

This drive cycle was originally implemented in 1970 and last updated in 1997 (Andre *et al.*, 1995). Its original intention was to provide a normalised emissions level testing regime that could be compared between countries to enable proper functioning of the common market. Until this point in history, differences in

local climate, driving styles, availability of precise emissions measurement equipment, and methodology varied greatly from country to country. The NEDC provided a unified methodology that would be independent of region (Samuel, Austin and Morrey, 2002), in which it succeeded for many decades.

Due to technological limitations at the time of its implementation, and the mechanical nature of engine control, it was necessary for a human driver to achieve the required drive cycle within a tight boundary for engine speed and load. This forced the use of unrealistic constant acceleration and constant speed portions of the map, to ensure the operator had a good chance of following it. Failure to stay in the required bounds would result in the test having to be repeated, leading to lengthy and costly delays.

This was sufficient when vehicles were slower, with low acceleration and power at the time of its introduction. Since the introduction of electronic fuel systems, turbochargers and efficient engine design in recent decades, the accelerations seen during real world driving have moved further away from the load regime represented by the linear ramps and speed of the test.

1.2.2 EU5 commercial vehicle emissions test regime

For EU3 to EU5 emissions levels, commercial vehicle testing involved 3 tests on an engine dynamometer, The European Transient Cycle (ETC), European Steady State Cycle (ESC), and European Load Response (ELR) as shown in Figure 1.6.

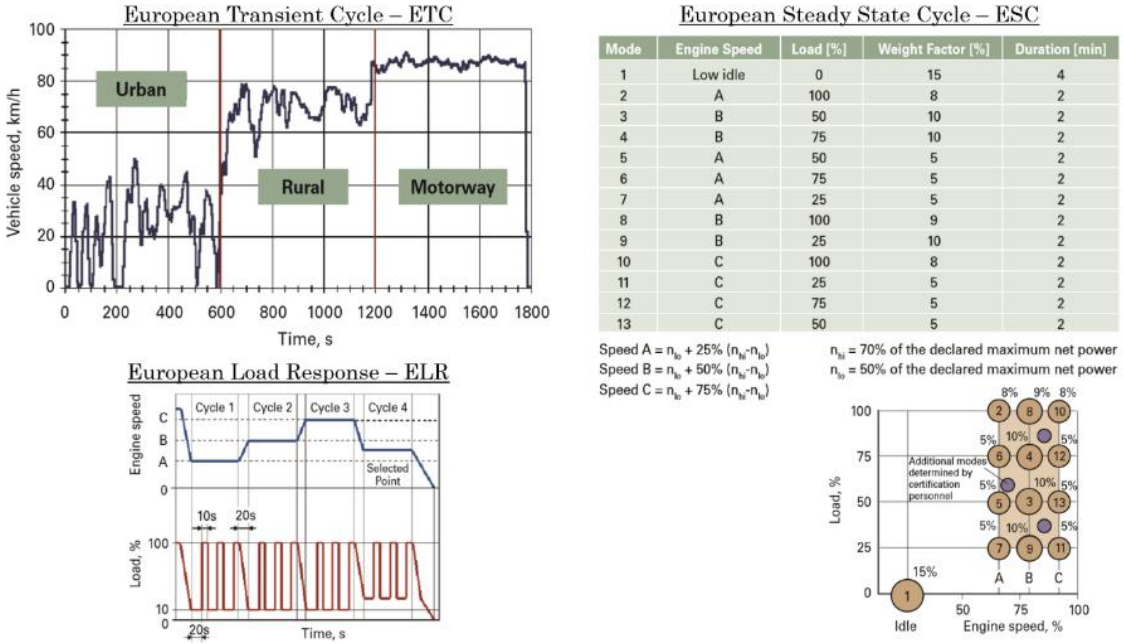


Figure 1.6: Heavy-Duty EU5 Emissions test regime. Adapted from (Delphi, 2016)
Top Left: European Transient Cycle (ETC);
Top Right: European Steady State Cycle (ESC);
Bottom Left: European Load Response (ELR);
Bottom Right: ESC load points represented by engine map position

The ETC was based on real road duty cycle measurements of heavy-duty vehicles (Delphi, 2016), containing start/stop urban city driving with a maximum speed of 50km/h, rural driving starting with a heavy acceleration, and motorway driving with steady average speeds of around 88 km/h.

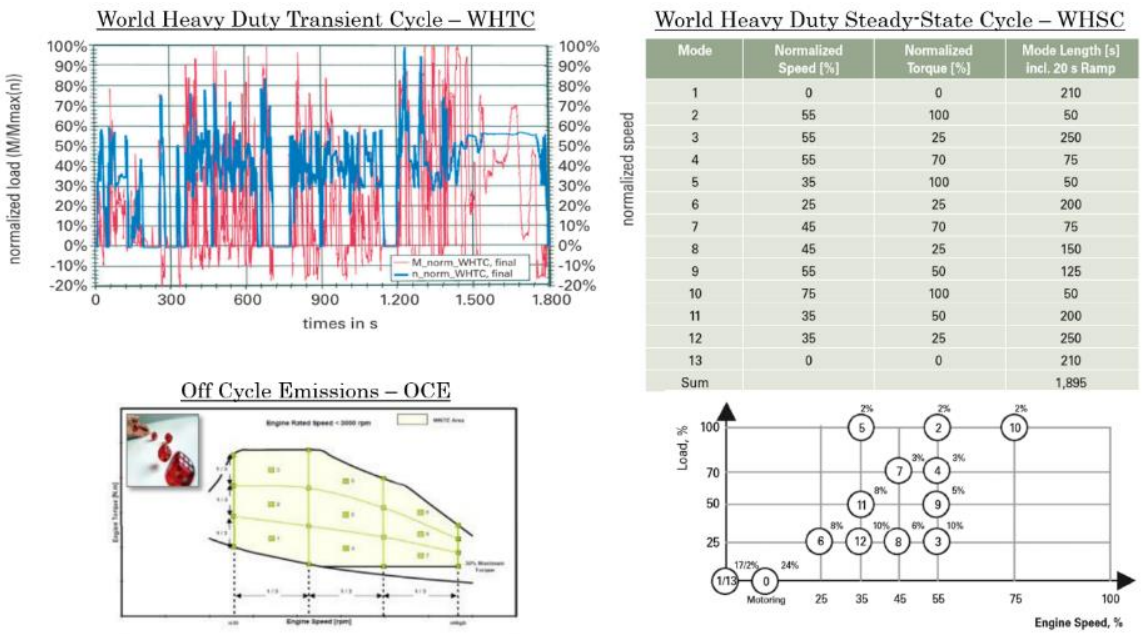
The ESC is carried out at set engine load points for a fixed time period. Engine speed must be controlled to within ± 50rpm, with maximum torque held to within a ± 2% limit. The emissions are then averaged across time with weighting factors applied. The engine speeds A, B and C correspond to low medium and high speeds. With C being the speed at which the engine condition develops 70% of declared net peak power, and A is the engine condition that develops 50% of declared net peak power. There is also a smoke test called the ELR that measures average smoke levels at 4 separate load conditions at different engine speeds.

The ETC was already based on real world driving data at the time of its launch in 2000, unlike the NEDC used for light duty applications. This was possible because of the use of computerised electronic control of fuel injectors in all heavy duty commercial vehicles since EU3 emissions levels. This enabled near instantaneous control inputs to the engine under test on the dynamometer, by sending instructions to the Engine Control Unit (ECU) that controls the fuel system timing. Therefore, heavy-duty testing was not subject to the limitations of whole vehicle testing or a reliance on human operators to control the engine demand, as seen in light duty testing. This is evidenced by the nuanced and erratic trend possible for the ETC cycle, when compared to the flat trends of the NEDC cycle.

Hence, the diesel fuel emissions of commercial vehicles were under greater scrutiny earlier on, in terms of regulatory requirements, than light-duty vehicles. Despite the industry overcoming all the challenges presented by this strict test regime for EU3, EU4 and EU5 heady-duty emissions, the changes to the test requirements for EU6 presented the need for a technological leap forward in design and capability of diesel engines fuel systems.

1.2.3 EU6 CV emissions test regime

For EU6 emissions levels, Heavy-Duty testing involved 3 new test cycles on the engine dynamometer: the World Heavy-duty Transient Cycle (WHTC); the World Heavy-duty Steady-state Cycle (WHSC); and the Off Cycle Emissions test (OCE) as shown in Figure 1.7.



Mode	Normalized Speed [%]	Normalized Torque [%]	Mode Length [s] incl. 20 s Ramp
1	0	0	210
2	55	100	50
3	55	25	250
4	55	70	75
5	35	100	50
6	25	25	200
7	45	70	75
8	45	25	150
9	55	50	125
10	75	100	50
11	35	50	200
12	35	25	250
13	0	0	210
Sum			1,895

Figure 1.7: Heavy-Duty EU6 Emissions test regime. Adapted from (Delphi, 2016).
Top Left: World Heavy Duty Cycle (WHTC)
Top Right: World Heavy Duty Steady-State Cycle (WHSC)
Bottom Left: Off Cycles Emissions randomised testing (OCE)
Bottom Right: WHSC load points represented by engine map position.

The WHTC was based on the worldwide patterns of commercial vehicle use, as compiled by the UN ECE GRPE group (Steven, 2001). The test is performed on an engine dynamometer under cold start conditions and then repeated for hot start conditions. The emissions levels are measured cumulatively with an overall limit for the cycle. The initial period of the cold start test is often responsible for more than half of the cumulative emissions, because of the requirement to raise exhaust emissions systems to their required operating temperatures.

When comparing the WHTC to the ETC, is it apparent that the new test contains far more aggressive acceleration and deceleration ramps at an increased frequency across the cycle. Therefore, the WHTC cycle was far more dynamic, and hence difficult to plan for, than the ETC previously used. To enable engine calibration engineers to guarantee the emissions levels over a wider performance range of the new test cycle, the timing and quantity of fuel injection events had to be defined and measured over a broader range of running conditions

The WHSC is similar to the ESC in that it is a steady state test at defined engine load conditions, with these conditions modified as specified by the UN ECE GRPE group. This test was conducted under hot start conditions on an engine dynamometer.

The last and most significant portion of the test regime is the addition of the OCE test. Under this test, a control area for the engine map is divided into a

grid. Three grid cells are selected at random and the emissions levels are measured at three points within these cells. The emissions levels are evaluated against Not to Exceed (NTE) limits for the entire test. The random nature of this test ensures that the emissions of the engine application will meet these requirements for the entire engine map, as the specific conditions to be tested cannot be known beforehand.

Without the presence of OCE testing up to EU5 emissions levels, it was possible to characterise fuel injectors across a small number of steady state load conditions during production measurement, to calibrate an engine application sufficiently to pass the test. The additional uncertainty of the OCE test forced the measurement of injection timing and quantity across the whole engine map in production for the first time, as the characteristics of injection had to be guaranteed for all load conditions. This also brought about the requirement for testing under transient conditions in production, as it was no longer possible to use a steady state testing methodology within the constraints of a short production cycle time.

The OCE requirement applies to Portable Emission Monitoring (PEMs) on the road emissions testing for the entire life cycle of the vehicle. For EU6, this is defined as up to 700,000km or 7 years, whichever is reached first. Hence the emissions controls and fuel delivery systems have to operate optimally for this period. With the aggressive work cycles of commercial vehicles, this presented a challenge in terms of powertrain component durability. It was now a requirement to guarantee the timing and quantity of fuel injection systems for their entire working life. This required that the initial characterisation test performed in production be as precise as possible, to limit the effect of any drift in performance over life because of component wear.

An initial solution to address these stringent emissions requirements was the use of 1700bar peak injection pressures paired with Selective Catalytic Reduction (SCR) emissions control technology, that injects a liquid-reductant agent directly reducing NO_x content in exhaust fumes. This practice is being replaced, as the latest EU6 applications favour >2000bar EGR heavy strategies, offering reduced engine out emissions and hence SCR reductant agent costs.

The need to achieve the required emissions levels at any engine condition in combination with an aggressive transient test, drove forward a technological leap in fuel system design. To meet the emissions levels at any engine condition, new capability was needed to dictate injection pressure, timing and quantity, independent of the position in the engine map. This was not possible with the EUI fuel system design, because of its dependence on cam speed to develop injection pressure.

1.2.4 Delphi EU6 common rail injector design

To meet EU6 emissions levels, common rail fuel systems were necessary and introduced to the commercial vehicle market (Hardy *et al.*, 2012). By using a high pressure common rail accumulator volume as an injection pressure source, injection can occur independent of engine timing and operating speed. This enables full flexibility of fuel injection parameters across the entire engine map, as required by the EU6 emissions test.

This was achieved by supplying fuel to the common rail via electronically controlled pumps, that maintained the desired pressure in the rail for the connected injectors. Even at low engine operating speed, the pumps could be controlled such that they still develop high pressure to the common rail and injectors. This strategy was achieved by Delphi Technologies using 3 different approaches as shown in Figure 1.8.

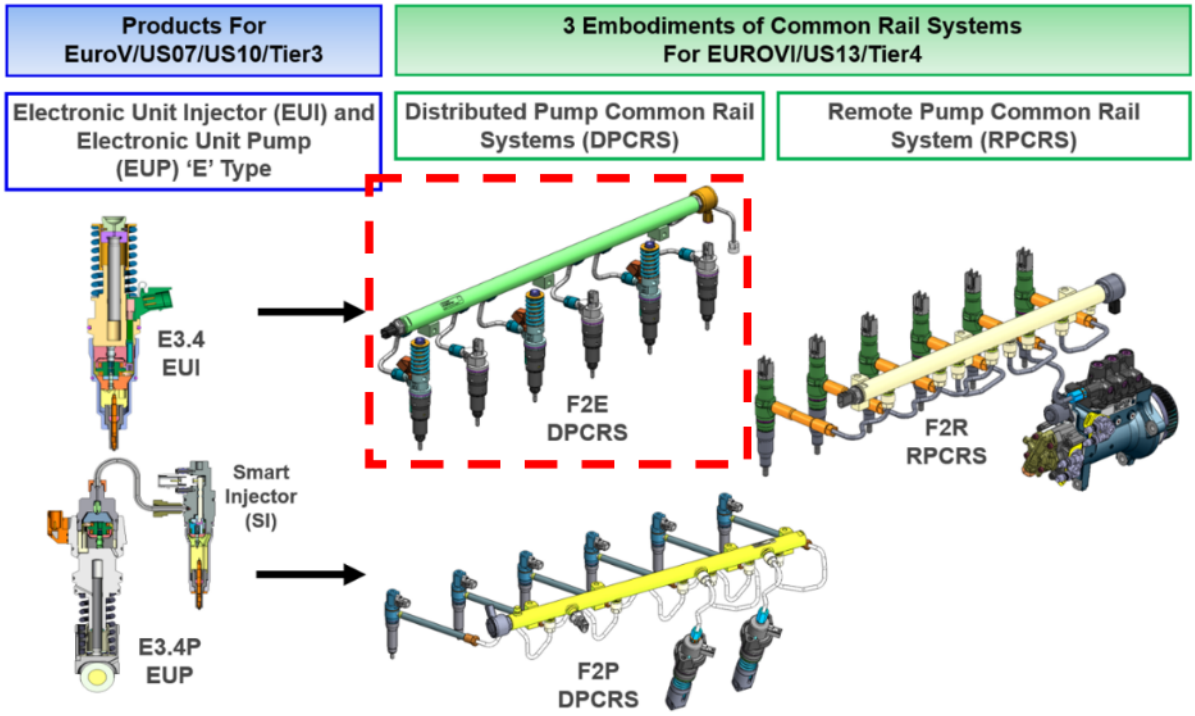


Figure 1.8: Delphi Technologies EU5 EUI and EU6 common rail fuel system product family. F2 system used in this work highlighted in dashed red.

The focus of the present work is on the F2 DPCRS product, which acted as a direct replacement for the E3 EUI product previously used for EU5 emissions levels. Typically, three of the injectors would have pumping elements to develop pressure in the rail for all injectors, with the remaining three injectors consisting only of an injector body, NCV and nozzle. This product is made by Delphi Technologies for Volvo Trucks EU6 engine applications and is manufactured at the Stonehouse site, where this research was conducted.

All EU6 fuel system designs all share a common theme, the pressure development is separated from the injector and stored in an accumulator volume. With the previous EUI design, the pumping element was integrated into the injector and connected to the nozzle via a short internal connection line with no accumulator. On the F2 design, the outward appearance for the pumping injectors is similar to the EU5 E3 EUI design. However, inside there is no connection between the pumping element and the injector nozzle as before. Instead, the pressure developed by the pumping element is redirected to the common rail via latching Outlet Metering Valve (OMV), which replaces the role of the SCV in an E3. When the NCV releases pressure behind the nozzle needle to initiate injection, the fuel is drawn separately from the rail. Hence the pumping and injection elements of an F2 injector can be considered independent devices.

The versatility of these systems allows for a multitude of fuel injection parameters to be selected across the engine map. With additional requirements of OCE randomised testing and on the road life cycle emissions, this presented a challenge for fuel system OEMs. The performance of the injector, with regard to injected quantity and timing, had to be characterised across the entire engine map, to the strictest requirements in terms of production limits so far. This led to a change in end of line diesel injector test strategy for the EU6 fuel systems. The challenges involved in using this new strategy is the primary motivation for the present research.

1.2.5 Diesel fuel system calibration trim strategy

When a new engine application is calibrated to meet emissions requirements, an initial batch of diesel fuel injectors will be supplied to the engine manufacturer. These injectors are often referred to as 'golden' nominal reference injectors. The engine map will then normally be fixed for the life of the application, once it is certified by the appropriate regulatory bodies. This requires that every injector supplied for that engine application, must perform the same as the original 'golden' reference injectors supplied, to ensure that they perform as expected across the whole engine map.

Due to manufacturing variance of hydraulic valve component features down to the sub-micron level, no two diesel fuel injectors perform exactly the same. Therefore, there is a requirement to measure and adjust the performance of each injector to match the original 'golden' injectors supplied for the initial engine tuning at start of production. This is achieved by measuring the delivery and timing of each injector, comparing it to the 'golden' reference injector performance, then adjusting its electromechanical control timing and duration accordingly to compensate for performance differences.

This adjustment is referred to as injector 'trim', achieved by shifting, extending, or shortening of the electronic drive signal. These trims must be measured to within a 5 microsecond resolution for timing, and to within a milligram for injected quantities. The trims are calculated during end of line testing of the diesel fuel injectors by comparing their performance to the 'golden' injector reference.

The trims are later laser marked onto a 2D matrix on the injector electrical connector. This matrix is scanned upon installation of an injector in the engine. So that the ECU can apply the trims to achieve nominal injector performance for each engine cylinder. Any injector with a trim outside of these tolerances, that would cause abnormal performance at any part of the engine map, is rejected.

For example, if the injector being tested delivers fuel later than the 'golden' nominal reference injector set, then the electronic drive of that injector can be adjusted to start earlier. So that the actual injection event shifts later in time and matches the effective timing of the 'golden' nominal reference injector set, as shown in Figure 1.9.

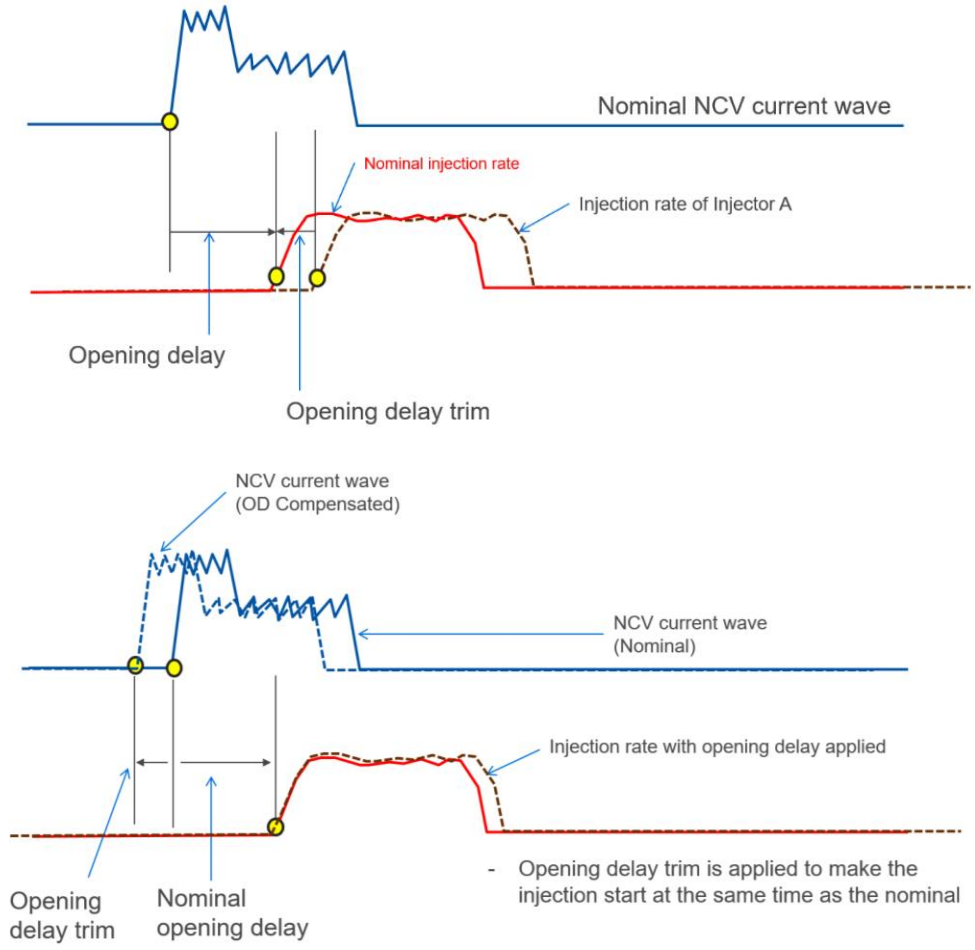


Figure 1.9: Injector Opening Delay (OD) injection timing trim calculation.
Top: Measurement of OD start of injection timing trim.
Bottom: Application of OD start of injection timing trim.

The implication of this process is that the precision and reproducibility of end of line injector testing has a direct impact on engine emissions achieved in the real world. Any errors in the injector timing and fuel quantity calibration trims will translate into an abnormal performance of the injector in the engine and potentially increase its emissions levels in the field. It is because of this link to real world emissions consequences that the calibration stability of end of line production injector calibration test equipment must be strictly monitored and maintained.

The additional requirements imposed on engine calibration engineers by the EU6 Heavy-Duty WHTC, WHSC and OCE cycles, meant that slow steady state test strategies could not measure emissions performance across the whole engine map within an acceptable production cycle time. To achieve an order-of-magnitude increase in the number of individual test conditions within the production cycle times required, the test strategy shifted to fast transient load testing. This challenging requirement to ensure precise measurement of injection timing and fuel quantity under dynamic transient load conditions, is why the F2 EU6 end of line injector calibration test is the focus of this work.

1.3 Objectives

The overall aim for this work was to improve reproducibility and repeatability of commercial vehicle diesel injector calibration. This work was required to provide both short-term commercial outcomes and meet requirements of fuel measurement systems for future legislation.

The objectives are:

1. To develop an understanding of the effects of production test environmental variables and measurement system hydraulic configuration, on the measurement variance of a F2 EU6 injector calibration test machine.

The causes of calibration instability in the F2 EU6 injector calibration test process are not known and hence cannot be controlled. With insight into the sources of variance, both the test strategy and hydraulic parameters of the measurement system can be optimised to minimise their impact on daily production calibration precision and stability. The production measurement system under consideration has a consecutive injection standard deviation of 2-3 mg at maximum injection loads. The aim is to bring the system in line with commercially available measurement systems, which are capable of a standard deviation of less than 1 mg for consecutive identical injections.

2. To evaluate novel numerical methods for extracting knowledge of and to predict sources of measurement variance.

The production test equipment under examination for the present study produces a wealth of data for greater than 5000 injector tests a day. Current methodologies are not capable of extracting detail about the sources of measurement variance from this deluge of data, because this development of the F2 EU6 injector calibration test measurement system has stalled. Therefore, this work will aim to automate the extraction of knowledge of sources of measurement variance from this data, by the use of advanced data science methodologies.

3. To experimentally evaluate the effect of rapid transient load test strategies on the sources of variance found within an F2 EU6 production rate tube injection measurement system.

Little is known about how the measurement variances are affected by a fast, transiently changing load input into the system. This objective was to better understand how EU6 transient injector production test strategy affected sources of variance identified during objective 1. Then develop strategies to mitigate any

undesired influences on the measurement of injector performance in continuous production conditions because of transient loads.

1.4 Commercial motivations for research

All the objectives combined will result in improved Overall Equipment Effectiveness (OEE), shown in Equation [1.1], which is the key measure of productivity for the EU6 injector test process.

$$OEE = Availability \times Performance \times Quality \qquad [\ 1.1\ ]$$

If less than 1 mg consecutive injection standard deviation is achieved during objective one through design optimisations, then the daily yield for tested injectors will improve, due to reduced occurrences of rejected test cycles from calibration instability. This improvement in yield will result in improved *Quality* output of the injector test process.

By implementing novel data mining and visualisation techniques for objective two, downtime of the injector test process should be reduced, as faults present within the process will be identified in less time by the engineers responsible for maintaining the process. This will result in improved *Availability* of the injector test process.

By identifying the influence of transient test strategies on injection measurement for objective three, it will be possible to optimise the test sequence to reduce the overall process cycle time per injector, resulting in improved *Performance* of the test process.

Increased OEE will also result in lower labour costs per test, reduced energy consumption per test, reduced injector rework activities, and a capacity uplift for the bottleneck EU6 injector test process.

As shown in the US Supertruck program (Delgado and Lutsey, 2014), common rail injector technology can enable fuel efficient mild hybrid strategies. Enabling a potential solution to the stagnating 20 year fuel economy trend for class 8 commercial vehicles in the EU, as shown in Figure 1.10.

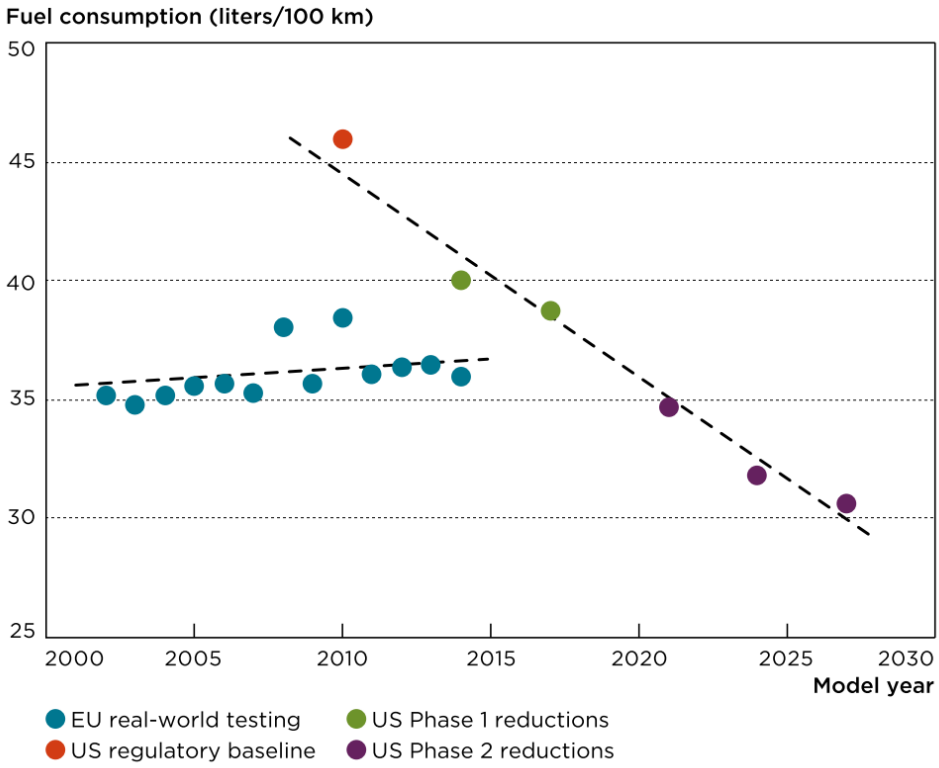


Figure 1.10: Fuel consumption trends of Class 8 commercial vehicles. Sourced from (T&E, 2015).

Therefore, end users of the F2 EU6 fuel injection system will reap benefits from this work in terms of running costs, as the product becomes more available from increased production capacity.

Near future reductions required by US Phase 1 emissions legislation is below the previous trend and hence must be improved upon. The International Council for Clean Transportation (ICCT) estimates that engine optimisation alone, made possible by common rail fuel systems, could represent up to 10% improvement in fuel economy for commercial vehicles by 2030 (Delgado *et al.*, 2016). Therefore, improvements in fuel system measurement capability outlined in the objectives of the present work, must be achieved to make this future fuel economy improvement possible.

1.5 Environmental motivations for research

In the European Union (EU), 30% of road transport CO_2 emissions are produced by commercial vehicles (Muncrief and Sharpe, 2015), accounting for 5% of the total EU $C0_2$ emissions. Volvo trucks have a 19% market share in the EU, the primary customer of the F2 fuel system. By converting the existing Volvo fleet of commercial vehicles to EU6 F2 fuel systems, it is estimated that approximately 3 Mega tonnes of $C0_2$ could be saved per year in the EU.

Hence, by increasing the production capacity of the F2 EU6 production line as part of this work, there will be a significant reduction in carbon emissions responsible for climate change.

1.6 Human welfare motivations for research

In terms of human health, it is known that oxides of nitrogen are particularly harmful. For example, air pollution in London has been shown to stunt the growth of children's lung capacity by up to 5% less than normal in the most polluted areas (Mudway *et al.*, 2019), potentially leading to significant health problems throughout their life. To combat this terrible impact, Transport for London (TfL) have implemented the Ultra-Low Emissions Vehicle zone (ULEV) for all vehicles types (TfL, 2016). In this zone, only EU6 certified commercial vehicles are allowed to travel without incurring significant financial penalties. This action was taken after TfL modelled the impact of converting all commercial vehicles in London to the EU6 emissions standard. They found that it had the greatest single impact of any emissions legislation measure they could implement for all vehicle types as shown in Figure 1.11.

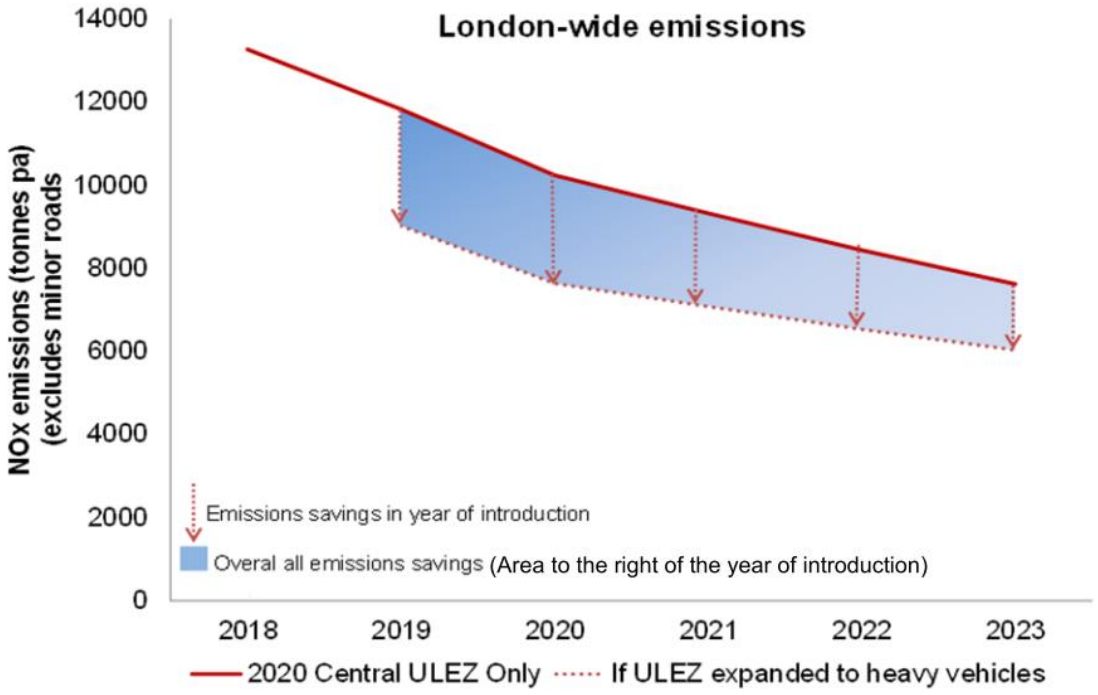


Figure 1.11: Total NOx emissions from heavy-duty vehicles across London, showing the savings brought about from implementing EU6 emissions stand London-wide. Sourced from (TfL, 2016).

Therefore, increasing the production capacity of the F2 EU6 production line as part of this work, will have a significant impact on the long term health of inner city children exposed to diesel exhaust emissions from commercial vehicles.

1.7 Research Approach

The present body of research was limited to use of equipment and computing resources available within a manufacturing production environment. The experimental apparatus already exists to a specific configuration, so changes to experimental hardware in the form of production test equipment could only be temporary, restricting their scope.

To overcome this, initial investigations were carried out on unmodified production equipment and in simulation space. Lessons learned from those investigations are used to devise a new experimental scheme, in terms of a heavily modified production injector test machine designed for targeted investigations.

The only injectors available for study are F2 EU6 injectors because of the specialisation of the Stonehouse production site. This was not deemed an issue, as it is the measurement system variance that was of interest. A common injector and running conditions are used throughout, so that all experimental schemes have directly comparable results. The F2 injector represents the most advanced commercial vehicle injector available at the start of the present work and was deemed appropriate for the study.

The design of the experimental procedures conformed to that of a production injector test cycle, due to the nature of the apparatus and intended goals of the work. This is intentional, so that experimental results were representative of the production environment.

The research is conducted in a production environment, in isolation from other research activities in the company and collaborating university. There was no onsite academic support regarding existing literature and discussion of experimental results. The resources available at Oxford Brookes are online and were readily available. Weekly supervisory meetings were held to discuss results and progress. This was to ensure the focus of the work remained academically grounded. Instead of conforming to the norms of a typical commercial investigation, with limited scope.

The production environment provides a wealth of live continuous data output that can be cross-referenced with experimental results. When common relationships were observed between experimental and production data, the knowledge gained was actionable within the production environment. The observed effect of these changes were then assessed using months of production data.

For each experimental scheme, a specific experimental procedure was devised and strictly adhered to, with conditions for a controlled experiment defined

beforehand. If the dataset for an experimental trial did not meet these conditions, then the data was rejected, and the experiment repeated.

An extensive review of existing knowledge regarding sources of measurement variance was carried out. A list of known sources of measurement variance that have yet to be fully characterised was then compiled. Initially, a deductive approach was applied to test existing assumptions and knowledge gained from the review. Then the research activities shifted to an inductive approach, using simulation space to explore novel experimental results, not explained by deductive reasoning. Generating novel theories that can then be tested on a custom experimental apparatus, designed using an abductive research approach. These novel theories were then modified and iterated, dependent on additional observational data.

1.8 Thesis Organisation

This thesis is organised into nine chapters. Chapter 2 provides a literature review of published work relevant to the field of study. Leading to a discussion of challenges presented by near future legislation requirements. Then a breakdown of diesel injector performance characterisation technology for a production environment is provided. Closing with a critique of the available literature for the known measurement sensitivities of the system for study.

Chapter 3 details the different experimental schemes used to achieve the stated objectives. The purpose of each experimental scheme, its critical parameters and experimental setup are discussed.

Chapter 4 presents a summary of the potential sources of measurement variance, around which this work is structured.

Chapter 5 details the work carried out on experimental hardware and in simulation space, to characterise the source of low frequency signal baseline variance. An optimised hydraulic measurement system design, based on insights gained during this work, is then demonstrated.

Chapter 6 describes a spectrogram analysis used to characterise the high frequency content in the measurement signal. A novel Cepstrum quefrency analysis is then presented as a method to identify sources of periodic electrical signal noise.

Chapter 7 explores a new automated temperature to speed of sound mass calibration procedure, using large datasets to improve its accuracy.

Chapter 8 details three sources of end of injection variance. The source of an artefact commonly seen at the end of injection is presented. The relationship between measurement system temperature over time and a signal offset is discussed. Finally, a description of novel numerical methods capable of revealing subtle unknown sources of variance, such as supply pressure wave activity, is provided.

Chapter 9 summarises the core findings of this work, highlighting the additions to knowledge in the field. This chapter concludes with recommendations for further research.

2 LITERATURE REVIEW

This literature review discusses the legislative drivers of emissions reduction technologies, that lead to increasingly stringent production injector test tolerances. The challenges that future applications present were identified as increasing injection pressures enabling improved engine efficiency, the measurement precision required to characterise close coupled multiple injection events, and the ability to assess critical injector performance parameters.

The reason continuous flow meter technology is unsuitable for this application was identified as an inability to distinguish between individual injection events. A review of commercially available injection-to-injection (shot-to-shot) rate measurement technology and their suitability for this application is presented. Mitigation of sources of measurement variance in a rate tube injection meter is provided as justification for their study in the present work.

The goal of the present work was identified as achieving the unique capability of stable injected mass measurement, in parallel with a high fidelity injection rate signal. The original signal fidelity of a rate tube injection meter identified it as the best method for study to achieve this goal.

Sources of measurement variance inherent to a rate tube injection meter were categorised as low frequency hydraulic pressure waves, high frequency activity driven by cavitation, accuracy of a signal magnitude compensation algorithm, and injection rate profile distortion found at the end of injection.

A potential source of injector performance variance in the form of resonances in the high pressure supply system is presented. How this knowledge informed the experimental activities in the present work is then summarised.

2.1 Near future commercial vehicle emissions

The primary legislative drivers are in Europe and America with regards to NO_x, PM and CO and CO_2. Sharp *et al.* (2017) demonstrated that traditional approaches will not be sufficient to achieve the 0.02g/hp-hr NO_x target proposed by California Air Resources Board (ARB) (Johnson, 2015). Additional requirements are now faced, with the introduction of low emissions zones in densely populated city centres.

Whilst reducing NOx emission levels is perceived as the main challenge, many new technologies have been demonstrated for improving fuel economy and reducing greenhouse gas emissions (CO_2), during the first stage of the Supertruck development program by Department of Energy (Delgado and Lutsey, 2014).

One recent example of technology transfer from the above research program is the 2017 Volvo truck VNL model offerings, featuring the D13 turbo compound engine (Nelles, 2019). These models boast significantly improved fuel economy over previous models through exhaust energy recovery via turbo compound technology, enabling down-speeded fuel efficient engine running conditions, innovative piston crown designs, and a F2 high pressure common rail fuel injection system as studied in the present work (Meek *et al.*, 2014). This increasing variety of engine strategies presents a diverse set of future challenges in terms of Fuel Injection Equipment (FIE) design and characterisation.

2.1.1 Tighter production tolerances

Lillington, Chetwynd and Jones (2015) emphasised that one of the most significant challenges has been ever more stringent production tolerances to the injected quantity and timing of FIE, required to meet every new emissions legislation as shown in Table 2.1.

Table 2.1: Developing injector control trends, adapted from (Lillington, Chetwynd and Jones, 2015)

Emissions tier; year	Pressure Rating (bar)	Number of timing corrections	Timing Accuracy (µs)	Typical number of fuelling corrections	Typical target fuelling accuracy (%)
EURO 1; 1992	1500	0	40	0	4
EURO 2a; 1992	1700	0	40	0	4
EURO 2b; 1998	1700	0	40	0	4
EURO 3; 2000	2000	1	< 10	1	5
EURO 4; 2005	2000	4	< 10	1	< 5
EURO 5; 2008	2500	4	< 10	2	< 5
EURO 6; 2013	2700	> 10	< 5	> 10	< 1.5
EURO 7; TBD	3600	> 10	< 2	> 10	< 0.5

The key challenges arise from injection pressures above 2500bar resulting in increased energy input into the measurement system, the injection quantity and timing accuracies at these increased loads, and additional requirements to characterise close coupled multiple injection events for EURO 7 (EU7) applications (Gibble and Amar, 2013). To meet these near-future challenges, sources of measurement variance must be characterised.

2.1.2 Increased injection pressure

High pressure diesel sprays have been shown to improve mixing within the engine cylinder. This results in improved combustion efficiency and lower soot formation because of increased turbulence and atomisation of the spray. The

turbulence is driven in part by cavitation in the nozzle holes formed at high injection pressures, as characterised by Dembinski, Angstrom and Winklhofer (2014). The improved hydraulic efficiency of the latest generation of diesel injectors makes high pressures up to 3600bar feasible for multiple injection strategies (Graham *et al.*, 2014). Increased injection pressures between 2000 and 4000bar have been shown by (Jia *et al.*, 2016) to provide further benefits regarding diesel spray penetration. In contrast, Strotos *et al.* (2015) described how fluid friction effects and cavitation activity lead to increasing spray temperatures at elevated injection pressures. Hence, elevated pressures will increase temperature of the fluid medium in injection rate measurement systems.

2.1.3 Close coupled multiple injection

In solenoid actuated injectors, hydraulic losses can occur when their control valves are operated. To speed up response times and reduce parasitic losses in the control valves, injector valves are being continually miniaturised (Hardy *et al.*, 2012). Smaller clearances and mating surfaces within the injector equate to lower leakage. A fast control valve response allows for a quick succession of multiple injection events. Also known as digital rate shaping, the main injection is split up into a quick succession of smaller pulses (Herrmann *et al.*, 2012), resulting in reduced noise and soot emissions. An example of a typical EU7 multiple injection strategy is shown in Figure 2.1.

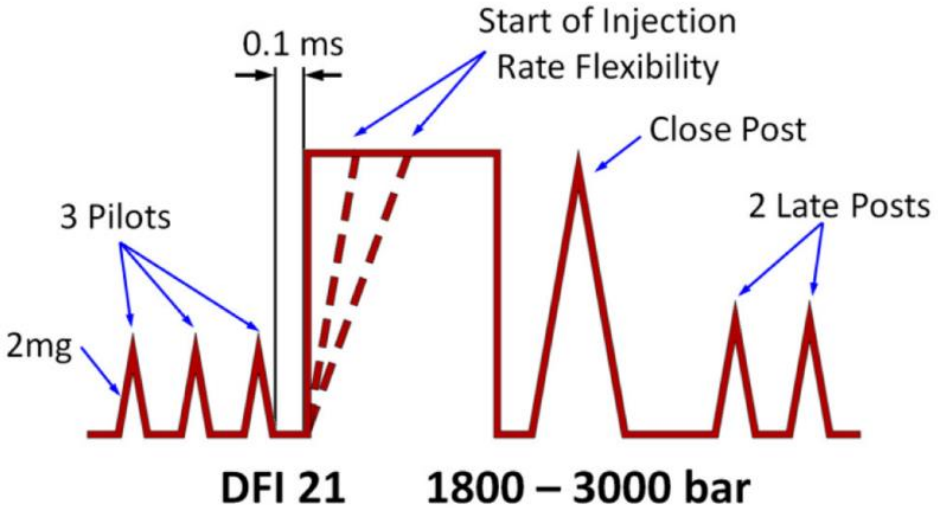


Figure 2.1: Pulsed injection rate shaping possible on DFI21 EU7 injectors. A true replication of the original as presented by Graham et al. (2014)

With each additional injection pulse, comes increased turbulence in the measurement system (Postrioti *et al.*, 2014). The sensitivity to this effect must be understood to mitigate its impact through improved hardware and injector test strategy design.

To achieve this, it must be possible to characterise injection events with dwell times of 200µs and less between injections (Ferrari *et al.*, 2018). Hence, injection rate measurement systems require improved injection timing and fuel quantity resolution.

2.1.4 Injection rate shape characterisation

With advanced injector design, it is possible to have precise control over the injection rate (Payri *et al.*, 2011). This has resulted in 2 distinct product categories for the F2 injector: Fast rising injection rate at high pressures for EGR heavy applications; and slower rate of rise for SCR heavy applications (Morgan *et al.*, 2015), as shown in Figure 2.2.

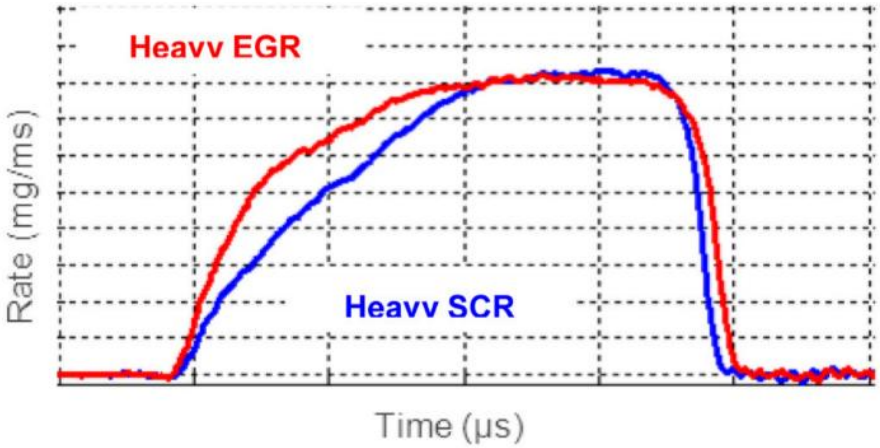


Figure 2.2: Example of start of injection rate profiles for different EU6 F2 injector applications. Sourced from (Meek et al., 2014).

To fully characterise these shapes, it is crucial that the true rate does not become distorted. To combat fluctuations within a rate measurement system, filters are often used on their signal (Takamura *et al.*, 1992; Dahlander, Iemmolo and Tong, 2015), to separate the instantaneous flow rate of the nozzle from high frequency noise. To test this injector performance criteria without distortion, it is critical to distinguish between high frequency noise and the true injection rate signal.

2.2 Review of injector characterisation technology

There are a variety of methods available to measure fuel delivery and injection rate used in both industrial and laboratory settings. The following Section describes the use cases of continuous flow rate meters, why they are inappropriate, and why individual shot-to-shot injection measurement systems must be used. An overview is provided of piston-displacement, Zeuch chamber, and rate tube shot-to-shot measurement system solutions. A justification for rate tube injection meters as the chosen focus of this work is then provided.

2.2.1 Continuous flow meters

Continuous flow metering systems are often used to measure the aggregate flow from an injector over a wide time-span (Kaub, 1993). The average delivery per injection can then be determined by dividing the flow rate by the firing rate of the injector, originally achieved by filling measuring beakers and observing their volume change. Whilst simple to implement, this method is too imprecise for the calculation of injector trims and finds use solely as a coarse functional check when reworking old injectors (Emerson, 1977).

The most capable form of continuous flow measurement device is known as a coriolis meter, which uses the principle of coriolis force, that acts perpendicular to the direction of flow. This is achieved by exciting a U bend flow tube with its natural frequency, via an electromechanical drive coil controlled by a microprocessor. The resultant deflection of the flow tube and its frequency of vibration can then be used to derive a precise flow rate and fluid density. This method offers a more precise flow rate and greater measurement range than available with traditional gear flow meters (Simms, Gandhi and Sommer, 2009). However, unlike gear flow meters, the principle of operation of coriolis meters requires that they be isolated from environmental vibration. Continuous flow meters cannot distinguish the injected mass of individual injection events, nor their start and end of injection timings. One near future promising technology to overcome this is a shot-to-shot coriolis meter system called PRISM using frequency notch filters to distinguish the flow rate between events. Until this technology is commonly available, the use of traditional Coriolis meters in this application, is limited to providing a precise reference value for average injected mass. A discussion of commonly used shot-to-shot measurement techniques to achieve individual injection event characterisation are described in the next Section.

2.2.2 Shot-to-shot injection rate meters

The three primary techniques used in industry to acquire shot-to-shot fuel delivery and injection rate timing measurement are described in this Section. These are Piston-Displacement meters utilising mechanical motion, Zeuch meters that rely on pressure rise in sealed chambers, and rate tubes that derive injection rate from an observed pressure wave. Other optical (Jeshani, 2013) and direct measurement of the momentum (Luo, Cui and Dong, 2014) in the injection spray are also available, but unsuitable for a production environment because of their complexity of implementation. Each type of shot to shot injection meter is discussed in the following 3 sub-Sections.

2.2.3 Piston-displacement

Piston-displacement meters are mechanical devices (Komaroff and Melcher, 1966), that measure the movement of a low mass, nitrogen gas backed piston, using a precise Linear Variable Differential Transformer (LVDT), as shown in Figure 2.3.

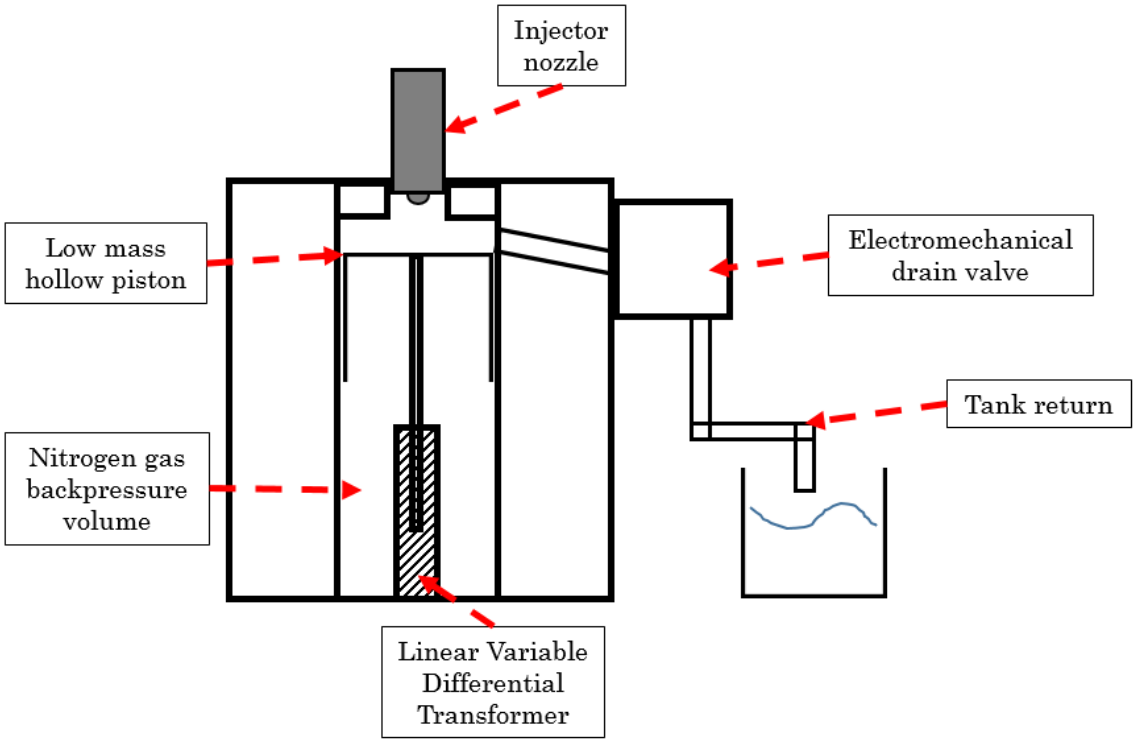


Figure 2.3: Schematic diagram of a piston displacement injection rate meter.

They are fitted with a fast-acting drain valve, capable of measuring at firing rates of up to 30Hz on heavy-duty applications. The displacement of the piston with each injection event provides an injected volume, which is converted to mass using temperature measurement of the fluid medium and a density lookup table. Whilst capable when measuring injected quantities, this meter suffers from significant distortion of the injection rate shape, induced by internal Helmholtz resonances of the piston chamber, that superimpose as sinusoidal frequencies on top of the injection rate signal.

When measuring injection rates required for EU7 injection pressures, they suffer internal damage from the higher accelerations encountered (Pearce, 2013). They are unsuitable for future heavy-duty measurement applications, due to their lack of injection shape rate fidelity and limitations imposed by acceleration of a moving mass. .

2.2.4 Zeuch chamber

Another popular method is the Zeuch chamber (Takamura *et al.*, 1989), where pressure in a closed chamber rises proportionally to the quantity of mass injected into it, as shown in Figure 2.4.

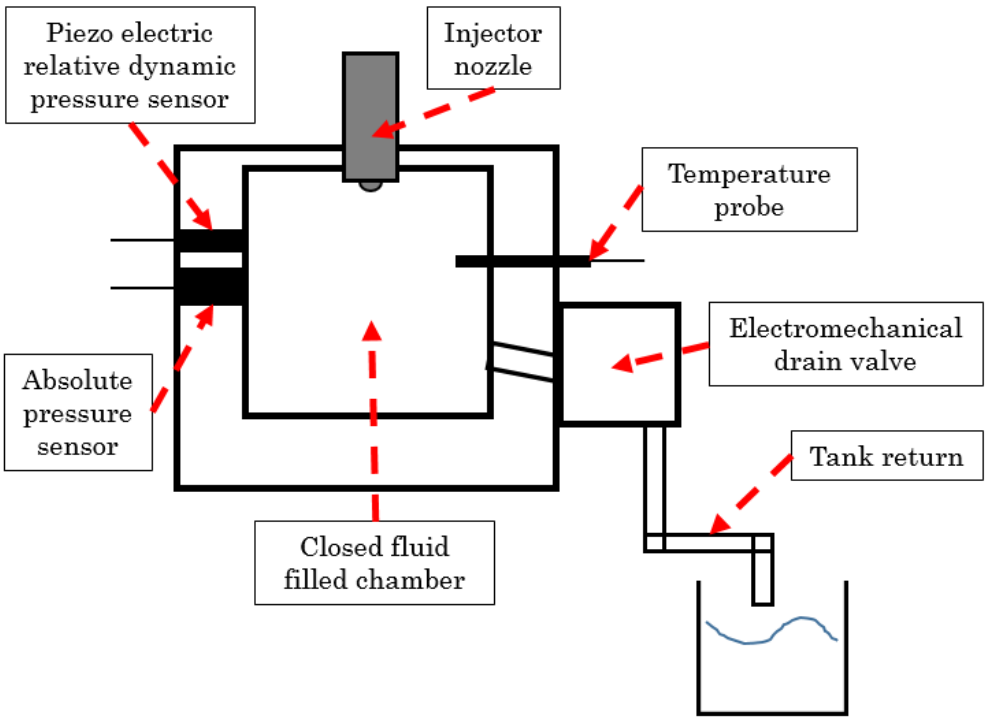


Figure 2.4: Schematic of a typical Zeuch chamber method rate of injection meter.

An estimation of bulk modulus is required, using pressure and temperature measurements inside the chamber and a compensation algorithm (Ishikawa *et al.*, 2000). Traditionally these meters used a timed dump valve to maintain system backpressure between injection events.

An alternative method of utilising continuous flow through a closed-loop controlled, throttled outlet valve, has been developed by Loccioni as part of the patented Mexus metering system (Perna, Baraldi and Gregori, 2012). Negating the need for a precisely timed and fragile pressure release valve. By pairing the Mexus with a coriolis meter at its outlet, a compensation map can be derived for the fluid properties within the chamber . This method provides the most precise quantity measurement commercially available. However, all variants of Zeuch devices suffer from significant Helmholtz resonance distortion superimposed on top of the injection rate, requiring the use of aggressive filters that distort the true injection rate (Takamura *et al.*, 1992; Dahlander, Iemmolo and Tong, 2015), as shown in Figure 2.5.

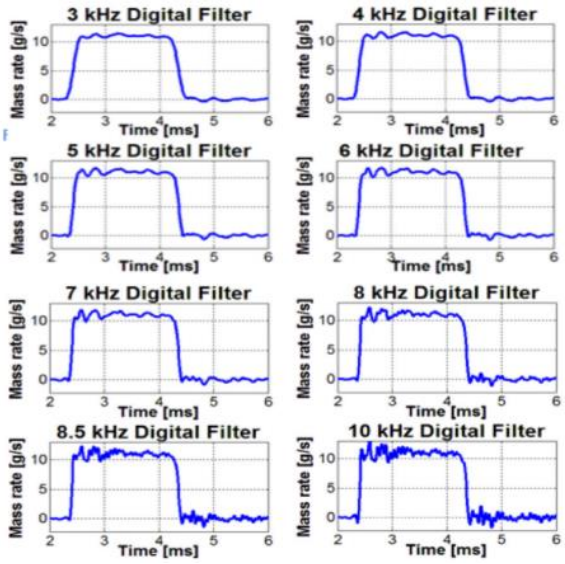


Figure 2.5: Effect of low pass filter cut of thresholds on observed signal distortion from a Zeuch chamber injection rate measurement system.
Sourced from (Dahlander, Iemmolo and Tong, 2015).

This effect is lesser than observed on piston displacement meters but will significantly impair the characterisation of injection rate shapes at peak injection pressures and loads encountered in heavy duty commercial vehicle injector testing.

2.2.5 Rate tube

Rate tube injection meters capture a pressure wave signal, induced by an injection event, into a fluid filled tube with a uniform cross sectional area and backpressure. Injection of fluid mass into the tube results in a pressure wave proportional to the rate of injection, the cross-sectional area and speed of sound in the fluid medium of the tube, as illustrated in Figure 2.6.

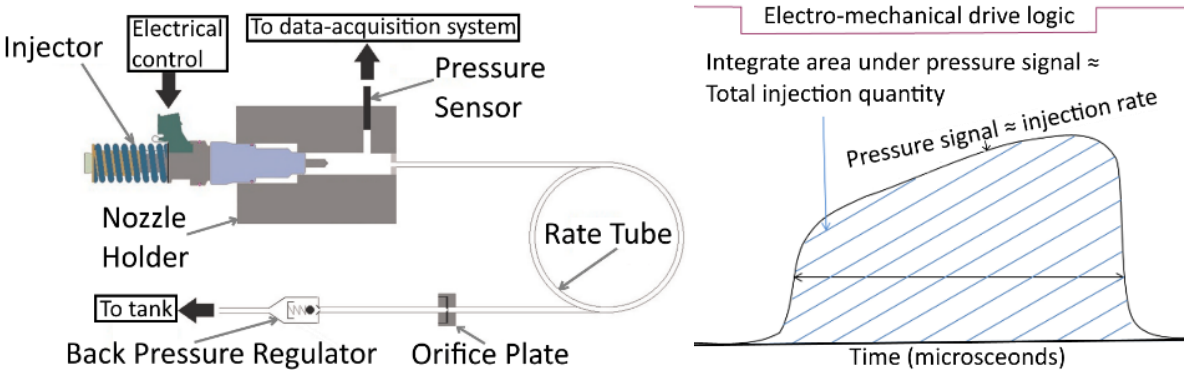


Figure 2.6: Principle of operation of a rate tube injection meter. Left: Generalised rate tube schematic. Right: Integration of area under the pressure wave to derive total injected fuel mass.

The injection rate is then derived by using a pressure sensor close to the injection event to measure the passing wave.

When the technique was proposed by Bosch (1967), the pressure-velocity equation for a wave in stationary fluid were used to derive volume flow rate as shown in Equation [2.1]:

$$Q_{inj} = \frac{A}{c\rho}\int_{t_{start}}^{t_{end}} P dt \qquad [\ 2.1\ ]$$

Where Q_{inj} is the total injected volume, A is the cross-sectional area of the tube, c is the speed of sound in the fluid, ρ is the density of the fluid, P is the measured pressure.

However, for modern injector test applications, total injected mass is used, rather than the volumetric flowrate, due to mass being relevant in terms of combustion performance.

The pressure-velocity equation valid for a single pressure wave in an in stationary flow [2.2] is used to derive mass flow rate in a pipe of cross sectional area A .

$$\dot{m} = \rho A v \qquad [\ 2.2\ ]$$

The measurement of mass in a Bosch rate tube relies on the relationship between pressure and velocity of a transient one-dimensional fluid flow (Currie, 2012), as described in the Equation [2.3], where v is velocity of the fluid.

$$P = c\rho v \qquad [\ 2.3\ ]$$

Rearranging for the unknown v results in Equation [2.4].

$$v = \frac{P}{c\rho} \qquad [\ 2.4\ ]$$

Substituting the equation for the fluid velocity v into the equation for mass flow rate $\dot{m}$ in a pipe provides Equation [2.5].

$$\dot{m} = \frac{\rho A P}{c\rho} = \frac{A}{c}P \qquad [\ 2.5\ ]$$

To determine the total mass flow rate of an injection event m_{total}, integration of the pressure term P between the start and end of the injection event is conducted, as shown in Equation [2.6].

$$m_{total} = \frac{A}{c}\int_{t_{start}}^{t_{end}} Pdt \qquad [\,2.6\,]$$

Where m_{total} is the total injected mass and Pdt is the pressure differential integrated between the time of the start, t_{start} and end, t_{end}, of the observed pressure wave.

The use of mass conservation principle and pressure-velocity equation valid for a single pressure wave observed in a stationary flow in Equation [2.2], requires the following assumptions.

(a) An isentropic process between t_{start} and t_{end},

(b) The flow considered is one dimensional, therefore any observed pressure changes are caused by the pressure wave induced by the injected mass alone. Not from additional sources such as flowrate induced shockwaves.

Assuming stationary flow requires that the flow field has time to stabilise from a locally turbulent, to evenly distributed flow. No consideration is made for the influence of the velocity of the injected mass and subsequent turbulent flow conditions caused by its fluid inertia. As seen when a single nozzle hole injector was measured on a rate tube by (Menucci, 2018), requiring the use of a flow diffuser to distribute the flow field.

(c) Isothermal conditions between t_{start} and t_{end}, due to the use of a fixed speed of sound term. Therefore, a potential source of error in magnitude of the observed signal could arise due to changing speed of sound in the fluid during the measurement event.

In the original study of this kind of meter (Bosch, 1967) an error of 3-4%, at average delivery quantities of 70mm/stroke, was observed, by measuring the travelling time of the hydraulic pulse. It was attributed to the effect of turbulent flows near the injection event, violating the one dimensional flow assumption. Subsequently it was proposed to compensate for this error by deriving a calibration adjustment for speed of sound at specific injection conditions.

In a rate tube, the injection pulse travels along a simple tube until it reaches an orifice, then partially reflects back. The initial pulse is measured and evaluated; the period containing the reflected waves is typically discarded. Before another measurement can be taken, the reflections have to be attenuated to the point at which quiescent conditions within the tube have been reached, as shown in Figure 2.7.

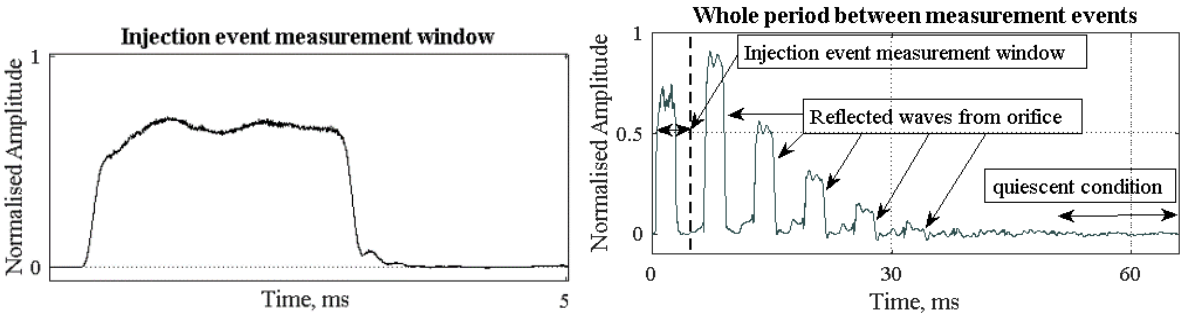


Figure 2.7: Injection rate signal for a rate tube injection meter.
Left injection rate trace measurement window.
Right Full 15Hz firing period between injection events

A limiting factor regarding the maximum injection firing rate that can be measured, is the need to wait for quiescent pressure in the tube before another measurement can be taken.

In Delphi Technologies, the quiescence requirement limits F2 EU6 production rate tube injection meters to a maximum firing rate of 15Hz. In contrast, laboratory studies that utilise rate tube injection meters typically use firing rates of 15Hz or less to guarantee quiescent conditions between consecutive measurement events (Arcoumanis, Baniasad and Banias, 1993; Phan, 2009).

This is viewed as a performance limitation when compared to the >25Hz possible using commercially available piston or Zeuch type meters. If quiescent conditions within a rate tube can be achieved earlier, this limitation could be overcome. Therefore, a secondary objective of this work was reducing the time to achieve quiescent conditions and enable faster injection firing rates.

This method of injection rate measurement offers the highest fidelity injection rate signal, without the need for aggressive signal filtration (Takamura *et al.*, 1992; Arcoumanis, Baniasad and Banias, 1993), as shown in Figure 2.8.

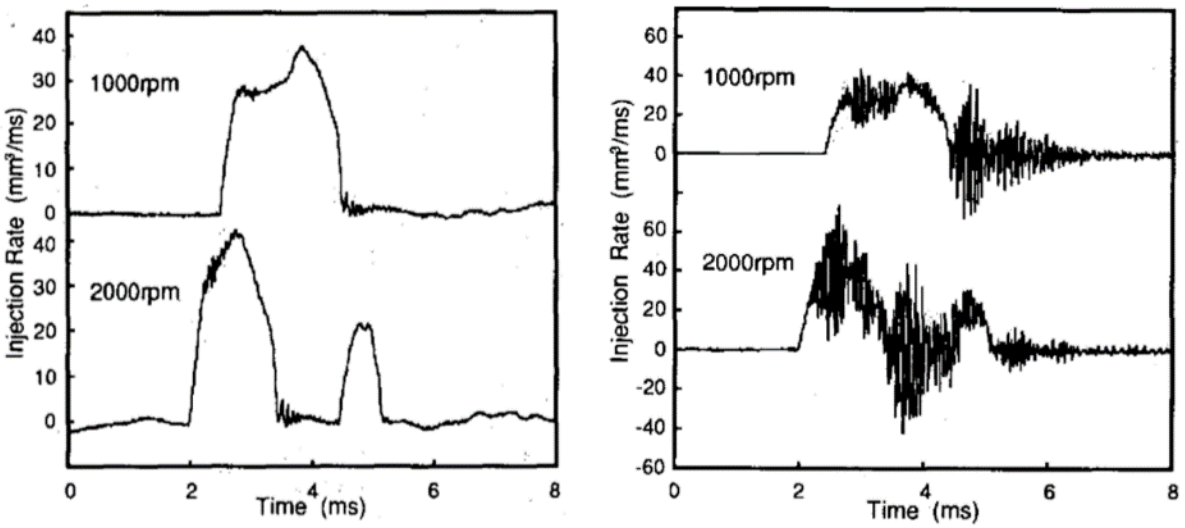


Figure 2.8: Comparison of original unfiltered injection rate waveforms from:
Left: Rate tube
Right: Zeuch chamber
Sourced from (Takamura et al., 1992).

A downside of this technique is that it struggles to maintain total injected mass calibration stability over time, because of multiple sources of measurement variance that must be mitigated.

To overcome this limitation, it is common practice in laboratory investigations to measure the injection rate and timing with a rate tube, then acquire an alternative reference value for injected mass, by pairing it with either a piston-displacement, Zeuch, or coriolis mass meter (Catania, Ferrari and Manno, 2005; Gandhi, Meinhart and Ortiz, 2009)

Issues with the Delphi Technologies' day-to-day mass calibration stability was the primary reason for this present work. The system has only been viable in production because of the oversight of multiple operations engineers. If the sources of measurement system variance were better understood within Delphi Technologies, then improved performance, product quality and machine availability would cause an increase in OEE. Leading to reduced costs associated with maximum throughput capability and less engineering oversight required to maintain the process.

The only known commercially available example is the IAV injection analyser (Armas, Mata and Martínez-Martínez, 2012), a simple coiled construction that uses bespoke algorithms to compensate for distortions of the injection rate, relative to a coriolis mass meter calibration carried out at a period of every 6 months. This device was revealed to have comparable injected mass measurement repeatability to the existing bespoke production measurement system, when compared by Delphi Technologies' test development teams (Hogg *et al.*, 2020). The conclusion of these studies was that the compensation

algorithms are highly application specific. Consequently, these compensations can run counter to their purpose, leading to increased shot-to-shot measurement variance, if not precisely tuned for each specific application. Due to their proprietary nature, this is not something that can be easily changed by injector test development engineers, limiting the scope of their use to less challenging light duty fuel injection applications in terms of a production environment.

The primary focus of this work was identified as finding a solution to meet all current and future commercial vehicle injector testing requirements. The rate tube injection meter method was chosen to meet this aim due to its high original signal fidelity. To achieve this, inherent sources of measurement variance, that are the cause of injected mass calibration instability, must be characterised and minimised.

A review of the literature into the sources of measurement variance on rate tube injection meters was carried out, to inform the experimental schemes devised for this work. The existing knowledge about sources of variance on a rate tube meter are introduced as zero value signal baseline variance and its potential hydraulic origins, high frequency signal noise that may contain previously unstudied information, difficulties with temperature to SOS signal height compensation using existing methods, a cumulative signal offset linked to fluid properties inside the measurement system, and an unexplained bump artefact present at the end of injection. Information from other areas of study are used to fill knowledge gaps where the commercially sensitive nature of this field of study limits the scope of information available.

2.2.6 Zero value baseline

The rate tube injection meter method relies on precise measurement of the incident pressure wave, caused by the injection event. If pressure wave activity is present within the fluid medium, that is not due to the input of mass from injection event, it will convolve on top of and distort the observed pressure wave and mass flow rate measurement.

One example of zero value variance was shown by Payri *et al.* (2008) to be induced by the reaction force of the injection event causing a displacement and oscillation of the injector nozzle tip in the fluid medium. Leading to a superimposing of sinusoidal zero value variance on top of the observed injection rate signal. That study did not explain how the injector was mounted and therefore constrained in the rate tube meter. Unlike most experimental setups, the production hardware at Delphi Technologies exerts a force of 15kN on the injector against a rigid frame, so this specific source of zero value variance may not be present with a robust injector clamping method.

Another source of convolved wave activity in the injection rate signal could be because of pressure waves inside the fluid medium, caused by hydraulic resonances. All hydraulic geometries have a resonant frequency and can produce complex convolved waveforms if left undamped (Hixson, Kahlbau and Galloway, 1962; Sewall, Wineman and Herr, 1973). Any flexible hoses in the system can also introduce complex dynamic pressure waves generated by the expansion of elastic walls, caused by the pressure waves travelling along the hose (Drew, Longmore and Johnston, 1997).

There are no known studies of other potential sources of zero value variance on a rate tube injection meter found in the body of available literature. This is likely because most researchers will simply reduce the firing rate of the injector, to allow more time for pressure waves to dissipate within the measurement system before another measurement is taken.

In a production environment, where cycle time is limited by injector firing rate, this is not acceptable. Therefore, it is critical to study additional potential sources of low frequency activity, to mitigate their magnitude and allow ideal quiescent conditions to be achieved in a shorter time

2.2.7 High frequency

High frequency activity inside a rate tube injection meter is typically approached from the perspective of what type of low-pass filter is required to produce a smooth injection rate signal (Arcoumanis, Baniasad and Banias, 1993). These filters are typically between 10-30kHz for injection rate meters, therefore frequency activity above this range has not been characterised.

It is known that at high pressures, reaching potentially greater than 3000bar (Jia *et al.*, 2016), diesel injectors generate significant amounts of cavitation (Dembinski, Angstrom and Winklhofer, 2014) when injected into a gaseous medium. When studying an experimental Zeuch chamber rate meter Takamura *et al.* (1992) demonstrated that increasing the injector nozzle backpressure from 2bar to 30bar reduced high frequency noise on the chamber pressure signal significantly. They also have observed negligible level of reduction in high frequency noise when the backpressure was increased from 30 to 60 bar. They surmised it was related to cavitation by observing a significant reduction in the white scatter cloud of a shadowgraph CCD image between 5 and 20 bar backpressure.

Work carried out by Pearce, Hardalupas and Taylor (2016) demonstrated the presence of cavitation in the fluid medium of a Zeuch chamber injection rate meter using optical methods. An OPENFoam CFD model provided an explanation of cavitation generated by vortices driven by the fluid shear of the

injection event into the fluid medium (Pearce, Hardalupas and Taylor, 2015). With the pulsation of the injection rate being driven by the nozzle and body resonant frequencies. If cavitation collapse is observed during an injection event into a fluid filled Zeuch chamber, then it will also be present in the fluid medium of a rate tube injection meter. Therefore increasing the system backpressure to suppress high frequency cavitation activity was a commercial goal of this work.

When high delivery Euro 6 heavy duty diesel injection were trialled in an IAV commercially available rate tube, significant zero value baseline errors were observed at the largest injections. Due to the backpressure regulation designed with more commonly encountered light duty injection loads. This demonstrated the need to achieve stable increased backpressure conditions for heavy duty injection loads as a primary goal of the present work.

A secondary benefit to increasing backpressure is the ability to closely match with higher injector nozzle backpressure of the heady duty diesel engine regime. Leading to a more representative injection event through similar levels of cavitation inception in the injector nozzle holes.

Crua and Heikal (2014) revealed for the first time that high frequency oscillations are present in the spray of a high pressure diesel injection event into a gaseous volume. These frequencies form distinct bands that are clearly visible using spectrogram analysis, with higher order frequency bands appearing as injection pressure increases. This type of study has not been carried out for an injection event into the fluid filled medium of an injection rate meter. Therefore, it is important to understand if the frequency activity that is normally filtered out contains useful information about the injector performance and resonant features that may be present.

Another source of high frequency oscillation could be from resonances of the injection rate pressure sensor and its port, as has been demonstrated when the same sensors are used in engine cylinder measurements (Dey, 2012). The ports used in engine cylinder applications are multiple times longer than the 3mm long port used on the production application studied in this work. Therefore, it is expected that any quarter wave resonances observed will appear at a higher frequency. Excitation of natural frequency resonance of these sensors has been demonstrated during shock tube sensor calibration activities by Knott and Robinson (2020). Therefore, it may also be present for injection rate meters. These resonant sensor effects have not been studied on rate tube injection meters and therefore must be characterised.

2.2.8 Speed of sound (SOS)

According to the rate tube mass injection rate Equation [2.6], for a fixed cross-sectional area, the magnitude of the observed pressure wave will be determined by SOS in the fluid medium. There are 3 currently used methods employed: direct measurement using ultrasonic sensors; measurement of wave travel time as a function of the reflected wave; use of a state equation as a calibration function using injection temperature inside the pipe to derive speed of sound.

Direct SOS measurement is possible using an ultrasonic sensor to measure wave travel time, as implemented to measure fluid properties in the Bosch-Moehwald HDA Zeuch chamber injection rate meter (Manual, 2008; Busch and Miles, 2015). An example for the use of direct ultrasonic measurement is found in Minnetti *et al.* (2017). No known commercial examples of ultrasonic sensor use exist for a rate tube meter. An ultrasonic sensor was developed by Delphi Technologies, but it could not withstand the shock loading present when placed near the injection rate event observation point.

Wave travel time from start of injection to the time the first reflected wave is used to derive speed of sound on some rate tube injection meters for experimental work (Dernotte *et al.*, 2012). This is not a common practise in a production environment, due to the increased signal processing complexity required for a longer acquisition period, necessary to observe the reflected wave.

The final method utilises a reference mass calibrated state equation to compensate for adiabatic speed of sound changes known to occur between separate measurement events (Ferrari and Zhang, 2019). The equation for speed of sound to calibrate for test to test differences in fluid properties is shown in Equation [2.7].

$$c = \sqrt{\frac{K_e}{\rho}} \qquad [2.7]$$

Where $K_e$is the effective bulk modulus of the system, which includes air entrainment in the fluid, compressibility effects of the system and the fluid bulk modulus (Gholizadeh, Burton and Schoenau, 2011).

If the process is considered Adiabatic between separate measurement events, then the SOS for a single mole of ideal gas can be considered (Hansen, 1951), shown in Equation [2.8].

$$c = \sqrt{(\gamma R T)} \qquad [2.8]$$

Where γ is the ratio of specific heats (adiabatic index), R the individual gas constant and T the absolute temperature. As γ and R are constants, it

demonstrates that speed of sound will change according to temperature dependant fluid properties for an adiabatic process.

An adiabatic speed of sound assumption neglects the effect of any pipe wall compliance and the presence of entrained air in the fluid. Both of which will influence K_e the effective bulk modulus and hence speed of sound of the system.

This method also assumes a laminar flow, hence does not take into account mutli dimension compressibility effects driven by fluid inertia, or shockwaves generated by high pressure supersonic flows as observed by (Jia *et al.*, 2016).

The method used by Delphi Technologies to generate a state equation calibration utilises an injection temperature measurement, a concurrent mass measurement, and the observed pressure wave, to develop a temperature to SOS transfer function. This technique requires that a calibrated mass meter be attached to the system to derive the transfer function. The existing technique is a manual process, using a measuring beaker on a calibrated weighting scale, in place of the return line from the measurement system. The accuracy of this method is limited by a single data point for each part of the calibration map and results in significant production downtime.

Therefore, it is important to develop an improved method, acquiring more data-points, that will enable the development of a more accurate temperature to SOS transfer function, whilst minimising the impact of this process on daily production output.

2.2.9 Rate float

The injection rate signal cumulative offset phenomenon is the most widely known source of variance (Gandhi, Meinhart and Ortiz, 2009; Menucci, 2018; Hogg *et al.*, 2020) in a rate tube injection meter. It describes an offset present at all injection conditions, that varies with injection pressure and duration, where the signal magnitude rises between the start and end of injection. Resulting in an injection rate offset error away from baseline by the end of the injection event.

This effect has been attributed by (Payri *et al.*, 2008) to increases in temperature and pressure in the fluid medium, caused by an input of fluid velocity energy, additional to the pressure rise induced by injected mass input into the measurement system. A signal correction was proposed, based on a derived compensation coefficient as described by Equation [2.9].

$$C = |z - r'|_a^b \qquad [\,2.9\,]$$

Where z is the measured signal and $r'$is the cumulative signal error. The downside of this methodology is that it requires thresholds a and b to be acquired without distortion after the injection event has finished, as shown in Figure 2.9.

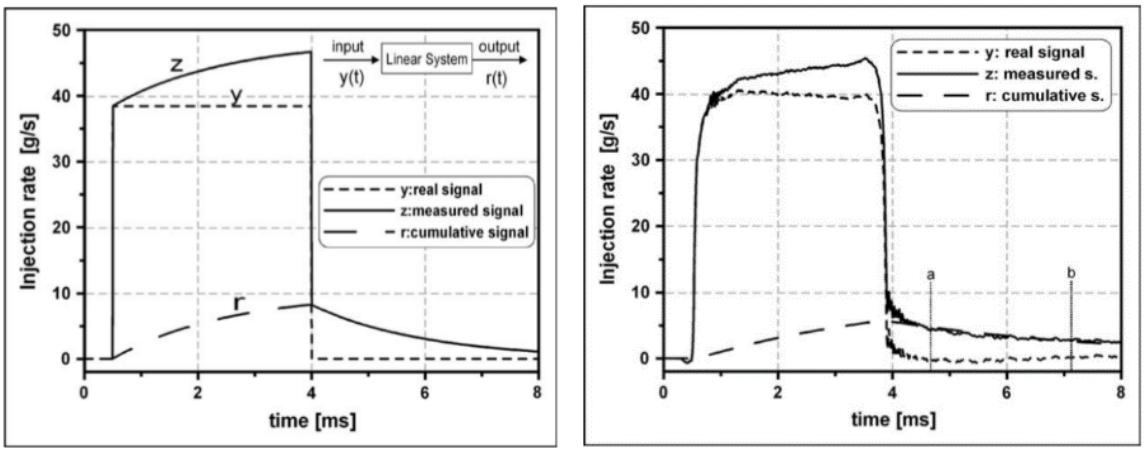


Figure 2.9: Illustration of injection rate float / the cumulative offset correction algorithm and the signal thresholds required to implement it. Sourced from (Payri et al., 2008)

If any signal distortion is present after the end of injection from other sources of variance, it will significantly degrade the accuracy of this compensation method, which makes it unsuitable for the production application that is the focus of this work.

A 1D simulation model was constructed by van Bebber and Reuter (2017) in collaboration with IAV which attributes the source of this variance to three factors: fluid friction against the rate tube wall, pressure dependent properties, and temperature dependent fluid properties, as shown in Figure 2.10.

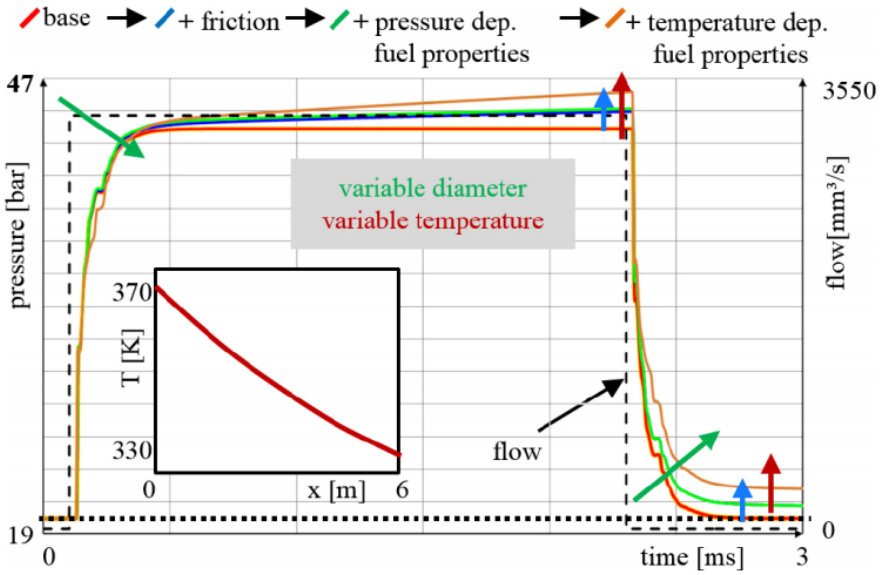


Figure 2.10: Simulation of the influences of fluid friction, pressure dependent and temperature dependent fuel properties on injection rate float. Sourced from (van Bebber and Reuter, 2017).

Among these sources of variance, the temperature dependent fluid properties was identified as the key component for study. The pressure and friction dependent properties will be relatively constant between repeat measurement events and can is assumed to be a fixed effect that can be easily offset.

This understanding leads to the conclusion that, to compensate for the rate float variance, its relationship with observed temperature of the fluid medium must be fully characterised.

2.2.10 End of injection bump

A bump artefact at the end of injection has been observed on all (Ferrari *et al.*, 2018; Menucci, 2018) rate tube injection meters for both production and research environments, as shown in Figure 2.11.

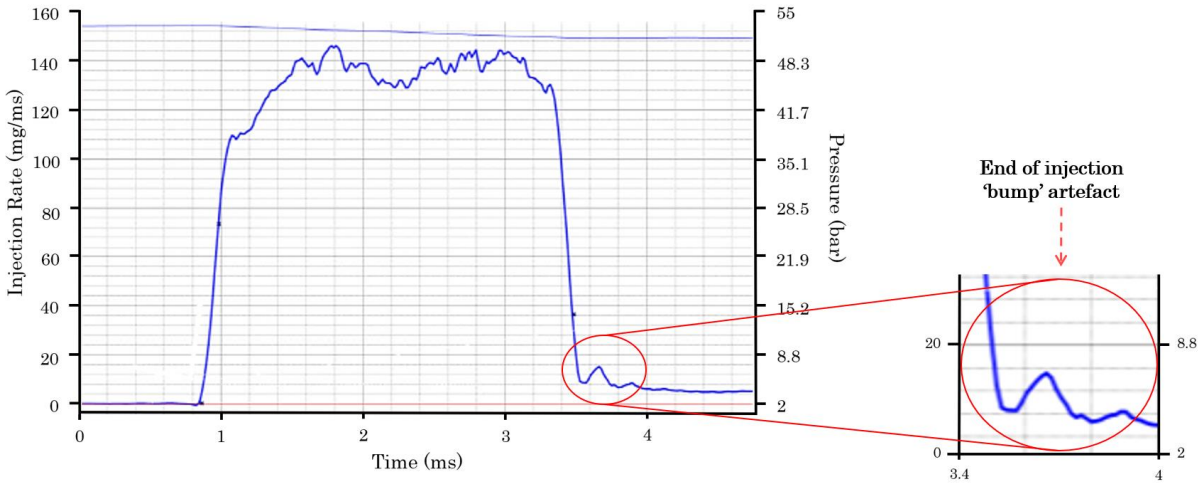


Figure 2.11: End of injection Bump artefact illustrated. Taken at Peak power engine condition for the F2 injector on existing production measurement equipment.

The source of this artefact in a rate tube injection meter has not been characterised. One explanation has been provided by Sykes *et al.* (2019), when studying injection into gas held at engine cylinder environmental conditions. That work observed a tendency of high pressure diesel injector of the nozzle needle to oscillate or 'bounce' once it has closed at the end of injection, leading to an ingestion and release of fuel, additional to the main injection event. This effect was characterised by Sykes using optical measurements around the nozzle holes, as shown in Figure 2.12.

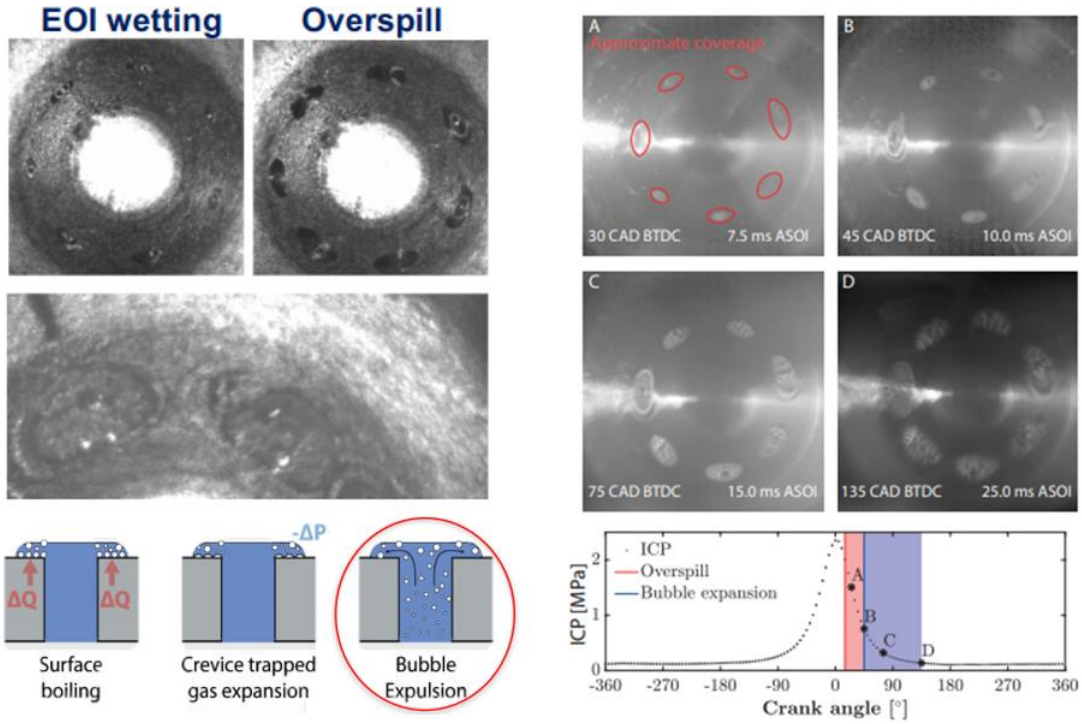


Figure 2.12: Images of EOI wetting and overspill known to occur after end injection when injecting into gaseous volume. A potential source of the bump artefact on the signal of a rate tube meter. Sourced from (Sykes et al., 2019).

This phenomenon was observed when injecting into a gaseous and not fluid filled medium of an injection rate meter, so the findings are not directly transferrable. Therefore, it is important to understand if this artefact is a product of end of injector nozzle dynamics, or a product of signal distortion introduced by the configuration of the rate tube injection meter.

2.3 Sources of injector performance variance

There are known sources of injector performance variance that will affect the repeatability of injected mass quantity (Chaufour *et al.*, 2004; Bingqi *et al.*, 2015). It is necessary to differentiate between sources of injector performance variance and sources of measurement variance inherent to the injection rate measurement system. A potential source of real injector performance variance that could arise from the high pressure supply configuration was identified.

A widely known source of variance in common rail diesel fuel injection systems originates from hydraulic resonances in the high pressure supply system (Herfatmanesh *et al.*, 2016), specifically the accumulator common rail volume and its connecting pipe to the injector (Catania *et al.*, 2008; Ferrari *et al.*, 2016). These pressure fluctuations will significantly influence the performance of the injector in terms of start and end of the injection event and the overall injected quantity.

This is of particular concern when multiple injection strategies are necessary to achieve EU6 emissions regulations standards. To address this, F2 EU6 diesel engine fuel maps use an algorithm referred to as Pressure Wave Compensation (PWC). It is derived by mapping the intended application on an engine test bed (Herfatmanesh *et al.*, 2016), to determine the variances in fuel delivery for different injection separations and durations.

Therefore, it is important that this interaction between injector rail pressure fluctuations and the true injector performance be ascertained, so that this source of true injector performance variance can be differentiated from sources introduced by the environment of the rate tube injection meter.

If the sources of measurement variance in a rate tube measurement system can be characterised and mitigated, then it will significantly improve the ability of operations engineers in a production environment to carry out targeted investigations into the underlying causes of injector performance variances away from the ideal case. Leading to the possibility of using advanced data mining analytical techniques to derive the transfer function that describes the relationship between critical injector parameters such as nozzle needle lift, control valve lift, injector drive stator properties, and internal orifice diameters (Bingqi *et al.*, 2015).

2.4 Summary

Increasingly stringent emissions and efficiency regulations give rise to the need for novel mild hybrid engine applications, that impose stricter requirements on injection quantity and timing measurement capability with each technological step.

Near future challenges were identified as increasing injection pressures and energy input into the measurement system, the capability to characterise close coupled multiple injection events, and the ability to assess critical injector performance information contained within the characteristic shape of the injection rate signal. To meet these challenges, it is necessary to achieve a measurement system capable of providing a precise representation of the injection rate signal, concurrently with a stable and accurate injected mass quantity value.

A review of production capable injection rate measurement methods revealed significant Helmholtz resonance induced signal distortion present on piston-displacement and Zeuch chamber injection rate meters, concluding that they are incapable of providing a precise representation of the true injection rate signal. Therefore, a rate tube injection meter was confirmed as the target method to

study, due to its high injection rate signal fidelity and as yet uncharacterised sources of injected mass quantity measurement variance.

The established body of knowledge regarding known sources of measurement variance in a rate tube injection meter suggested specific target areas for study. Sources of zero value signal baseline variance, from pressure waves induced by hydraulic resonances. High frequency activity, known to be present in the spray of a high pressure diesel injection, potentially leading to excitation of resonances associated with the injection rate sensor port. Improving the accuracy of the temperature to SOS algorithm that dictates signal magnitude, by increasing the number of data-points used for its derivation. Characterising the relationship between temperature dependent fluid properties and the rate float cumulative signal offset, given that pressure and friction dependent fluid properties are likely to be consistent between repeat measurement events. Identifying whether the source of the bump artefact found on the injection rate signal after the end of the injection event is inherent to rate tube injection meters, or a potential release of pressure from the nozzle after the injection ends, as has been observed during optical engine experiments. A potential source of injector performance variance, related to resonant pressure wave activity in the high pressure supply system was identified.

To test the theories derived from the body of available literature, several experimental capabilities had to be developed, and are discussed individually in the following Section.

3 EXPERIMENTAL METHODOLOGY

This section discusses the experimental hardware and scheme of experiments devised for the present work. A justification is provided for the selection of the injector type, the specific rate tube measurement platforms, and the acquisition hardware used for this study. Then a summary is provided of the specific experimental schemes and methodologies, devised to meet the stated objectives of the work.

3.1 The Injector

The injector type used in the present work is an F2 Delphi common rail diesel injector (Meek *et al.*, 2014), as shown in Figure 3.1.



Figure 3.1: Delphi Heavy Duty F2 EU6 injector.

This is the current generation of EU6 commercial vehicle injectors rated at pressures up to 2700bar, with multiple injection capability. To ensure the greatest excitation of sources of measurement variance, a mild hybrid, turbo compound product application variant, operating at the highest pressure and fastest rate of fuel injection, was selected for this study (Nelles, 2019). This injector application's peak injection rates, results in the fastest release of energy from the injector per unit of time. Selected to induce the greatest excitation of the sources of measurement variance studied.

3.2 Rate tube production measurement system

This project uses a rate tube measurement system as previously outlined in Section 2.2.5. A rate tube is essentially a tube [B] with a termination orifice [C] and backpressure regulation [D] as shown in Figure 3.2.

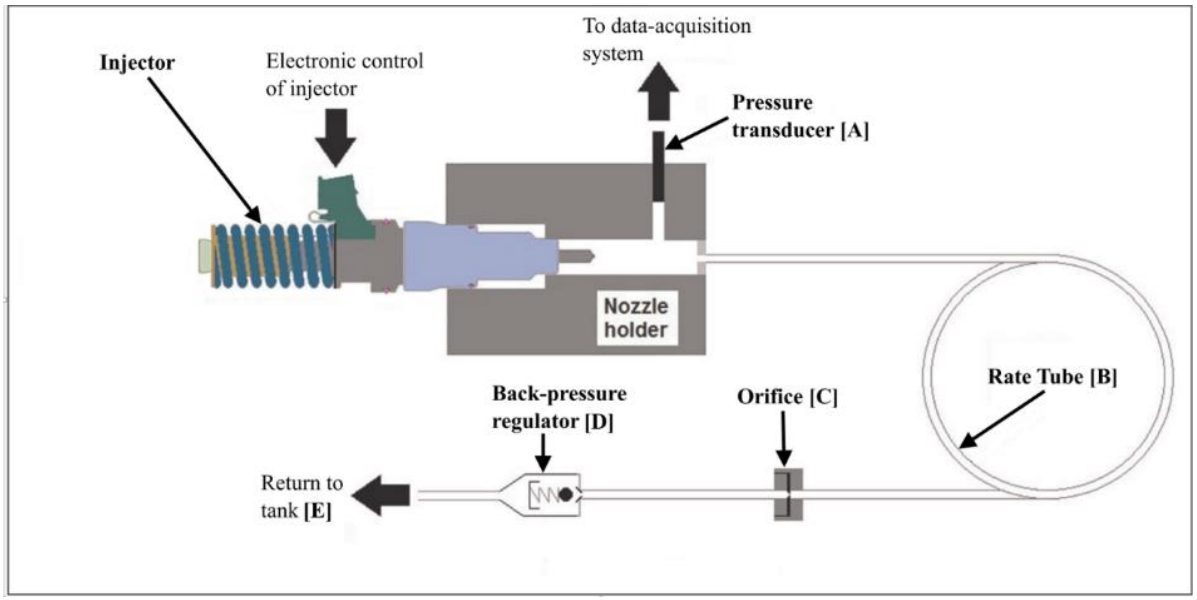


Figure 3.2: The Bosch fuel rate indicator, Sourced from (Lillington, Chetwynd and Jones, 2015).

This is the basic layout of all the experimental schemes used to study rate tube measurement variance. To reveal the sources of variance, this design was changed in terms of construction, control, or signal processing.

The specific hardware used for this study is a bespoke design created by Delphi Technologies. Originally developed for EU5 injector event timing measurement in series production, then adapted to enable both timing and total injected mass characterisation for EU6 Production in 2012, as illustrated in Figure 3.3.

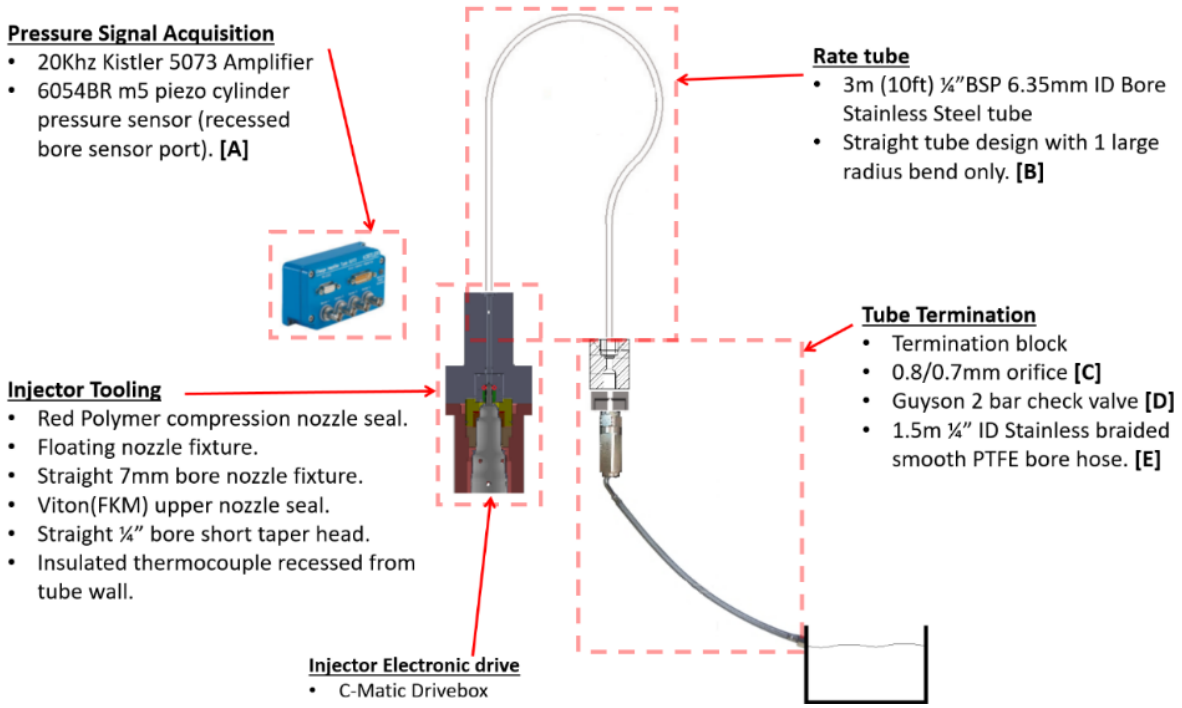


Figure 3.3: Original Delphi Technologies EU6 rate tube production measurement system design schematic (not to scale).

The critical features of this system were a Kistler 6054 piezo electric pressure transducer [A], 3m long stainless steel tube mounted in an upright position with a single bend [B], rate tube Internal Diameter (ID) of 6.35mm (1/4") [B], 0.8mm tube termination orifice [C], a 2bar Guyson check valve backpressure regulation [D], and a flexible hose fuel return to the main fuel reservoir.

3.3 Production measurement system platforms

Delphi Technologies used this design in two separate arrangements. For initial product launch and calibration test development in 2012, a low volume batch production development platform was initially used. It was fitted with a single rate tube measurement system, as shown in Figure 3.4.

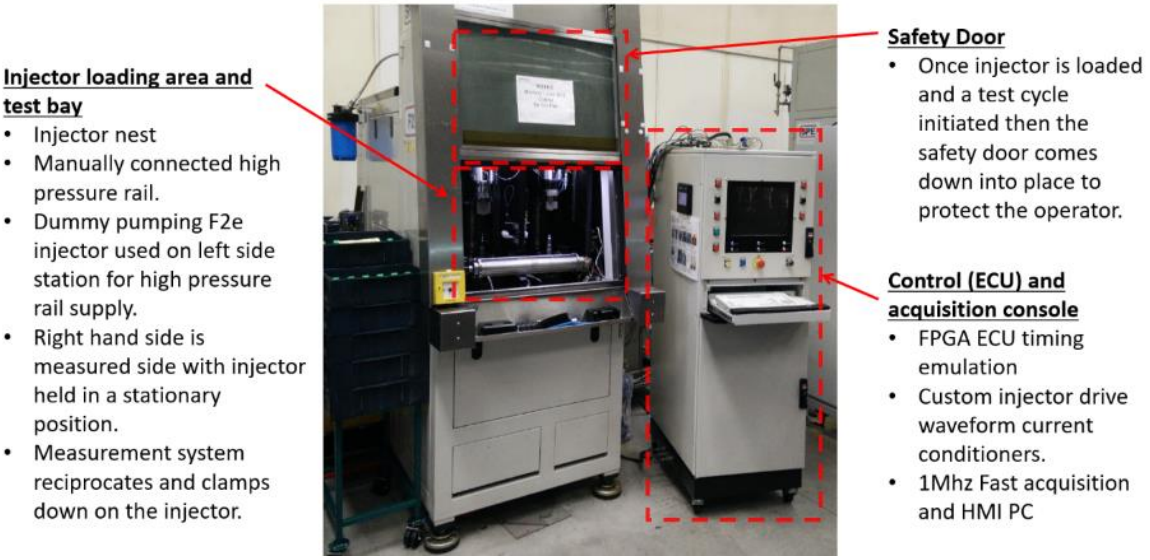


Figure 3.4: Front view of the original EU6 prototype development injector calibration test machine fitted with a single rate tube measurement system. Retired from series production and required refit.

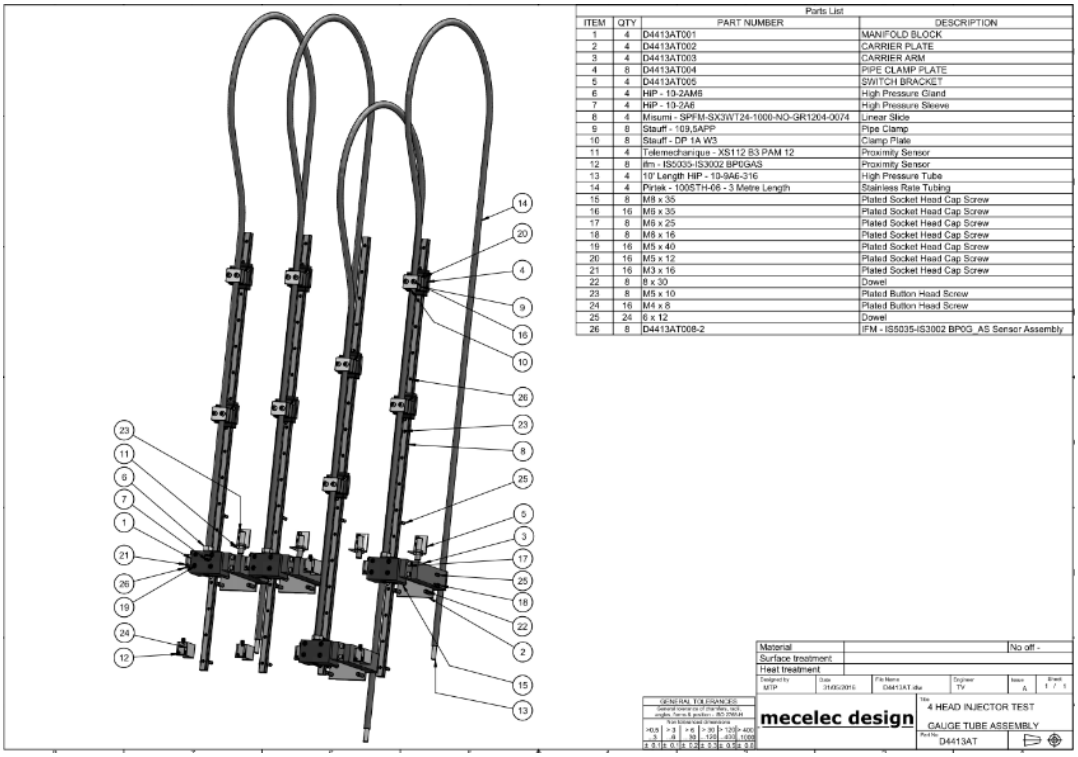
Once the initial EU6 injector test development work had been completed in 2014, that development platform was retired. To supersede it, a new series production injector test machine configuration was developed. To enable increased throughput, they feature four synchronised identical rate tube measurement systems, capable of testing four injectors in parallel, as shown in Figure 3.5.



Figure 3.5: Front view of an EU6 production injector calibration machine fitted with 4 synchronised identical rate tube measurement systems.

As of 2020, Delphi Technologies had 6 of these production injector calibration test machines, housing 24 identical measurement systems. Used for the EU6 F2 injector product family, in a continuous production environment. This platform was the basis for the first experimental scheme.

To give a sense of scale, a 3D CAD assembly of the four parallel rate tube measurement system design is shown in Figure 3.6.



Parts List

ITEM	QTY	PART NUMBER	DESCRIPTION
1	4	D4413AT001	MANIFOLD BLOCK
2	4	D4413AT002	CARRIER PLATE
3	4	D4413AT003	CARRIER ARM
4	8	D4413AT004	PIPE CLAMP PLATE
5	4	D4413AT005	SWITCH BRACKET
6	4	HIP - 10-2AM8	High Pressure Gland
7	4	HIP - 10-2A6	High Pressure Sleeve
8	4	Misumi - SPFM-SX3WT24-1000-NO-GR1204-0074	Linear Slide
9	8	Stauff - 109,5APP	Pipe Clamp
10	8	Stauff - DP 1A W3	Clamp Plate
11	4	Telemechanique - XS112 B3 PAM 12	Proximity Sensor
12	8	ifm - IS5035-IS3002 BPDGAS	Proximity Sensor
13	4	10' Length HIP - 10-9A6-316	High Pressure Tube
14	4	Pirtek - 1005TH-06 - 3 Metre Length	Stainless Rate Tubing
15	8	M8 x 35	Plated Socket Head Cap Screw
16	16	M6 x 35	Plated Socket Head Cap Screw
17	8	M6 x 25	Plated Socket Head Cap Screw
18	8	M8 x 16	Plated Socket Head Cap Screw
19	16	M5 x 40	Plated Socket Head Cap Screw
20	16	M5 x 12	Plated Socket Head Cap Screw
21	16	M3 x 16	Plated Socket Head Cap Screw
22	8	8 x 30	Dowel
23	8	M5 x 10	Plated Button Head Screw
24	16	M4 x 8	Plated Button Head Screw
25	24	6 x 12	Dowel
26	8	D4413AT008-2	IFM - IS5035-IS3002 BP0G_AS Sensor Assembly

Material | No off -
Surface treatment
Heat treatment

mecelec design

4 HEAD INJECTOR TEST
GAUGE TUBE ASSEMBLY
D4413AT

Figure 3.6: 3D CAD assembly of the four parallel reciprocating stainless steel tube configuration used in series production injector calibration test machines.

The following Figure 3.7 highlights a single production rate tube measurement system, from the perspective of the front loading bay, with safety panel removed.

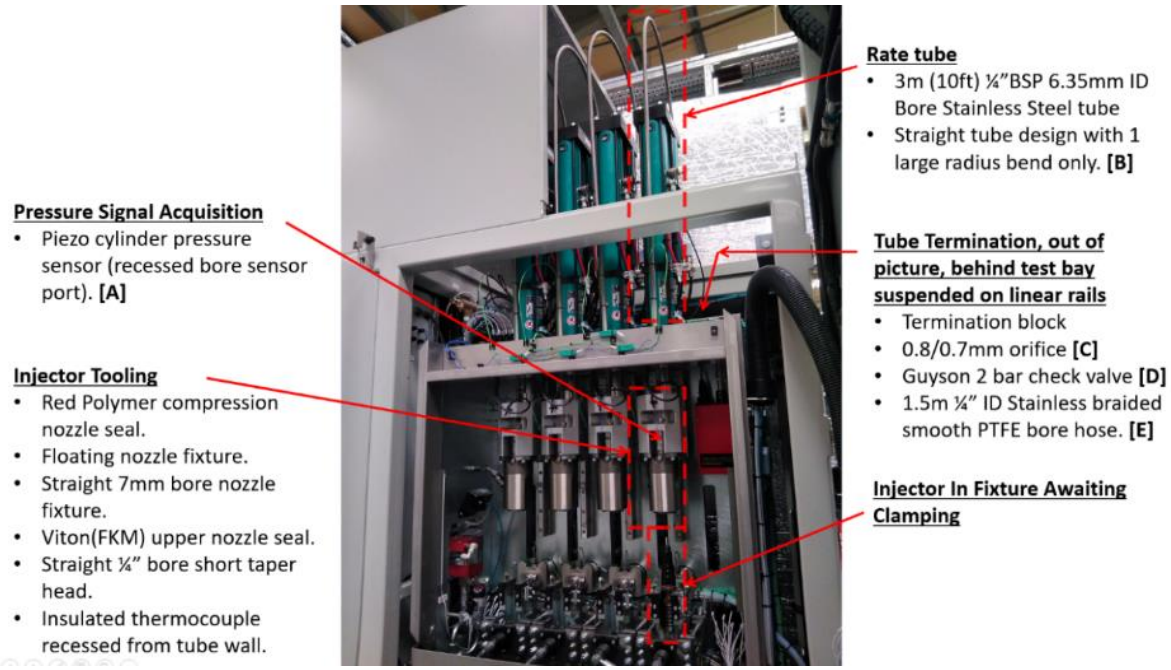


Figure 3.7: Front view of an EU6 production injector calibration machine with front enclosure removed and a single reciprocating rate tube measurement system annotated.

The cycle of these machines begins when four injectors are loaded into a part fixtures inside the loading bay and a test start command is sent by the operator. The rate tube measurement systems are slowly lowered onto each injector, rigidly clamping them in place using 15kN of hydraulic force. The test cycle is then carried out, synchronised between the four injectors. When the test completes, the injector clamp system releases the injectors from the part fixtures ready for unloading.

This design allows for a near ideal rate tube meter, featuring only a single large bend radius, a constant inner diameter for its length, and minimal use of hydraulic fittings.

This 'straight tube' design strategy presents a few unique challenges, such as the requirement of an additional 2m of vertical clearance, compared to the typical package requirements of commercially available injection rate measurement systems listed in Section 2.2.2.

Clamping the injector by reciprocating the entire injection rate measurement system, instead of moving the injector, is a design unique to Delphi Technologies Stonehouse. To enable this reciprocating action, the use of a flexible tank return hose is required, which is a unique limiting factor that must be considered during measurement system design optimisation.

3.3.1 Test machine engine emulation

The engine emulation system used on these machines is shown in Figure 3.8.

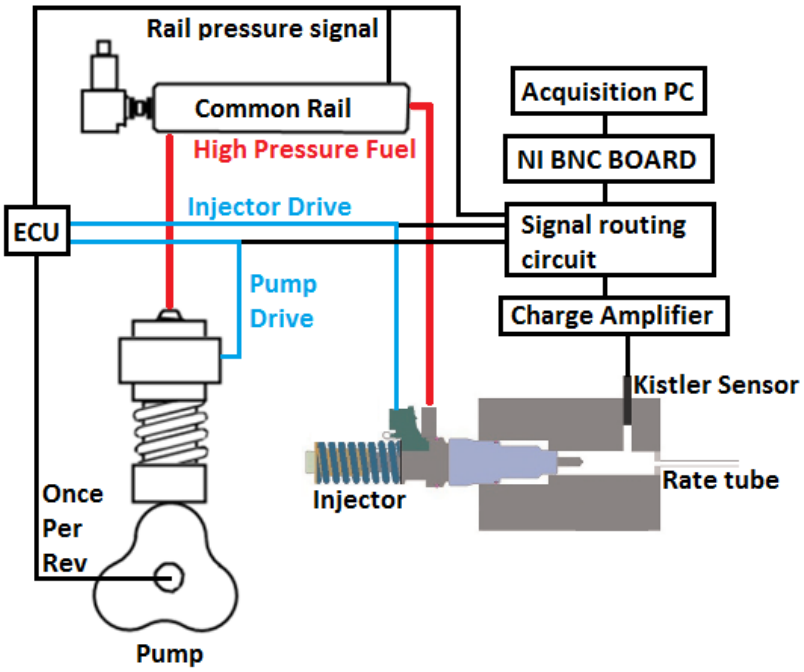


Figure 3.8: Engine environment emulation system schematic. Comprising of the injector drive, high pressure supply, and acquisition sub-systems.

This system mimics the injector's environmental conditions as seen on the engine. It is composed of the injector electronic drive circuit, high pressure fuel supply, and injection event signal acquisition subsystems.

High pressure fuel is supplied to the common rail by a Delphi EU6 F2P pump (Hardy *et al.*, 2012)' mounted in a cambox driven by a powerful 38kW three-phase electric motor. This high-pressure pumps demand is electronically controlled by a proprietary feed-forward ECU algorithm, designed to maintain stable EU6 pressure levels inside the common rail accumulator volume.

All sub-systems activity is synchronised to a once per rev (1/rev) high-pressure pump cam box timing signal from the ECU. This ensures reproducible pressure wave activity in the high pressure supply system, relative to the start time of the injection event.

The injection rate measurement signal is acquired with a Kistler 6054 piezoelectric pressure sensor, mounted near the injector nozzle. The signal is passed into a charge amplifier, through a signal routing circuit, then acquired at 1MHz sampling rate by a 14-bit 6133 National Instruments analogue signal acquisition card. Sensor data is then digitised, filtered, parametrised and stored live on a networked SQL database.

The injector test sequence and data management is performed by a proprietary injector test software platform, designed and implemented by the Test Development Integration team at Delphi Technologies Stonehouse. Its development arising from the need to minimise heavy-duty EU6 injector calibration test cycle times, using fast transient injector test cycle strategies.

All subsystems are PLC controlled and safety interlocked. The sub-system configurations presented here are common to all experimental schemes used in the present work. The changes made to the production measurement system hardware for each experimental scheme is discussed in the following Section.

3.4 Scheme of experiments

To meet all the objectives stated in Section 1.3, four experimental schemes were devised. The purpose of each scheme was to:

1 Experimentally investigate the influence of different hydraulic configurations, on observed pressure wave activity, using steady state injector test conditions.

The influence of changing the hydraulic configuration on low frequency baseline variance, as discussed in Section 2.2.6, was evaluated under steady state test conditions. The injection rate signals were manually acquired with an oscilloscope, then compared before and after making a production hardware change.

The insight gained about the influence of hydraulic configuration, on the nature of variance observed in the injection rate signal, directly contributed to objective one of this work.

2 Investigate the influence of different hydraulic parameters on observed low frequency pressure wave activity, using simulations of a rate tube meter, under steady state test conditions identical to experimental scheme one.

Experiments conducted on production equipment were limited by the necessity to return it to a standard production ready configuration between experiments. To overcome this limitation, a 1D model of the rate tube injection measurement system was constructed. With this method, the work was not constrained by the need to schedule time on the production hardware.

Working in model space also allowed for greater freedom to test the influence of different hydraulic parameters to a level of detail not possible on production hardware. Such as extreme changes to tube geometry, material stiffness, orifice characteristics, pressure regulation parameters and fluid properties. Low frequency pressure wave activity could also be inspected for any position within the rate tube measurement system, enabling its source to be revealed.

The work carried out in simulation space helped satisfy objective one, through deeper insight into the relationships between system parameters, and low frequency variance. Its development and use also satisfied objective two, to devise novel numerical methods to identify sources of variance. The knowledge gained was vital to the subsequent design of experimental schemes three and four.

3 Separate true injector performance from measurement system variance on production equipment, using synchronised Coriolis mass flow data acquisition, automatically acquired for steady-state running conditions.

To separate the true injector performance from measurement system variance, a secondary calibrated Coriolis mass flow rate measurement device was attached to a production measurement system. A steady state test cycle was carried out daily for a set of four known repeatable injectors. A rich mass flow enhanced production dataset was acquired for each injector over a three-month period. Then used to improve the accuracy of the temperature to SOS transfer function, introduced in Section 2.2.8. The hydraulic design required to achieve this arose from knowledge gained using experimental schemes one and two.

4 Emulate transient production test cycles on a custom experimental apparatus, satisfying objective three, characterising sources of measurement variance under transient test conditions. Also acting as a platform for development and demonstration of strategies to minimise sources of measurement variance.

To emulate the transient production test, an automatic sequence of injector running conditions were controlled by a novel transient injector test program, control computer, and signal acquisition hardware.

Additional sensors, acquisition channels, and improved data resolution enabled the automated capture of system activity at critical observation points, identified in simulation space during experimental scheme two.

Data from transient and steady state test cycles were compared, relationships between transient test conditions and sources of measurement variance were revealed, and subsequently mitigated using novel measurement system optimisations demonstrated on this novel apparatus, satisfying objective three of the present work.

3.4.1 Experimental scheme hardware strategies

To meet the commercial objectives of this work, an update was required for the EU6 measurement system design and calibration test strategy, that minimise sources of measurement variance.

To investigate the effect of potential production measurement system design optimisations, it was necessary to attain the capability to conduct automated steady state and transient testing under experimental conditions.

A summary of the capabilities and overall strategy of each experimental scheme is shown in Table 3.1 and

Table 3.2.

Table 3.1: Scheme of experiments

#	Scheme Name	Steady state/ Transient	Experimental hardware	Data Acquisition	Back pressure (bar)	Time series / Integer Summary data to be saved	Key Variables to be Measured	Number of test Conditions	Number of Integers / Time series per test condition
1	Production hardware	Steady state	Production	Manual	2	Time series (66ms)	Rate Tube pressure (rate), Injector drive, Rail pressure	1* to 4	0 / 4
2	Simulation space	Steady state	Simulation	Automatic	30	Time series (66ms)	Rate Tube pressures, Mechanical Regulator response	1*	Multiple
3	Coriolis mass meter trial	Steady state	Production	Automatic	30	Time series (~5ms) / Integer	Rate Tube pressure (rate), Rate tube temperature, Injector drive, Rail pressure, Coriolis Mass flow, Integer summary production data	16	20 / 5
4	Custom hardware	Transient / Steady state	Custom	Automatic	2, 30, 60	Time series (~5ms) / Time series (66ms) / Integer	Rate Tube pressure (s), Rate tube temperature(s), following hose pressure(s), Injector drive, Rail pressure, Coriolis Mass flow, Integer summary experimental data (extended)	182	34 / 11

*consists of many cycles in 1 test.

Table 3.2: Time required for experimental plan

#	Steady state/ Transient	Time per test (min)	Number of configurations	Repeat runs	Total No. tests	Time (hrs)
1	Steady state	15	72	1*	72	18
2	Steady state	180	25	1*	25	75
3	Steady state	20	3	100	400	34
4	Transient / Steady state	10 / 13	85 / 70	5 to 30 / 3	1364 / 257	228 / 56
					Total (hours):	411

3.4.2 Common parameters

A table of parameters common to all experimental schemes are shown in Table 3.3.

Table 3.3: Summary of parameters common to all schemes

Parameter description	Common value
Injection frequency	15Hz
Calibration fluid	ISO 4113 oil
Injector leak off circuit pressure	6bar
Injector leak off circuit flow	6L/min
Injector electronic drive waveform	Delphi F2 engine waveform
Clamp load	15

A 15Hz firing frequency is the equivalent of 1800rpm on a heavy duty engine and is a typical firing frequency for motorway speeds. This frequency is used on all Delphi F2 test equipment fitted with rate tubes as standard. ISO4113 calibration fluid is the industry standard diesel substitute used when testing diesel injectors. It is a kerosene based fluid that is hard to combust but with similar fluid properties to diesel (Grigg and Heinz, 1989). The low pressure leak off circuit pressure and flow is set to 6bar and 6L/min, the same as the engine application provided by the customer specification. The injector drive waveform is the same as used on the engine ECU. The clamp load is as per the installation drawing on the engine for F2 injectors.

3.4.3 Production hardware

To start hydraulic characterisation activities, the first experiments were carried out on standard production injector test hardware. Requiring manual control and data capture that forced the use of steady state test conditions.

Experimental results had to be post processed, to compare the effects of hydraulic configuration changes on the injection rate signal, because they could not be accessed live on the machine.

A top-down schematic view of the EU6 production calibration injector test machine initially studied, is provided in Figure 3.9.

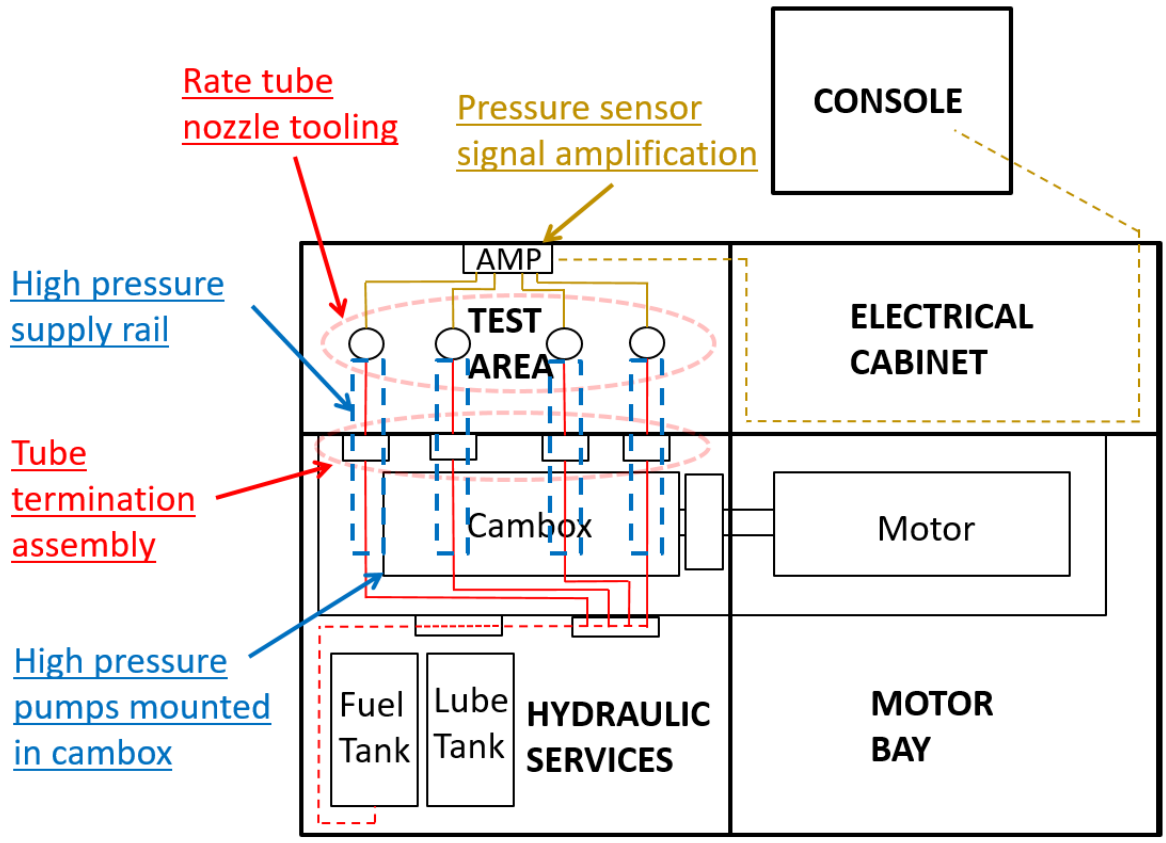


Figure 3.9: Top down schematic view of the EU6 production injector calibration test machine used for experimental scheme one

The rate tube measurement systems were the focus of study at this stage and are highlighted red in the schematic. All other elements remained unchanged.

The primary injection condition used a 2400bar pressure 2300µs injection duration injection condition, and a 15Hz firing frequency. Resulting in a highly energetic spray, rapidly delivering >300mg of mass per injection. This condition was chosen to represent peak load conditions on down-sped, heavy EGR, mild hybrid heavy duty engine applications (Nelles, 2019).

Injection duration then remained fixed at 2300µs whilst injector supply pressure was swept down in four steps between 2400bar and 450bar. Each of the four test conditions were maintained for 15 minutes, necessary to achieve thermally stable, steady-state measurement system conditions at each injection pressure.

Control and acquisition system hardware limitations of the production platform, meant it was not possible to automate acquisition of datasets for the 66ms period between injection events.

To work around this limitation, a novel data logging oscilloscope was devised to enable this experimental scheme. Running bespoke high speed C# software capable of capturing four analogue channels, for 1 second, at a sampling rate of

0.1MHz, for a maximum of 15 consecutive injection events. The manual triggering of the oscilloscope data capture was carried out every 3 minutes, using a stopwatch as a reference time base, so that the effect of different measurement system temperatures on production hardware could be studied.

3.4.4 Simulation space

Delphi Technologies has expertise in Simcenter Amesim by Siemens PLM one dimensional (1D) hydraulic simulation software (LI and LI, 2006). This software specialises in simulating fuel injection systems (Chaufour *et al.*, 2004), pre-loaded with the ISO4113 production calibration test oil specification, as used in the rate tube injection meter. By drawing upon this in house expertise, a unique 1D rate tube model of experimental scheme one was developed.

Long simulation execution times meant the maximum simulated period was capped at one second, or 15 injection events at a 15Hz injection frequency. Each simulation run used system parameters initialised to steady state quiescent conditions. Reducing the number of wasted injection events required to stabilise hydraulic parameters in the simulation from ten down to two.

Excitation of pressure wave activity in the model was achieved using a mean injection flow rate input profile, derived from the 2400bar pressure, 2300μs duration injection event data captured on experimental scheme one. To limit overall execution times, the single most energetic high pressure condition was selected for study. The pressure wave activity in simulation space was then compared with experimental results, to validate the model and iterate its construction.

The Amesim software enables time series data of any fluid or mechanical property, to be recorded at any point in time or position in the model. The time step resolution of the simulation was set at 10 microseconds, which offered the best balance between execution time and fidelity of low frequency activity. Parameters such as pressure waves, regulator mechanical response and orifice flow dynamics were scrutinised. Providing a unique perspective of how the pressure waves generated by the mass input event progress through, then interact with, components of the rate tube measurement system.

These additional perspectives provided a significant improvement over the single observation point of standard production hardware used during experimental scheme one. Fulfilling the core purpose of the work in simulation space, to identify the fundamental source of low frequency variance observed on production hardware. So that novel hydraulic circuit configurations could be devised. Thus, enabling the work carried out on experimental scheme three and four, as described in the following Sections.

3.4.5 Coriolis mass meter production trial

Experimental scheme three was achieved with a three-month trial carried out under production injector test conditions, to record the mass flow rate data, used as the target for novel data mining techniques. Also providing a rich dataset to test methods to improve the accuracy of the temperature to SOS signal magnitude compensation algorithm.

To gather this valuable dataset, a novel production measurement equipment hydraulic configuration was needed, with the capability to capture Coriolis mass flow values synchronised to injection rate data automatically.

Using knowledge gained pursuing objective one on the previous experimental schemes, a series of prototype configurations were devised, then briefly tested on the production hardware used for experimental scheme one. Once a suitable solution had been found, it was temporarily installed for three months to fulfil the stated objective of this experimental scheme.

A schematic layout of how this was achieved in a series production injector calibration test machine is presented in Figure 3.10.

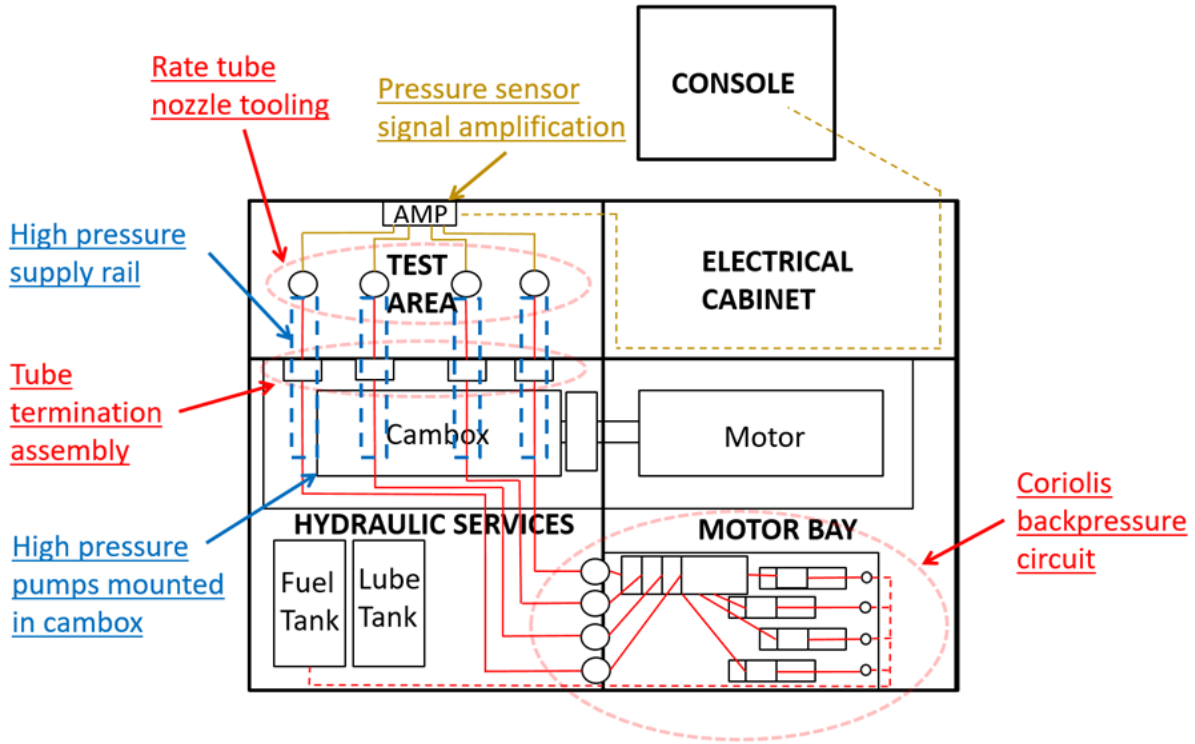


Figure 3.10: Top down schematic view of the EU6 production injector calibration test machine used for experimental scheme one, with Coriolis mass flow meter backpressure circuit retrofit that was used for experimental scheme three.

The Coriolis mass meters were installed in the motor bay and are highlighted red in the schematic. All other elements of the test machine not associated with the rate tube injection meters remained unchanged.

A special set of injectors were created using known repeatable 'golden' nominal injectors. They were tested daily on a custom steady state test program, containing all 16 EU6 calibration trim load conditions, measured when steady-state thermal trends, necessary for a reproducible Coriolis mass flow measurement, had been achieved. The stabilisation periods were discerned when tuning the test cycle, by scrutinising the measurement system temperature trends.

Data acquisition was carried out automatically using the production test machine computer running the steady state test program. The Coriolis mass flow measurement was automatically recorded in parallel with standard production test data. When the special set of master injectors were loaded into the machine, they trigger the steady state Coriolis test program. Hence, synchronous Coriolis mass flow data could finally be continuously acquired, by production operators loading master injectors into the production injector calibration test machine, previously used as the platform for experimental scheme one.

The calibration test analogue time series and integer summary data was uploaded live to an SQL database, for the three-month time-span of experimental scheme three. Allowing near instantaneous access to the production dataset using bespoke data visualisation tools, developed in the Matlab coding environment.

3.4.6 Custom hardware

Using knowledge gained during the first three experimental schemes, a custom experimental apparatus was devised. The platform for this apparatus was the EU6 prototype development injector calibration test machine first shown in Figure 3.4. This apparatus was upgraded using the latest available hardware. Its core capabilities derived from knowledge gained on the previous experimental schemes. Such as 1MHz acquisition of the 66ms period between injections, synchronous Coriolis mass flow measurement, and automated data acquisition.

A top down schematic view of the EU6 prototype development injector calibration test machine, used for experimental scheme four, can be seen in Figure 3.11.

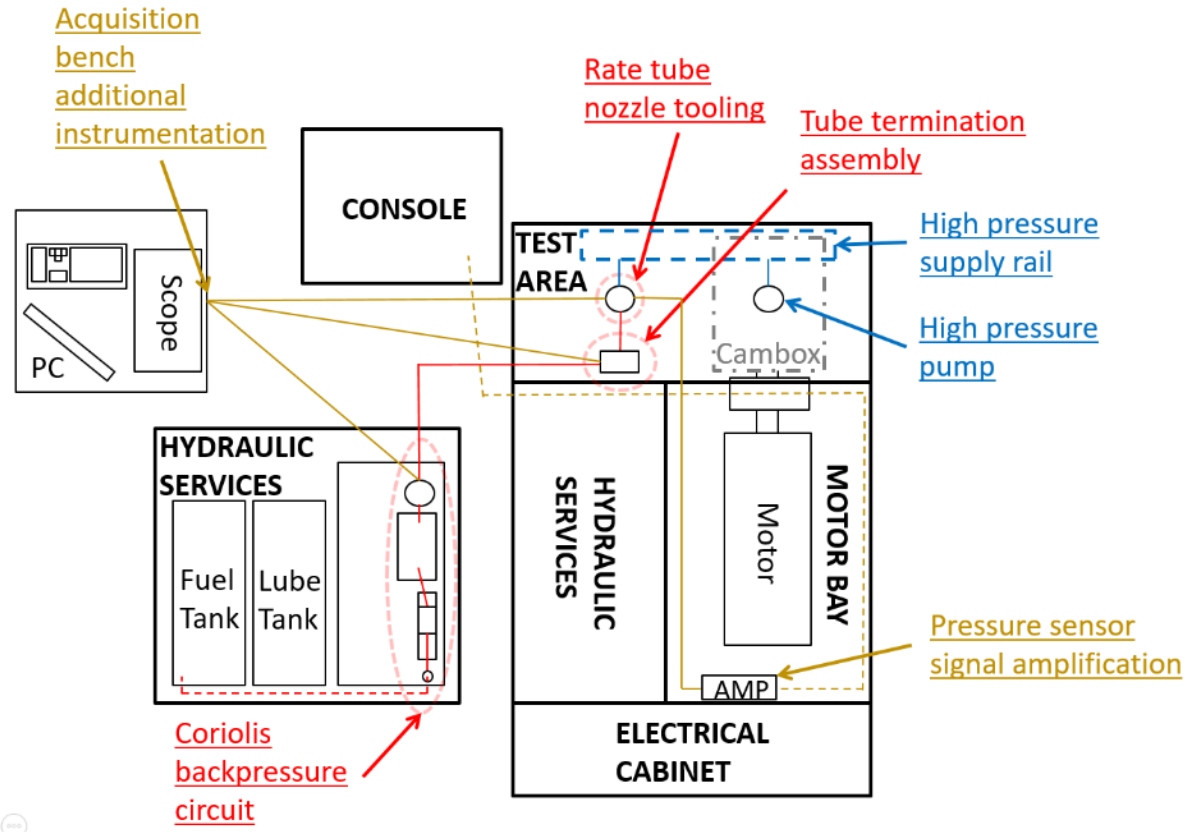


Figure 3.11: Top down schematic view of the upgraded EU6 prototype development, injector calibration test machine used for experimental scheme four.

The decommissioned development test machine platform was upgraded and adapted for use as experimental scheme four. Unlike experimental schemes one and three, it was less constrained, in terms of opportunities for potential hardware changes, due to it being a test development, rather than series production, experimental scheme platform.

Once it was recommissioned and upgraded to the highest available standard, this unique experimental apparatus could characterise >200 transient injector test conditions. As required to emulate the production injector test cycle that characterises the entire injector performance envelope in less than five minutes. The 16 condition steady state test cycle, developed on experimental scheme three, was updated and used as an additional comparative test program. Therefore, this novel apparatus could record all necessary steady state and transient test data, at identical injection conditions, for the first time.

Additional photographic images of each experimental scheme are provided in Appendix 11.1 for additional context.

How each source of measurement variance was characterised, using data from all experimental schemes, is discussed in the following chapters.

3.5 Division of responsibilities

Commercial role of the author

The present work was carried out in a commercial work environment. The role of the author was that of a lead injector test development engineer for new production applications. The author specialises in advanced production data analytics and injector test process optimisation. The author was also responsible for researching novel technologies to meet future heavy duty injector test requirements.

This role was carried out within a team of up to 10 engineers in a department called Test Development Integration (TDI), a multidisciplinary mechatronic engineering department, responsible for development of novel production injector test processes, to characterise new heavy duty injector applications under continuous production conditions. This activity was necessary to bridge the gap between product samples and product launch into full scale production.

The bespoke production injector test machine designs used in experimental scheme 1 & 3 in the present work was developed by TDI. The building of the machine frames was subcontracted to bespoke industrial equipment manufacturers. The measurement systems, control hardware and software were developed in-house and commissioned into production by the TDI team.

Role of the author for the present work

The present work was initiated after the author completed a review of existing technologies, highlighting a requirement to develop novel techniques for near future heavy duty injector test applications, as discussed in Section 2.1. The outcome of this review was used as commercial justification for the present work.

The author was responsible for all design of experiment activities described in Section 3.4. Including development of simulation model for experimental scheme 2 detailed in Section 5.2; design and commissioning of the experimental scheme 3, coriolis mass measurement described in Section 3.4.5; reconfiguration of experimental scheme 4, novel injector test platform described in Section 3.4.6; development of the novel hydraulic configurations described in Section 5.4; and injection rate signal measurement modifications discussed in Chapter 6.

Project management was carried out by the author, with commercial approval for all proposed activities obtained from the authors line manager. Once an experimental scheme had been commissioned, the author was responsible for validating the methodologies and establishing baselines. All experimental data was collected, validated, analysed, and documented by the author. The present document was written solely by the author.

4 THE EFFECT OF ENVIROMENTAL VARIABLES

4.1 Introduction to sources of measurement variance identified

In the following chapters, the influence of environmental variables on the variance of the measured fuel result are examined. The pressure wave activity within the rate tube will affect the variance of the injected mass measurement, due to the principle of operation of a rate tube that requires an integration of the incident pressure wave, without distortion, to derive a total injected mass value. Hence, any pressure wave activity in the measurement system not caused by the mean flow rate of injection, can cause artefacts in the injection rate measurement signal.

The temperature of the measurement system can affect the total injected mass value, as the equation to derive rate tube mass injection rate [2.6] requires knowledge of fluid properties during the injection event, which is inferred from a fluid temperature measurement. Temperature of the measurement system fluid medium can also influence the timing of low frequency pressure wave activity within it. The supply pressure to the injector dictates the pressure drop across the injector nozzle and therefore directly influences the mean flow rate of injection. The rate tube pressure signal acquisition hardware can distort the pressure wave signal from the measurement system and the resultant mass measurement. The interaction of these environmental variables with different hydraulic configurations were explored to understand sources of measurement variance in the injected mass value for a rate tube injection meter.

The sources of variance identified through the initial literature review are introduced in brief. Each source of variance and their relationship to environmental variables is then discussed separately, drawing upon data gathered from all experimental schemes. The contributions to knowledge for each variance are summarised in the conclusions in chapter.

A deconstruction of the injection rate signal was performed to illustrate the sources of measurement variance inherent to the rate tube method. This summary of the sources of variance identified are shown in Figure 4.1.

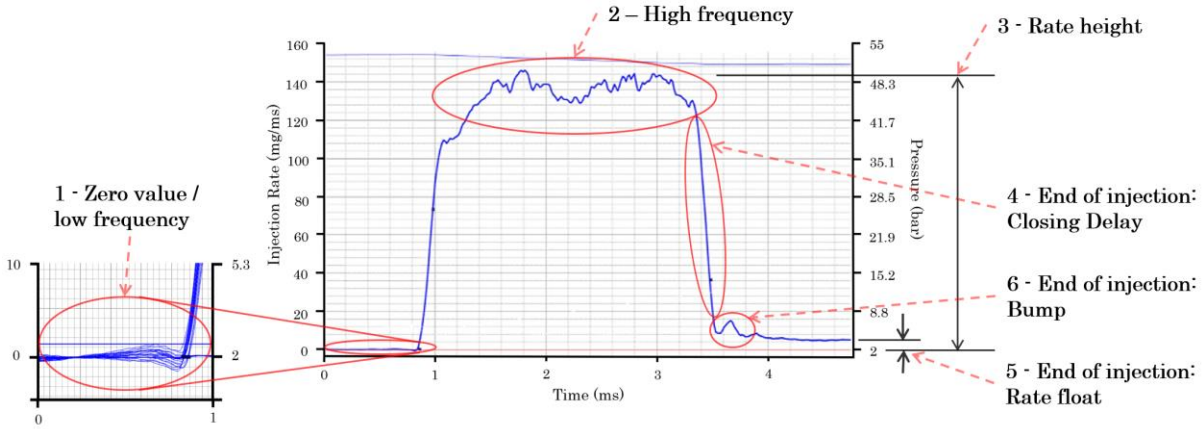


Figure 4.1: Sources of variance identified for an injection rate measurement device

The discussion of each source of measurement variance is organised across the following thesis chapters and described here in brief.

4.1.1 Zero Value variance

Low frequency pressure waves in the fluid medium inside the rate tube can cause the injection rate zero value baseline to vary. These artefacts in the baseline will convolve on top of the pressure wave induced by mass input from the injection event. Adding error to the injected mass value calculated from the area under the observed pressure wave in the rate tube. Therefore, zero value variance is not a true feature of the injection rate signal. The objective of this work was to reduce it to the point where its effect on the injection rate signal is an insignificant factor for the total injected mass measurement. This source of variance can affect both consecutive injection measurement and the reproducibility of measurements made across different separate production test cycles. This source of variance is discussed in Chapter 5.

4.1.2 High frequency variance

High pressure injections of greater than 1000 bar are known to drive cavitation in the spray from high pressure diesel injectors (Dernotte *et al.*, 2012). This effect is found inside the injector nozzle and within the fluid medium of the measurement system itself. The objective of this work was to characterise, then reduce the effect this cavitation has on the injection rate signal. When cavitation activity is severe, it can result in an unstable injection rate when the maximum injection rate has been reached. This instability can be observed in Figure 4.1 for the segment where the nozzle is fully open and peak injection rate is achieved. It is possible to extract information about cavitation activity from this segment of the injection rate trace. This effect typically averages out if enough measurements are taken and is thought to only affect consecutive measurement variance. This source of variance is discussed in Chapter 6.

4.1.3 Rate height

The rate tube mass injection rate Equation [2.6] is the integral of the observed pressure wave multiplied by a value derived from fluid properties. This multiplier derived from fluid properties dictates the overall height of the injection rate trace. In Figure 4.1, point 3 shows the rate height observed from the injection rate signal. This scaling of the pressure wave to derive an injected mass value is also a source of variance that is dictated by the accurate characterisation of fluid properties in the measurement medium to derive the multiplier value.

In the current system, the fluid properties are not directly measured, but inferred from a temperature measurement near the injection event, hence inaccuracies in the mapping of measurement system temperature to fluid properties is a potential source of injected mass variance. If the accuracy of the mapping of fluid properties to system temperature is improved, then the influence of this source of variance will be reduced. It was assumed that fluid properties are consistent for consecutive measurements, so this source of variance is most likely to affect the reproducibility of different test cycles. This source of variance is discussed in Chapter 7.

4.1.4 End of injection: Bump

In a rate tube injection analyser, the signal at the end of injection often has multiple inflection points, once injection ends and the pressure inside the tube has fully decayed. Described as a 'bump' in the injection rate signal, located after the end of injection. A close up view of this artefact can be seen in Figure 4.2, which is linked to point 6 in Figure 4.1.

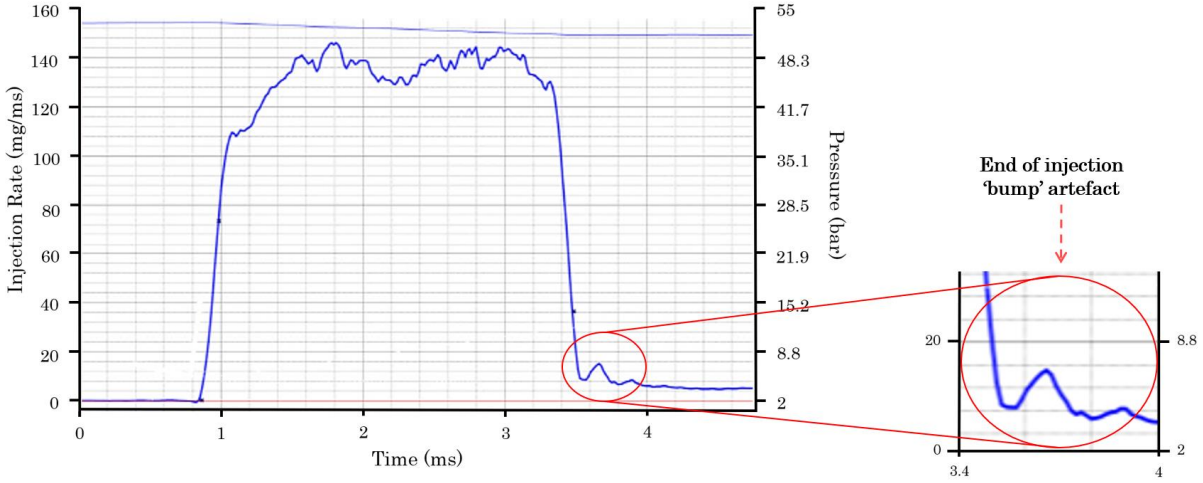


Figure 4.2: End of injection 'bump' artefact magnified view

The magnitude and characteristic shape of this artefact is driven by high injection pressures and is present across the whole performance envelope of the injector. The exact mechanism that drives this characteristic was not known before this work. This feature in the rate signal made implementing a robust end of injection threshold for the pressure wave integration to finish, as a challenging task. As stability of the end of injection threshold will be differ across injection loads. The goal of characterising the hydraulic feature responsible for this bump artefact at the end of injection was achieved and discussed in Section 8.2.

4.1.5 End of injection: Rate float

In a rate tube injection meter, the rate signal does not return to baseline at the end of injection as shown in point 5 of Figure 4.1, an effect linked to high injection pressures and durations. It has been associated in literature to fast changes in fluid properties inside the rate tube meter as discussed in Section 2.2.9. It is thought that fluid temperature is the primary driver and will be consistent for consecutive injection event measurements. Hence, this source of variance mainly affects test to test injection rate measurement reproducibility. A criteria for when this error will be consistent test to test was extracted by studying measurement system environmental variables on experimental scheme one, and is described in Section 8.2.

4.1.6 End of injection: Closing Delay

The reproducibility of the position and gradient of the decaying slope at the end of injection, is linked to supply pressure activity at specific injection event durations. The time between the end of the electronic drive signal and the decaying slope, is referred to as Closing Delay (CD), as shown in point 4 of Figure 4.1. If the temporal position of this decaying slope varies, then it will change the area under the pressure wave due to the injection event, and be observed as variance in the total injected mass value. It is caused by a genuine variability in the closing time of each injection event, leading to variability in injected mass. Not an artefact of the rate tube measurement system. This knowledge was attained using normalised datasets from experimental scheme four and using them as inputs to advanced numerical methods, satisfying objective two of this work. How this was achieved is described in Section 8.3.

5 ZERO VALUE VARIANCE

The rate tube mass injection rate Equation [2.6] assumes that the column of fluid in the rate tube is held at a constant backpressure, and any observed change in pressure is down to the input of fuel into the tube from the injector. This assumption relies on the pressure within the rate tube reaching a quiescent condition before another injection event can be measured. If the pressure in the tube does not reach quiescence, then any residual pressure waves will convolve on top of the subsequent injection measurement and will distort the injection rate signal as explained in Figure 5.1.

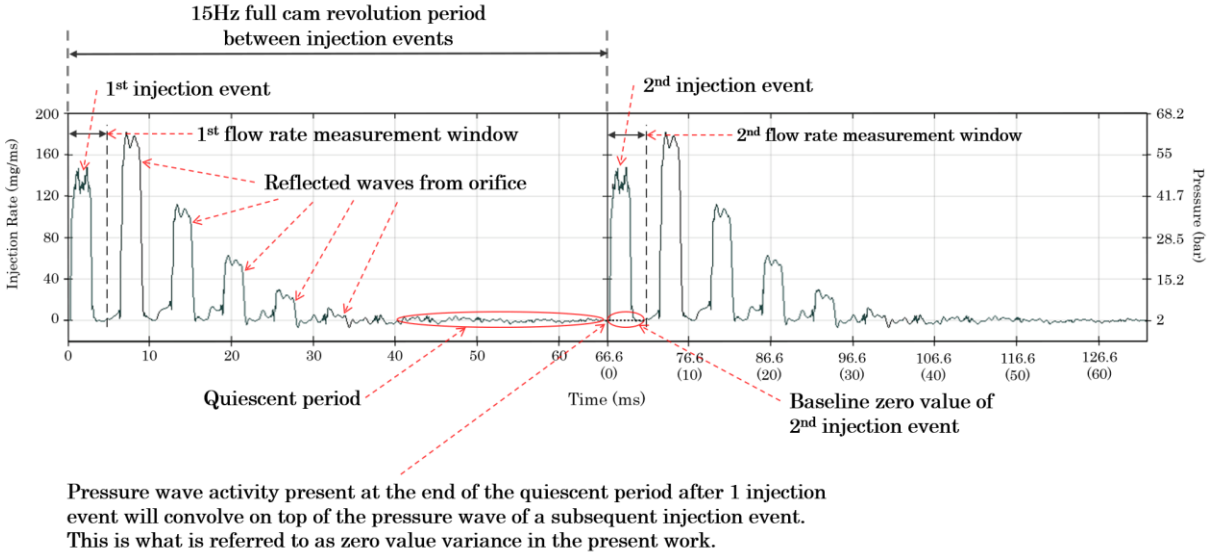


Figure 5.1: Schematic diagram of the method of action of zero value variance.

There are several hydraulic circuit parameters that can superimpose a low frequency, less than 5kHz, low amplitude wave on the measurement signal and hence are potential sources of unwanted zero value measurement variance.

This Chapter is split into 4 Sections, each investigating zero value variance on a different experimental scheme, with all 4 experimental schemes being utilised. In Section 0 manually acquired injection rate signals are evaluated for simple empirical trials on the production hardware of experimental scheme 1 to gain insight into the mechanisms driving changes in zero value variance observed empirically. The construction and evaluation of the experimental scheme 2 one dimensional model of a rate tube is discussed in Section 5.2. The influence of temperature on zero value variance observed during a 3 month coriolis meter retrofit in production conditions on experimental scheme 3, are presented in Section 5.3. Finally in Section 5.4 the knowledge gained from the first three experimental schemes was used to devise an optimised hydraulic circuit design that minimises zero value variance using the bespoke test research platform.

5.1 Influence of hydraulic configuration

This section details the knowledge gained during experimental scheme one, where the influence of changing the hydraulic configuration from the tube termination orifice to the end of the following hose was examined.

This characterisation was necessary because little is known about what influences the low frequency wave activity in a rate tube measurement device. In literature and with commercial rate tube measurement devices, any problems with zero value variance are normally solved by reducing the firing rate of the injector so that the pressure in the tube has a larger amount of time to reach a quiescent condition. This is why rate tubes are thought to be slow measurement devices compared to other available alternative methods of measuring injection rate (Gandhi, Meinhart and Ortiz, 2009). This is not normally a problem when conducting fuel system design and development activities where the time to characterise an injector is not critical. However, the present work is concerned with a production environment where cycle times and measurement reproducibility are paramount. Hence, the objectives of this work dictate that zero value variance be well understood, to enable design changes to the hydraulic configuration and minimise cycle times. Without causing additional zero value variance in the injection rate measurement.

The aim of this present work was to develop a Coriolis mass meter circuit design that could be implemented in production for experimental scheme three. This had to be achieved without allowing more time to achieve quiescence and hence lowering the firing rate of the injector and raising the injector production test cycle time. The intention for experimental scheme three was to place the Coriolis meters in the motor bay because of installation constraints on the production hardware as shown in Figure 5.2.

First, the implications of a non-constant cross Section near the tube termination is examined. Then the impact of moving the back pressure regulation, labelled [D] in Figure 5.2, to the end of the following hose, labelled [E] in Figure 5.2, is discussed. The effect of changing the following hose internal diameter is examined. A custom fuel chiller is then added to the end of the circuit to allow the fitment of a Coriolis meter. A backpressure regulator set to 30bar is added to the system before the fuel chiller and its influence on backpressure stability is examined. The observation point for these early zero value characterisation experiments is shown labelled [A] in Figure 5.2.

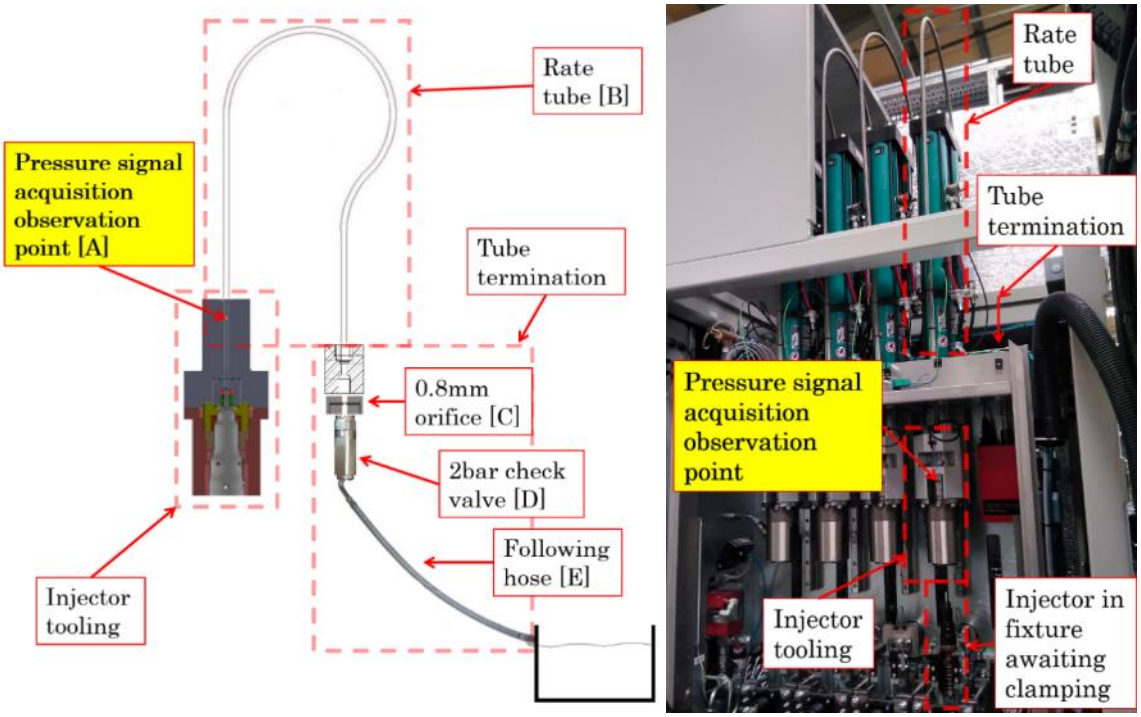


Figure 5.2: Injection rate pressure signal observation point in the production measurement system.
Left: Schematic diagram with position of piezoelectric pressure transducer highlighted.
Right: Production injector test machine with piezoelectric pressure transducer highlighted.

5.1.1 Quiescence target

To define a target for acceptable variance at the end of the quiescent period, the standard production configuration was observed for both new and fault conditions. When no fault is present, the standard production configuration displays less than ±1mg/ms at the end of the quiescent period. At this magnitude, no observable effect on measurement variance is observed. Under fault conditions, such as a damaged backpressure regulator, it is known that pressure waves in the injection rate only need to exceed ±2mg/ms in amplitude to contribute to zero value variance. This small magnitude is difficult to perceive next to a peak injection rate value during the measurement window of greater than 100mg/ms. Hence all the results presented in this Section show the full 15 Hz firing period between injections with a magnification of the quiescent period to highlight these small variances. The zero value variance acceptance limits of ±1 are shown in green with unacceptable limits of ±2mg/ms shown in red.

5.1.2 Changes in rate tube geometry

The theory used to derive the rate tube mass injection rate Equation [2.6] relies on one dimensional (1D) wave theory. This assumes the rate tube, as labelled

[B] in Figure 5.2, is constructed using a pipe of constant diameter from the point where injection occurs up to the termination orifice.

To understand if the production standard tube termination conformed to the 1D wave assumption of a constant cross Section, an analysis of the hydraulic fittings near the tube termination and their internal geometry was undertaken. The production standard tube termination composed of a tube termination block as shown by point 1 of Figure 5.3. A ¼"BSP hydraulic blank fitting that is precision drilled in its centre to 0.8mm, as shown by point 2 of Figure 5.3. Details of how these components are arranged and attached to the 2bar check valve for the tube termination assembly are shown in point 3 of Figure 5.3.

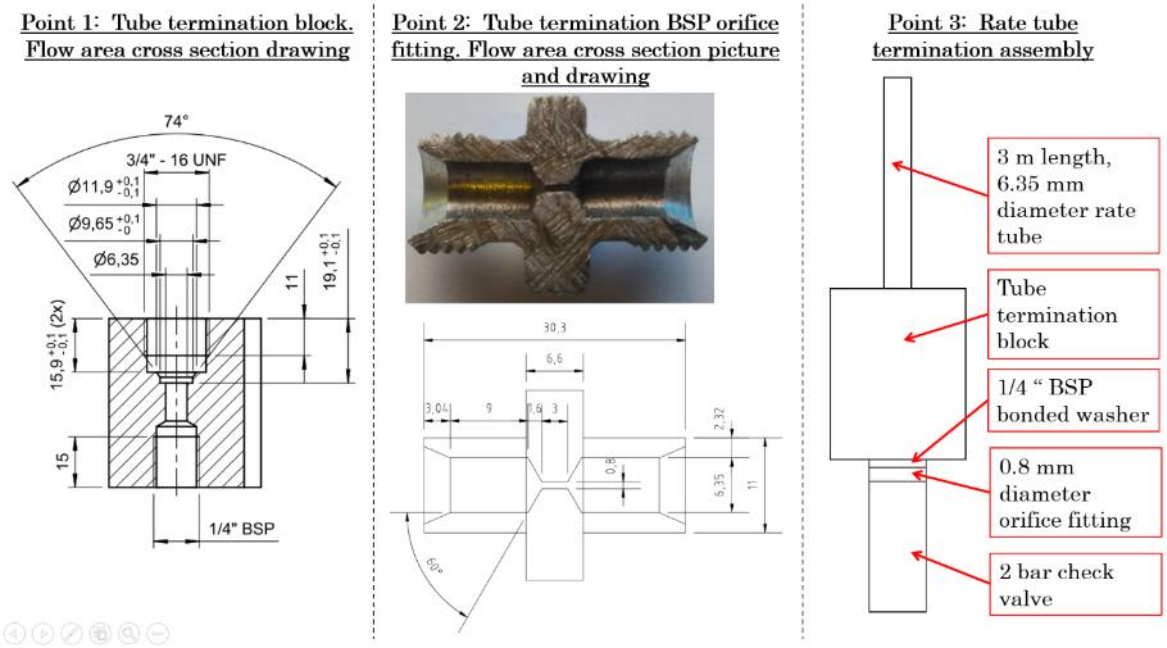


Figure 5.3: Left: Tube termination block cross Section diagram. Middle: 0.8mm ¼"BSP orifice fitting cross Section drawing and picture. Right: Rate tube termination assembly diagram.

This result revealed that the stack of hydraulic fittings before the tube termination orifice did not provide a flow area of constant cross Section. The flow area up to the tube termination for the standard configuration is shown in Figure 5.4. The end of the 3m length rate tube interfaces with the tube termination block without a change in the 6.35mm diameter cross Sectional flow area. However, there is a significant expansion to allow space for a ¼"BSP thread for the orifice fitting to attach to. The flow area expands from 6.35mm to an 11mm ¼"BSP threaded bore. Then contracts back down to a 6.35mm bore before the orifice is encountered by the pressure wave. This means that the standard rate tube termination assembly has an expansion volume that could superimpose additional frequencies into the observed pressure wave relative to its geometry.

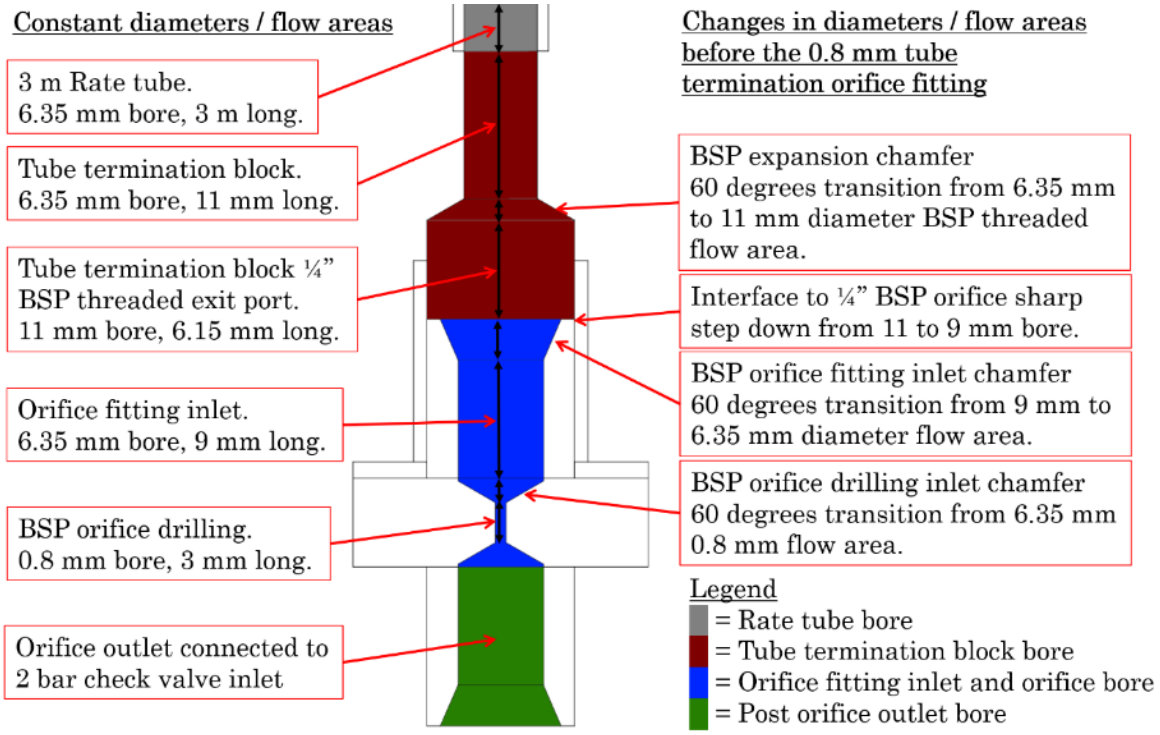


Figure 5.4: Illustration of non-constant cross Section prior to the orifice, caused by the geometry of the production standard rate tube termination block.

To determine whether this change in tube diameter near the orifice had any effect on the observed pressure signal, an alternative termination was fitted to the end of the tube. The termination block that the orifice was normally housed in was cut into two pieces. Then a precision drilled 0.8mm orifice plate was inserted and sealed between them, and the two halves of the block bolted rigidly back together. The flow area up to the tube termination orifice for this modified configuration is shown in Figure 5.5.

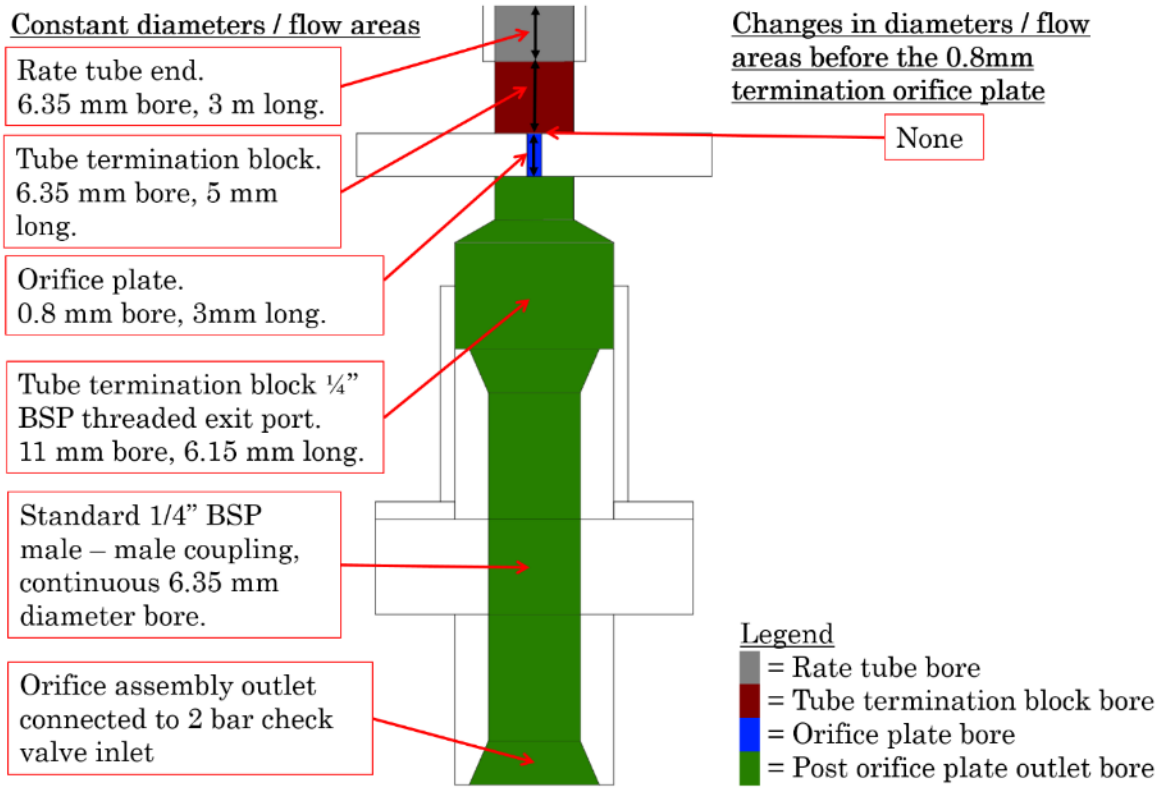


Figure 5.5: Illustration of 6.35mm constant diameter cross Section prior to the orifice achieved by modifying the standard rate tube termination block to allow use of a custom orifice plate.

When using the standard configuration tube termination orifice with non-constant cross Section, there is a corresponding high frequency oscillation observed at the start of the reflected wave. Every time the wave arrives at the non-constant cross Section near the orifice, another oscillation is observed as shown in point 1 of Figure 5.6. The addition of fast pressure oscillations then ceases once the reflected waves have been attenuated by the termination orifice. However, the observed oscillations then continue into the quiescent period and would convolve on top of the next injection event as shown in point 2 of Figure 5.6.

When an orifice plate is fitted, that maintains a constant cross Section, the oscillations observed in the pressure wave are no longer present. This result confirms that this artefact in the pressure wave is caused by the expansion volume found near the tube termination in the standard configuration. It also shows the importance of maintaining a constant cross-sectional flow area up to the tube termination orifice to minimise artefacts that can cause zero value variance in the next injection event.

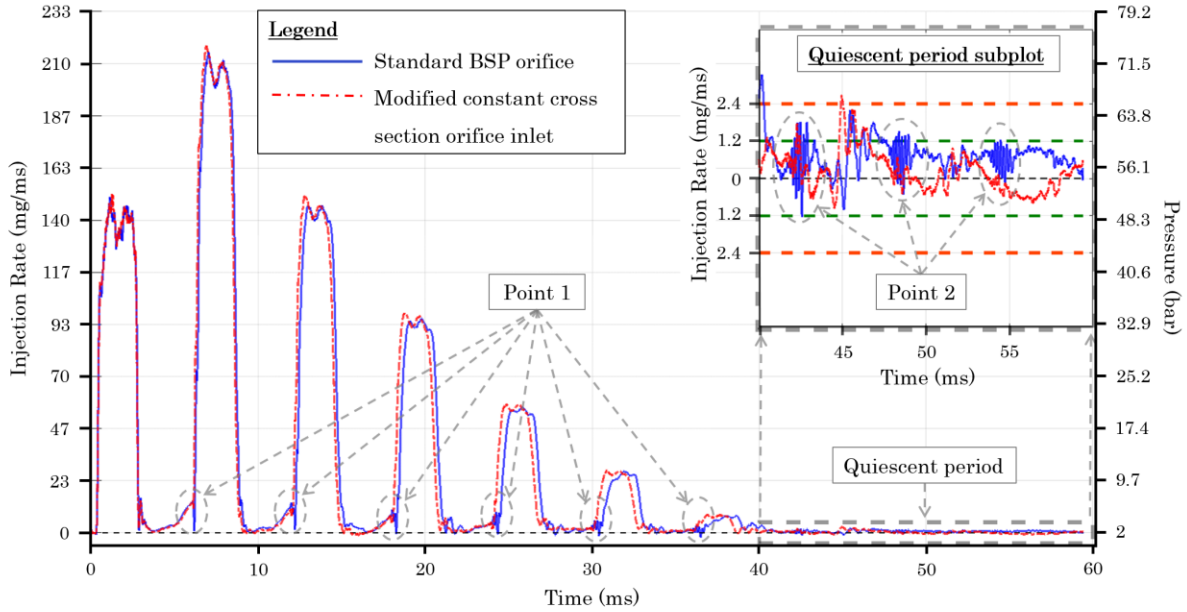


Figure 5.6: Modified constant cross section orifice inlet vs standard drilled BSP blank rate tube termination orifices.
2400bar pressure 2300µs duration injection condition.
Blue: Standard production 2bar system with drilled BSP blank termination orifice.
Red: Modified 2bar production measurement system with modified constant cross Section termination orifice.

This result demonstrated that even slight changes to the rate tube diameter before the termination orifice can cause significant sources of error in the zero value baseline that would affect the next injection. The author is not aware of any literature that explores the influence of tube termination geometry and hence this finding is a new contribution to knowledge.

Once the effect of non-ideal hydraulic configuration before the tube termination orifice had been determined, the work moved on to characterising the effect on zero value variance of changing the hydraulic configuration after the tube termination orifice, and is discussed in the following Section.

5.1.3 Position of the backpressure regulator

The backpressure regulator in a rate tube measurement device is required to satisfy the assumption of a constant baseline pressure used to derive Equation [2.6]. It is assumed that any differences in observed pressure waves from one injection to the next, are a product of only the injected mass. The effect of the position of this regulator in the hydraulic circuit on the observed pressure characteristic was not well documented or understood, and so was selected for study.

At the start of EU6 production in Delphi Technologies Stonehouse, the 2bar check valve was used as a robust but rudimentary backpressure regulator on the

standard production measurement system as shown in Figure 5.7. The first production configuration trialled had this check valve positioned at the end of the following hose.

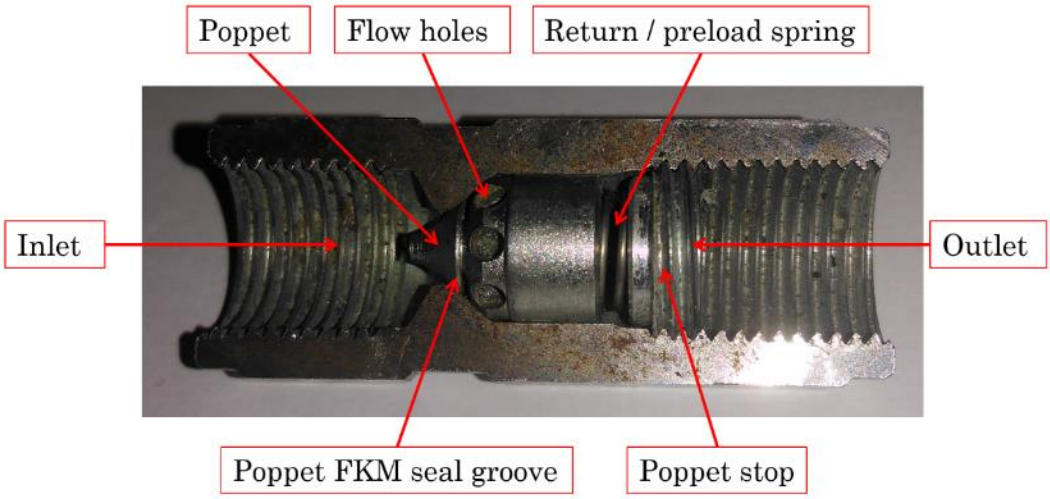


Figure 5.7: Gyson Gromelle R4000 series 2bar non-return valves.

Previous work carried out at Delphi Technologies (Tebbs, 2014), suggested less zero value variance was present during the quiescent period before the next injection if the check valve was moved from the end of the following hose to behind the tube termination orifice. However, this previous work was not carried out under controlled conditions and no explanation was given as to the mechanism that caused this effect. To better understand the previous result, the characterisation was repeated and the two system configurations considered are shown in Figure 5.8.

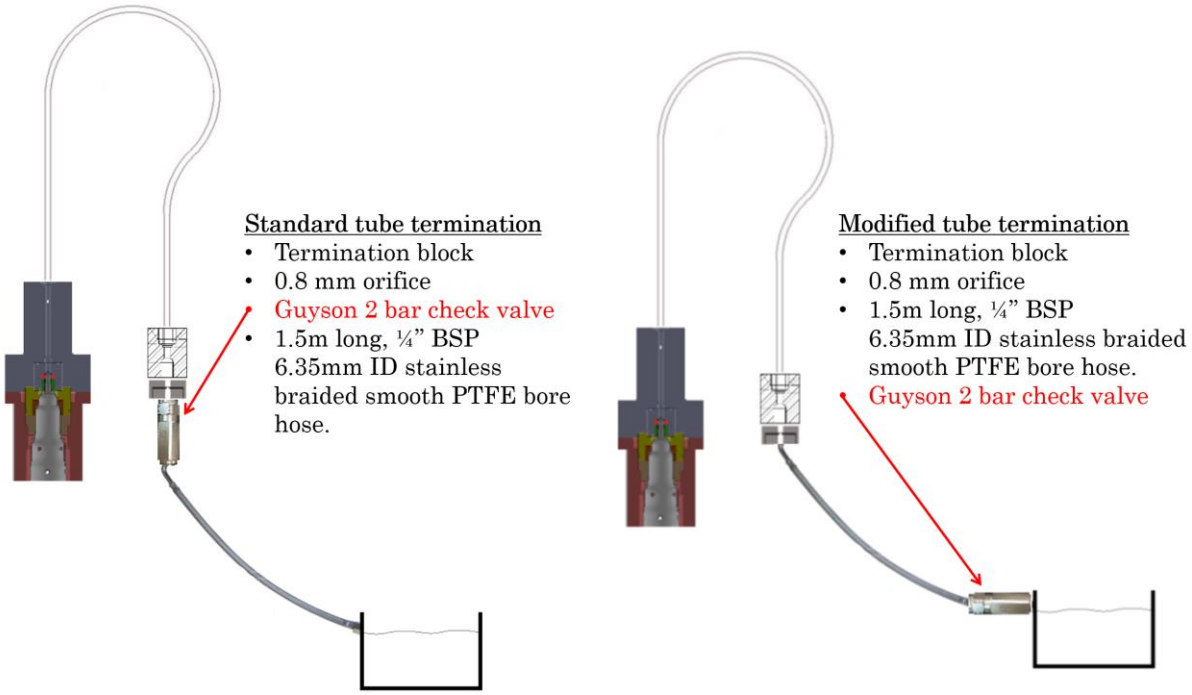


Figure 5.8: Check valve backpressure regulator position at the start vs the end of the following hose.
Left: Standard production 2bar measurement system with check valve after the tube termination orifice.
Right: Modified 2bar production measurement system with check valve after the end of the following hose.

For the configuration where the check valve is placed after the following hose, a significant difference in baseline activity can be seen immediately following the first reflected pressure wave, as highlighted by point 1 in Figure 5.9, when compared to the configuration with the check valve at the tube termination.

For both cases, the zero value variance falls within the acceptance limits of ±1mg/ms by the end of the quiescent period as shown in point 1 of Figure 5.9. However, when the check valve is placed after the following hose, some residual pressure ripples of higher amplitude than the standard configuration remain that would convolve on top of the next injection event. Therefore, even though both systems are acceptable for production use, the configuration with the check valve placed at the end of the hose would cause marginally higher variance.

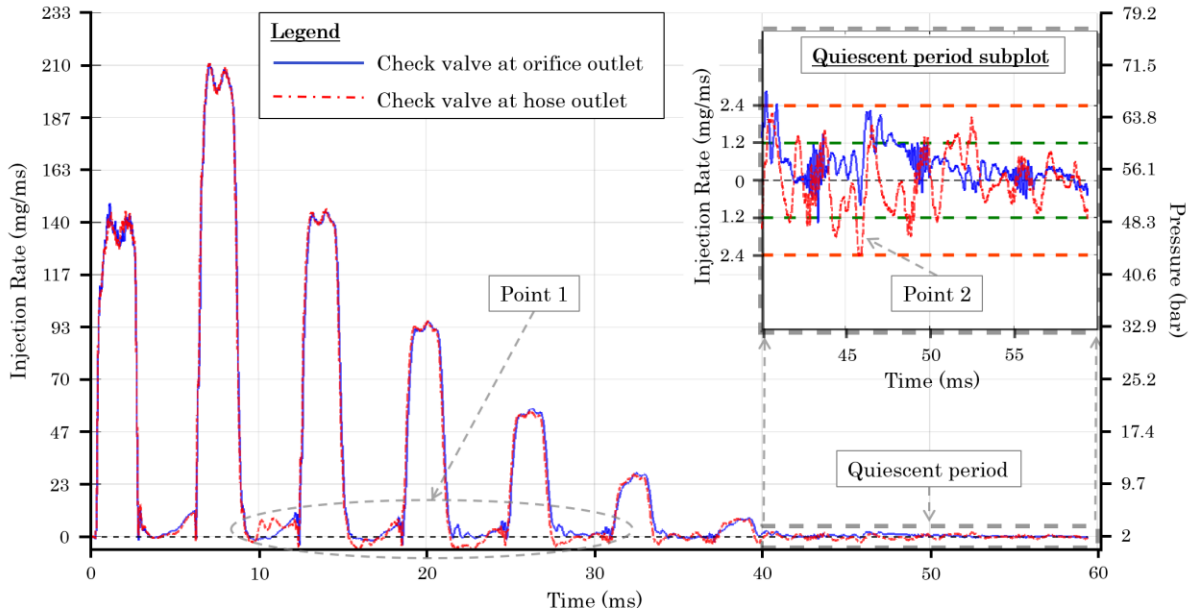


Figure 5.9: Effect on observed pressure wave of moving the check valve from the start to the end of the following hose. 2400bar pressure 2300µs duration injection condition. Blue: Standard production 2bar system, check valve after the termination orifice. Red: Modified 2bar production measurement system, check valve after following hose.

This demonstrated that the influence of hydraulic component configuration, after the termination orifice, is observable in the pressure wave characteristic. This effect had not been described for rate tubes found in literature. Likely because in most applications the firing rate would be reduced to allow more time for quiescent pressure conditions to be achieved.

Therefore, the influence of hydraulic components after the termination orifice on low pressure waves, and zero value variance, must be understood to overcome one of the primary rate sources of variance in a tube measurement device.

5.1.4 Internal bore of the following hose

To study the effect of pressurising the following hose further, the effect of changing the hose internal diameter was investigated as shown in Figure 5.10. The aim of this characterisation was to determine the level of influence the magnitude of pressure activity has on zero value measurement variance. The magnitude of pressure activity in the following hose can be increased by reducing the internal diameter. This results in a pressure rise inside the hose because of the smaller internal cross sectional area of the hose. If the pressure inside the following hose was higher because of a smaller internal bore diameter, it was expected that it would influence pressure differential across the tube termination orifice and influence the zero value variance.

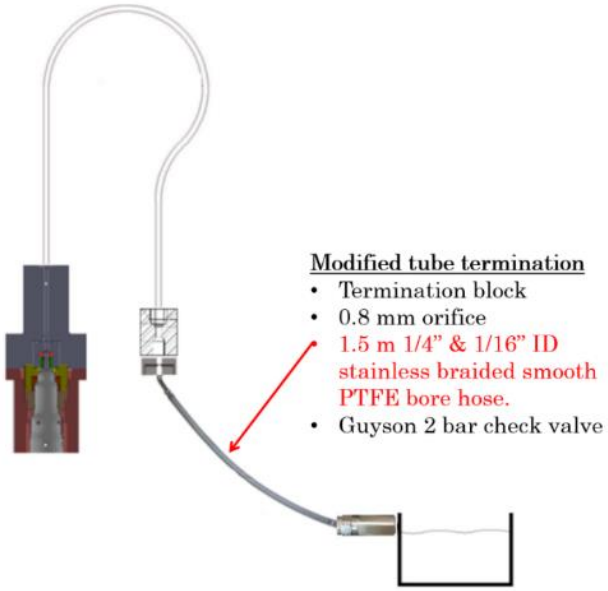


Figure 5.10: Modified 2bar production measurement system with check valve after the following hose, with the following hose to be modified highlighted.

The following hoses originally specified for this system were 1.5m long 6.35mm (¼"BSP) bore internal diameter. To study the influence of the hose characteristics on the observed pressure signal, a smaller internal diameter following hose of 4.76mm (3/16"BSP) was compared to the standard configuration. There was a significant difference in the zero value characteristic between reflections in the tube as shown in point 1 of Figure 5.11.

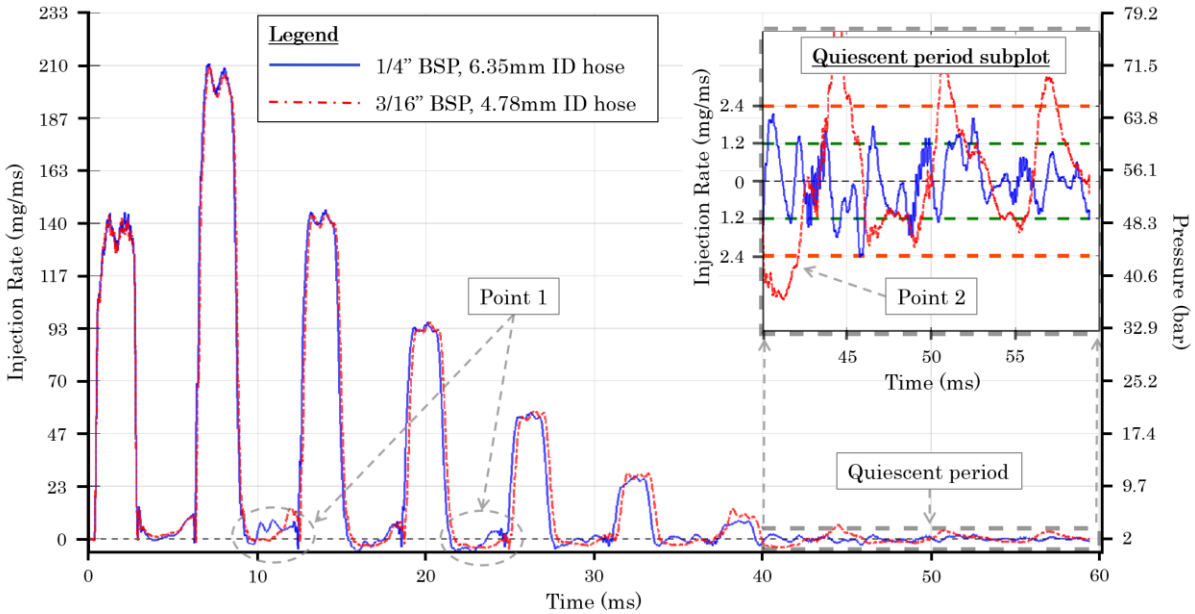


Figure 5.11: Influence on observed pressure wave of different following hose ID. 2400bar pressure 2300µs duration injection condition.
Blue: 1/4" ID hose, 2bar measurement system, check valve after the following hose.
Red: 3/16" ID hose, 2bar measurement system, check valve after the following hose

There is also a clear difference in the characteristic of zero value pressure wave activity during the quiescent period for the smaller hose internal diameter as

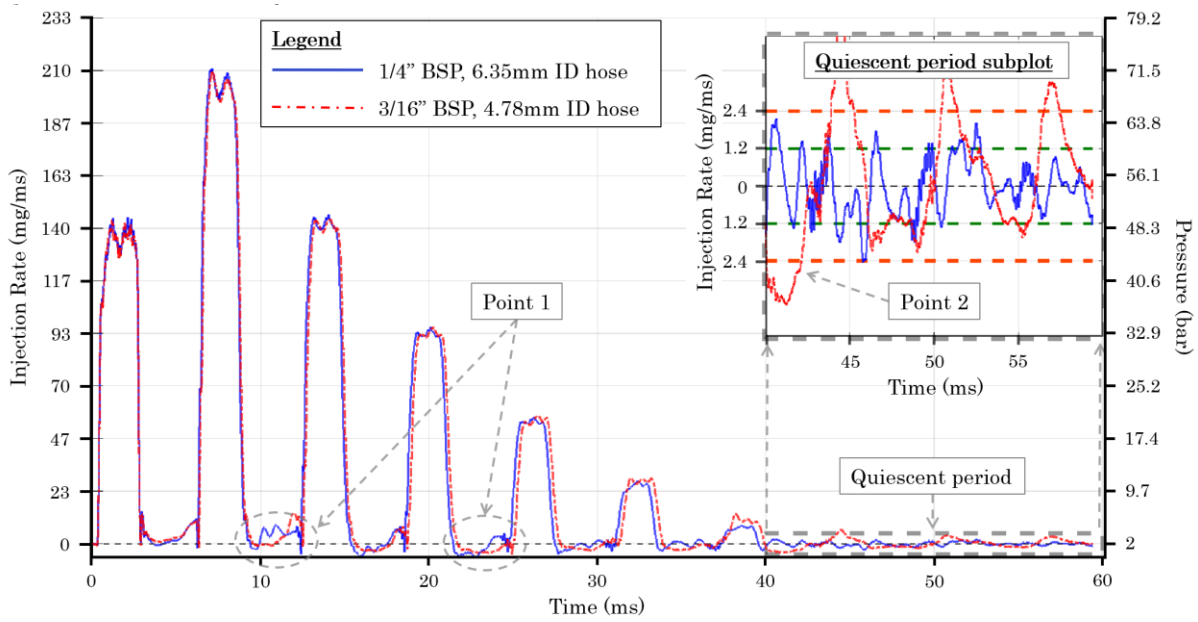


Figure 5.11. The degree to which the following hose influences the quiescent period is increased. A clear sinusoidal oscillation with higher overall magnitude is present with the smaller diameter. This oscillation would convolve on top of the pressure wave due to the next injection event after quiescence and cause additional measurement system variance. This result shows that if the back pressure regulation is placed after the following hose outlet, then the hose will become pressurised and there will be a significant influence of the following hose properties, such as internal volume and bore diameter, on the zero value variance observed during reflections and leading to quiescence. Hence, the influence of following hose properties on the observed pressure waves in the system must be understood to minimise zero value variance.

5.1.5 Flow restriction before the regulator

One of the main commercial objectives of the work was to fit a Coriolis mass meter to the circuit. Hence a trial was conducted where a mass measurement circuit, comprising a bespoke fuel chiller and Bronkhorst® Coriolis mass meter, was fitted to the production measurement circuit.

It is known that there is an influence of the hydraulic configuration after the tube termination orifice, on the observed pressure signal zero value variance. As demonstrated by changing the internal bore of the following hose. This experiment was required to characterise the effect of adding this more complex chiller and Coriolis mass meter circuit to the end of the following hose. The two circuit configurations considered can be seen in Figure 5.12.

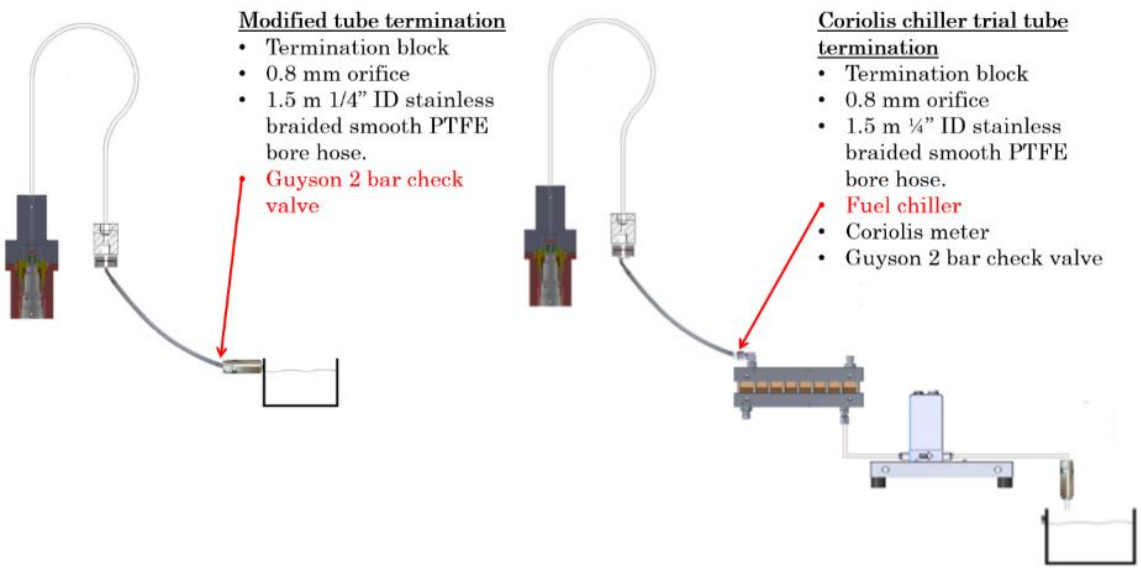


Figure 5.12: Left: Modified 2bar system with check valve after the following hose. Right: 2bar measurement system with Coriolis chiller circuit after the following hose.

The fuel chiller was necessary because the Coriolis mass meter selected had a maximum operating temperature of 70 degrees Celsius (ºC) and the fluid temperature at the end of the tube was observed to reach temperatures above 100ºC during extended steady state testing. The measurement trace for the full 15Hz firing period was evaluated alongside the standard production configuration. As with the previous cases of moving the regulator and changing the following hose bore, there is a significant change in the zero value pressure wave characteristic between reflections as shown in point 1 of Figure 5.13.

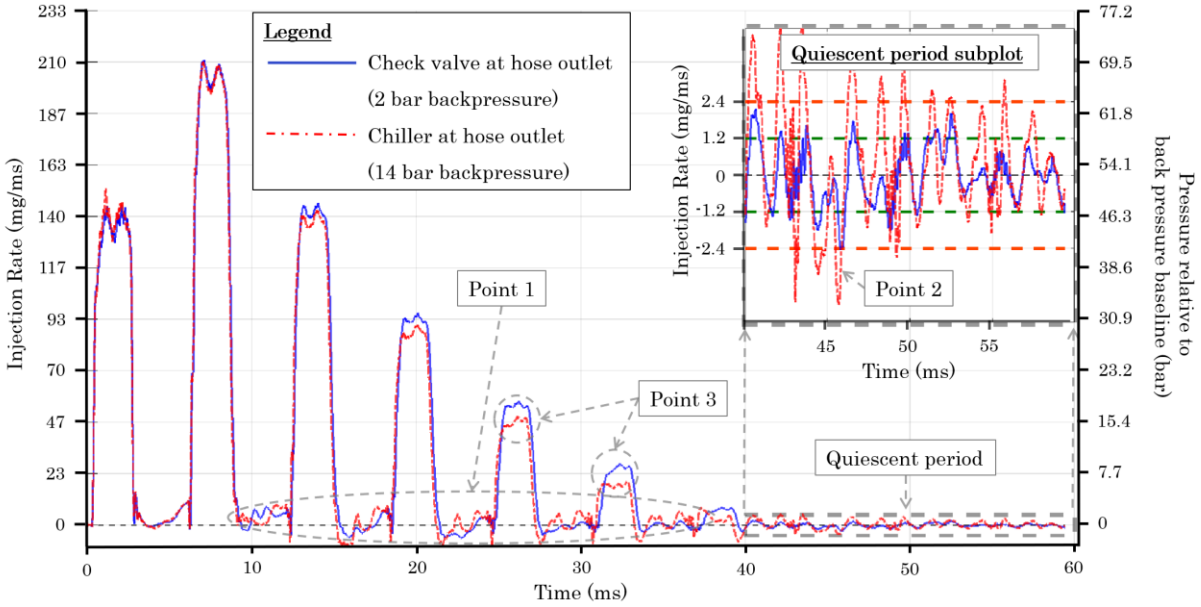


Figure 5.13: Effect on observed pressure wave of adding a fuel chiller and Coriolis meter at end of the following hose. 2400bar pressure 2300µs duration injection condition. Blue: Modified 2bar system with check valve after the following hose. Red: 2bar system with Coriolis chiller circuit after the following hose.

When a flow impedance in the form of this chiller is fitted to the hose outlet, increased zero value variance is present during the quiescent period where the next injection would take place, as shown by point 2 in Figure 5.13.

To examine the effect of this hydraulic configuration on the frequencies present in the observed pressure wave and their amplitude, a single sided amplitude spectrums were compared for the full firing period between injection events and quiescent period window. With the aim of this comparison was to characterise the source of the frequency activity driving the increase in quiescent period zero value variance before the next injection.

The signal was acquired at 0.1Mhz sampling rate, for a single injection event, with a measurement signal partition of 0 to 60ms for analysis of the full firing period, and between 40 to 60ms for analysis of the quiescent period. The pressure amplitude was scaled to match expected injection rate. A moving average smoothing filter was then applied to the signal using a span of 0.05ms. Zero padding and windowing functions were not applied to the signal. The frequency analysis was conducted in MATLAB using its built in FFT function. A single sided amplitude spectrum for a single injection events 15Hz firing period derived from these data is shown in Figure 5.14.

Point 1 of Figure 5.14 represents the square wave shape of the injection pulse and its reflections, as square waves are made up of multiple sinusoidal frequencies when represented in the frequency domain. These frequencies are all clustered at 50Hz and below because the injection pulse lasts 2.3ms.

Point 2 of Figure 5.14 represents the reflected wave period of the main rate tube. In other terms, it represents the primary quarter wave resonant frequency of the rate tube, which is dictated by its length and SOS in the tube.

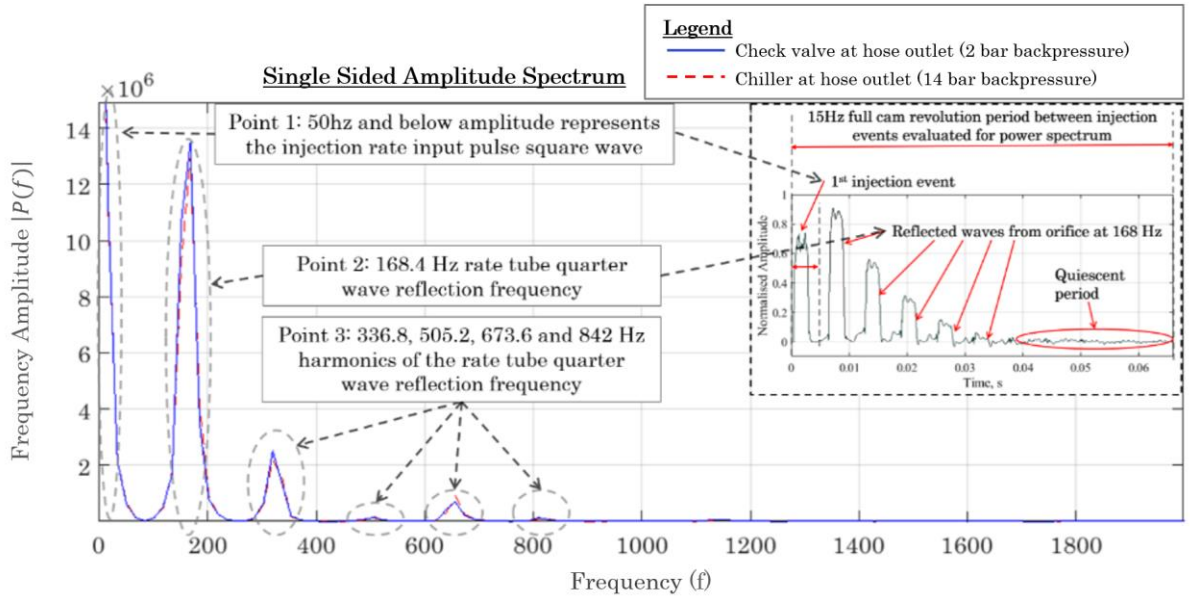


Figure 5.14: Left: Modified production 2bar system with check valve after the following hose.
Right: 2bar production measurement system with Coriolis chiller circuit after the following hose.

Point 3 of Figure 5.14 highlights a group of frequencies with a consistent spacing. To determine if these frequencies were higher order harmonics of the primary rate tube quarter wave resonant frequency, an analysis of the frequency interval between them was carried out. If these frequencies are higher order harmonics of the primary resonant frequency, they should be multiples of it . These frequencies can be seen in Table 3.1 and match closely the predicted higher order harmonics of the 168Hz rate tube quarter wave resonance. There is an error of -16.8Hz from the prediction, but this can be accounted for, as it is the resolution of the frequency bins calculated for the power spectrum DFT given the available signal length.

Table 5.1: Rate tube harmonic frequencies

	Observed frequencies (Hz)	Predicted harmonics (Hz)	Delta between observed and predicted (Hz)
Fundamental rate tube resonant frequency	168.4		
First harmonic	320	336.8	-16.8
Second Harmonic	505.2	505.2	0
Third Harmonic	656.8	673.6	-16.8
Fourth Harmonic	825.2	842	-16.8

The presence of harmonic modes for the full 15hz firing period did not indicate if they were responsible for the increased activity with the chiller fitted, shown in point 2 of Figure 5.13, near the end of the firing period. To assess if residual magnitudes from the higher harmonic frequencies would influence the next injection event, the time window for analysis was windowed to the 40ms to 66ms period, after the majority of the primary harmonic wave activity has disappeared.

A single-sided amplitude spectrum of the quiescent period is shown in Figure 5.15. Because of the windowing of the time series to a shorter time frame, the maximum frequency resolution of the analysis was approximately 50Hz.

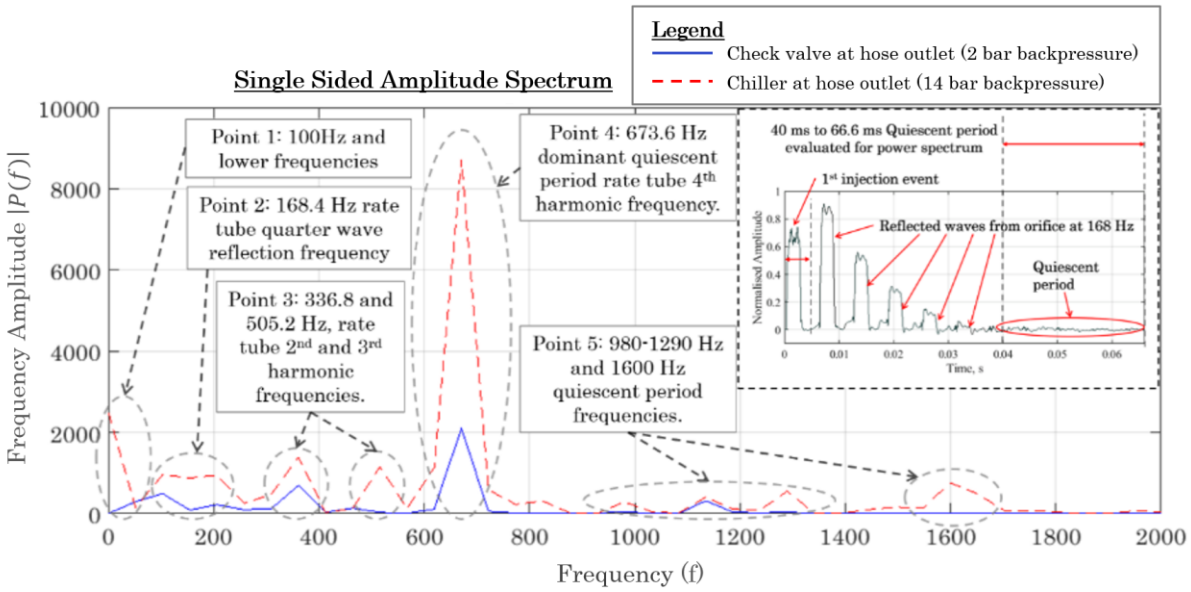


Figure 5.15: Power Spectrum DFT analysis of adding a fuel chiller and Coriolis meter at the end of the following hose. 2400bar pressure 2300µs duration injection condition. Blue: Modified 2bar system with check valve after the following hose. Red: 2bar measurement system with Coriolis chiller circuit after the following hose.

Point 1 of Figure 5.15 highlights that the high power amplitude frequencies below 50Hz observed previously are indeed due to the square wave of the injection rate pulse. As they are no longer present when the time series is windowed to the quiescent period where no reflected injection pulse square waves are present.

Point 2 and 3 of Figure 5.15 highlights the quarter wave resonance of the rate tube and its first two harmonic frequencies. A small increase in frequency power amplitude is seen at these harmonics when using the Coriolis chiller circuit configuration.

Point 4 of Figure 5.15 highlights a significant increase in frequency power of the 4th rate tube harmonic frequency. This amplitude is much higher than the other frequencies observed in the quiescent period and must be representing the increase in baseline variance observed in point 2 of Figure 5.13.

Point 5 of Figure 5.15 highlights the higher order harmonics of the primary resonant frequency activity. A significant increase in the highest modal orders can be observed. Indicating that the magnitude of high frequency artefacts, will increase for the chiller circuit case as highlighted by point 2 of Figure 5.13.

The frequency highlighted by point 4 of Figure 5.15, is dominant in the quiescent period for both configurations examined and hence must be influenced by the hydraulic configuration after the tube termination orifice. Therefore, the addition of the chiller to the end of the following hose did not change the fundamental frequencies in the zero value variance, but it increased their

influence significantly. These frequencies convolve on top of and increase the zero value measurement variance of the next injection event.

To understand how this increase in harmonic frequency amplitude could occur, an analogue dial pressure gauge was fitted to the inlet of the chiller to make note of increases in backpressure due to the restriction created by the chiller design. An orifice was fitted to the dial gauge inlet to record an average pressure level and protect the gauge from transient pressure inputs. At 2400bar injection pressure and 2300μs injection duration, as shown in Figure 5.13, the observed pressure was 14bar inside the following hose. This is 12bar higher than the standard production measurement system configuration, where the 2 bar check valve is the dominant factor governing backpressure. This increased pressure in the following hose also changes the conditions at the tube termination orifice, as evidenced by the difference in reflected wave height in point 3 of Figure 5.13. Hence changes in system backpressure will influence the magnitude of reflected waves present in the rate tube.

The backpressure observed on the dial pressure gauge was 14bar at the 2400bar rail pressure, 2300μs injection duration. However, at lower rail pressures and injection durations, the pressure in the following hose lowered, as displayed by the dial pressure gauge. The backpressure observed in the following hose was linked to the injected mass and rate of injection. This is consistent with the effect that a fixed restriction would have on the system. As mass flow at the orifice lowers, so does the backpressure.

This result shows that the pressure activity in the following hose is the dominant factor in terms of the zero value frequencies observed, whereas the backpressure dictates their magnitude.

The restriction that raised the backpressure to a peak of 14bar was because of the chiller design. It is a bespoke Delphi Technologies design that used a very narrow rectangular slot between two copper plates to ensure near complete contact of the fluid to be chilled with the cooling surfaces. This allowed for very efficient thermal transfer between the fluid and the cooling plates. This design presented a very narrow flow area with a high degree of fluid friction effects due to the high contact surface area of the chiller plate with the test fluid.

When trialled at 2400bar rail pressure and 2300μs duration for an extended period of time at steady-state conditions, the temperature in the following hose could reach greater than 100ºC after ten minutes. Temperatures at the Coriolis chiller were recorded at 40±5ºC at all conditions trialled. This narrow temperature variance at the Coriolis meter protected it from thermal shock during extended trials, allowing freedom for it to be used safely regardless of injection load and temperature of the measurement system.

The fuel flow area between the copper chiller cooling plates is 0.05mm high, by 50mm wide, as shown in point 1 of Figure 5.16. The flow area is 150mm long as shown in point 2 of Figure 5.16. The entry area to the copper plates is 2.5mm^2. The cross-Sectional flow area of the 2bar check valve, as previously used on the baseline production hardware, was 20mm^2. The chiller presents a significant restriction compared to the check valve previously used.

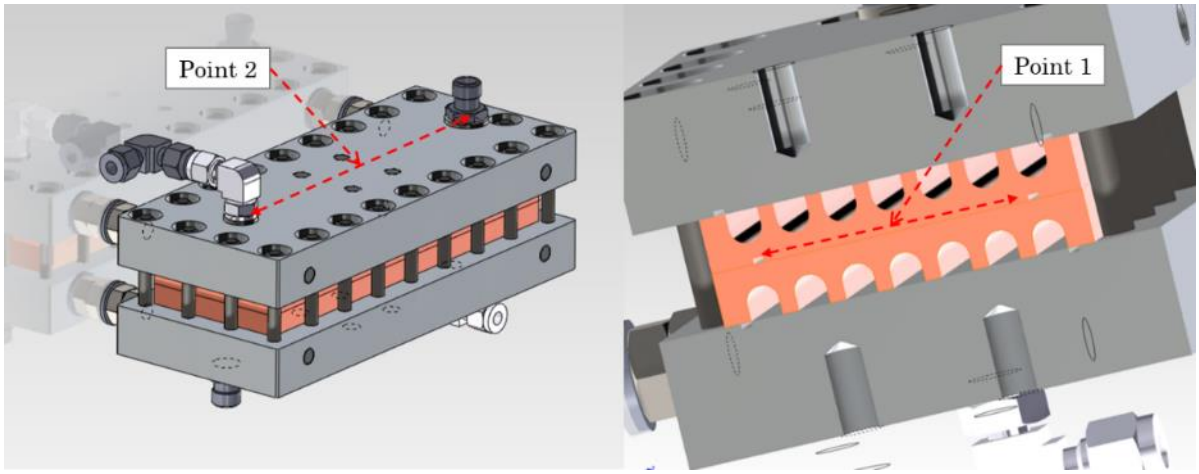


Figure 5.16: Delphi Technologies bespoke fuel chiller with narrow flow area.

A flow area of 2.5mm^2 is five times larger than the area of the 0.8mm diameter tube termination orifice that has a flow area of approximately 0.5mm^2. Hence, due to area alone, the chiller should not produce a higher backpressure than that observed at the tube termination orifice.

The chiller has a low flow cross-Sectional area and a very high contact surface area with the fluid flow. It was assumed that the fluid friction effects along the maximised chiller plate surface area are responsible for the 14bar backpressure observed in the following hose. This is verified later during simulations of the chiller in Section 0.

This model of Coriolis mass meter is known to be insensitive to temperature in its measurement. However, it is recommended by the manufacturer that the temperature gradients be kept to below 1°C per second (Cori-Tech, 2014). When zeroing the device before each test, a zero flow and repeatable pressure and temperature in the device must be achieved. Hence, maintaining a Coriolis meter flow temperature within a 10°C range with slow gradients was seen as beneficial to producing a consistent mass measurement from one injector test to the next. Hence a solution was sought that would allow the use of this chiller design whilst minimising or eliminating its influence on zero value variance magnitude.

5.1.6 Increased backpressure

It is known that increasing backpressure is desirable to better emulate in-cylinder engine regimes alongside the beneficial effect of suppressing cavitation activity, as discussed in literature review Section 2.1.2 and explored experimentally in Appendix 11.3.2.

Raising the system backpressure above 14bar was also seen as necessary to remove the influence of the chiller restriction on zero value variance. To work towards this goal a trial was carried out where the backpressure in the following hose was raised to 30bar.

To achieve this increase in back pressure inside the following hose, a backpressure regulator was placed before the fuel chiller. By raising the system baseline pressure greater than the value caused by the chiller restriction, it should be maintained at a stable value dictated by the regulator, instead of varying by injection quantity and hence flow rate in the system when only the chiller is present.

Initially, a high flow capacity regulator not specified for this application was trialled called an ARO® with part number 651791-B1E-B. This regulator was chosen for study because they were robust and already in use with ISO 4113 fluid medium and pressure regime studied. These regulators were typically used for handling large flow values within the injector calibration test machine fluid supply circuits of up to 22.7L/min. Whereas the highest flow rates from the EU6 injector applications studied were less than 1L/min. Therefore, they would not typically be specified for this flow regime. It was fitted as standard with a 1mm inlet orifice. The two different circuit configurations trialled are shown below in Figure 5.17.

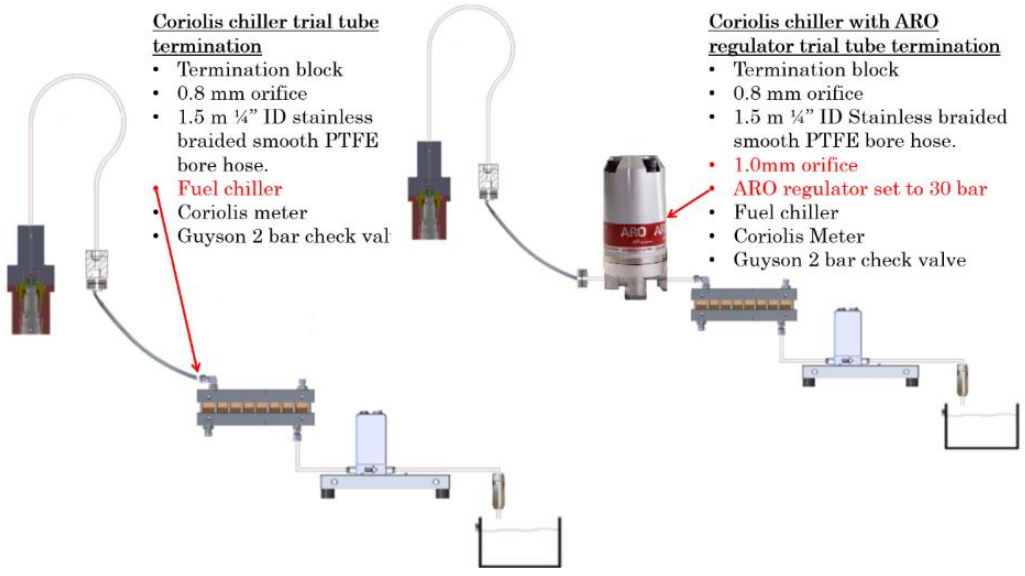


Figure 5.17: Left: 2bar measurement system, Coriolis chiller circuit after following hose.

Right: Trial measurement system, Coriolis circuit and ARO® back pressure regulator after following hose.

There is an additional additive low amplitude effect to the baseline when the regulator is present compared to the standard system as shown in the observed pressure wave at point 1 of Figure 5.18.

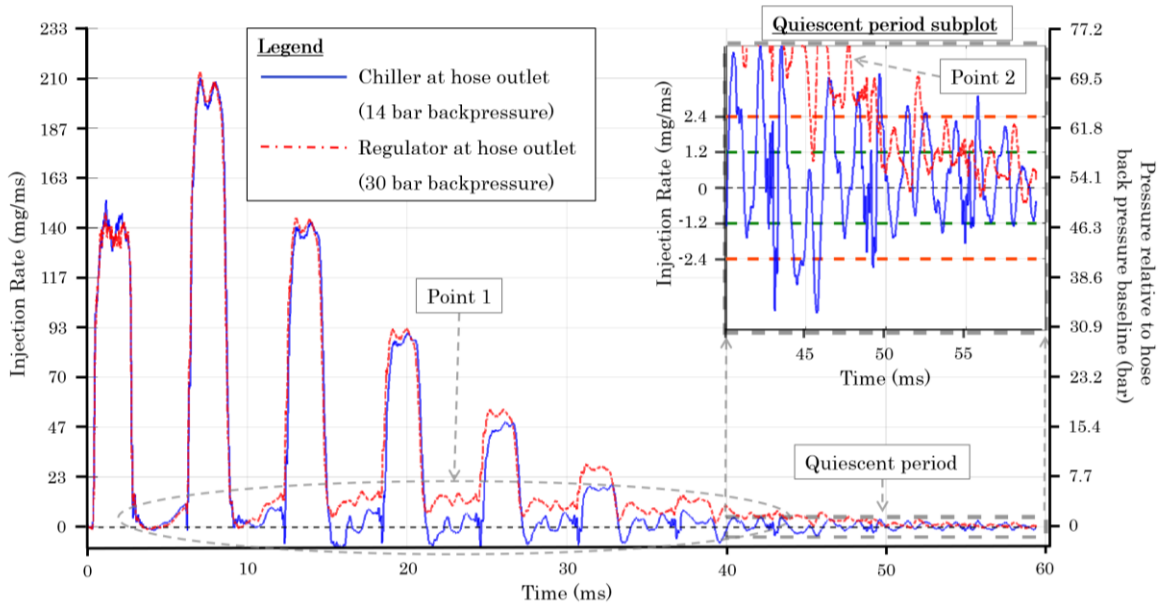


Figure 5.18: Effect on observed pressure wave of adding 30bar ARO® regulator before the Coriolis mass meter chiller. 2400bar pressure 2300µs duration injection condition. Red: Coriolis Chiller with ARO® regulator trial tube termination. Blue: Coriolis chiller trial tube termination.

To assess the impact of adding the ARO® regulator on these frequencies further, a DFT power spectrum analysis was carried out for the quiescent period as shown in Figure 5.19.

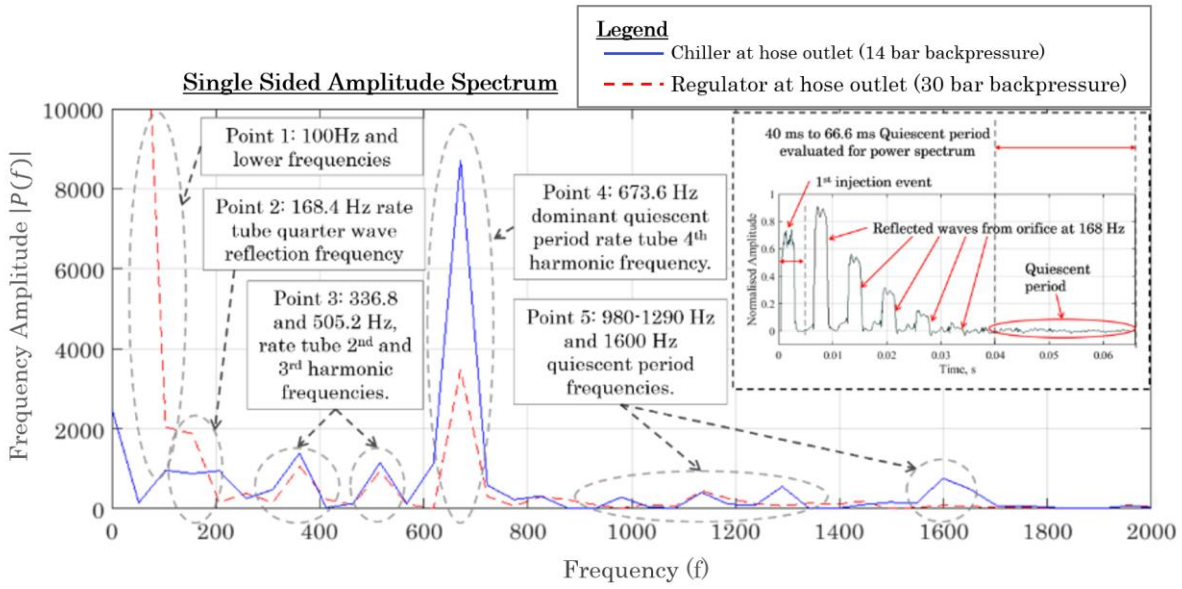


Figure 5.19: DFT Power spectrum of the effect on the observed pressure frequencies of adding a 30bar ARO® regulator before the Coriolis mass meter chiller restriction. 2400bar pressure 2300µs duration injection condition.

Red: Coriolis Chiller with ARO® regulator trial tube termination.
Blue: Coriolis chiller trial tube termination.

Point 1 of Figure 5.19 highlights a large increase in the low frequency components observed when using the regulator and will be related to the low amplitude effect highlighted by point 1 of Figure 5.18. Point 2 of Figure 5.19 highlights a slight increase in residual rate tube quarter wave resonant frequency.

There is no significant difference with or without the regulator on the 2nd and 3rd rate tube harmonics as highlighted by point 3 of Figure 5.19. There is however a significant reduction in frequency power at the 4th rate tube harmonic at 673Hz when a regulator is fitted before the chiller inlet. This is the same frequency that saw a significant increase in amplitude between the standard configuration and the addition of the chiller alone as described point 4 in Figure 5.15. Hence the addition of a regulator helps to reduce the dominant high frequency components present in the quiescent period when a chiller is fitted to the end of the following hose.

Previous configurations studied on this experimental scheme indicated that the backpressure wave activity in the following hose is the dominant factor that determines the zero value baseline characteristic. The change in harmonic frequencies observed when using a regulator suggests that the increased backpressure induced by the regulator is interacting with the following hose to attenuate the dominant 673Hz frequency observed.

The induced low frequency wave introduced by the regulator achieves quiescence just before the end of the quiescent period as highlighted by point 2 in Figure 5.18, so the use of a regulator in this way would prevent any increase in injection event firing rate beyond the 15Hz. The injection condition studied is a peak engine load condition and represents the largest excitation of the measurement system for the F2 EU6 injector family. Rates of injection are likely to increase beyond the EU6 levels studied here, as is expected for future EU7 applications (Morgan *et al.*, 2015). Any further increased rate of injection will increase the size and rate of increase of the input pressure pulse to the measurement system. Resulting in a need to reduce the firing rate below the current standard of 15Hz to achieve quiescent zero value conditions. Hence any increase in load beyond that studied here would require a reduced firing rate and increased production cycle times, when a backpressure regulator of this type is fitted, and the backpressure is increased to 30bar.

These results show that a lower amount of high frequency zero value variance can be achieved when using a 30bar regulator, instead of only attaching the Coriolis fuel chiller that acts as a dominant restriction. However, a significant low frequency effect is introduced that superimposes a gradient on the baseline

of the next injection. The mechanism by which this occurs is revealed later in Section 5.2.12.

The ARO regulator could not maintain a stable backpressure at injected mass flow rates of less than 0.15g/s. Which meant it could not measure critical Minimum Drive Pulse (MDP) calibration trims measured at the lowest injected fuel values. Making it unsuitable for this application. Hence, a regulator designed for low or no flow conditions was sought. The details of this application specific investigation are provided in Appendix 11.2.

5.2 Model space hydraulic characterisation

A model of the production standard rate tube measurement system studied during experimental scheme one was constructed for experimental scheme two. By studying the pressure wave activity in model space, many detailed observations can be made throughout the system to gain knowledge of the drivers of its dynamic behaviour. This could not be ascertained with the single observation point used during experimental scheme one.

The goal of the work in model space was to gain enough knowledge of the system dynamics to enable the development of an optimised hydraulic configuration. A configuration that would enable the installation of a Coriolis meter, with minimal zero value variance, for extended production trials during experimental scheme three.

The model was constructed using a 1D lumped-parameters and multi-ports approach. It was built in LMS IL Amesim (LI and LI, 2006) a 1D lumped parameter multi-disciplinary powerful simulation tool. Commonly employed to study pressure wave dynamics of fuel systems due to specialised models toolkits for representing diesel fuel injection systems (Chaufour *et al.*, 2004). It was chosen for the construction of a rate tube model due to its extensive hydraulic model library and pre-built fluid property libraries for common fuels.

This section discusses the construction of hydraulic model elements in Amesim in general terms. Then the specific types of sub model used to construct a rate tube model, as listed in the legend of Figure 5.23, are presented and the assumptions inherent in the chosen modelling technique are discussed. Finally, a brief overview of the mechanical models used to construct the regulator models is provided.

5.2.1 Hydraulic Modelling

The model libraries in Amesim use a lumped parameter approach for system modelling. The parameters are inertial (I), capacitive (C) and resistive (R). For

basic models the parameters are lumped into one element. With a series of lumped elements being employed for some models using a distributive approach.

Two 1D lumped parameter modelling approaches are commonly used in Amesim for modelling fuel system hydraulic circuits (Furno and Gonard, 2011). The first includes mass and momentum conservation equations, combined with Bodes equation of state (Bode, 1990) and the assumption of adiabatic fuel properties transformation from provided fluid properties look up tables or bespoke fluid property models. This approach uses the Hydraulic and Hydraulic Component Design libraries, the state variables of which are pressures for capacitive elements and volumetric flow rates for inertial elements.

The second approach utilises the Thermal Hydraulic and Thermal Hydraulic Component Design libraries to introduce the energy conservation equation alongside the mass and momentum conservation equations.

The first approach was chosen in this work, assuming an adiabatic system, no work done by the fluid. Therefore, the effects of thermal conduction in terms of heat transfer between fluid particles; viscous dissipation in terms of heat generated by fluid shear; and thermal conduction to the pipe walls were neglected in the present work.

Fluid properties model

The Amesim software has a set of fluid property sub models pre-loaded for simulations of injector dynamics. The fluid properties sub-model selected for this study is called "Robert Bosch adiabatic diesel" for standard ISO4113 diesel, it was developed as part of a commercial partnership between Robert Bosch GmbH and Siemens Automation (Furno and Gonard, 2011) by performing measurements in the following range of pressure and temperature for several types of diesel fuels: Temperature range of 10 to 120°C and pressure range of 0 to 2000 bar. Value outside of these ranges can be extrapolated if required.

This fluid sub-model also includes cavitation and entrained air. It is assumed that these fluids are used in fast acting injection systems and there is no time for the air content to dissolve in the fluid (Siemens, 2013). The user sets a fixed temperature, and the local temperature evolution along the hydraulic circuit is computed using an approximate relationship for an adiabatic compression from atmospheric pressure to current pressure. Therefore, the Robert Bosch adiabatic diesel sub-model provides an adiabatic relationship between temperature and pressure, through use of a polynomial expression derived from fuel properties swept experimentally.

Hydraulic line equations

There are various types of model available in the Amesim hydraulic library. The equations that derive their state variables are presented, then a comparison between lumped and distributive hydraulic line models is provided.

The Amesim models for hydraulic lines solve the 1D Navier-Stokes equations (Currie, 2012) for continuity and momentum, as shown in Equations [5.1] and [5.2].

$$\frac{\partial \rho}{\partial t} + \frac{\partial (\rho u)}{\partial x} = 0 \qquad [\ 5.1\ ]$$

$$\frac{\partial \rho}{\partial t} + \frac{\partial (\rho u)}{\partial x} + \eta_{friction} = 0 \qquad [\ 5.2\ ]$$

Where ρ is the density, u the mean velocity, and $\eta_{friction}$ is the friction term.

For lumped and distributive parameter hydraulic line sub-models, these equations are reduced to a set of Ordinary Differential Equations (ODE) which are then passed to the Amesim solver to be integrated over time (Siemens, 2013). Amesim also offers additional hydraulic line models that solve the Navier-Stokes equation use "Lax-Wendroff CFD" numerical schemes applied within the sub-model.

For the rate tube model presented here, the simpler lumped and distributed ODE hydraulic line model types were used to represent the hydraulic tubing. As they provide segregation of important fluid dynamics effects such as compliance, inertance and pressure drop as separate discrete state elements.

The relationships between pressure and flow in a lumped or distributive Amesim hydraulic line model are provided by the following equations that represent the *system compliance*, *fluid inertance* and *pressure drop* due to fluid resistance.

The *system compliance* relates to the pressure dependant variation of fluid density. The relationship between ideal compliance, fluid flowrate and line pressure are shown in Equation [5.3] (Doebelin, 1998).

$$C_f \triangleq \frac{\int Q dt}{P} \qquad [\ 5.3\ ]$$

The *fluid inertance* relates to the kinetic energy of the fluid flow and its relationship to flowrate and pressure changes are given by Equation [5.4] (Doebelin, 1998).

$$\Delta P \triangleq I_f \frac{dQ}{dt} \qquad [\ 5.4\ ]$$

The *fluid resistance* uses the equation for pressure drop across a horizontal straight tube with fully developed, steady state and incompressible flow provided by the Darcy-Weisbach Equation [5.5] (Rouse, 1943).

$$\Delta P = f_c \times \frac{l}{D_h} \times \frac{\rho Q^2}{2A_{min}^2} \qquad [\ 5.5\ ]$$

Where D_h is the hydraulic or equivalent diameter, l is the length of flow of the segment, and f_c is the friction coefficient of the segment of length $l \div D_h = 1$. The total friction factor f_f is provided by Equation [5.6].

$$f_f = f_c \times \frac{l}{D_h} \qquad [\ 5.6\ ]$$

The friction coefficient f_c is derived from the relative roughness (Binder, 1973) of the pipe wall and Reynolds number of the fluid flow from the relationship known as the harp of Nikuradse (Nikuradse, 1932).

Inclination

All Amesim hydraulic library sub-models consider an inclination relative to gravity $\sin\theta$ to account for gravitational influence inducing pressure changes in the fluid flow. For all sub models used in the rate tube model, θ was set to 0, hence the effect of gravitational influence on fluid pressure are not represented.

Orifice equations

For shorter components that result in a localised pressure drop, the flow through their orifices is expressed Equation [5.7] for non-turbulent flows (Merritt, 1967).

$$Q = C_q A \sqrt{\frac{2}{\rho}|\Delta P|}Sign(\Delta P) \qquad [\ 5.7\ ]$$

Where C_q is the flow coefficient that assumes laminar flow and which varies with changes in orifice area, e.g. poppet valves opening to larger clearances, and secondly varying with Reynolds number. The numerical approach employed by Amesim uses an explicit scheme with C_q depending on a flow number λ, not the Reynolds number that would otherwise lead to an unrepresentative implicit scheme. The equations used by Amesim to calculate C_q and λ are given below in Equations [5.8] and [5.9] (Siemens, 2013).

$$C_q = C_{q_0} \times \tan\left(\frac{2 \times \lambda}{\lambda_c}\right) \qquad \lambda = \frac{D_h}{v} \times \sqrt{\frac{2 \times \Delta P}{\rho}} \qquad [\ 5.8, 5.9\ ]$$

Fixed hydraulic volume equations

For fixed hydraulic chamber volumes the calculation used is shown in Equation [5.10].

$$\frac{dP}{dt} = \frac{B}{V} \times \sum_{i=1}^{N} Q_i \qquad [\ 5.10\ ]$$

Pipe volumetric expansion

To account for adiabatic expansion of pipe walls due to pressure, the effective system bulk modulus B_{eff} is calculated for all metal pipe models by taking into account pipe wall volumetric compliance, calculated. The Equation [5.11] provides the relationship between B_{eff}, B_{fluid}, H_{wall} the pipe wall thickness, and E_{wall} the Youngs modulus of Elasticity of the pipe wall (McKee and Broerman, 2009).

$$B_{eff} = \frac{B_{fluid}}{\left(\frac{H_{wall} \times B_{fluid}}{E_{wall}} + 1\right)} \qquad [\ 5.11\ ]$$

Distributed parameter hydraulic line models

Most hydraulic line sub-models in Amesim consist of a 0D lumped parameter that assume a homogeneous state along the axial length of the pipe. Consequently, all the fluid dynamic effects (inertial, capacitive, and resistive) are combined into one element (CIR).

Distributed parameter hydraulic line models are representative of the 1D numerical solutions because the fluid properties are dependent on pressure along the axial length of the hydraulic line (Furno and Gonard, 2011). They are preferred for when charactering fast transient pressure wave frequencies in a pulsating hydraulic circuit (Siemens, 2013). The number of internal nodes being iteratively determined to satisfy the trade-off between CPU time and transient pressure wave fidelity. A diagram demonstrating the distribution of CIR nodes in a distributed line model is shown in Figure 5.20.

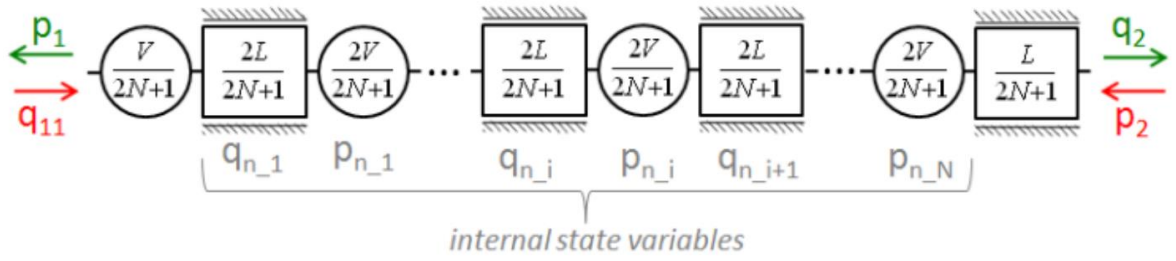


Figure 5.20: Internal state variables of line lumped model.

Source: (Siemens, 2013; Neto and Góes, 2017)

Model node pressure and flow

The LMS Amesim software uses similar or adapted forms of the above equations outlined above to determine pressure and flow derivatives at the model nodes.

Frequency Dependant Friction (FDF)

To account for fast transient or high frequency flows, some Amesim sub-models such as Distributed hydraulic line sub-models, have the capability to represent Frequency Dependant Friction (FDF). Amesim uses Equation [5.12] for head loss per unit length due to FDF friction as derived by Zielke (1968).

$$h_{FDF} = \frac{16v}{gD^2}\int_0^t \frac{\partial u(\tau)}{\partial t} W(t-\tau)d\tau \qquad [\ 5.12\ ]$$

Where h_{FDF} is the head loss per unit length, W is the weighting function of past velocity changes, D the pipe diameter, g the acceleration due to gravity and v the kinematic viscosity. The implementation of FDF in Amesim line models uses the Kagawa (1983) approximation of the weighting function W, shown in Equation [5.13].

$$h_{FDF} = \frac{16v}{gD^2}\sum_i y_i \qquad [\ 5.13\ ]$$

Where y_i are the state variables for FDF derived using their time derivatives as shown in Equation [5.14].

$$\frac{dy_i}{dt} = m_i\frac{du}{dt} - \frac{4vn_i}{D^2}y_i \qquad [\ 5.14\ ]$$

Where m_i and n_i are tabulated coefficients (Furno and Gonard, 2011).

Flexible hose volumetric expansion

In the special case of flexible hose sub-models, the wall behaviour is represented with a viscoelastic standard linear solid model, consisting of two springs and a dashpot for one half of the hose as shown in Figure 5.21.

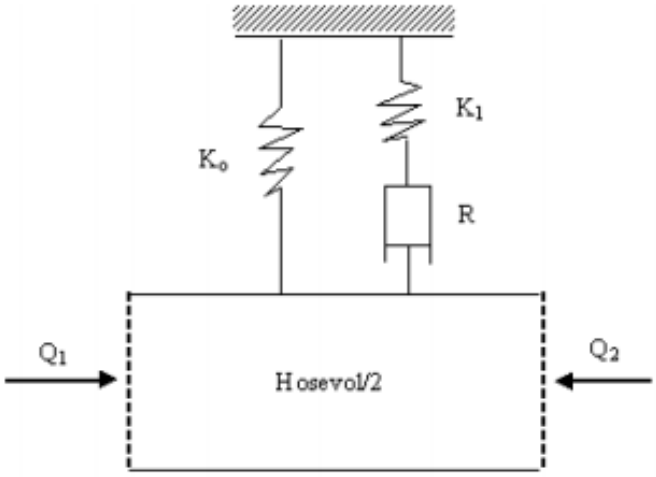


Figure 5.21: Viscoelastic behaviour of a hose wall, represented as a standard linear solid model. Source: (Siemens, 2013; Neto and Góes, 2017)

The mechanical stiffness of the hose K_0 is linked to the hose wall bulk modulus B_{hose} by Equation [5.15].

$$K_0 = \frac{B_{hose}}{0.5 \times V_{hose}} \times (\pi \times d \times \frac{l}{2})^2 \qquad [\ 5.15\ ]$$

Where V_{hose} is the hose volume, d is the hose diameter and l is the hose length.

The hose volume and bulk modulus can be determined in 3 ways: From H_{wall} and E_{wall} as already discussed for hydric pipe models; A user supplied effective bulk modulus B_{eff} combined with the bulk modulus of the fluid under reference conditions; and using experimental volumetric expansion data. Full details of the 1D mass model equations can be found in Appendix 11.6.1.

Injected flow input

A simple mean flow rate profile over time was used to represent the rate of input of fuel from the injector nozzle into the system, as is shown in Figure 5.22. Due to lack of available simulation data, this flow rate profile was taken from simulated flow rates for a different EU6 heavy duty diesel injector than the one studied. With a nozzle flow rate of 7L/min instead of the theoretical flow rate of 10L/min expected for a 140mg/ms injection rate observed on experimental scheme 1. The profile of the injection rate from experimental scheme 1 was then simplified and scaled to the 7L/min maximum flow rate from the available dataset. This simulated mean injection rate profile from the injector was input into the model at a 15Hz frequency as per the experimental setup during scheme one.

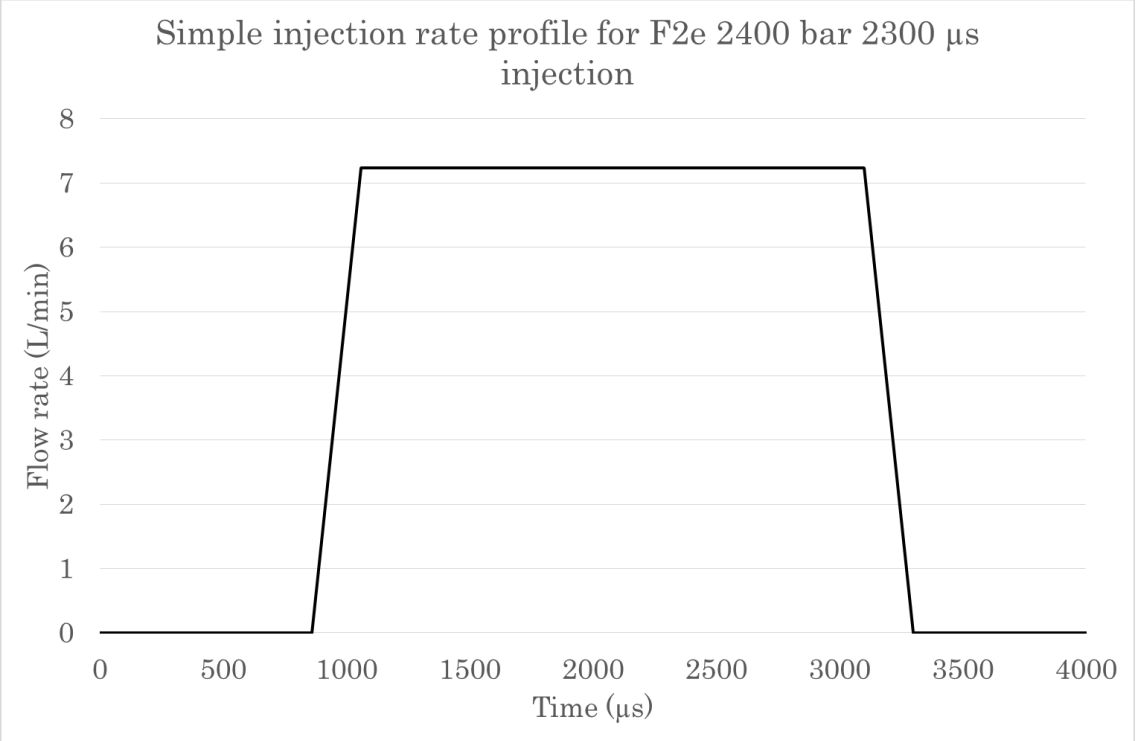


Figure 5.22: Mean flow rate profile used to simulate the 2400bar pressure 2300µs duration injection condition.

Whilst the magnitude of the volumetric input may have been 30% lower than theoretically calculated for the injector of study, its transient time dependent characteristic in terms of mean volume flow is representative.

This simple volume flow rate input does not account for fluid velocity out of the injector nozzle, turbulence caused by cavitation in the injection event, or any high frequency resonant pressure wave activity present in the spray.

The goal of the work in model space was to gain understanding of how low frequency activity interacts with the hydraulic configuration of the measurement system. When the max flow rate of the profile presented in Figure 5.22 is swept, it does not influence the frequencies observed. As it was the interactions of low frequencies being studied, scaling the magnitude and using a simplified volume flow input was deemed acceptable for use in the present model.

5.2.2 Hydraulic Component Modelling

The hydraulic component library in Amesim can be used to construct dynamic valve models that include geometry and momentum influence, as well as pressure and flow connections at specific nodes. A combination of moving poppet valve, mass blocks and submerged springs with interconnected volumes are employed to construct the dynamic pressure regulator models used.

Poppet model

The poppet models are numerically represented using adaptions of Equations [5.3, 5.4, 5.5, 5.8, 5.9 & 5.10]. The net force on the poppet is a combination of pressure force inside the volume and external forces such as a mass or end stop. The chambers inside the poppet are represented as a variable volume with changing inlet restriction based on geometry, full detail of which is provided in Appendix 11.6.2.

Mass model

The dynamic motion due to the mass of the valve assemblies is represented by a simple two ports mass block capable of one dimensional motion.

This model includes parameters for friction forces, modelled as Karnopp friction (Romano and Garcia, 2008), stiction, Coulomb friction, viscous friction and windage. It can also consider the dynamic friction force by using the principle of the Stribeck effect.

For the case of the present rate tube model Coulomb friction, viscous friction and windage friction is set to 0 and therefore ignored. The Stribeck effect is not considered. Only a 2bar stiction force found using parameter sweeps, end stop positions and the momentum of the mass are considered. Full details of the 1D mass model equations can be found in Appendix 11.6.3.

Spring Models

The spring model chosen in this work represents a part of a valve where both spring force and pressure act on a piston.

The flow in the model is assumed to be unobstructed by the piston. The hydraulic volume inside the model is computed from the displacement of the piston. This spring model is useful for constructing a valve model where the setting spring is inside the fluid volume. The method for defining spring stiffness was to set it as a constant value derived by compressing the springs to a known force and measuring the displacement. Full details of the 1D moving spring and piston model equations can be found in Appendix 11.6.4.

5.2.3 Rate tube system model

The goal of the work carried out in model space was to gain understanding of how low frequency pressure wave dynamics influence zero value variance. To achieve this goal, a hydraulic system model of a rate tube was constructed using the above physical laws and equations. The standard 2bar production rate tube configuration model constructed is shown alongside the previous schematic diagram for experimental scheme 1 in Figure 5.23.

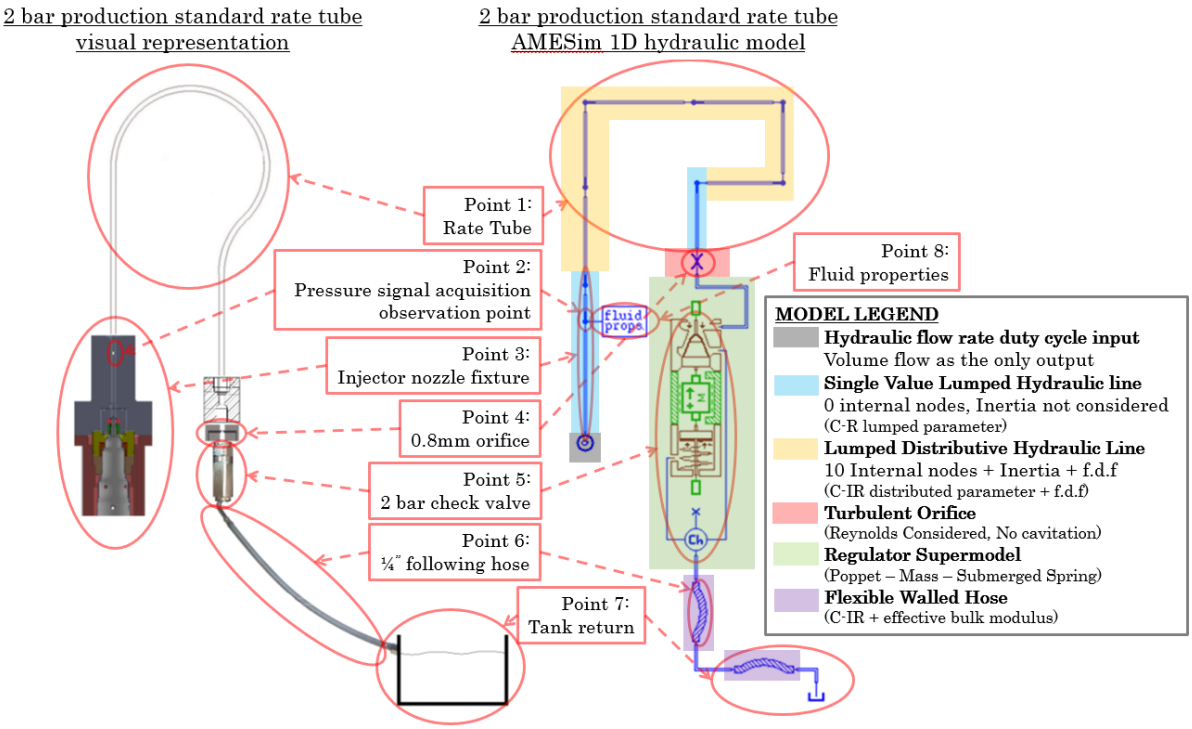


Figure 5.23: Final model iteration for standard 2bar production measurement system.
Left: visual representation
Right: Final Amesim model.

5.2.4 Initial settings

All hydraulic elements in the model were initialised to the backpressure value of the regulator or check valve used to start the model at a stable system pressure. In the case of the check valve, this would mean all model elements initialised to 2bar. This represents a measurement system free from air after purging and ramping up to the regulator or check valve pressure. This meant that a reproducible result would be achieved by the third simulated injection event.

5.2.5 Rate tube system sub models

Rate tube pipe

To preserve the detail of pressure wave effects, a distributed pipe model with fluid inertia effects was used for the rate tube, as shown by point 1 of Figure 5.23. The model type used is referred to as HL040 in Amesim. The number of nodes per pipe length had to be tuned to achieve a stable result. To do this, the 3m length of the tube was split into six elements of 0.5m each, ten nodes in each length. Hence, the modelling of frequency effects was assessed every 0.05m for 60 nodes across its length. It was observed that setting the number of nodes too low could cause distortion of the reflected waves and instability in the model, leading to crashes. The rate tube model development demonstrated that to build a stable model, the number of nodes chosen is vital. The number of nodes must

be empirically tuned by comparing the pressure waves observed in the model to those on experimental hardware to ensure no significant distortion is present.

To accurately represent the fluid friction effects of the tube walls, Amesim can consider bore relative roughness, which is defined as the absolute roughness divided by the bore diameter. An absolute roughness estimate for the rate tube and following hose were determined for similar materials (Binder, 1973; ToolBox, 2003). Relative roughness used in the model are shown in Table 5.2.

Table 5.2: Relative roughness values for the tube lengths in the model.

Pipe name	Material	Bore diameter D (mm)	Absolute roughness *e* (mm)	Relative roughness *e* / D (ratio)
Rate tube	Stainless steel drawn tubing	6.35	0.0015	0.00023622
Following hose 1/4" BSP	PTFE	6.35	0.0015	0.00023622
Following hose 3/16" BSP	PTFE	4.7625	0.0015	0.00314960629
Nozzle tooling	Hardened steel	6.35	0.001	0.00015748
Coriolis inlet	Stainless steel drawn tubing	4	0.0015	0.000375

For short hydraulic features such as the orifice and check valve, the roughness was set to the same value as the smooth rate tube bore. This value is only significant if the length of the feature being considered is measured in meters. This is because when tuning the model, it was observed that the pressure waves have to travel a significant distance, such as greater than 1m, in order for fluid friction effects at the bore wall to have an observable effect on their magnitude.

Pressure signal observation point

The model has a simple node for the pressure sensor observation point, as shown by point 2 of Figure 5.23, with all sensor port geometry removed. Initially, the full geometry of the sensor port was modelled for the observation point of the piezo electric Kistler (6054BR) pressure sensor in the tube. It was found that modelling the 3mm long sensor port introduced high frequencies and instability into the simulation. By simplifying the sensor port to an observation node, these high frequency effects are removed. This was deemed acceptable, as the objective of this experimental scheme was to characterise low frequency (Hz), not high frequency (kHz) wave dynamics. The high frequency effect of the sensor

port identified from the modelling led to the change in the experimental scheme four. The result of that investigation into the source of high frequency activity is explored in Section 6.1.3.

Injector nozzle fixture

The position of the nozzle tooling in the rate tube system model is shown in point 3 of Figure 5.23. Material properties and bore roughness of the nozzle tooling fixture were taken from Table 5.2. The geometry was set to a tube of constant diameter connecting the flow input to the rate tube inlet.

Initially, a flow area bore diameter change in the measurement system nozzle tooling was included in the model. A comparison between the experimental and initial model space nozzle tooling fixture geometry is shown in point 1 of Figure 5.24.

This feature was then removed from the model and the change in the simulated pressure wave evaluated. It was determined that minor changes in the bore diameter local to the nozzle flow input had little influence on the simulated pressure wave at the observation point. To improve simulation runtime, the 7.35mm to 6.35mm change in bore diameter geometry was removed and simplified to a straight tube of constant 6.35mm diameter, as shown by point 2 of Figure 5.24.

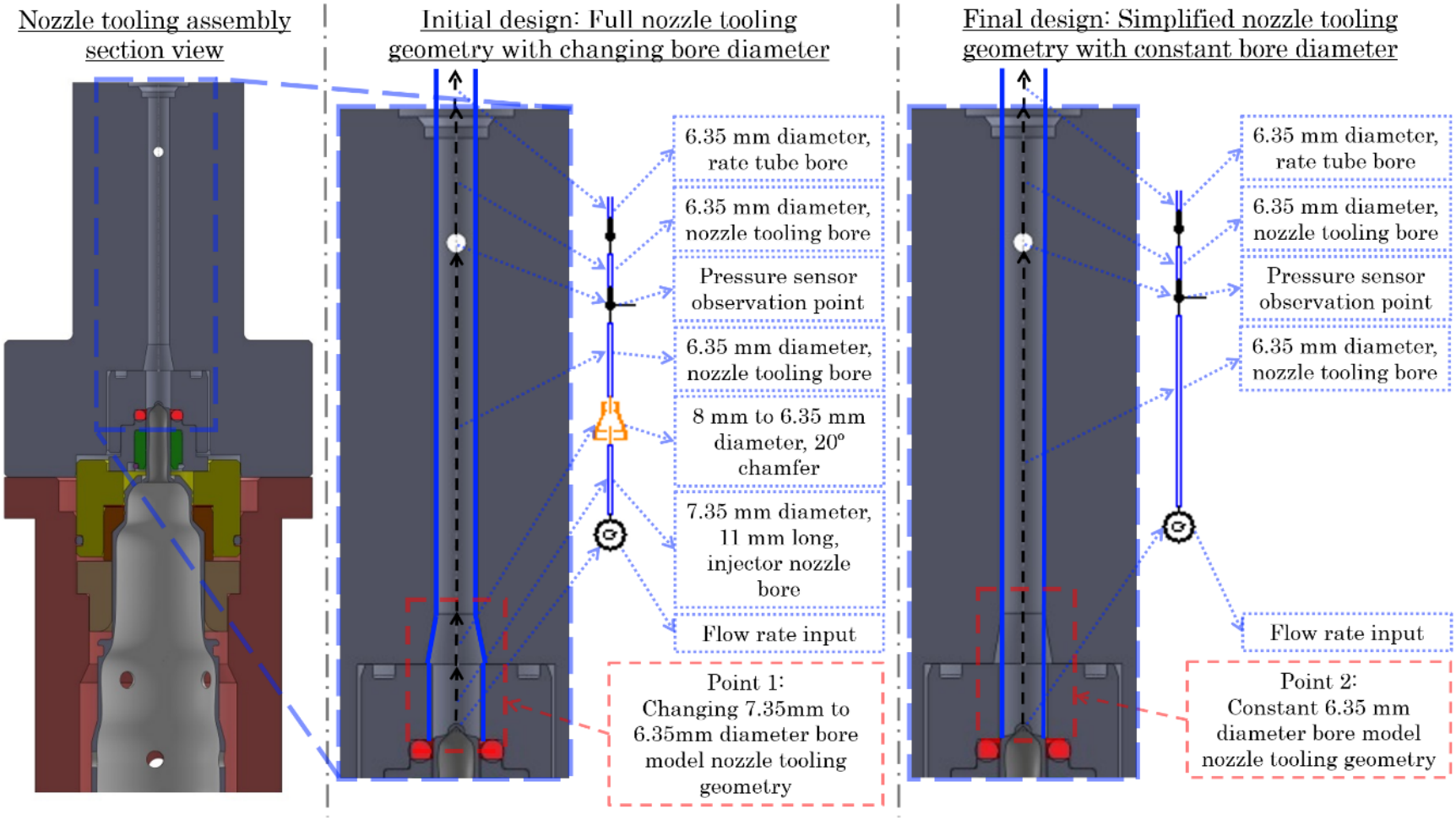


Figure 5.24: Initial vs final nozzle tooling geometry represented in the model.
Left: Section view of nozzle tooling assembly.
Middle: Initial model design with full nozzle tooling geometry represented.
Right: Final design with simplified geometry and a constant bore diameter.

Rate tube termination orifice

The 0.8mm rate tube termination orifice is shown in point 4 of Figure 5.23. It was represented using sub model BHO011 in Amesim, comprising a simple orifice, with zero volume, and no cavitation effects.

An orifice maximum discharge coefficient of 0.68 was provided from previous experiments carried out in Delphi Technologies by Pearce (2013). On a fuel pump test machine featuring identical orifice, pipe diameters, approximately 300 bar, steady state flow values x10 higher than delivered by an injection pulse at 15Hz. The discharge coefficient of the orifice was calculated using pressure and flow rate either side of the orifice.

The discharge coefficient provided by Pearce was characterised by sweeping a high pressure fuel pumps significantly higher flow rate, a flow regime that has minimal transient pressure pulsation compared to the fast transient water hammer characteristic of a rate tube injection meter. Hence, the provided value was calculated for different fluid property states and a different Reynolds flow regime than would be encountered in an injection rate meter. As it was the closest characterisation of this specific orifice geometry available, the difference in flow regimes was deemed acceptable and the provided value of 0.68 maximum flow coefficient was used in the rate tube model.

A comparison of the real orifice and the orifice model can be seen in Figure 5.25. All other orifices implemented during this work used the same sub model and flow coefficient.

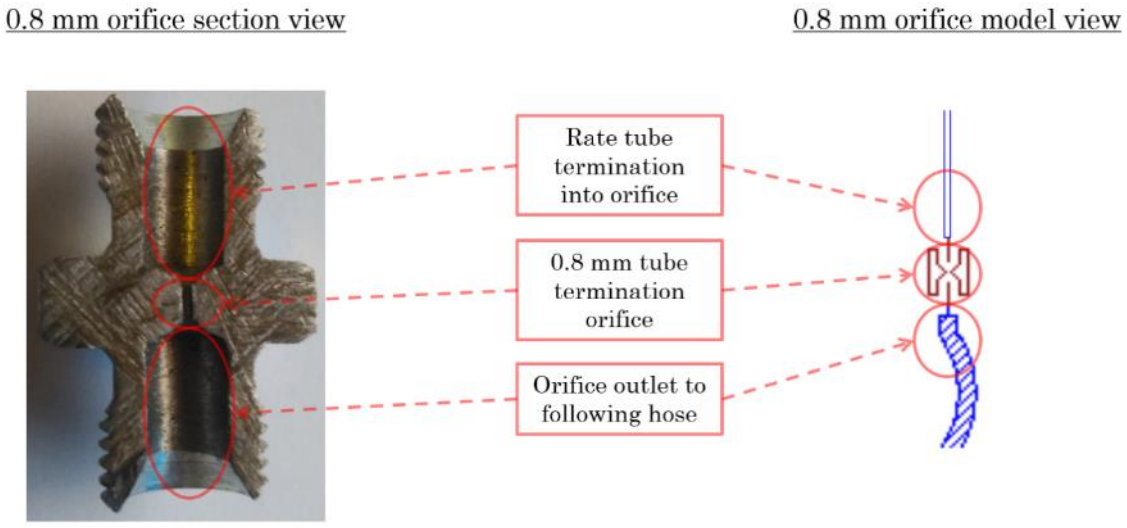


Figure 5.25: Rate tube termination orifice model description.
Left: Picture of Section view of the 0.8mm tube termination orifice.
Right: Amesim orifice sub model.

Check valve

Using the doctoral thesis of Sadeghi Reineh (2012) as a guide, a poppet model was produced to represent the dynamic behaviour of the standard production system 2 bar check valve as shown in point 5 of Figure 5.23. The check valve model included the mass of the components, spring rate of the return spring, and influence of flow areas, as seen in Figure 5.26. For the poppet valve, the stiction force had to be empirically tuned by comparing with experimental observations until a stable result was achieved. If the stiction friction is too weak, then unstable flow rates can occur because of a lack of damping present on the experimental hardware (Choudhury, Thornhill and Shah, 2005).

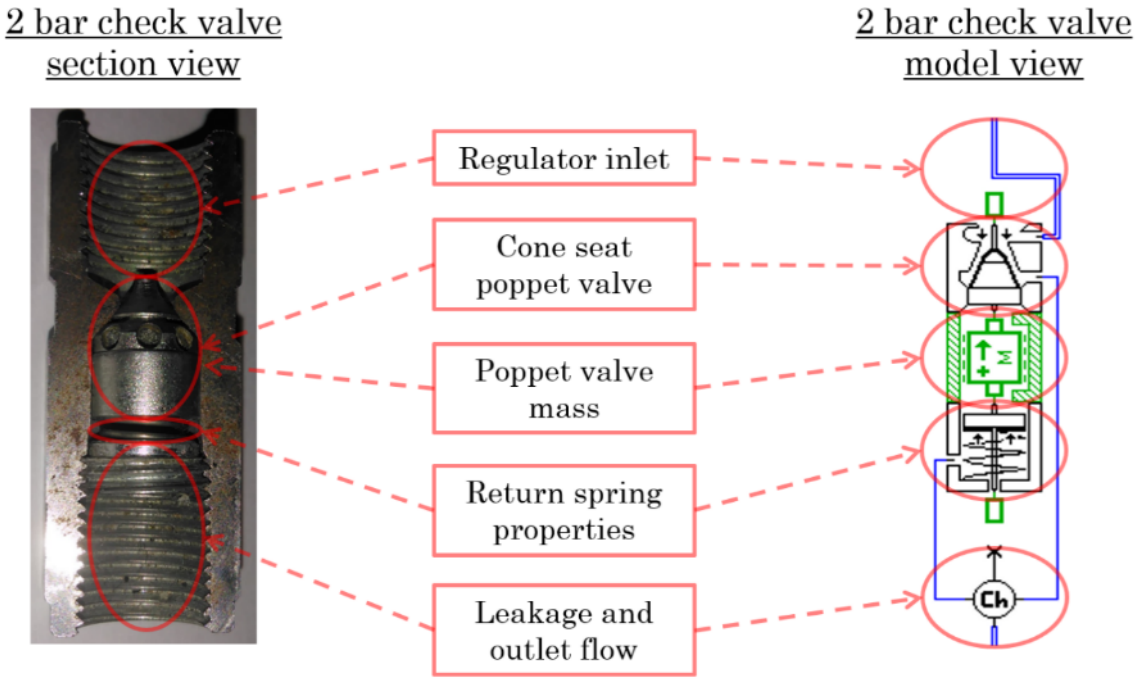


Figure 5.26: 2bar check valve dynamic model description.
Left: Picture of Section view of the 2bar check valve.
Right: Final Amesim check valve model.

Following hose

The following hose, as shown by point 6 in Figure 5.23, has flexible elements that can influence frequency activity and system volume dependent on the stiffness of the hose wall (Drew, Longmore and Johnston, 1997). Amesim provides representations of flexible hoses that can represent the following hose dynamic behaviour. Sub model HH06 was chosen because the compressibility of the fluid and expansion of the hose wall with pressure are taken into account. An accurate value for bulk modulus of a hose wall must be determined to represent volume changes due to pressure fluctuations in the hose with sufficient fidelity.

A value for bulk modulus of hydraulic hoses was not available from literature or product datasheets.

The case of a user supplied B_{eff} was used in the present model. The value used was ascertained using parameter sweeps across different simulation runs to find the value that best represented the empirical data from experimental scheme one. A flexible hose B_{eff} of 2184bar was used for all viscoelastic hose sub-models.

Tank return hose

A flexible hose was added to the model after the following hose to represent a large bore flexible return hose to the fuel supply tank, as shown by point 7 of Figure 5.23. The tank return hose is open to atmosphere at the tank end.

5.2.6 Critical model parameter tuning

Air content

The diesel fluid injected into the measurement system will have a certain amount of air entrainment. This air content acts as seeds for the cavitation to form at negative pressures. Amesim has a fluid property to define the amount of air content in the fluid by mass. Its fluid density input tables assume no air entrainment. When the fluid pressure drops below -0.6bar a density at atmospheric pressure and 0ºC of 1.293kg/m^3 is used to model the cavitation activity formed from the air content.

The "Robert Bosch adiabatic diesel" fluid properties pre-set has an air content ratio of 0.1% by mass. This default setting initially produced a result with a long reflection time and with unexpected high frequency content as highlighted by point 1 of Figure 5.27.

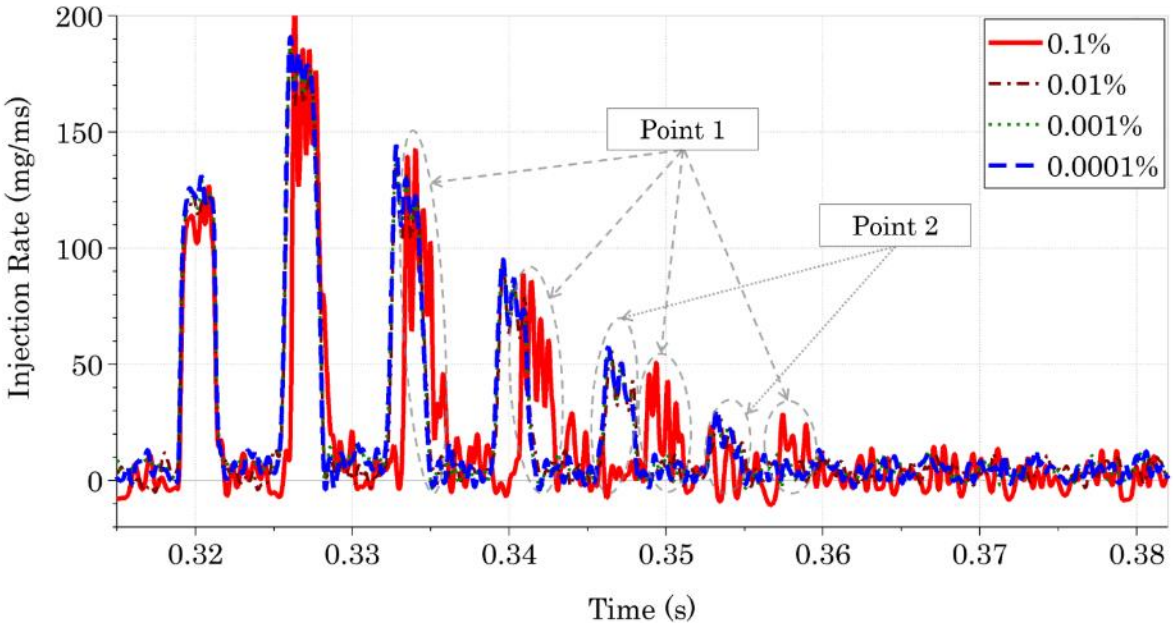


Figure 5.27: 2bar model simulated injection rate for different air contents.
Point 1: high frequencies present at 0.1% air content.
Point 2: Faster reflected wave travel time and less high frequency activity at lower air contents.

The different fluid properties were swept to establish the cause of the slow reflected wave travel time and high frequency content in its output. The model output, when fluid air content ratios are set to 0.01% or lower, displayed a reduction of the high frequency activity and a faster reflected wave travel time, as highlighted by point 2 in Figure 5.27.

To establish the cause of the wave propagation times within the modelled fluid, the SOS within the fluid at the observation point was studied at the different air content ratios and shown in Figure 5.28. The default 0.1% air content, highlighted by point 1 of Figure 5.28**Error! Reference source not found.**, displays the highest level of fluctuations in the SOS value of the air contents studied. This fluctuating SOS is outside the expected range of 800-1200m/s for diesel test fluid at these temperature and pressure ranges (Chorążewski *et al.*, 2013).

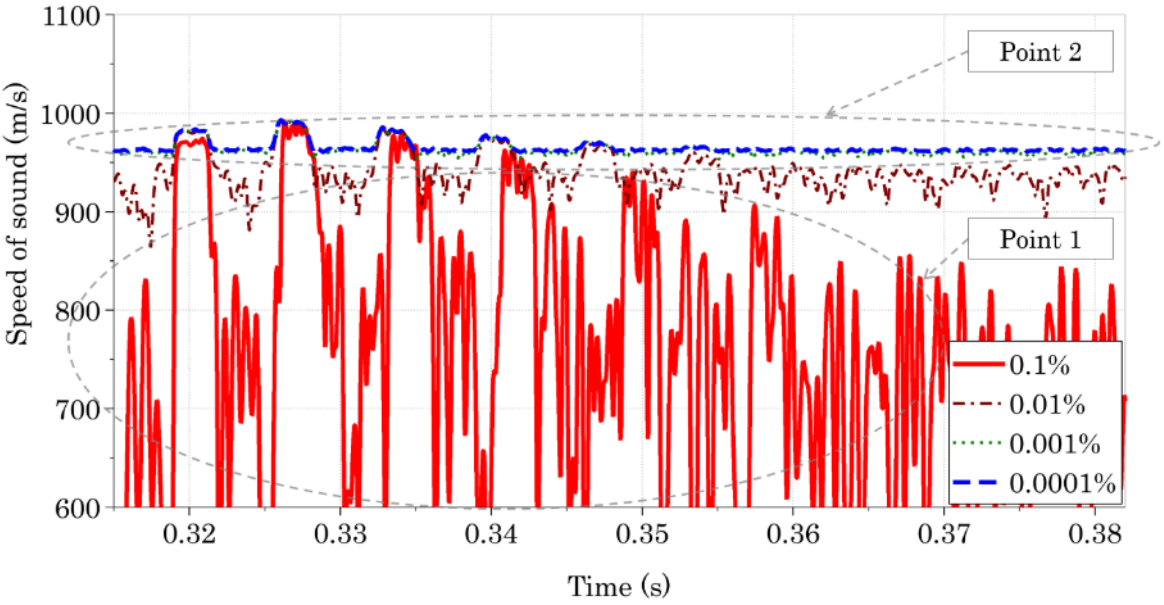


Figure 5.28: 2bar model simulated SOS at the observation point for different air contents.
Point 1: Large SOS variance at 0.1% air content in the fluid.
Point 2: Stable SOS in the expected range at lower air content in the fluid.

At higher pressures the air will eventually become dissolved. At low pressure bubbles will form leading to a phenomenon known as air release. Cavitation occurs when pressure of the hydraulic fluid goes below the saturated vapor pressure of fluid. As the liquid changes to vapor, the bulk modulus becomes almost zero (Siemens, 2004; Franc and Michel, 2006).

This change of state in the fluid subsequently lowers the SOS and hence wave propagation speed in the modelled fluid. This is shown when removing air content by setting it to 0.0001%, the SOS remains stable and within the expected range, as highlighted by point 2 of Figure 5.28.

The Amesim diesel fluid settings are typically used for simulating high frequency cavitation effects inside diesel injector components with pressure between typically 2000-3000bar. When Amesim is used for lower pressure hydraulic circuits, the frequency activity is typically in the sub kilohertz frequency range, such as hydraulic power circuits (Alex Duggan, 2014). Therefore, the cavitation models used by Amesim are not appropriate for modelling high frequency effects at low back pressures. However, the purpose of the work in model space was to study low frequency effects on zero value variance from the tube termination, not high frequency effects due to vapour formation. The model output using 0.0001% air content was used to remove vapour formation calculations from the model output so that low frequency effects could be studied.

Fluid temperature

For a fixed backpressure and injection conditions, as used in this model, pressure will be repeatable, hence changes in speed of sound between separate injection events can be considered isobaric. It is known from previous characterisation of ISO4113 test fluid properties by Chorążewski *et al.* (2013) that for an isobaric (constant pressure) lowering of fluid temperature, SOS in ISO4113 increases.

Experimental scheme one identified a 30ºC temperature gradient between the start and end of the rate tube, the location is shown in point 1 of Figure 5.23. The heat in the system is generated by fluid shear and cavitation activity (Strotos *et al.*, 2015) from the injector and would dissipate as the fluid travels the length of the rate tube. This was assumed to be caused by heat losses from the rate tube outer surface along its length to the environment.

The adiabatic model assumption assumes no heat loss gradient across the rate tube length, due to thermal dissipation from the rate tube wall. Therefore, if an adiabatic model is to be representative of experimentally observed undamped low frequency pressure waves, the simulated average SOS in the rate tube must be aligned to best match empirical data from experimental scheme 1.

An average SOS value was determined by comparing the reflected wave travel time between model space and experimental results. The magnitude of the baseline production experimental scheme 1 data was normalised to the magnitude of the simulated pressure wave at 120 ºC. The simulated reflected wave travel time for different fluid temperatures were then compared to the baseline production result from experimental scheme one, as shown in point 1 of Figure 5.29.

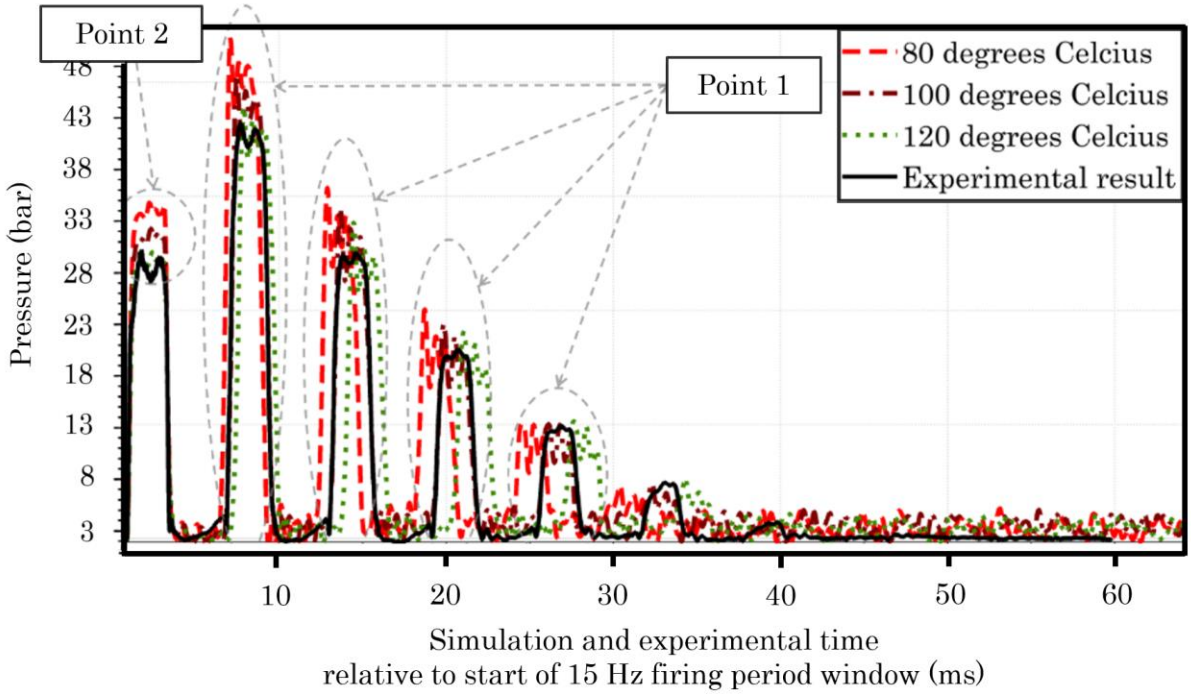


Figure 5.29: Simulated injection rate for different fluid temperatures in the rate tube vs experimental result from experimental scheme one.
Point 1: different reflected wave periods for different temperatures.
Point 2: Changing temperature effect on height of the signal.

The output of the simulation produced good agreement with the experimental result reflected wave travel time, at an average fluid temperature of 100°C, and was subsequently fixed as the default fluid temperature within the model.

Rate height

After aligning speed of sound between model space and experimental data, the phasing of the reflected wave activity will be representative, but not the magnitude and subsequent influence on zero value variance. Hence the injection rate magnitude in model space must also be evaluated against the experimental result, as shown by the different Y axis of Figure 5.30.

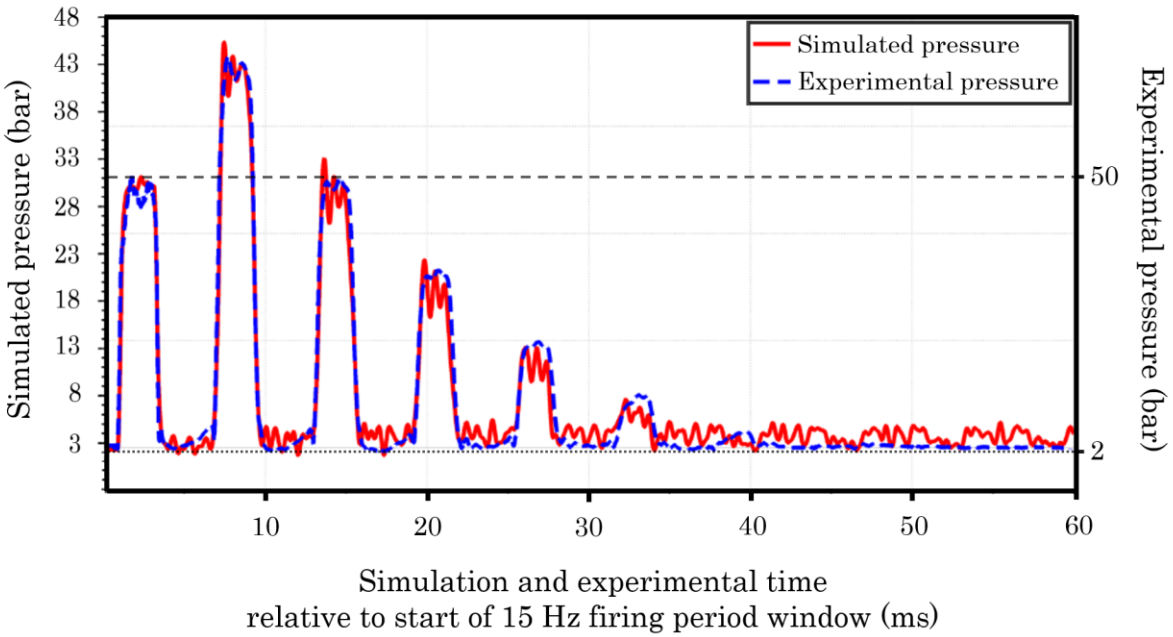


Figure 5.30: Final tuned 2bar model simulated injection rate vs experimental result from experimental scheme one.

The modelled pressure wave magnitude due to flow input to the model was approximately 30bar. However, the experimental data reached 50bar for the 2400bar injection pressure and injector studied. This represents a pressure wave magnitude error of approximately 40%.

The volume flow rate profile used in the rate tube model used data from a different injector than the one studied on experimental scheme one, as discussed in Section 5.2.5. The majority of observed pressure wave magnitude discrepancy between modelled and experimental data is due to a maximum nozzle flow rate difference 30% less than that of the injector studied on experimental scheme one.

The remaining magnitude discrepancy could be explained by differences between the adiabatic fluid properties in the model and the experimental apparatus used during scheme one. The simple flow rate input does not account for fluid heating due to fluid shear or cavitation present in the injection event of experimental data (Strotos *et al.*, 2015). A transient isobaric increase in temperature will result in a faster speed of sound in the fluid (Bazile *et al.*, 2012), which in turn will increase the magnitude of the observed pressure wave, as demonstrated on a rate tube meter by van Bebber and Reuter (2017).

The difference in magnitude will influence the intensity of pressure wave activity throughout the system, thus having a scaling effect on the zero value variance observed. To address this discrepancy, the height of the 100°C model result was aligned to the height of the signal from experimental scheme one as shown in Figure 5.30.

The magnitude alignment was deemed acceptable, as the objective of the model development was to study the influence of different hydraulic configurations on low frequency zero value variance. The high frequencies and temperature input caused by cavitation in the injection event were not studied at this stage. These effects were explored experimentally and are discussed in Section 0.

This final 2bar model simulated result shown in Figure 5.30 has good agreement with the experimental result in terms of low frequency wave activity. Therefore, the model was deemed acceptable for studying the influence of hydraulic configurations on low frequency zero value variance.

5.2.7 Reflected wave height

During experimental scheme one, it was observed that the first reflected wave could be of greater magnitude than the input pressure pulse to the rate tube caused by the injection, as shown in Section 0. The root cause of this is not identified in the body of available literature.

To understand this effect, the reflected wave activity was evaluated at different observation points along the tube length for the 2bar model. The standard injection rate observation point shown by point 1 of Figure 5.31 and at the centre of the 3m tube length as shown by point 2 of Figure 5.31. When the injection rate is observed at the middle position, the waves reflected from both ends of the rate tube are separated in time as shown in point 3 of Figure 5.31.

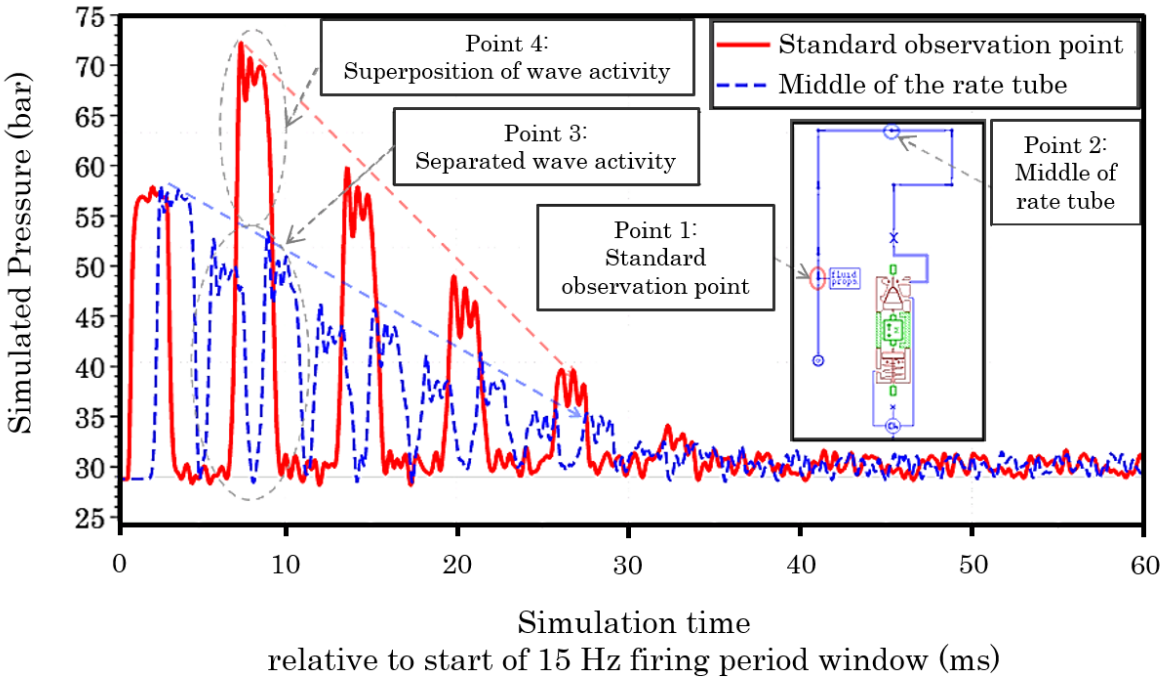


Figure 5.31: Simulated injection rate with superimposed wave activity at the standard observation point and separated wave activity at the middle point of the rate tube.

When observed from the standard observation point at the start of the tube the reflected waves from each end of the tube will superimpose on top of each other and appear as one as shown by point 4 of Figure 5.31. Resulting in a wave approximately 2x higher than the reflected wave from the orifice. This was not previously understood within the field. Reflected wave heights and timings were typically tuned by empirically changing the rate tube geometry and orifice size to suit the application.

5.2.8 30bar Regulated Coriolis meter system model

There is limited information in the available literature as to the influence of hydraulic configuration on zero value variance. To counter zero value variance, the typical approach used for commercially available devices is to "leave the entire electrical system unchanged and only modify the hydraulics" for each application (IAV, 2019). This is typically achieved by increasing the hydraulic length of the rate tube and slowing the firing rate, to allow adequate time for quiescent pressure to be observed in the tube before the measurement of the next injection event. This is acceptable in an experimental context where sub 15Hz firing rates are acceptable, but cycle time is an important consideration when operating in a production environment where firing rates are typically 15-25Hz. The influence of hydraulic configuration on zero value variance must be understood to minimise measurement variance in production testing environment.

During experimental scheme one, evidence was found that the 2bar measurement system had minimal pressure wave activity in the following hose that follows the tube termination. This is because the following hose is connected to a return tank at its exit and hence atmospheric pressure as shown by point 1 in Figure 5.32. This means that any pressure waves entering the following hose will dissipate down to atmospheric pressure.

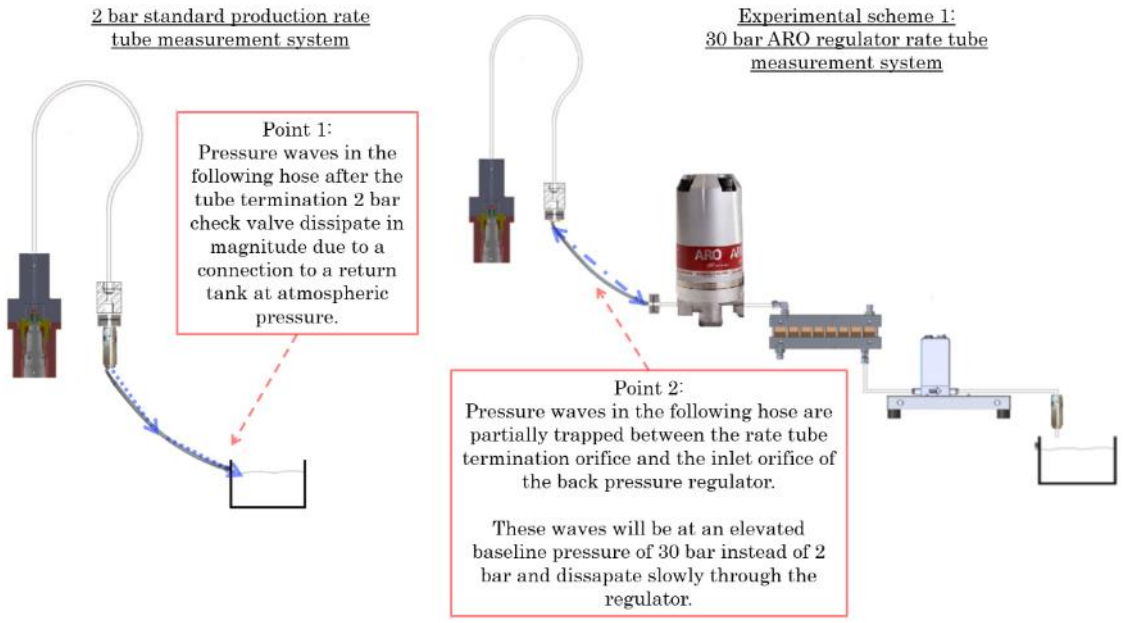


Figure 5.32: Illustration of pressure waves in the following hose dissipating to atmosphere in the standard 2bar system. Also, the location of trapped pressure wave activity in the following hose in the 30bar system from experimental scheme one.

When studying the 30bar regulated Coriolis circuit during experimental scheme one, it was observed that the magnitude of zero value variance is in part dependent on the diameter of the following hose as discussed in Section 5.1.4.

With a backpressure regulator at the hose termination, it would be pressurised to 30bar instead of atmosphere. The location of the trapped pressure in the following hose on the 30bar regulated circuit is highlighted by point 2 in Figure 5.32.

Increasing the backpressure was desirable due to the improvement in matching in-cylinder engine regime and suppressing cavitation from the injection event, as discussed in literature review Section 2.2.7. This goal dictated that characterising the mechanism of increased zero value variance at higher backpressures be a primary objective of the model based work.

To meet this objective, a second Amesim model was developed to identify the mechanism by which the 30bar regulated circuit studied interacted with the now pressurised following hose to influence zero value variance. To achieve this, the 30bar ARO® regulator, and Coriolis meter circuit studied during experimental scheme one, were created in model space using the 2bar system as a base. The 30bar Amesim model is shown in Figure 5.33. The details of the modelling scheme used to create this second model is described in the following Sections.

ARO® regulator and fuel chiller sub models

A detailed description of the 2bar model can be found in Section 5.2.1. The additional elements required to construct the 30bar backpressure regulated model are described here. The primary additions were the ARO® backpressure regulator, low-volume fuel chiller and coriolis meter as shown in point 7, 8 and 9 in Figure 5.33. A detailed breakdown of the sub models used for the regulator and fuel chiller are shown in Figure 5.34.

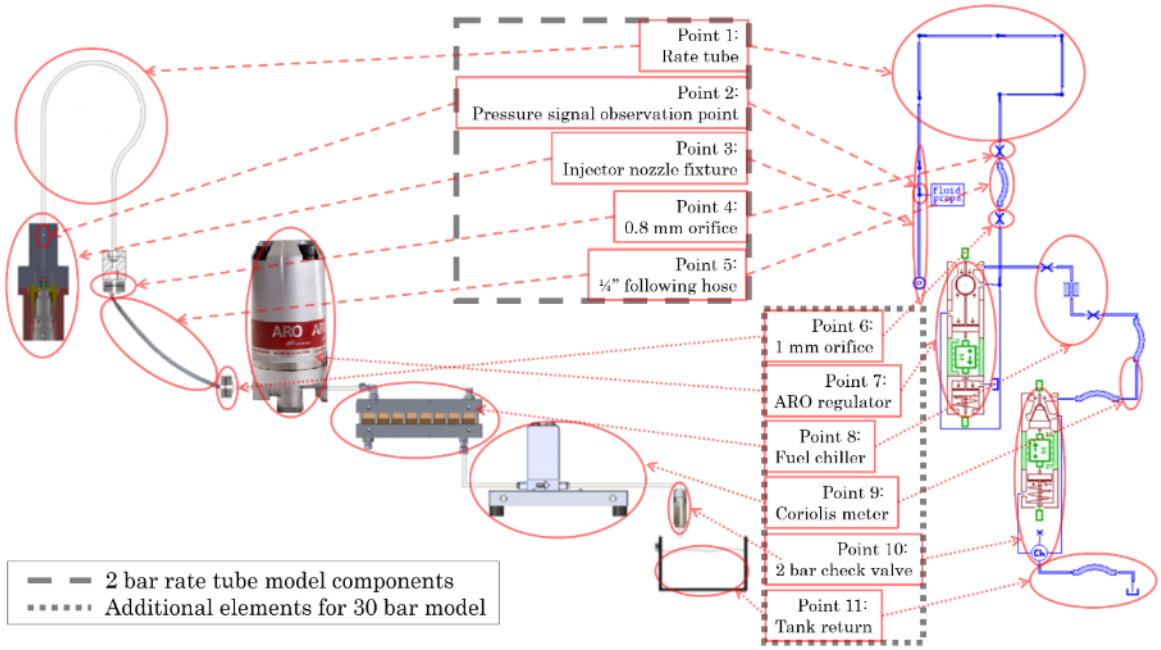


Figure 5.33: Final model iteration for standard 30bar regulator measurement system.
Left: Visual representation.
Right: Final Amesim model.

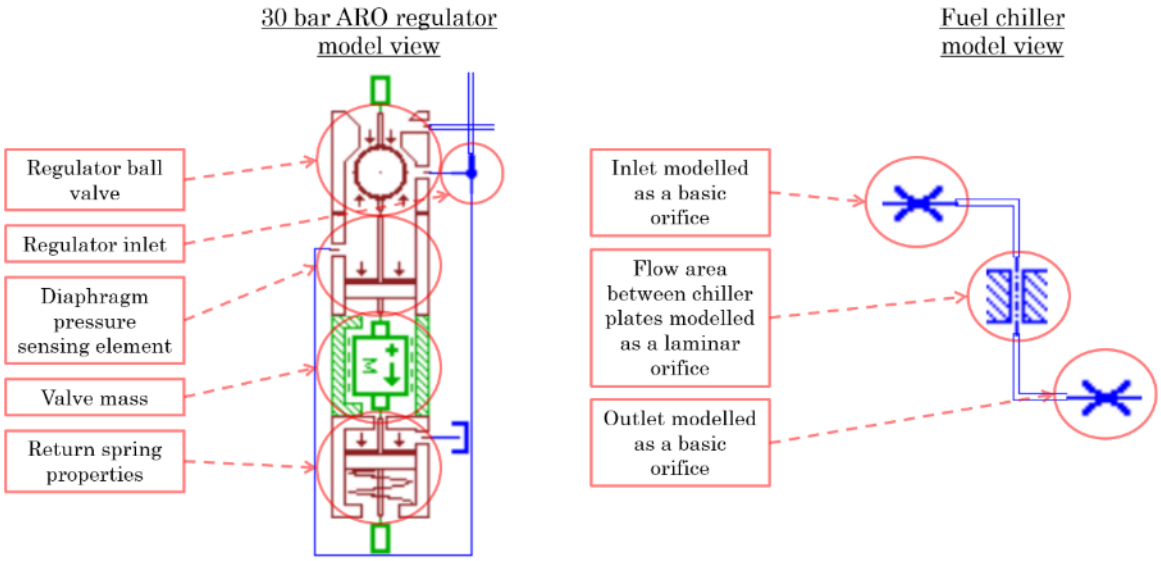


Figure 5.34: Additional model elements to construct 30bar system model.
Left: ARO® regulator model construction.
Right: Fuel chiller model construction.

The ARO® regulator differs from the check valve model, due to the use of a ball valve in place of a conical poppet valve. The pressure sensing is also carried out by a diaphragm that will lift the ball valve off its sealing interface when the set point is exceeded.

To construct these model elements, the geometric parameters were obtained from the ARO® regulator. The return spring rate of 186N/mm was identified from the datasheet for the spring used. The spring compression was found out from the pitch of the preload setting screw for the spring and the number of turns required to achieve 30bar back pressure. Using these parameters, the model produces a backpressure of approximately 28.8bar. This is within a 4% error from the 30bar experimentally observed value. Spring rate values can have an error of up to 20% in their manufacture (Parrish, 2014). Therefore, this level of error meant that the ARO® regulator model element shown on the left of Figure 5.34, was deemed acceptable for study.

The coriolis meter is modelled as a simple pipe of constant diameter connected by two short flexible nylon pipe vibration isolation hose connections, as highlighted by point 9 of Figure 5.33. By observing the mean flow rate in this pipe, a value for mass outflow of the system can be observed as would be captured by a coriolis meter.

The fuel chiller is modelled as a 180mm long x 50mm wide x 0.05mm deep laminar orifice and is shown on the right of Figure 5.34. An inlet and outlet orifice are used to represent the hydraulic fittings.

During experimental scheme one, the coriolis fuel chiller was initially trialled without a backpressure regulator. A pressure dial gauge was used to observe an average 14bar pressure at the chiller inlet for the injection condition studied. The effect of backpressure due to chiller restriction alone was also measured and introduced in the model by replacing the regulator sub model with a straight connection pipe. The simulated instantaneous dynamic pressure wave activity at the fuel chiller inlet shown in Figure 5.35 has an average value of 12bar, in contrast to the 14bar observed experimentally. An observation error on the dial pressure gauge used could be up to 0.6bar (WIKA, 2020), with additional thermal drift of at the temperatures above 60ºC observed at the chiller inlet. The aim was to study of the pressure wave dynamics that influence zero value variance in model space. Hence, a relative magnitude error of 14% between model space and experimentally observed results was deemed acceptable.

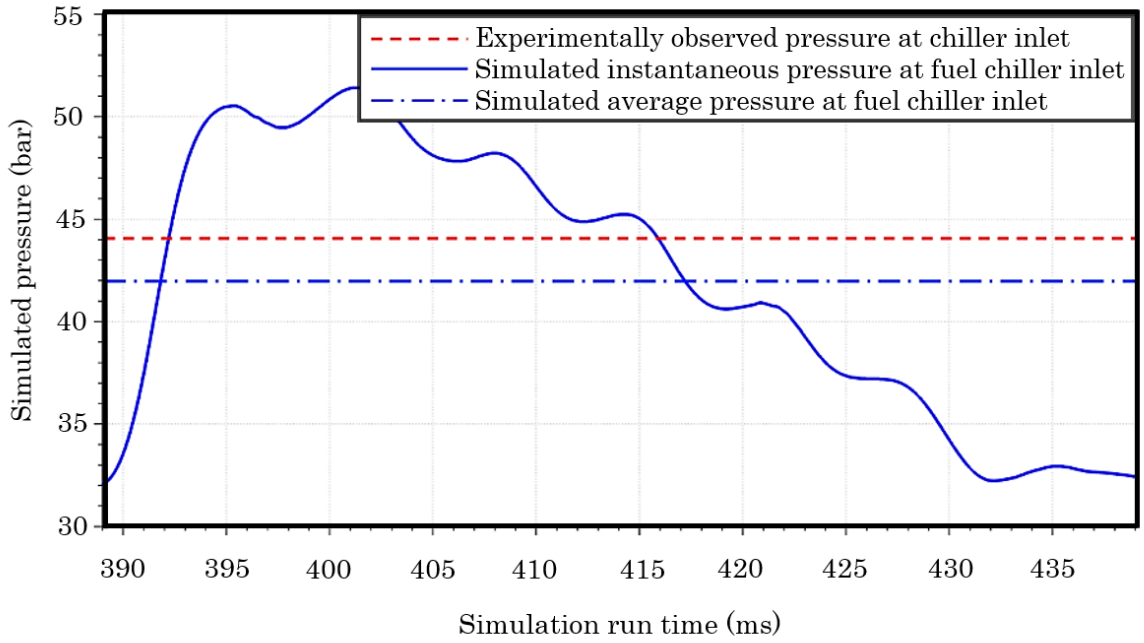


Figure 5.35: Simulated and experimentally observed pressure at chiller inlet for the 30bar system model and experimental scheme one. Average of the dynamic simulated result shown in dash-dot blue line.

The author is not aware of any literature that features low volume, restrictive laminar orifice fuel chillers paired with rate tube measurement systems. Most rate tubes use conventional chillers with large flow volumes that result in significant additional time lag between the injector and flow meter (Goris, Rauznitz and Awad, 2006). Whilst the time lag is acceptable for steady state laboratory test cycles, it would lead to unacceptable production injector transient test cycle times.

Close alignment of the 30bar model components with experimental results shows that the present method used to construct them is effective at representing pressure wave dynamics in a rate tube measurement system termination assembly with elevated back pressures.

5.2.9 Following hose diameter

The diameter of the internal bore of the following hose was shown to influence zero value variance on the 2bar production measurement system in Section 5.1.4. This demonstrated that the influence of hydraulic component configuration, after the termination orifice, is observable in the pressure wave characteristic. This effect had not been described for rate tubes found in literature. Likely because in most applications the firing rate would be reduced to allow more time for quiescent pressure conditions to be achieved.

Therefore, the influence of hydraulic components after the termination orifice on low pressure waves, and zero value variance, must be understood to overcome one of the primary rate sources of variance in a tube measurement device.

To understand the mechanism of zero value variance influence and how it behaves at elevated back pressures, the 30bar simulation result was compared for both 1/4" BSP and 3/16" BSP internal diameter stainless steel braided hose cases. Pressure at the injection rate observation point and at the start of the following hose for both following hose types are shown in Figure 5.36. The corresponding pressure at the following hose inlet is shown in Figure 5.37 for both bore diameters.

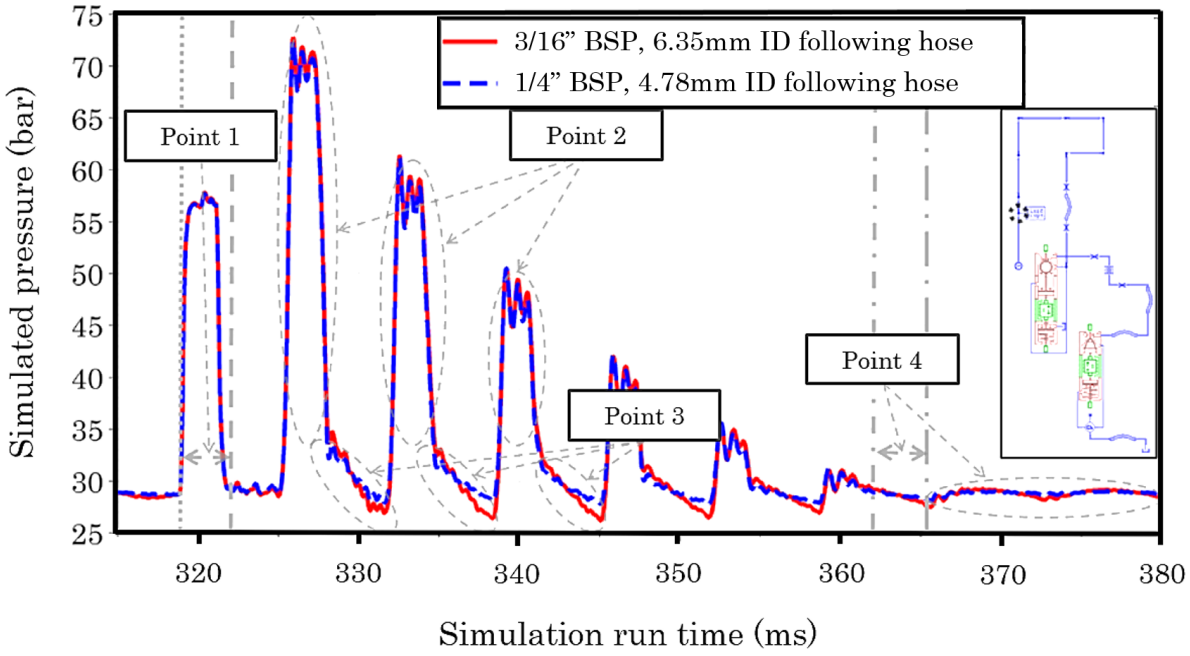


Figure 5.36: Comparison of pressure at the injection rate observation point for 1/4" and 3/16" BSP bore flexible hoses fitted to the 30bar system model.

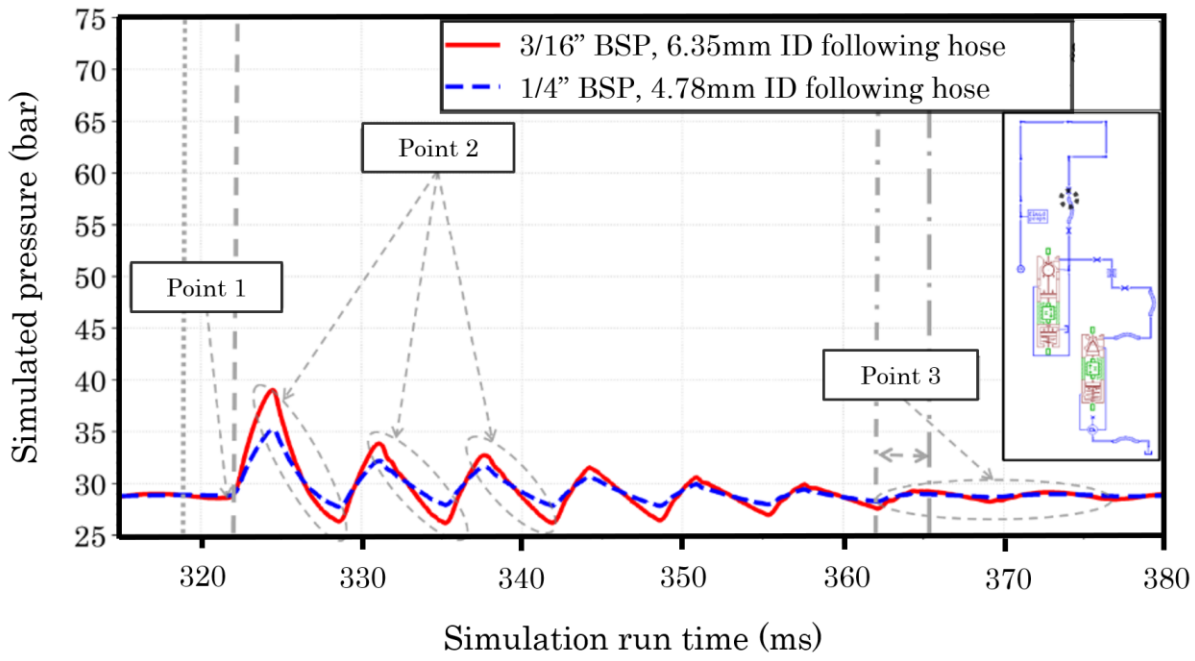


Figure 5.37: Comparison of pressure at the following hose inlet for 1/4" and 3/16" BSP bore flexible hoses fitted to the 30bar system model.

The time for the input pressure wave at the observation point to reach the following hose inlet is shown by point 1 of Figure 5.36 and Figure 5.37. This result shows that pressure activity inside of the following hose is phase shifted in time compared to the input pressure wave and hence frequency activity inside the rate tube. The SOS in the fluid medium inside the rate tube will dictate this observed phase shift, as the input pressure wave has to travel the length of the rate tube before pressure wave activity will be observed at the following hose inlet.

The magnitude of each reflected pressure wave within the rate tube reduces each time it is reflected back from the termination orifice, as by point 2 of Figure 5.36. This reduction in reflected wave height is caused by the partial pressure release through the termination orifice when a pressure wave reaches it. It is these partial pressure waves that excite the pressure within the following hose but to a much lower magnitude than in the rate tube. The input pressure pulse due to the injection event into the rate tube must pass through the termination orifice before entering the following hose inlet. Therefore, the magnitude of frequency activity present in both the rate tube and following hose will be dictated by the size of the rate tube termination orifice.

The 3/16" following hose case displays a steeper pressure gradient between the reflected waves in the rate tube as highlighted by point 3 of Figure 5.36. This same change in pressure gradient between pressure pulses can be observed in the following hose as shown by point 2 of Figure 5.37. The delay between the first change in pressure gradient in the following hose and the change in

gradient between the reflected waves in the rate tube is in line with the delay highlighted by point 1 of Figure 5.37.

This delay is due to the input pressure wave travelling from the rate tube start, reflecting off of the tube termination orifice as a partially closed tube end, to then travel back to observation point at the start of the rate tube. The input pressure pulse will have reached the orifice by half the period between the start of the input pressure pulse and the start of the first reflection at the standard observation point. Hence, the phase delay between pressure wave activity at the standard observation point in the rate tube and at the following hose inlet is half the rate tube quarter wave resonant period and vice versa.

Some minimal pressure wave activity is still observable in the following hose just before the time of the next injection event, as shown by point 3 of Figure 5.36. This same pressure wave characteristic can then be observed on the zero value variance in the rate tube pressure, just before the next injection event, as shown by point 4 of Figure 5.36. The phase shift between pressure wave activity in the following hose and in the rate tube is the same as the delay highlighted by point 1 of Figure 5.36.

This result demonstrates that low magnitude pressure waves from the following hose influence the delta pressure across the tube termination orifice. Becoming superimposed on top of the rate tube pressure wave magnitude during the quiescent period. Therefore, pressure wave activity after the rate tube termination orifice will influence the magnitude of zero value variance observed during subsequent injection measurement events.

The pressure wave magnitude is greater for the 3/16" rather than with the 1/4" following hose in both the following hose and rate tube, as shown by point 2 of Figure 5.37 and by point 3 of Figure 5.36 respectively. Hence the geometry of the hydraulic circuit after the rate tube termination orifice can influence the magnitude of zero value variance observed.

This highlights a significant design optimisation parameter for rate tube injection meter. To minimise zero value variance, the design of the hydraulic geometry after the tube termination must be optimised to minimise the magnitude of pressure wave activity within it.

To investigate the optimal hydraulic design parameters further, the influence of following hose length on zero value variance is discussed in the following Section.

5.2.10 Following hose length

The hydraulic volume of the following hose can be represented as a dissipative hydraulic muffler with flexible walls (Du Tao and Dazhuan, 2015). The flexible

walls will move axially to the flow as they expand due to a pressure rise within the hose. This dynamic movement of the hose walls acts as an impedance to pressure activity travelling its length (Drew, Longmore and Johnston, 1997).

To study the influence of the following hose length on zero value variance, a sweep of three different hose lengths was conducted. The 3/16" BSP hose internal diameter was chosen as it showed the greatest influence on zero value variance during the quiescent period as shown in Figure 5.37 point 3. The pressure at the following hose inlet for 1m, 1.75m and 3m long is shown in Figure 5.38. An FFT of the pressure wave activity at the following hose inlet is shown in Figure 5.39.

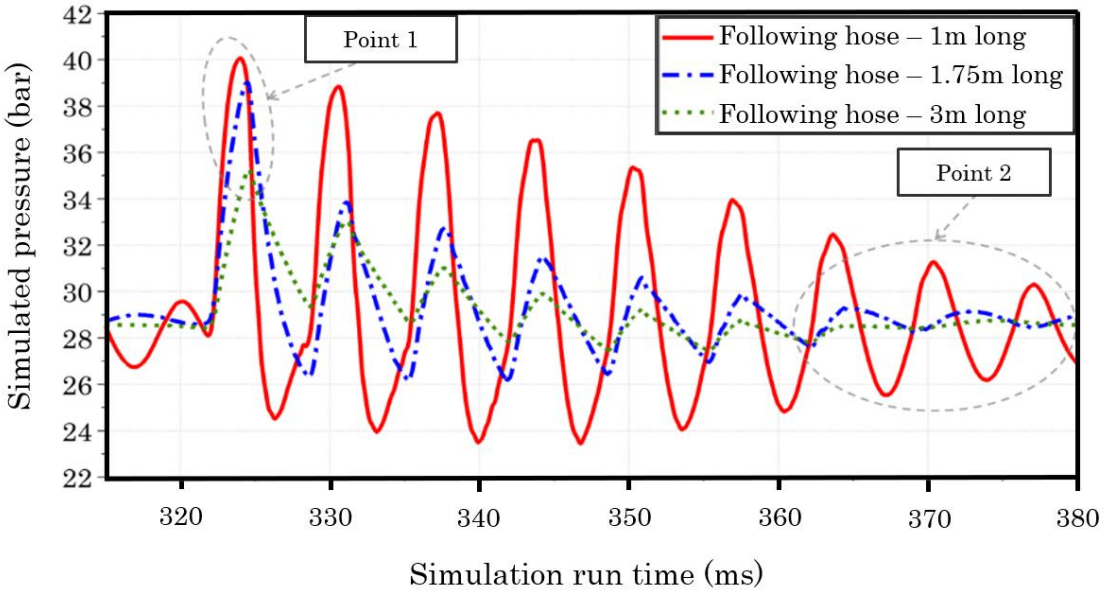


Figure 5.38: Simulated pressure at the following hose inlet with 3/16" bore diameter and 1m, 1.75m, 3m hose lengths.

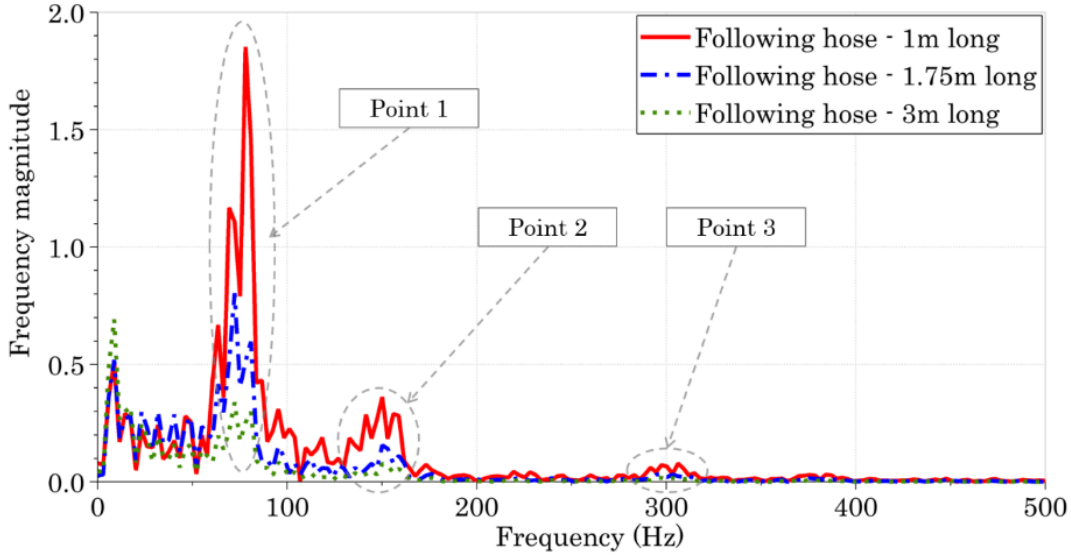


Figure 5.39: FFT showing the frequencies and magnitude of the simulated pressure wave activity at the following hose inlet with 3/16" bore diameter and 1m, 1.75m, 3m hose lengths.

The magnitude of the pressure wave activity in the following hose increases as hose length decreases, as shown by point 1 of Figure 5.38 and Figure 5.39. This is in line with the theoretical effect of reduced transmission losses induced by the flexible internal bore of the hose.

The dominant frequency range observed at the following hose inlet is at 75Hz for all cases, as shown by point 1 of the FFT in Figure 5.39. This is half the 150Hz rate tube primary resonant frequency in the model driven by the reflection period as shown in Table 5.3. During experimental scheme one, a rate tube resonant frequency of 168.4Hz was observed as described in Section 5.1.3.

Table 5.3: Rate tube resonance frequency orders observed within the following hose.

		Rate tube	**Following hose**		
		3m	1m	1.75m	3m
	Harmonic order	**Frequency (Hz)**			
Half of fundamental	0.5	75	225	129	75
Fundamental	1	150	450	257	150
First Harmonic	2	300	900	514	300
Second Harmonic	3	450	1350	771	450
Third Harmonic	4	600	1800	1029	600
Fourth Harmonic	5	750	2250	1286	750

The half order rate tube resonant frequency is of highest magnitude in the following hose when using the shortest following hose length of 1m. The fundamental resonant frequency of the 1m following hose is three times that of the rate tube. Hence, the resonance of the following hose will be excited by the 3rd order of the input forcing frequency from the rate tube.

The 1.75m hose case does not have a resonant order that matches the rate tube resonant forcing frequency or its higher orders. The 3m following hose has the same resonance as the rate tube itself, so will be directly excited by it. However, as the transmission losses due to the dynamic behaviour of the flexible walls are much larger because of the increased length, the magnitude of pressure value activity will be reduced.

There is a slight shift in the half order and fundamental rate tube resonant frequency that increases in frequency as hose length is decreased, as shown by point 1 of Figure 5.39 and Figure 5.38. Previously it was shown the pressure waves will be aligned when the length is fixed but the volume is changed as shown in point 2 of Figure 5.37. Hence the length will influence frequencies observed and superimposed as zero value variance, whereas the overall volume will influence the magnitude. Therefor both the length and dynamic behaviour of the flexible internal bore of the following hose must be carefully selected to minimise the effect of the following hose on zero value variance observed within the rate tube.

This result demonstrates that the magnitude and frequencies of resonant wave activity inside of a rate tube measurement system can only be determined by considering the resonant characteristics of each subsystem in combination. Hence, any hydraulic geometry after the rate tube termination orifice must be carefully selected so that resonant modes of the rate tube itself are not excited. Otherwise resonant harmonics could appear in the zero value variance before the next injection, driven by the resonance of other hydraulic features in the measurement system.

5.2.11 Hose length and coriolis flow measurement

It is shown in the previous Section that the magnitude of pressure waves in the following hose contributes to the magnitude of zero value measurement variance observed. Therefore, a larger following hose internal diameter after the rate tube termination orifice will reduce zero value variance.

The 30bar circuit was designed with the aim to allow the use of a coriolis meter at elevated back pressures, to inform the design of experimental scheme three. The total volume in the system before the coriolis meter will dictate the coriolis measurement delay of injection flow rate because of its position at the end of the measurement system. The injector flow has to travel the length of the rate tube before reaching a stabilised average flow value per second at the coriolis meter. Once a repeatable injection condition is maintained the flow through the system will stabilise. However, when the injector nozzle flow is swept, as with production injector test cycles, the temperature and hence density of the system will change rapidly. Which will distort the measured coriolis flow because of fluid volume changes in the system with changing density.

Hence, to minimise measurement delay for the coriolis meter and minimise stabilisation times before a coriolis measurement is made, a minimal hydraulic system volume must be maintained. This measurement system design optimisation parameter of minimal coriolis meter measurement delay runs counter to the desire for a larger following hose internal diameter after the rate

tube termination orifice for lower zero value variance. Hence, a balance must be found between minimal coriolis flow measurement delay and minimal zero value variance if a coriolis meter is to be attached to the end of a rate tube measurement system.

5.2.12 Regulator leakage

During experimental scheme one, there was a low frequency wave present when the ARO® back pressure regulator was fitted to the measurement system, which is discussed in Section 5.2.12 and shown in Figure 5.18. The dynamic response of the backpressure regulator at end of the following hose must be characterised to achieve a stable baseline and minimal zero value variance.

It was theorised that the regulator may have a constant leakage across its sealing interface. To test this assumption, an attempt was made to simulate a leakage across the regulator seat in model space. To achieve this, the regulator poppet lift was artificially restricted to a maximum lift of 0.01mm to simulate a constant leakage across the regulator sealing interface as shown in Figure 5.40. The restricted poppet lift case will not allow the regulator to respond proportionally to the pressure at its inlet, instead forcing it to behave as a fixed flow impedance / orifice.

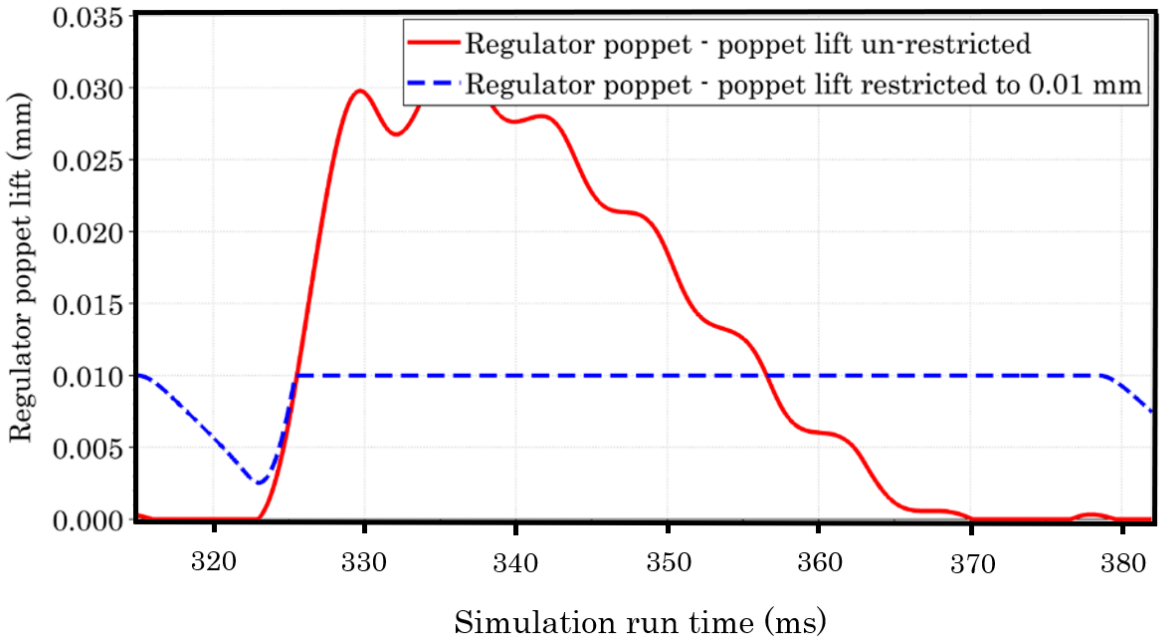


Figure 5.40: Restricted and unrestricted ARO® backpressure regulator poppet lift for the baseline 30bar system model.

The greatest poppet travel observed in simulation space was approximately 0.030mm. This is a small value compared to the overall travel of 5mm measured during the ARO® regulator disassembly. Therefore, the ARO® regulator was not

using most of its travel to regulate pressure. This result provides further evidence that a large regulator such as the ARO® was not suitable for low mass flow rates seen in this application.

When the pressure is observed at the injection rate observation point, the unrestricted case has a flat zero value variance trend whereas the restricted lift has a significant low frequency wave superimposed as shown in Figure 5.39.

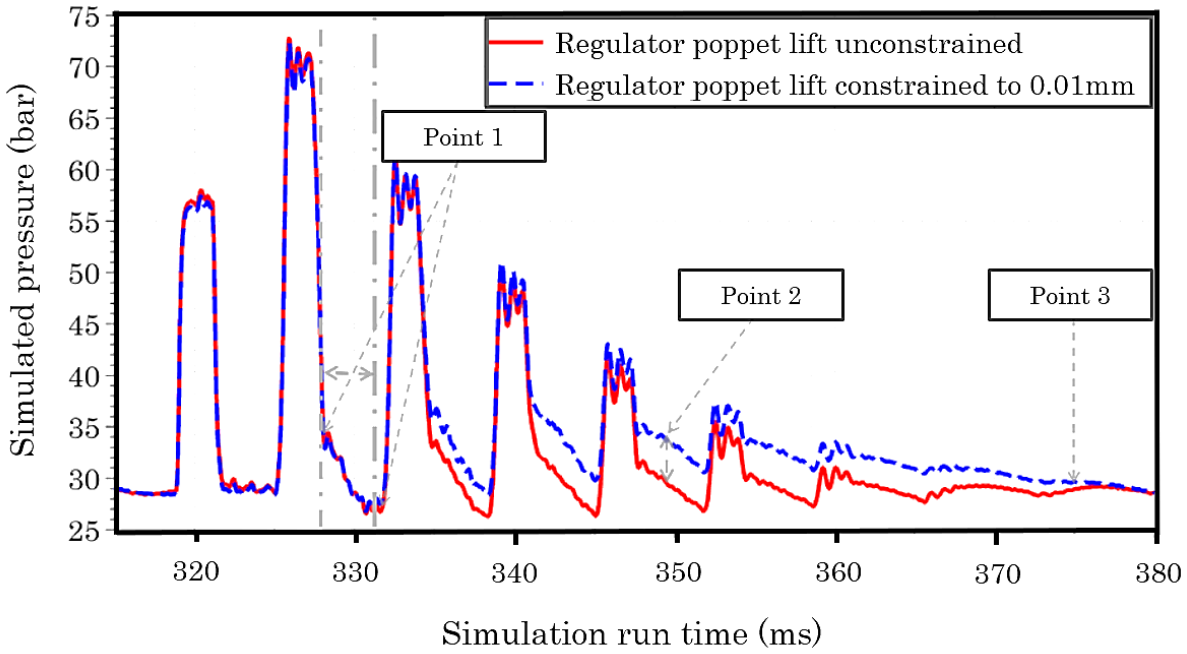


Figure 5.41: Simulated pressure at the injection rate observation point for restricted and unrestricted ARO® backpressure regulator poppet lift for the baseline 30bar system model.

This matches the observed characteristic during experimental scheme one in Figure 5.18 and confirms that the ARO® backpressure regulator is not responding proportionally to the pressure at its inlet. It is instead acting as a fixed restriction, which allows pressure in the following hose to rise and become superimposed on the pressure observed within the rate tube. Therefore, an appropriate regulator must have no leakage across its seat and move proportionally to the pressure at its input. If this important design characteristic is not well considered, then a low frequency wave artefact in the zero value variance can appear in the observed at the injection rate.

5.3 Zero value variance temperature sensitivity

This Section describes an observed temperature sensitivity for the zero value variance during the three-month production trial carried out on experimental scheme three. When using experimental scheme three under production conditions, it was discovered that the process had a lower yield because of day-to-

day calibration drift when compared to other standard production test machines. When evaluating the output of numerical methods to assess primary sources of variance on experimental scheme three, variables related to baseline zero value pressure and system temperature were significant contributors to the fuel value variance on the measurement systems trialled. How this was mathematically determined is discussed in more detail in Section 8.3.

An experiment was carried out to understand how temperature was numerically linked to zero value variance. A running condition of 2400bar 1500µs injection duration was used. This running condition was used because it represented the part of the production test that had the greatest calibration instability during experimental scheme three. The measurement system was run at 15Hz firing rate from ambient and a measurement trace was captured every 5 minutes up to a maximum of 15 minutes. The full 15Hz measurement period at three different system temperatures can be seen in Figure 5.42.

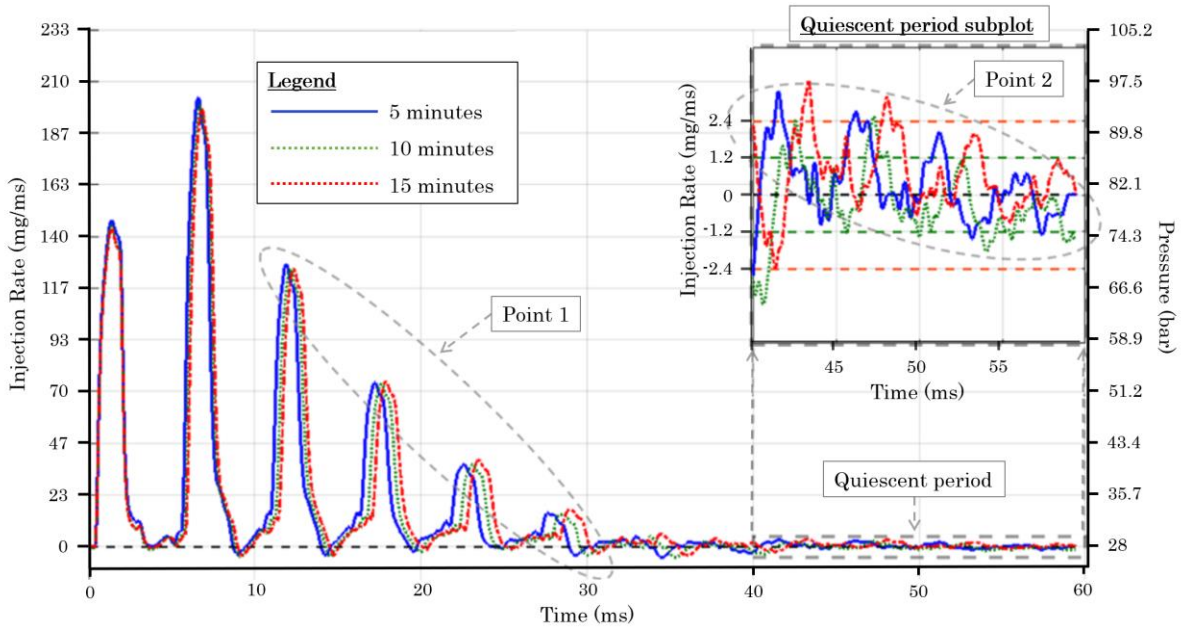


Figure 5.42: Full 15hz period injection rate for different system temperatures on experimental scheme three. 2400bar pressure 2300µs duration injection condition.
Blue: 5 minutes from ambient.
Green: 10 minutes from ambient.
Red: 15 minutes from ambient.

As the duration of the experiment increases, the measurement system temperature also increases. This is because of the heating effect of the injection event, which transfers heat into the body of the rate tube pipe. When the rate tube wall temperature changes so will the temperature of the fluid inside of it with each injection event. For a fixed injection condition and hence pressure inside the tube, when the fluid temperature changes, there will be a corresponding change in SOS (Bazile *et al.*, 2012). When SOS changes in the fluid, so will the resonant frequency of each hydraulic component in the

measurement system. This is demonstrated by point 1 of Figure 5.42, where the primary reflection period of the rate tube lowers in frequency as system temperature increases with time.

As discussed in 5.2.10 hydraulic component resonance after the rate tube termination can cause a low frequency wave to be present during the quiescent period. There is evidence of a residual low frequency wave present during this period that would affect the next injection as shown in point 2 of Figure 5.42. This wave in the quiescent period appears to change with system temperature. To identify the change in frequencies present and their source, an amplitude spectrum of the injection rate was inspected, as shown in Figure 5.43.

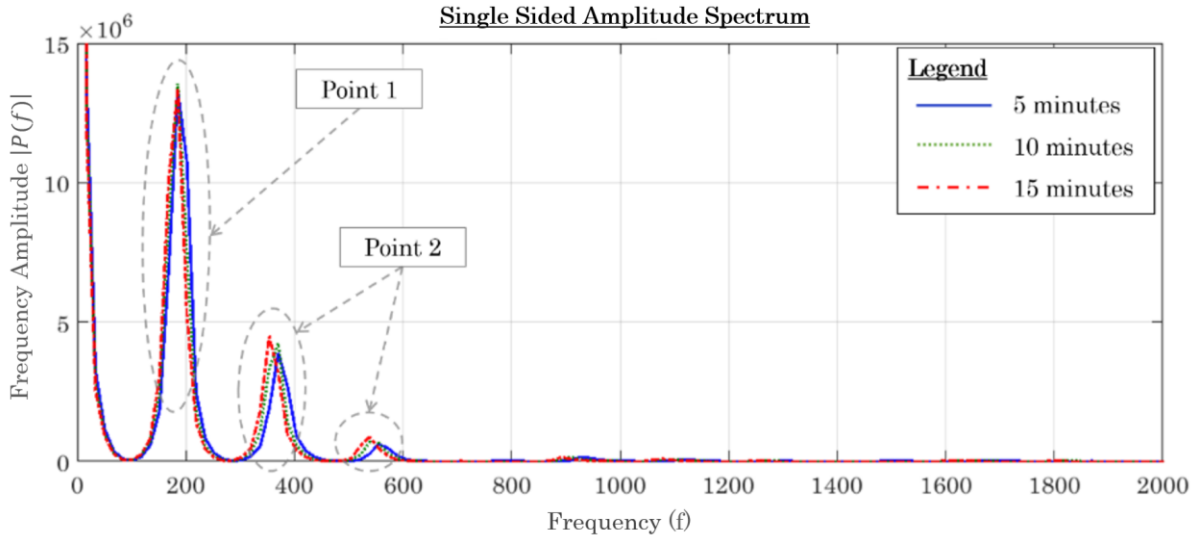


Figure 5.43: Amplitude spectrum of full 15hz period injection rate for different system temperatures on experimental scheme three. 2400bar pressure 2300µs duration injection condition.
Blue: 5 minutes from ambient.
Green: 10 minutes from ambient.
Red: 15 minutes from ambient.

The frequency resolution of the amplitude spectrum calculation was not sufficient to discern a difference in the primary rate tube resonant frequency, as highlighted by point 1 of Figure 5.43. There is, however, a significant difference in the first and second order harmonics for different temperatures, as shown in point 2 of Figure 5.43. These harmonics of the rate tube resonance have been identified in the quiescent period previously, in Figure 5.19, on experimental scheme one. Therefore, as SOS changes with system temperature for a fixed injection condition, there will be a corresponding shift in the frequencies observed in the quiescent period. Leading to changes in the zero value of the next injection event.

The implication of this meant that attaching the coriolis mass meter circuit resonates and introduces an additional frequency into the quiescent period. This

frequency then becomes a source of zero value variance driven by temperature. An effect that was not visibly present on the standard 2bar production system.

To reduce the impact of zero value variance in a 30bar regulated system, the frequencies observed because of rate tube resonance and its higher orders must be damped fully before the next injection event.

The focus of hydraulic optimisation activities during experimental scheme four was to satisfy objective one of the present work. This involved damping the dominant low frequency resonances observed at higher backpressures, as required to better represent the engine regime and suppress injector cavitation noise. The hydraulic optimisation activities are described in the following Section.

5.4 Optimised hydraulic configuration

The experimental work moved onto experimental scheme four, utilising the knowledge of the critical design criteria that influence zero value variance gained from experimental schemes one, two and three. The design optimisation target was to allow the fitment of a coriolis meter, with increased system backpressure, whilst also achieving less zero value variance than the standard 2bar production measurement system.

The previously used 1kHz maximum frequency resolution GEM sensors were replaced with 5kHz piezo resistive Kistler 4080A pressure sensors at various points in the hydraulic circuit. The arrangement of the additional sensors on the standard 2bar and experimental scheme three hydraulic circuit designs are shown in Figure 5.44.

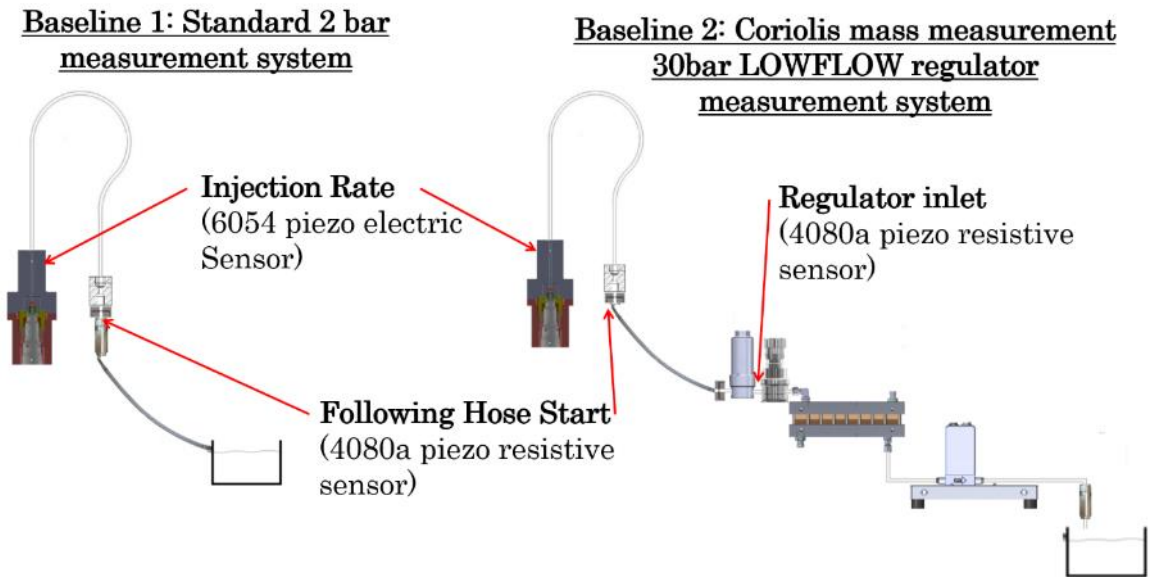


Figure 5.44: Additional pressure sensor instrumentation layout for. Left: (Baseline 1) Standard 2bar production measurement system. Right: (Baseline 2) experimental scheme three coriolis mass measurement 30bar LOWFLOW regulator measurement system.

This greater level of insight and quality of data acquired during experimental scheme four allowed sources of zero value variance, initially identified in previous experimental schemes, to be revisited in more detail. These sources of zero value variance were then minimised by empirically sweeping the design optimisation criteria discovered during experimental schemes one, two and three.

The transient production injector test cycles used on experimental scheme four collected data for >200 test conditions, under production injector test cycle running conditions. The following Section is focussed on the 2400bar pressure 2300µs duration injection condition evaluated in Schemes one and two. For this injection condition, injection rate and pressure traces for the full 15Hz firing period between injections are evaluated at the pressure sensor locations in the hydraulic circuit.

At the end of the empirical tuning exercise, a hydraulic circuit design that minimises zero value variance at all injection conditions studied was achieved. The optimised circuit design can be seen in Figure 5.45.

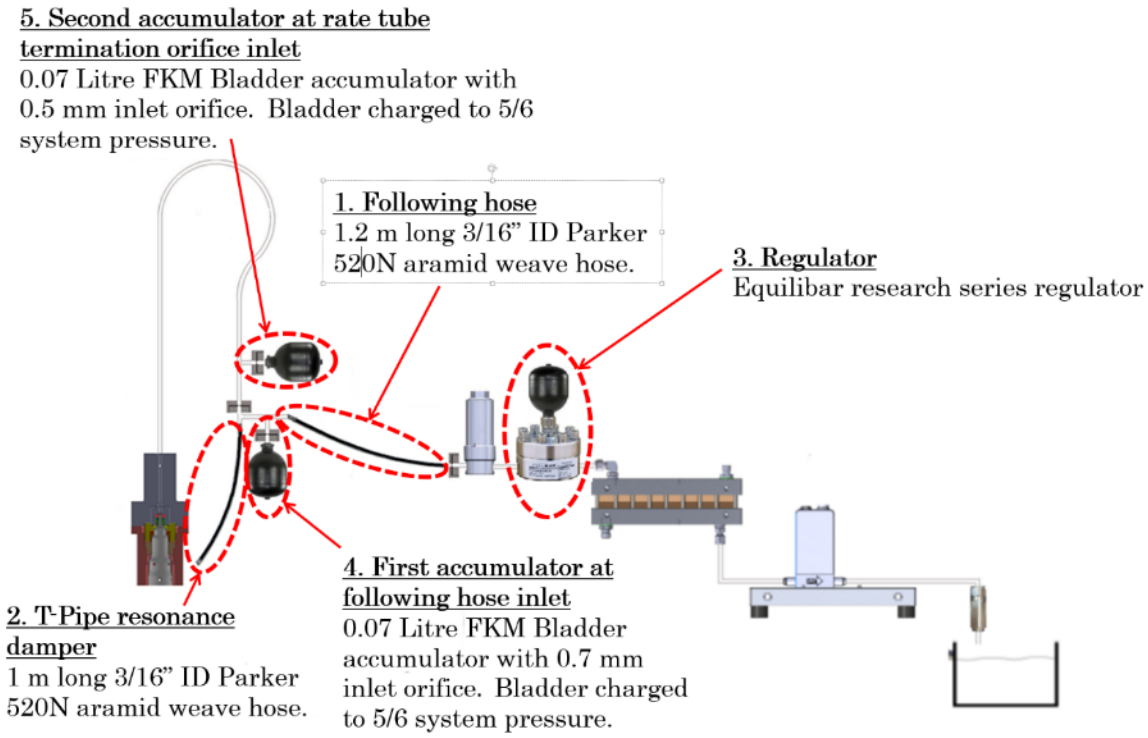


Figure 5.45: Optimised rate tube termination hydraulic design that minimises zero value variance.

The following Section describes the effect each design change has on the level and nature of zero value variance observed. For each design optimisation, the measurement circuit designs for the standard 2bar experimental scheme one and 30bar experimental scheme three circuit configuration baseline result to compare to.

The design aim was to achieve a zero value variance range of less than ±1mg/ms, which is what a standard 2bar measurement system achieves, whilst also allowing for increased back pressures and fitment of a coriolis meter.

5.4.1 Following hose length

It is known from the simulation work in Section 5.2.10 that the length of the following hose will change both the magnitude and frequencies observed when evaluating zero value variance. The length of the following hose will dictate its quarter wave resonant frequency and the transmission loss characteristic for a constant diameter. The frequencies observed during the quiescent period will also be dictated by temperature as discovered on experimental scheme three, discussed in Section 5.3.

The previous work evaluating the influence of following hose length carried out in model space had a fixed temperature for the entire measurement system. Whereas a real measurement system is constantly shedding heat to its

environment, which causes the end of the system to be cooler than the start where the hot injection occurs. This subsequently means that SOS is constantly changing throughout the length of the rate tube measurement system and would be difficult to simulate numerically. Therefore, to determine the optimal following hose length, it must be swept empirically under the transient injector test conditions that the measurement system will encounter in the production environment.

A trial was carried out where the hose length was swept from 3m down to 1m in 0.2m stages. The 1.2m length displayed the lowest range of zero value variance and is shown compared to the experimental scheme three baseline result in Figure 5.46.

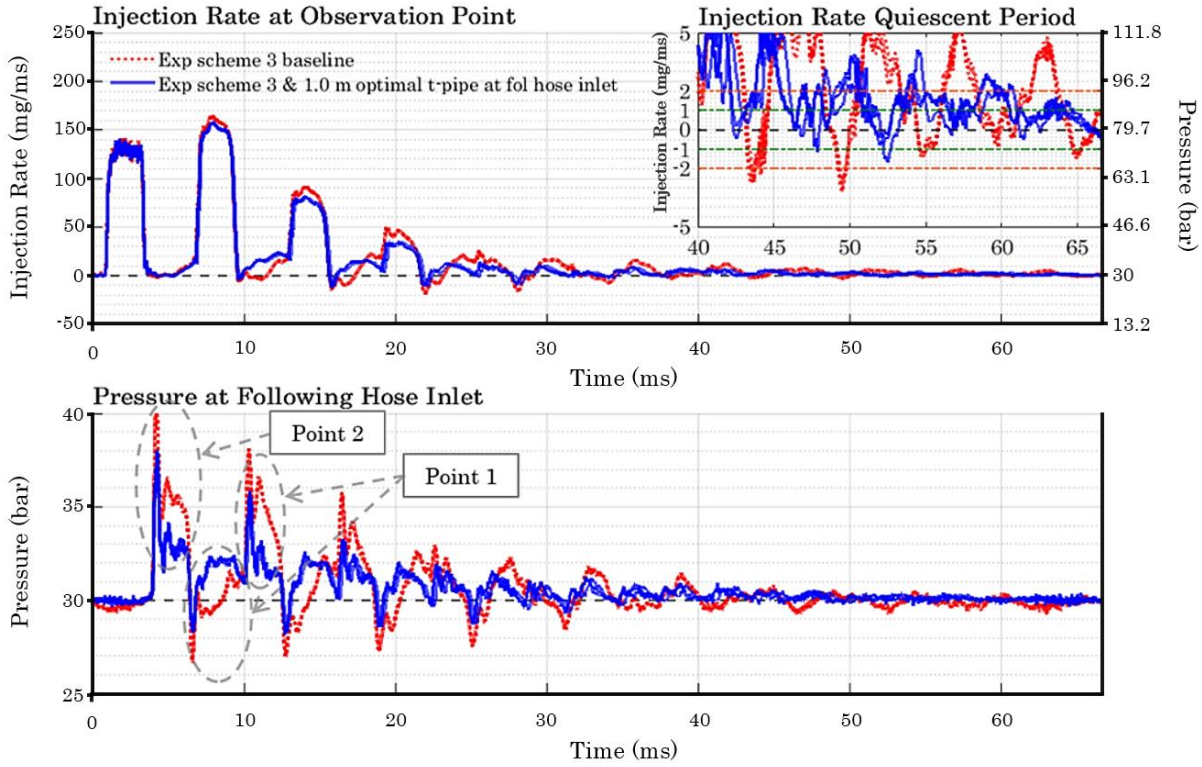


Figure 5.46: Following hose optimisation.
Blue: Experimental scheme three fitted with optimised 1.2m following hose length.
Red: Experimental scheme three fitted with baseline 1.8m following hose length.

There is a significant reduction in pressure wave magnitude after the first impulse into the following hose from the rate tube as highlighted by point 1 of Figure 5.46. The 1.2m length is significantly lower volume than the 1.8m hose length, which increases the magnitude of pressure wave activity observed within it, for the same level of excitation at its inlet.

It was observed during the empirical sweep that the degree of zero value variance is not linearly associated with hose length. As the length changes, the resonant modes of the following hose move in and out of frequencies that excite

the resonance of the 3m long rate tube. A length of either 1.6m or 3m both produce the highest levels of zero value variance. Which is to be expected as they are close to 1x and 0.5x the 3m rate tube length which would directly excite its resonant modes.

Based on the above result, it was determined that the 1.2m length was optimal for the following hose to minimise zero value variance on a 3m long rate tube when used with the transient production injector test conditions studied.

5.4.2 T-pipe resonant damper

A T-pipe is a form of resonant device used to attenuate a narrow frequency range in a hydraulic circuit that contains an input pulse at a specific frequency. They can often be found on hydraulic power lines, on equipment such as jackhammers, to reduce wear and vibration caused by pipe resonance (Ijas, 2007).

Their principle of operation uses the property of quarter wave resonance of a closed ended pipe length. The closed ended pipe will normally be connected at the point where resonant damping is desired. This pipe will then resonate according to its pipe length and SOS of fluid inside. If the T-pipe resonates out of phase with the input pressure pulse and existing resonant frequencies of the system, then it will act to dampen the magnitude of those frequencies as illustrated in Figure 5.47.

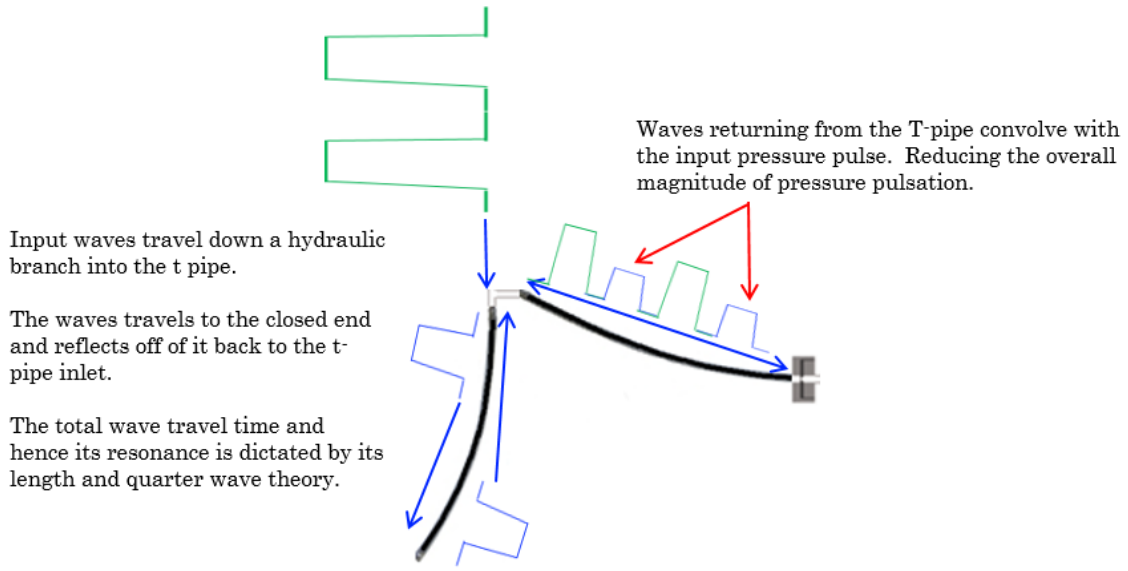


Figure 5.47: T-pipe installation and working principle schematic

A closed end T-pipe was attached to the following hose inlet on the 30bar coriolis meter hydraulic circuit from experimental scheme three. Its diameter and type was identical to the following hose.

The optimal quarter wavelength of the T-pipe should be the same as the optimal following hose length if the SOS inside of them are equal. The following hose also resonates with a quarter wave characteristic, as it has effectively closed pipe ends because of restrictions at its start and end. The optimal following hose and T-pipe length will be the one that dampens out the input pressure peaks and hydraulic resonances in the system via their quarter wave resonance characteristic. Hence the resonance and desired length of the T-pipe should be similar. It is known that the 1.2m following hose length is optimal. T-pipe length values that swept around this optimal target were selected for study. The following hose length remained fixed at 1.8m whilst the T-pipe length swept from 1.6m down to 0.6m in 0.1m steps. The amount of variance in the pressure wave magnitude during the quiescent period is then tested for each T-pipe length.

The 1.0m length displayed the lowest range of zero value variance and is shown compared to the experimental scheme three baseline result in Figure 5.48.

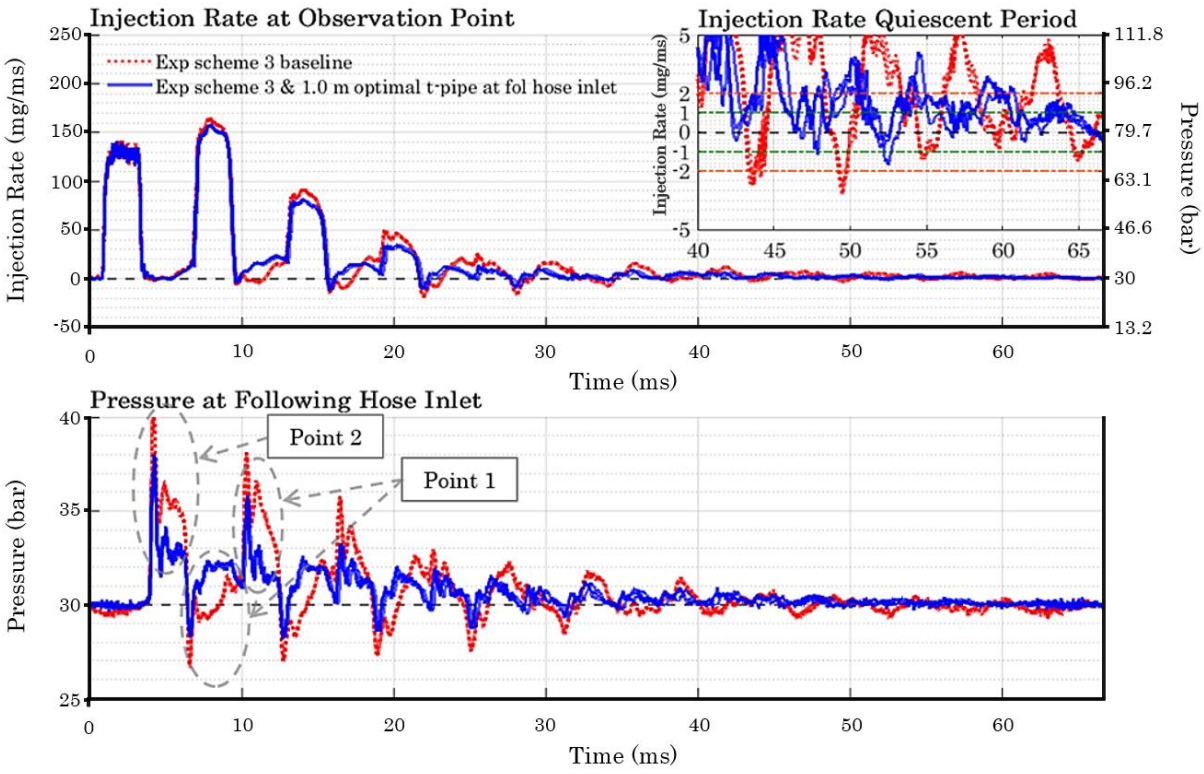


Figure 5.48: T-pipe optimisation.
Blue: Experimental scheme three with optimised 1.0m T-pipe at following hose inlet.
Red: Experimental scheme three baseline.

The reduction in frequency activity inside the following hose and at the regulator inlet is similar to the result achieved when using the optimal 1.2m following hose length, as highlighted by point 1 of Figure 5.48. Unlike the optimal following hose case, here is a reduction in the first input pressure pulse peak at the following hose inlet, as shown by point 2 of Figure 5.48. This is because half of

the input pressure pulse is now travelling down the T-pipe length and its magnitude is split between the following hose and T-pipe inlet areas.

It was expected that the T-pipe would have the same optimal length to the following hose, as their resonance is dictated by the same quarter wave principle. The T-pipe, however, is a tube with a dead end and hence effectively sees no hot fluid flow unlike the following hose that feeds the backpressure regulator. This means that the temperature in the T-pipe will be lower than in the following hose that feeds the backpressure regulator. It is known that speed of sound in ISO4113 test fluid will increase for an isobaric reduction in temperature (Bazile *et al.*, 2012). Hence, for a fixed system backpressure, a closed end T-pipe with colder stagnant fluid results in a faster SOS and higher resonant frequency value for the same length of following hose. Therefore, it can be expected that a T-pipe will require a shorter optimal length than the following hose due to these temperature differences.

This result demonstrated that the use of a T-pipe resonator is effective at reducing pulsation in the following hose when its length is targeted to counter the resonant frequencies of a rate tube. T-pipe and following hose both offer similar system optimisation outcomes. Therefore, their effect can be combined to further optimise the hydraulic circuit after the rate tube termination orifice. The use of a following hose and a T-pipe with optimal lengths will reduce frequency magnitudes in the following hose and therefore reduce the zero value variance sensitivity to changing system temperatures encountered during experimental scheme three.

5.4.3 Multiple orifice diaphragm regulator

On experimental scheme one, it was observed that different regulators produced significantly different zero value variance characteristics during the quiescent period of the injection rate signal. In model space, on experimental scheme two, it was ascertained that an ideal regulator must have zero leakage across its seat, or it may behave like a fixed restriction. This is why a LOWFLOW© spring backed pilot operated regulator, specialised for low flow rate applications, had been selected for production use on experimental scheme three.

The configuration of experimental scheme four allowed for the use of nitrogen backed, diaphragm based, dome loader backpressure regulators. A research series Equilibar© backpressure regulator (Barree, 1989) selected for this application was trialled. Its performance was then compared to the 30 bar coriolis meter experimental scheme three baseline result with the LOWFLOW© regulator, shown in Figure 5.49.

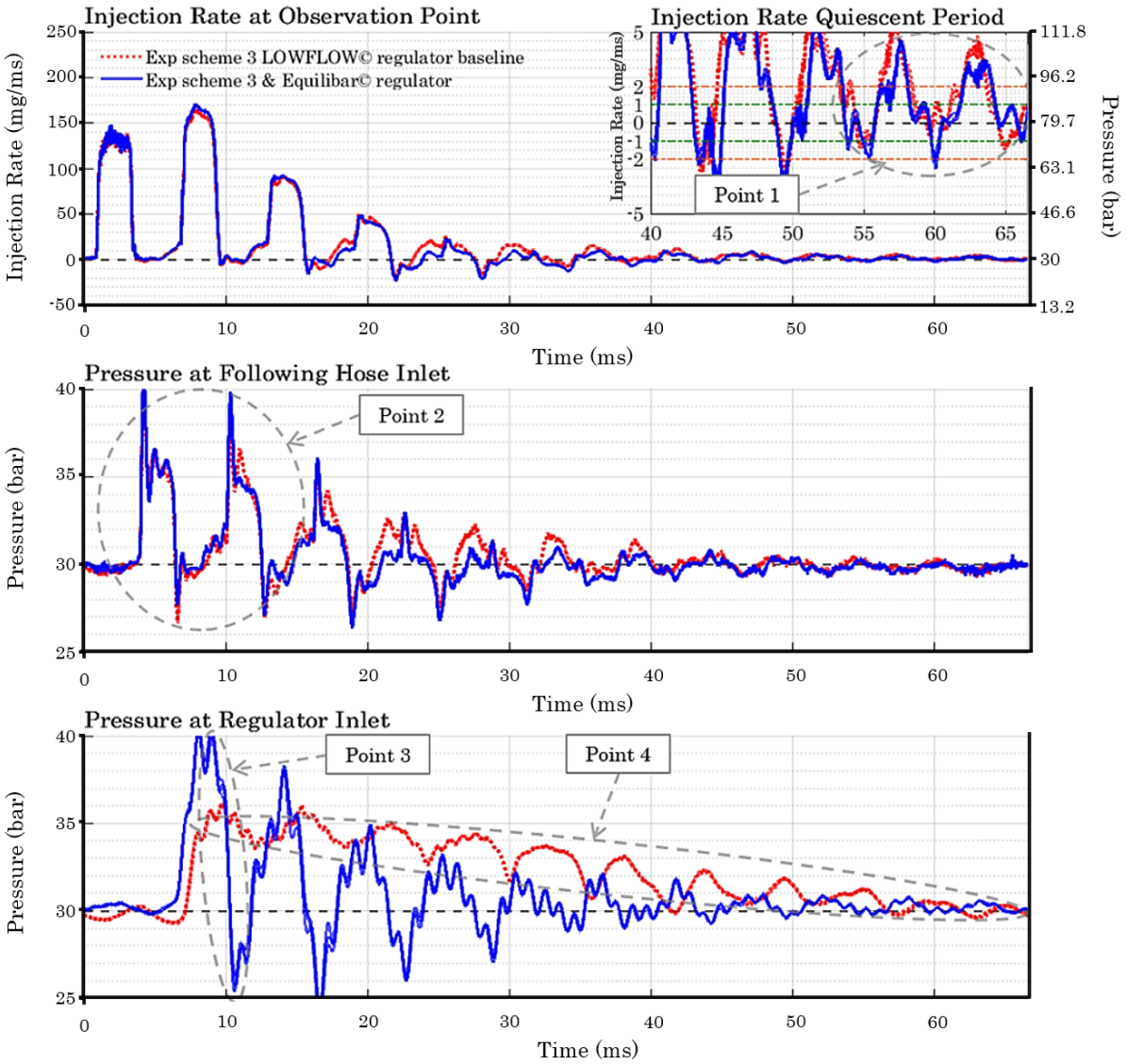


Figure 5.49: Single vs multiple flow orifice regulator comparison.
Blue: Experimental scheme three fitted with Equilibar© multiple flow orifice regulator.
Red: Experimental scheme three LOWFLOW© single flow orifice regulator baseline.

The Equilibar© regulator has similar frequency values and magnitude in the quiescent period as the LOWFLOW© regulator as highlighted by point 1 in Figure 5.49. These frequencies are due to the following hose wave activity and not the regulator characteristic as discussed in Section 5.2.10. This is further demonstrated by the frequency activity at the following hose inlet matches closely for the two results as highlighted by point 2 of Figure 5.49.

Both the LOWFLOW© and Equilibar© regulators met the requirement of stable backpressure and zero leakage at the smallest 20mg/sec flow rates encountered during a production injector test. Unlike the large flow area leaking ARO® regulator, studied in Section 5.2.12.

The fundamental difference in behaviour is that the Equilibar© regulator returns to its backpressure set point much faster than the LOWFLOW©, as highlighted by point 3 of Figure 5.49. This means that the fast response of the Equilibar© regulator does not superimpose a trend on the system backpressure, as is the case with the LOWFLOW© regulator. This decaying pressure trend can still be observed during the quiescent period for the LOWFLOW© regulator case, as highlighted by point 4 of Figure 5.49. An ARO® regulator model was forced to behave like a fixed restriction due to leakage and displayed a similar decaying simulated pressure trend as shown in Figure 5.41 of Section 5.2.12. In this case, the LOWFLOW© regulator behaves like a fixed restriction, because it uses a single, zero leakage, small internal flow orifice unable to release enough mass flow in time to drop pressure back to baseline before the next injection event.

The Equilibar© regulator is able to respond faster to the input pressure pulse due to its progressively revealed orifice design, as shown in Figure 5.50. This multiple orifice, diaphragm sealed design differs significantly from the traditional single orifice poppet seal style regulator such as the LOWFLOW©. The Equilibar© regulator relies on a progression of internal orifices that open up in line with deflection of its diaphragm. The diaphragm deflection changes according to the pressure at its inlet. So as a large pressure input is sensed by the diaphragm, the more it deflects, revealing more flow area and the pressure drops back to the set point rapidly after the input pressure decays. With a traditional regulator design, the flow and time taken to return to the set point pressure is dictated by a single orifice flow area.

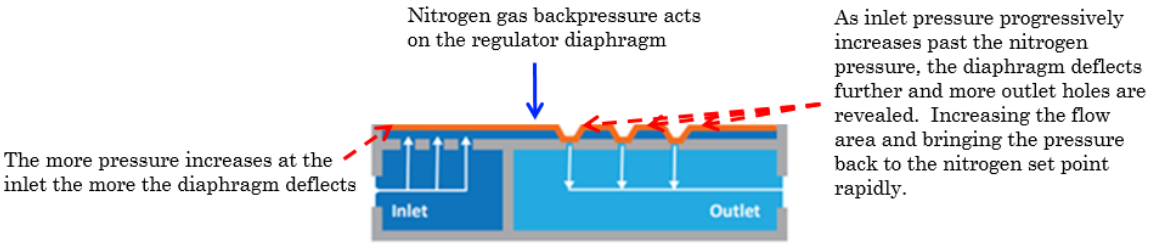


Figure 5.50: Equilibar© research series backpressure regulator principle of operation.

Therefore, when a traditional regulator with a singular restrictive flow area is used, there may be a decaying trend in the system backpressure that gets superimposed on top of the zero value during the quiescent period. The author is not aware of any literature that discusses the influence of this pressure decay on zero value variance observed. The time required to decay back to baseline is a production test cycle time limitation, as it limits the injection event firing rate. If the regulator takes longer to drain the pressure, then the firing rate must be reduced to allow more time for quiescent pressure to be achieved in the rate tube. Hence, most experimental studies ignore this issue of non-ideal regulator characteristics by reducing the firing rate.

If the oscillation in the following hose can be dampened, then so will the zero value variance observed during the quiescent period in the injection rate. If using the Equilibar© regulator, it subsequently removes a decaying trend during quiescence. A regulator that can respond quickly enough to fast pressure inputs should stop trends appearing in the injection rate baseline, and this suggests the Equilibar© is best suited for this application.

5.4.4 First following hose accumulator

Accumulators are often found in hydraulic systems to dampen impulsive flow inputs to preserve hydraulic system component life (Yu *et al.*, 1999; Ijas, 2007). The input into the rate tube injection meter can be thought of as a square wave pressure impulse at the 15Hz injected mass firing rate. If a hydraulic accumulator is fitted to the system, then it should dampen out a wide range of frequency activity. It is known, from work carried out in simulation space that a high degree of zero value variance is linked to frequency activity inside the hydraulic circuit after the rate tube termination orifice. If an accumulator volume is placed at the inlet to the following hose, it should reduce frequency activity within it and hence lower the amount of zero value variance observed in the injection rate measurement.

The smallest sized commercially available accumulator of 0.07L capacity was attached to the following hose inlet after the rate tube termination orifice, as shown in Figure 5.51. This size was selected because of the low ~0.02L volume of the rate tube measurement system.

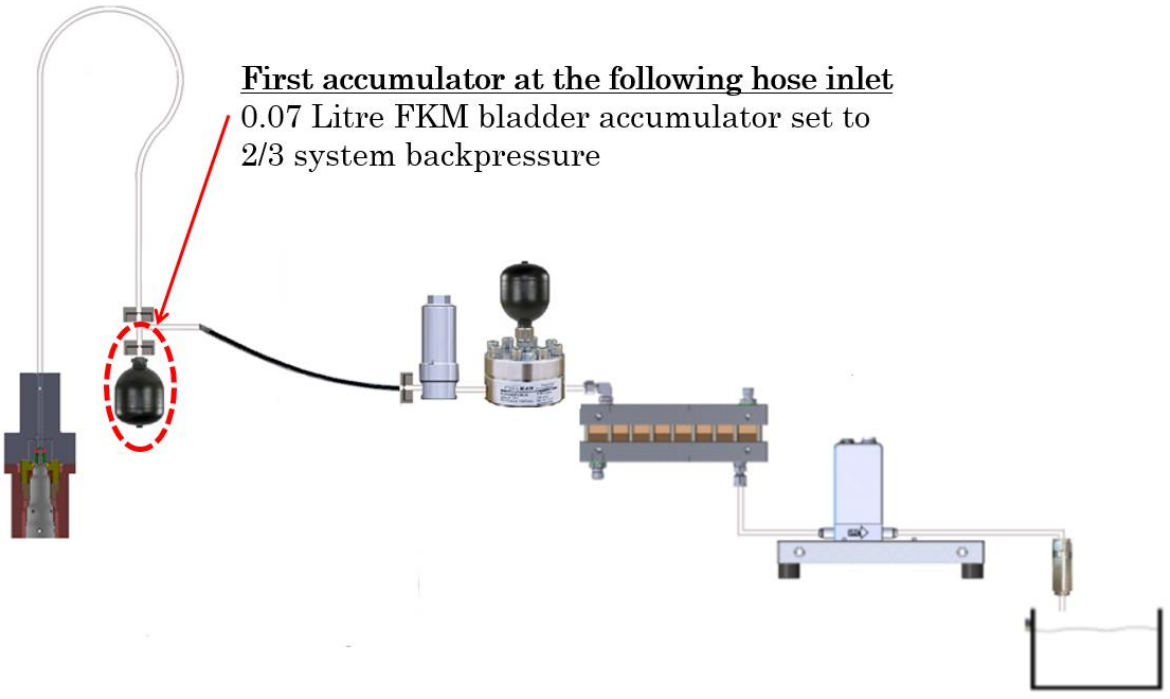


Figure 5.51: Schematic diagram of accumulator placement in system.

The Equilibar© was fitted to the experimental scheme three, to provide a comparative result without the decaying pressure trend caused by the LOWFLOW© regulator flow restriction.

Initially, the accumulator was fitted without an inlet orifice, the resulting injection rate and following hose pressure is shown in Figure 5.52.

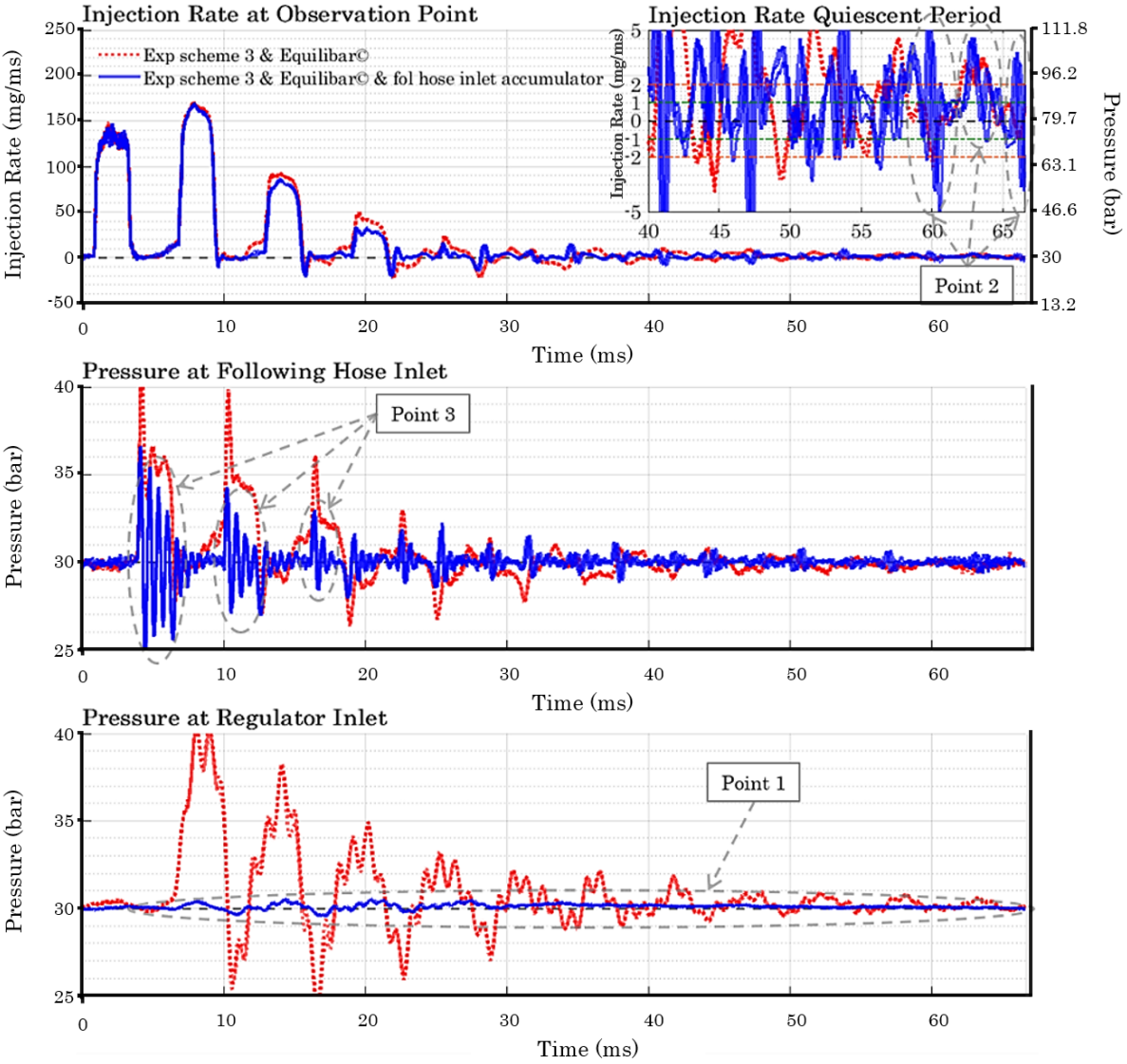


Figure 5.52: Effect of placing an 0.07L accumulator at the following hose inlet. Blue: Experimental scheme three fitted with Equilibar© regulator and 0.07L accumulator at the following hose inlet. Red: Experimental scheme three fitted with Equilibar© regulator.

When an accumulator is fitted to the following hose inlet, a significant amount of low frequency damping is evident, with little deviation from baseline backpressure at the regulator inlet, as highlighted by point 1 of Figure 5.52.

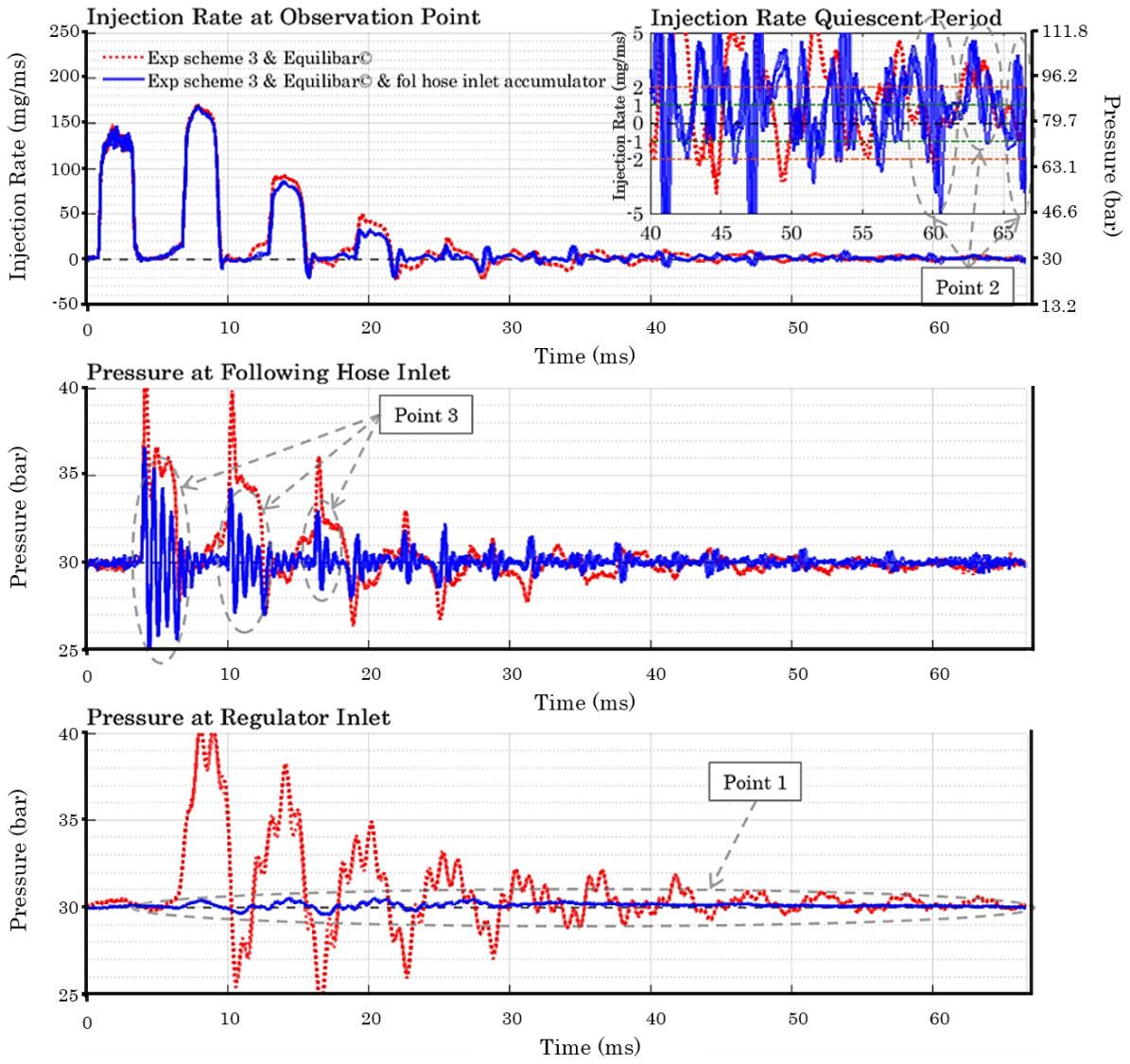


Figure 5.52. With the accumulator fitted, the magnitude of frequency activity during the quiescent period exceeds the ±1mg/ms threshold where the repeatability of injected mass measurement will be negatively affected, as shown by point 2 of Figure 5.52.

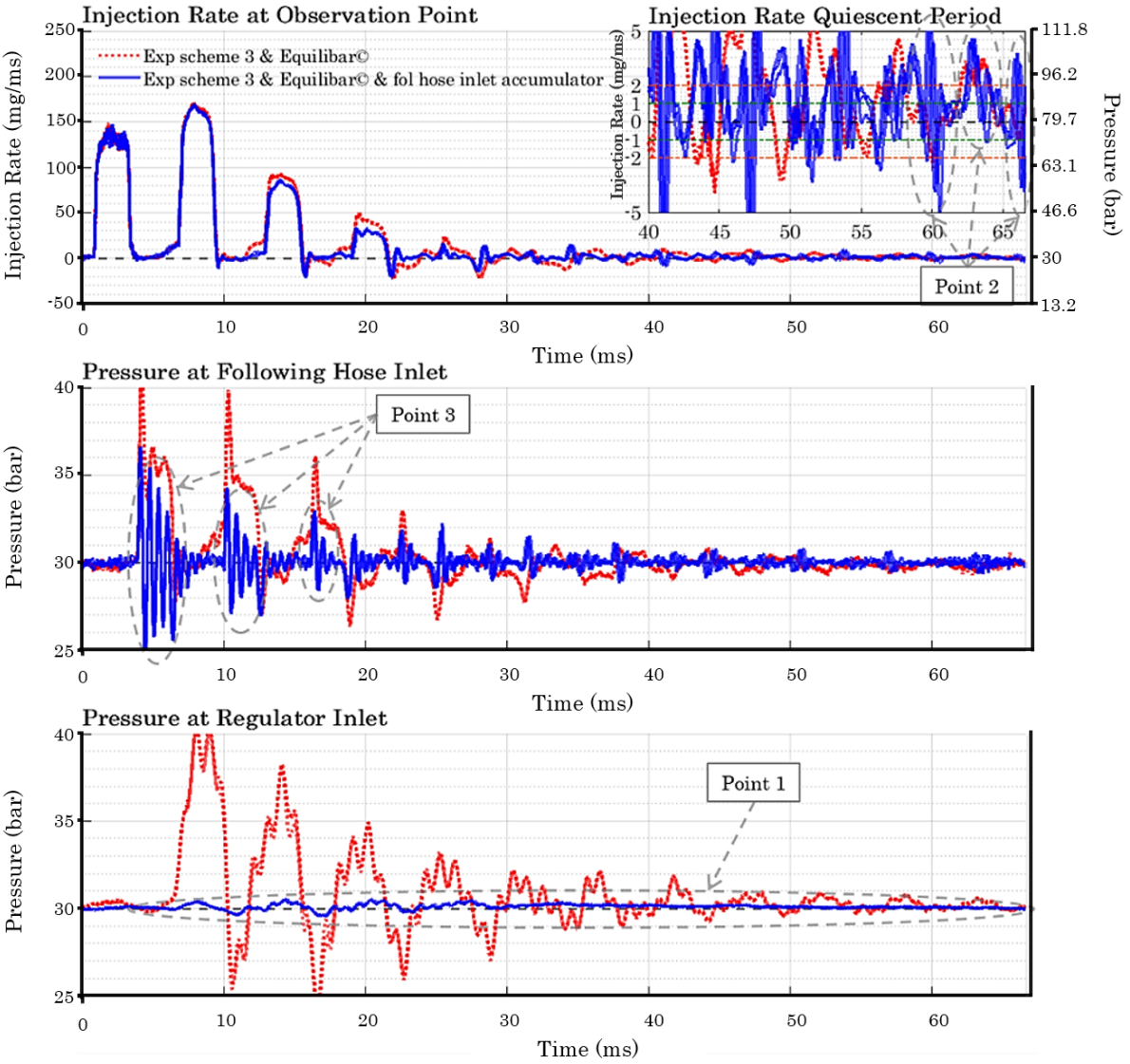


Figure 5.52. This frequency activity is apparent on the hose inlet pressure, and appears to be coming from the fitment of the accumulator, as shown by point 3 of Figure 5.52.

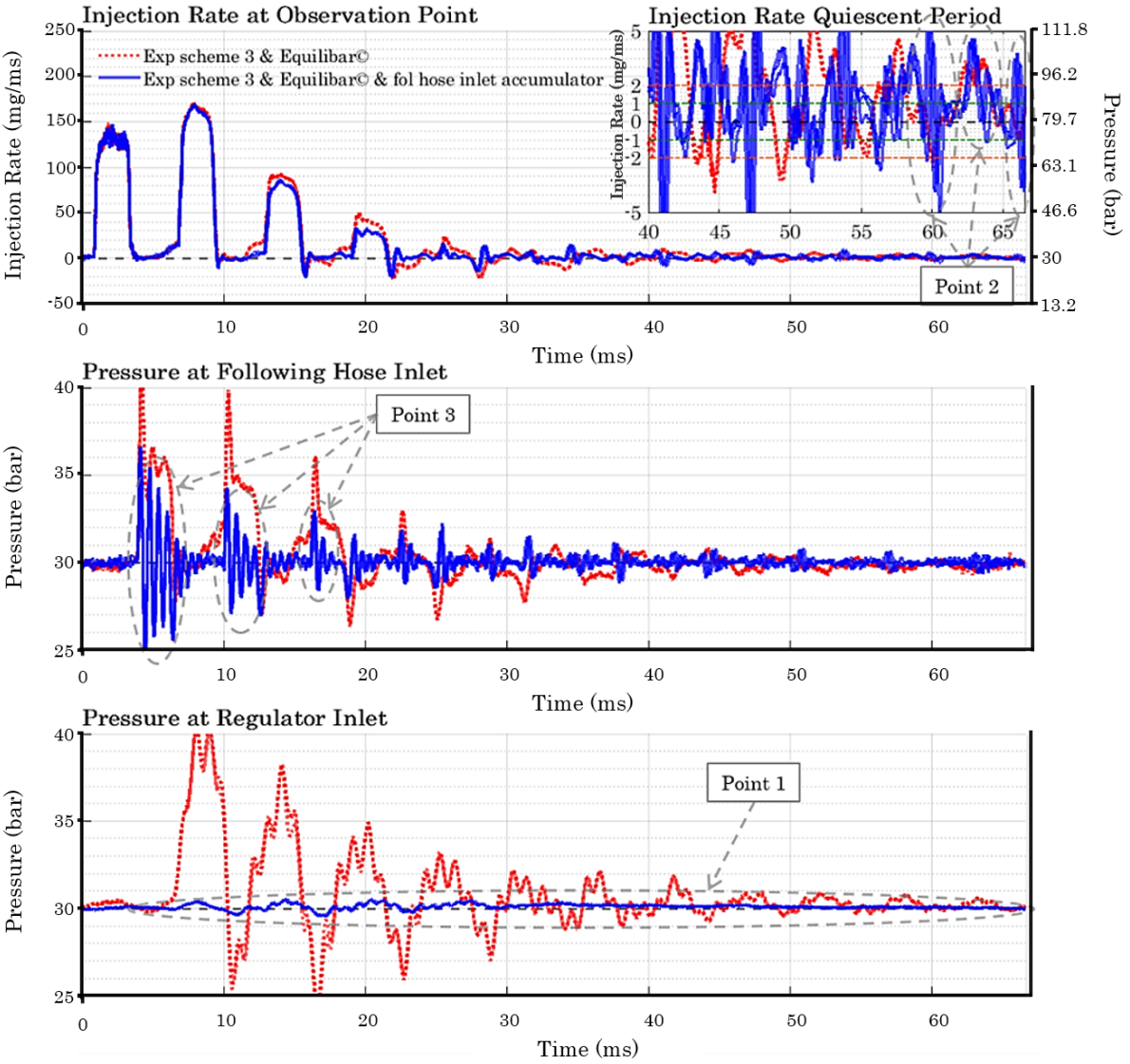


Figure 5.52. This additional high frequency activity can be observed during the quiescent period as a superposition of waves originating at the accumulator and reflecting off the following hose inlet and outlet orifices. Hence, the fitment of an accumulator will change the nature of zero value frequency observed, but will not help meet the ±1mg/ms pressure variance target, established for the quiescent period before the next injection event. Whilst this would be acceptable to maintain a stable average baseline pressure in a simple industrial hydraulic power circuit, it is not appropriate when high frequency measurements are taking place.

These frequencies are not present when the accumulator is not fitted to the system. They begin when the first pressure wave caused by the injection event arrives at the tube termination and excites the following hose inlet. Therefore, they must be a product of the hydraulic resonance of the accumulator fluid volume. The accumulator will act like a Helmholtz resonator with its inlet being

the neck of the resonator and the fluid volume around the nitrogen bladder forming the resonant chamber.

An inlet orifice was fitted to the accumulator to reduce the influence of any resonant frequencies caused by its hydraulic geometry. Inlet orifice size was swept from 0.5mm to 1.0mm in 0.1mm steps. The optimum result in terms of zero value variance was a 0.7mm inlet orifice and is shown in Figure 5.53.

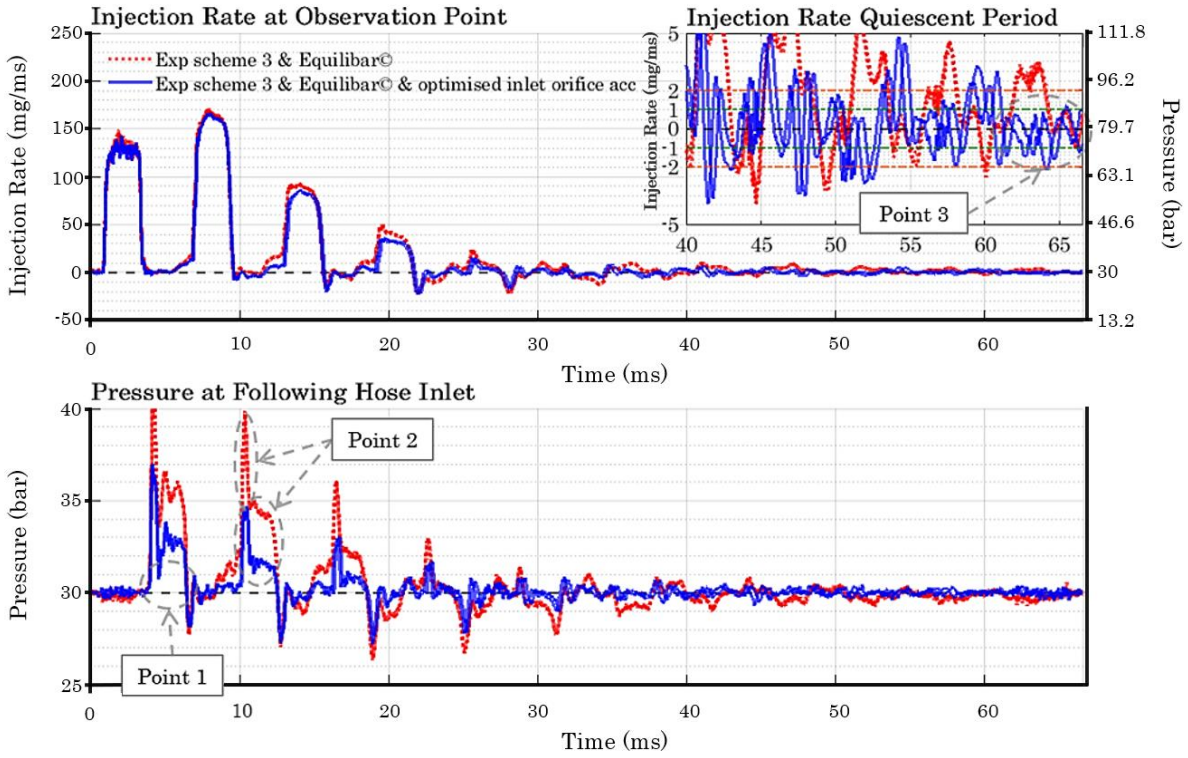


Figure 5.53: Effect of placing a 0.7mm orifice inlet restricted 0.07L accumulator at the following hose inlet.
Blue: Experimental scheme three fitted with Equilibar© regulator and 0.07L accumulator at the following hose inlet.
Red: Experimental scheme three fitted with Equilibar© regulator.

The high frequency ringing caused by adding an accumulator to the following hose inlet is removed by adding an orifice to its inlet as highlighted in point 1 of Figure 5.53.

Despite the accumulator's response to changing pressure constrained by an inlet orifice, it dampened frequency activity magnitude in the following hose by a factor of approximately 50% as highlighted by point 2 of Figure 5.53. The accumulator appears to be having a scaling effect on pressure magnitude inside the following hose. The result of which being quiescent pressure is achieved before the next injection event, as highlighted by point 3 of Figure 5.53.

The magnitude of damping depends on the hydraulic volume of the accumulator and the size of its inlet orifice. An accumulator inlet orifice size greater than 0.7mm on a 0.07L accumulator resulted in the reintroduction of resonant activity during the quiescent period. The size of inlet orifice must be carefully selected to achieve the desired low frequency damping characteristic, whilst also preventing introducing the resonant frequencies of the accumulator into the hydraulic system.

This result demonstrates that fitting a low volume accumulator, fitted with an appropriate inlet orifice immediately after the tube termination, will significantly reduce frequency activity magnitude in the following hose internal volume. In turn reducing frequency magnitude during the quiescent period inside the rate tube that gives rise to temperature linked zero variance as discovered on experimental scheme three.

As the effect of the accumulator is that of magnitude scaling, its mechanism of damping is separate to the targeted quarter wave damping mechanism of the following hose and T-pipe length optimisation. Therefore, an accumulator can be used in parallel with other hydraulic system design optimisations that have already been explored on experimental scheme four.

Whilst accumulators have been used in other rate measurement system designs before (Menucci, 2018; Ferrari and Zhang, 2019), no mention has been found regards the consequence of introducing an unrestricted volume to the existing hydraulic circuit that may have its own resonance. Hence the requirement to use an empirically selected orifice on a low volume accumulator is new knowledge in the field and a significant result.

5.4.5 Second rate tube accumulator

The first accumulator trialled was placed at the following hose inlet after the rate tube termination orifice, dampening frequency magnitudes present within the following hose volume. If frequency activity inside the rate tube volume before its termination orifice can also be dampened, then quiescent condition can be achieved earlier and hence the injection firing rate increased above the 15Hz. An increase in firing rate was one of the commercial objectives of the present work, to reduce production cycle times. An attempt was made to dampen frequencies in the rate tube volume by fitting a second accumulator before the tube termination orifice, as shown in Figure 5.54. This was carried out with all the previous design optimisations applied so that frequency activity after the rate tube termination would have minimal influence.

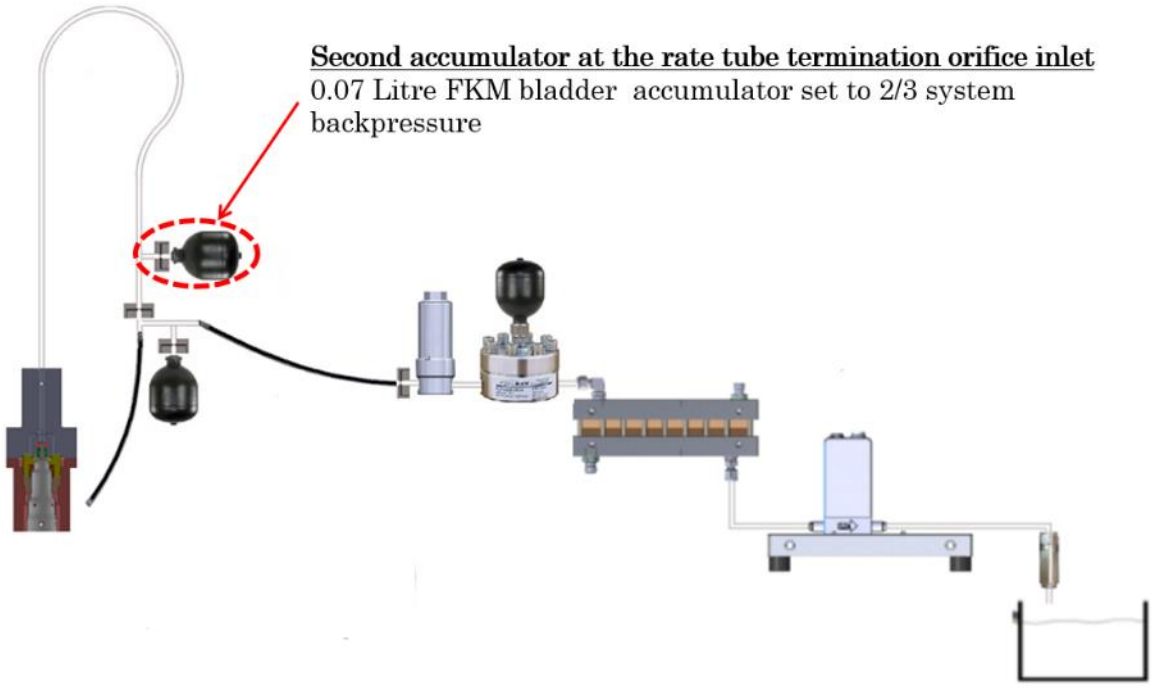


Figure 5.54: Schematic of second accumulator at the rate tube termination orifice inlet.

A second accumulator cannot be fitted to the rate tube inlet near the injection event because it would negatively impact the observed pressure wave used to derive injected mass flow during the period of the measurement window as shown in Figure 5.1. By placing the second accumulator at the inlet of the rate tube termination orifice, it will act to dampen the reflected waves that arrive at the tube termination orifice. This is after the initial injection event measurement window has ended and so will not interfere with the injected mass measurement.

The smallest machine able inlet restriction size of 0.5mm diameter was chosen for the inlet of the second-rate tube accumulator. An orifice diameter of greater than 0.5mm produced high frequency artefacts during the quiescent period that are related to the accumulator resonant hydraulic volume.

As expected, the time to reach quiescence is significantly reduced when a second accumulator is fitted to the rate tube termination as shown in Figure 5.55. Instead of four reflected waves to quiescence there are only two with the rate tube accumulator fitted, as shown by point 1 of Figure 5.55.

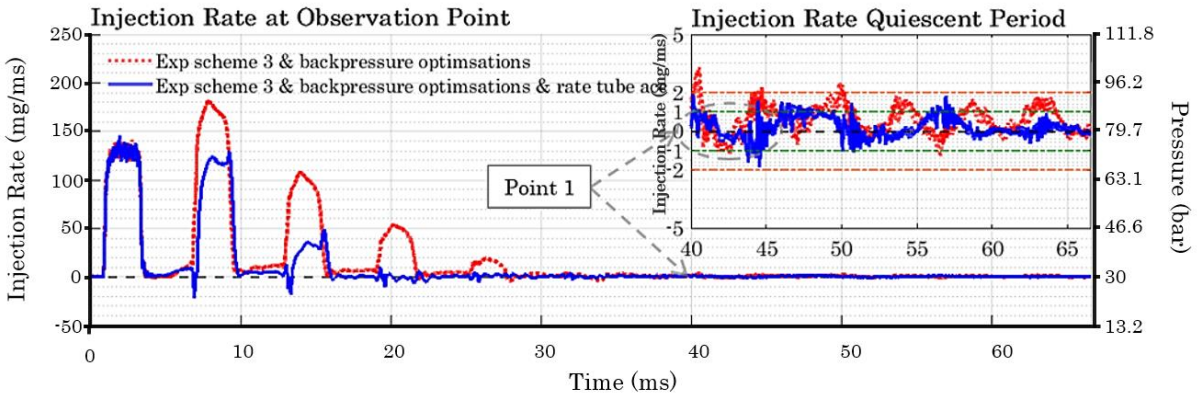


Figure 5.55: Effect of placing a 0.5mm orifice inlet restricted 0.07L accumulator at the rate tube termination orifice inlet.
Blue: Experimental scheme three fitted with backpressure system design optimisations and 0.5mm inlet restricted accumulator at the rate tube termination orifice inlet.
Red: Experimental scheme three fitted with backpressure system design optimisations and no accumulator in the rate tube volume.

Quiescent pressure conditions are achieved in the rate tube by 44ms or a firing rate of 25Hz as highlighted by point 1 of Figure 5.55. This is an important commercial outcome, as it is 66% faster than the current firing rate of the standard 2bar production measurement system. This brings the theoretical firing rate of a rate tube measurement system close to that of other commercial devices discussed in the literature review Section 2.2.2. The additional accumulator can therefore overcome the primary weaknesses of a rate tube injection meter, it's comparatively long cycle times.

5.4.6 Optimised hydraulic design vs experimental scheme 3

The hydraulic circuit design employed for experimental scheme three had a zero value variance sensitivity linked to temperature, as discussed in Section 5.3. It is known from simulation space that the source of the zero value variance observed was from frequency activity inside the hydraulic circuit after the rate tube termination orifice. The aim of this optimised hydraulic design was to eliminate the zero value variance sensitivity to temperature by damping out the resonant frequencies that cause it. A secondary commercial aim was to achieve a stable zero value in a shorter time, so that the measurement system firing rate can be increased and cycle time reduced.

The optimised hydraulic design for minimising zero value variance was based on experimental scheme three, with the following optimal system design parameters identified as a 1.2m following hose length, 1m T-pipe length, Equilibar© regulator, 0.07L accumulator with a 0.7mm diameter inlet orifice at the following hose inlet, and a second 0.07L accumulator with a 0.5mm diameter inlet orifice at the rate tube termination orifice inlet.

The hose length and T-pipe tuned lengths reduce the excitation of specific resonant frequency magnitudes in the following hose that area known driver of zero value variance. The Equilibar© regulator removes the issue of regulator flow restriction, which causes a decaying zero value trend that limits firing rate and cycle time. The inlet restricted accumulators in the following hose and rate tube volumes both act to reduce the overall magnitude of frequency activity in the system.

The optimised hydraulic design was compared to the measurement system design from experimental scheme three, and the result is shown in Figure 5.56.

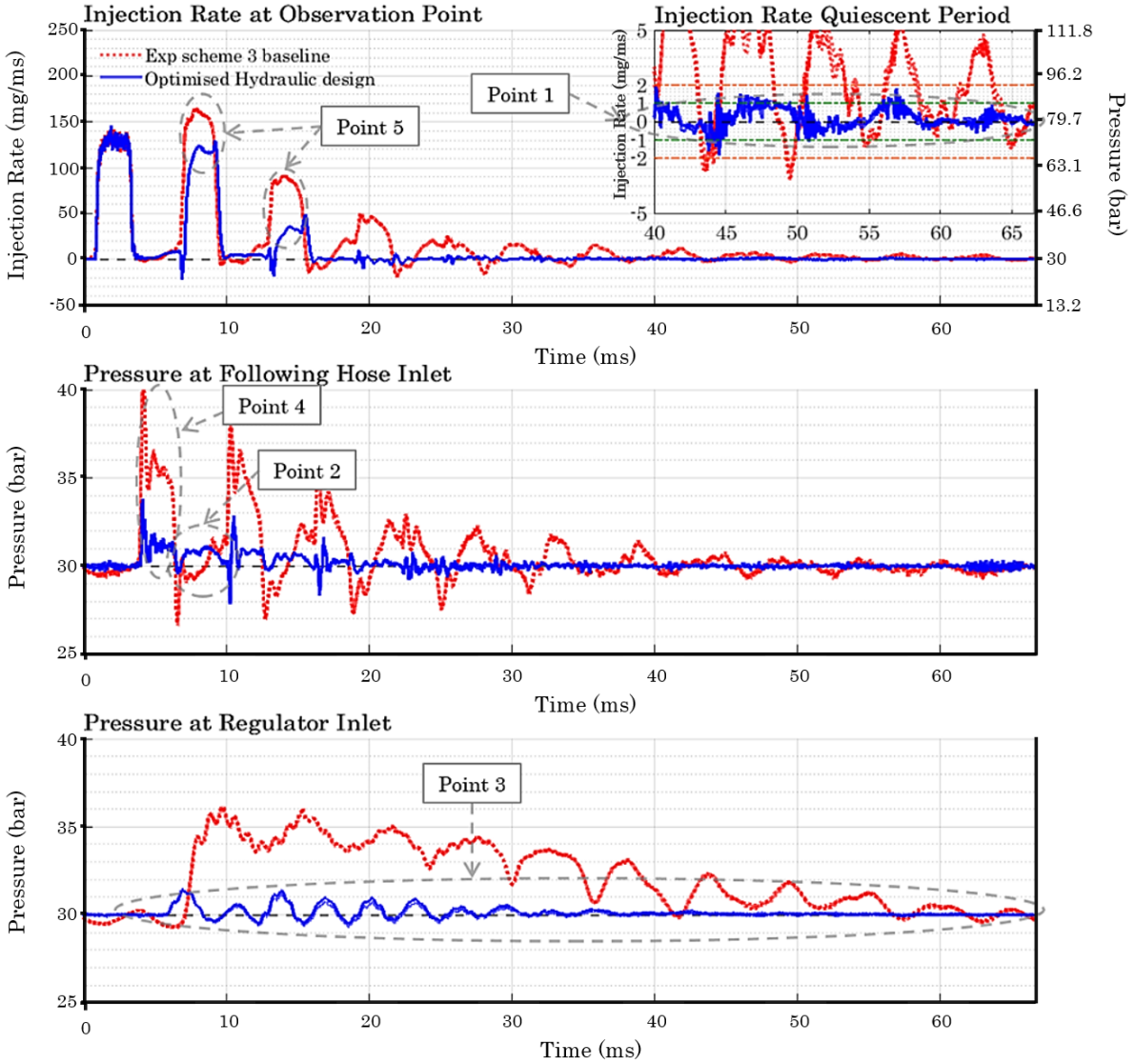


Figure 5.56: Result of all hydraulic design optimisations combined.
Blue: Optimised hydraulic design.
Red: Experimental scheme three baseline

With the optimised hydraulic design, the target of ±1mg/ms during the quiescent period is achieved, as shown by point 1 of Figure 5.56. This targeted resonant

damping characteristic of the following hose and T-pipe lengths is shown by point 2 of Figure 5.56. The baseline backpressure has no trend because of the proportional response of the Equilibar® regulator, as shown by point 3 of Figure 5.56. The reduction in pressure magnitude at the following hose inlet due to the first accumulator is shown by point 4 of Figure 5.56. The damping of reflected waves in the rate tube volume by the second rate tube accumulator achieves quiescence in a time that would allow a 66% increase in injected mass firing rate, as shown in point 5 of Figure 5.56.

Therefore, the optimised hydraulic design fulfils research objective one by minimising a known form of measurement system variance. It also fulfils the commercial objective of increasing the injected mass firing rate to bring it in line with the firing rates of other commercially available systems (Gandhi, Meinhart and Ortiz, 2009; Perna, Baraldi and Gregori, 2012; Hogg *et al.*, 2020). To understand the impact that the increased system backpressure would have on another source of measurement variance, high frequency cavitation is examined at different back pressures in the next chapter.

6 High Frequency Variance

In the previous chapter it was demonstrated that low frequency pressure wave resonance, that originates from the rate tube termination can impact measurement variance. That analysis was limited to frequencies below 1kHz and evaluated the entire 15Hz period between injection events. This chapter instead focusses on high frequency activity >10kHz that occurs during the injection event flow rate measurement window, as shown in Figure 6.1.

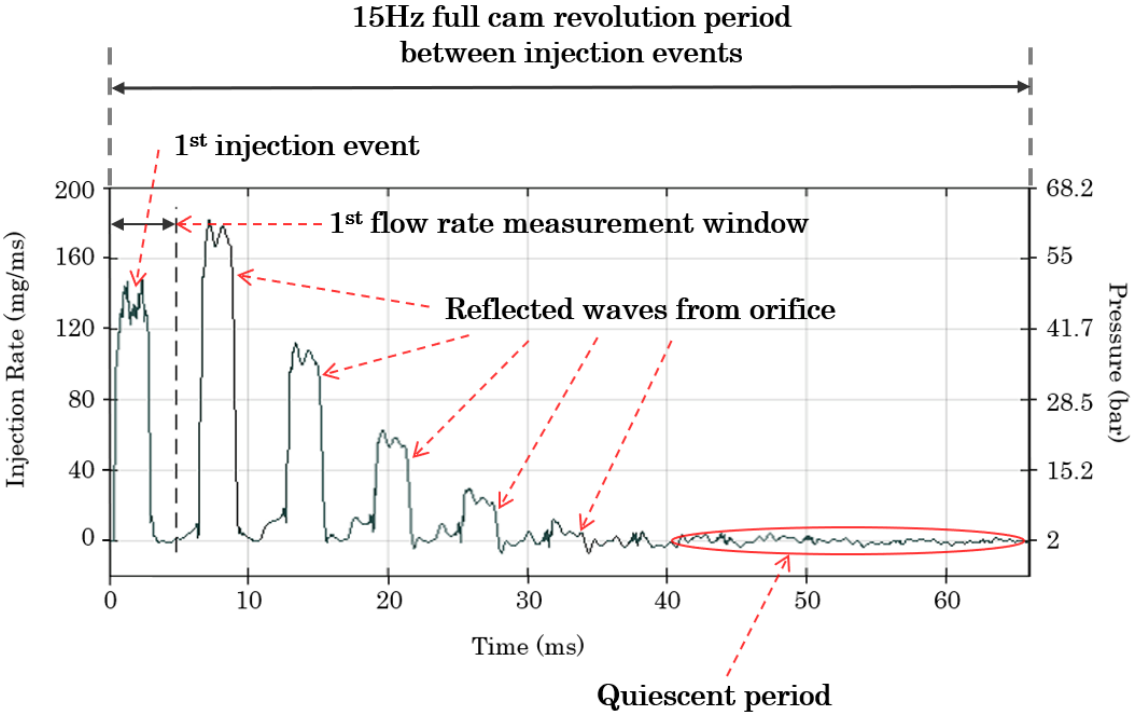


Figure 6.1: The injected mass flow rate measurement window period.

The location of this high frequency activity inside the injection rate measurement window is illustrated for a 2400bar pressure 2300µs duration original unfiltered injection rate signal, shown in Figure 6.2.

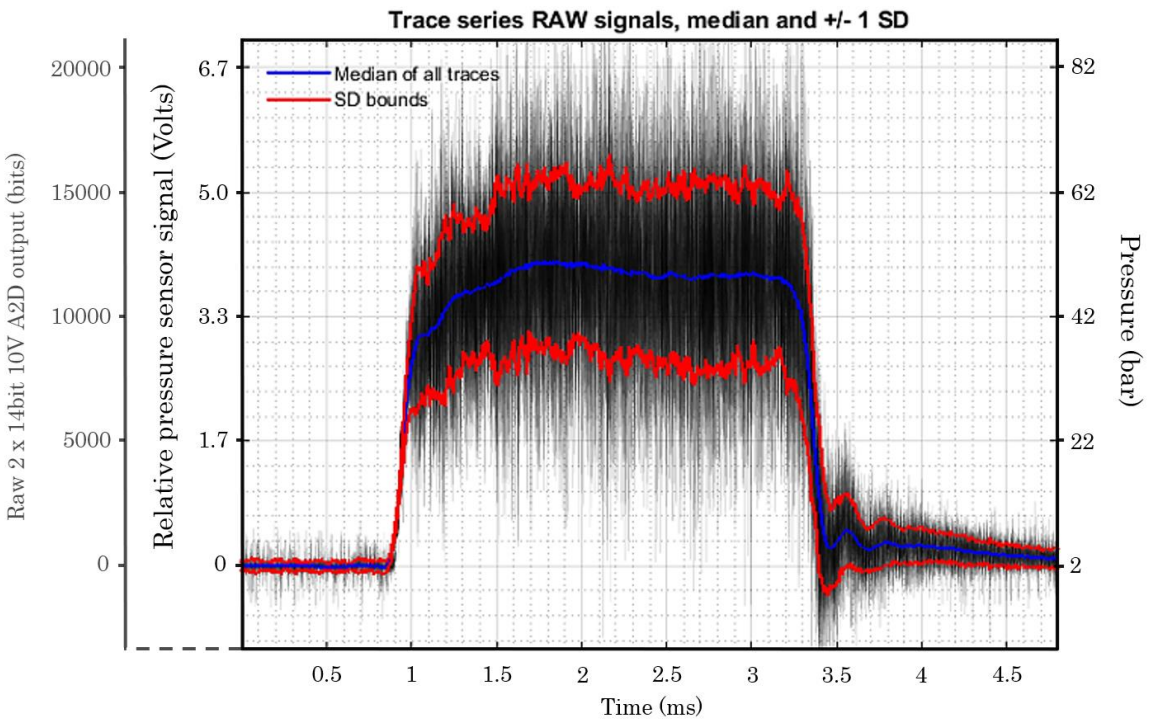


Figure 6.2: RAW original injection rate signal illustrated.
2400bar pressure 2300µs duration injection condition.
±1 standard deviation bounds in red for 5 separate events.

High pressure diesel sprays have been shown to improve mixing within the engine cylinder. The result of this is improved combustion efficiency and lower soot formation because of increased turbulence and atomisation of the spray. The turbulence is driven in part by cavitation in the nozzle holes formed at high injection pressures, as characterised by Dembinski, Angstrom and Winklhofer (2014). The improved hydraulic efficiency of the latest generation of diesel injectors makes high pressures up to 3600bar feasible for multiple injection strategies (Hardy *et al.*, 2012). High injection pressure can result in shock-waves due to cavitation collapse, within the fluid medium of an injection rate measurement system, as observed using a transparent fluid filled Zeuch based measurement device by Pearce, Hardalupas and Taylor (2016).

This Chapter is split into 5 investigations to analyse high frequency signal noise variance. First a discussion of potential sources of high frequency content in an injection rate signal on experimental scheme 3, are discussed in Section 6.1.1. Then the interaction of high frequency cavitation activity with the injection rate sensor and its port geometry is identified in Sections 6.1.2 and 6.1.3. The influence of pressure sensor signal amplifier and its characteristics that can cause measurement variance, by distorting this high frequency activity, is presented in Section 6.2.1. Finally, a demonstration of cepstrum analysis approach to identify previously hidden periodically occurring high frequency electrical signal noise, is presented in Section 6.2.2.

6.1 Characterisation of hydraulic sources of high frequency variance

This section details the characterisation of high frequency activity present in the injection rate signal, during the measurement window period. There are few studies exploring frequencies present in a rate tube injection meter. One prominent study was carried out by Manin, Kastengren and Payri (2012) and explored frequencies up to 2.5kHz. They focussed on 'the pressure waves travelling inside the injector and/or by an axial displacement of the injector itself' within its fixture. Through previous studies of injector test hardware at Delphi Technologies, it is known that the injector does not oscillate within the injector nozzle fixture design used for this investigation and so was not of interest.

When laser doppler-vibrometry was used by Crua and Heikal (2014) to characterise a 1600bar diesel injection spray event into gas, they demonstrated resonant bands were present up to 50kHz. To fully characterise the high frequency content present in a high pressure diesel injection spray event, frequency activity between 0-50kHz must be characterised without distortion.

To enable this investigation into frequency activity in the kHz range experimental scheme four could capture the unfiltered injection rate signal at a 1MHz sampling rate. This gives a nyquist frequency of the system of 500kHz. The Kistler SCP signal amplifier used was limited to 200kHz frequency range. Hence analysis of high frequency activity on experimental scheme four was limited to 200kHz.

To evaluate low frequencies that influence zero value variance, simple amplitude spectrums were used in Section 0. For this study, it was necessary to not only know the highest magnitude frequencies were present in the injection rate signal, but also when those frequencies occur. To evaluate both the intensity and duration of frequencies present in the injection rate signal, spectrogram analysis was carried out (Veggeberg and Zhang, 2009).

Charactering the high frequency content in the signal was achieved by processing rate tube pressure signal as an unfiltered voltage time series, prior to the application of software based moving average signal filters. This value is stored in the units of RAWBits, a count of 2x 14bit A2D across a ±10V range, giving rise to a value of 3276.6 bits per volt. The analysis period was matched to the 4750μs wide injection rate measurement window acquired, then logged automatically at a 1Mhz sampling rate.

The following signal processing was implemented to improve the frequency representation of strong resonant sinusoids in the rate signal. To smooth the representation of frequency peak magnitudes through interpolation, zero padding was applied before and after the signal at 10x its original duration. To

reduce spectral leakage, different windowing functions were trialled. Due to sinusoidal nature of potential resonant bands observed in the signal a simple Hanning window was applied, as it offered a good balance of signal magnitude fidelity, accurate frequency peak representation, whilst being effective at separating strong sinusoidal signals from non-periodic background noise present. Some loss of magnitude will be present with this window (Harris, 1978). The use of a simple Hanning window was deemed acceptable, as the objective of the analysis was to characterise the frequency values of dominant periodic signal elements relative to strong background noise, not their absolute amplitude.

The ensemble average spectrogram (Wang *et al.*, 2009) was generated by taking the average spectrum from five separate repeat tests, to further de-noise the result. Frequency magnitudes below a manually selected background level threshold were rejected, so that only strong sinusoidal frequency intensities induced by the injection event are displayed in the spectrogram. Set by evaluating the average quiescent signal magnitude, found before the excitation of the injection event begins.

To establish a baseline, a 2400bar pressure 2300μs duration injection event was initially evaluated on the standard 2bar production rate tube configuration. Its spectrogram and unfiltered injection rate signal with ±1 Standard Deviation (SD) boundaries is shown in Figure 6.3.

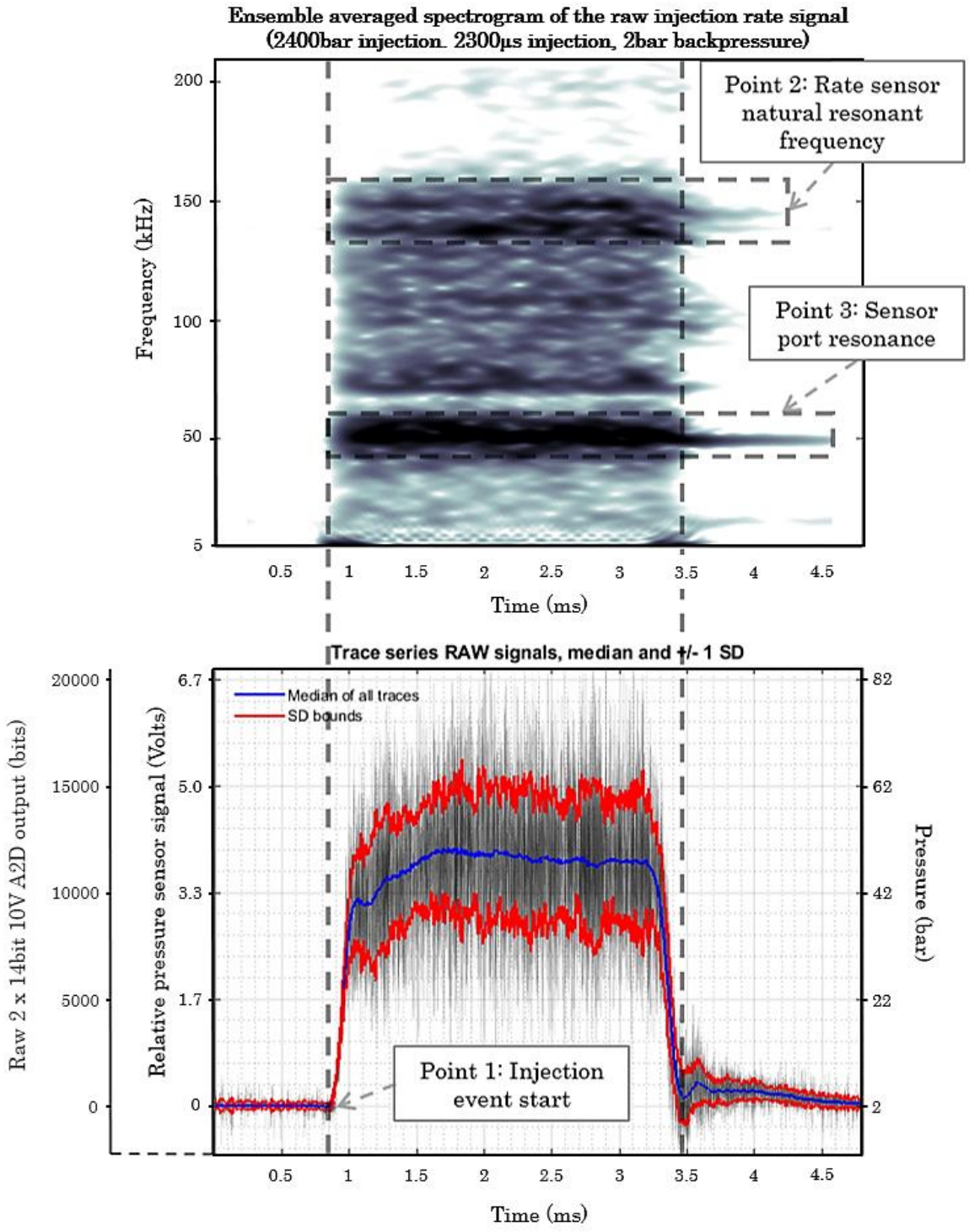


Figure 6.3: High frequency analysis of baseline 2bar production measurement system.
Top: Spectrogram of injection rate signal.
Bottom: Unfiltered injection rate signal with ±1 SD boundaries.
(An explanation of the Raw and voltage signals is provided in Section 3.3.1)

6.1.1 High frequency content of the injection event

This primary intensity of frequency information in the spectrogram begins and ends in line with the injection event, as shown by point 1 of Figure 6.3. Therefore, this frequency activity must be a feature of, or excited by, the injection event.

The frequency content of the injection rate spectrogram, shown in Figure 6.3, features frequency information spread out from 5kHz to 150kHz. In contrast, Crua and Heikal (2014) observed distinct bands of frequencies in a high pressure diesel injection spray up to 50kHz. One explanation for the distinct frequency bands they observed is that they injected into an open gaseous volume. Whereas for the present work, injection occurs into a fluid filled tube. The dynamics of injection will therefore be significantly different in a fluid instead of a gaseous medium. Hydraulic features and resonances of the rate tube injector tooling are also likely to influence the presentation of these frequencies relative to injection into an open volume.

They identified that potential sources of specific frequency bands higher than 25kHz are related to quasi-cyclic turbulence phenomena taking place inside the nozzle, which may include cavitation". They demonstrated that higher order frequency bands would appear with increasing injection pressures. Hence it is expected that a similar frequency band and its higher orders would be present within the measured injection spray, at the higher 2400bar injection pressures used on experimental scheme four.

One explanation for "quasi-cyclic turbulence phenomena" that starts on nozzle opening and remains consistent until the end of injection is the phenomenon referred to as cavitation strings. A visual representation of these cavitation string phenomena can be found in Figure 5 of a published study by Andriotis, Gavaises and Arcoumanis (2008), where they investigated "the formation and development of string cavitation inside transparent replicas of injector nozzles used with large 2-stroke diesel engines".

Cavitation string formation inside the nozzle is not the only source of cavitation expected. Cavitation driven by fluid shear external to the nozzle and caused by its spray is known to occur in injection rate measurement devices. A study in simulation space, carried out by Pearce, Hardalupas and Taylor (2015), demonstrated that large cavitation bubble collapse events occur due to vortices formed in the fluid medium of an injection rate meter, that "would add a source of noise to a real measurement device". This type of cavitation is induced in injection rate meters by vortices, that are caused by fluid shear between the stationary fluid medium of the injection rate meter and the high velocity injected mass into it.

This would also suggest that some frequency content may be caused by expanding pressure waves from cavitation collapse outside the nozzle, within the rate tube itself. These events are large enough to be observed inside a Zeuch type fluid filled measurement chamber with optical observation ports as demonstrated by Pearce, Hardalupas and Taylor (2016). It is expected that these pressure waves will be present and distinctly different from the effect of cavitation strings. An injection rate tube meter injects into a tube of constant cross Section and not a fluid filled Zeuch chamber. Hence the presentation of this effect will be different.

It is surmised that the main body of frequencies observed in line with the injection event start and end, are high frequency pressure waves driven by cavitation collapse. Without access to optical observations on experimental scheme four, it is not known what frequencies can be attributed to cavitation collapse events inside or outside of the nozzle.

6.1.2 Rate sensor natural frequency excitation

There is a dominant frequency band that appears at 150kHz that starts with injection, as shown by point 2 of Figure 6.3. This frequency band does not end in line with the injection, it instead continues to ring like a descending chirp after the excitation of the injection event has ended. The pressure sensor used on the baseline 2 bar production measurement system is a Kistler 6054BR piezo electric pressure sensor, with a natural frequency of 150kHz. If a structural or hydraulic resonance is excited by frequency activity present in the injection event, then it is expected that it will take some time after the excitation is removed before the resonant waves fall in magnitude. Therefore, this frequency band must be the excitation of the piezoelectric sensor's natural frequency.

6.1.3 Rate sensor port natural frequency excitation

The highest intensity frequency band seen at 50kHz starts in line with the injection event and continues to ring with descending magnitude after the injection event has ended as shown by point 3 of Figure 6.3. Hence this must also be a resonance that is being excited by the injection event and not a feature of the injection event itself. If resonance is present in the injection rate measurement signal, then it is not a feature of the true injection rate. Resonant frequencies could cause distortion of the measured injection rate if they are not effectively filtered, or if their frequencies are distorted by the measurement signal processing chain. This is likely why low-pass filters of 10 to 30kHz are used by commercially available injection rate measurement devices (Bosch, 1967; Arcoumanis, Baniasad and Banias, 1993; Ferrari and Zhang, 2019).

To characterise the source of this dominant 50kHz resonant band, this Section describes how the hydraulic geometry of the injection rate observation point was changed to produce an observable change in this frequency band, that can be predicted using quarter wave resonance theory.

Two of the most common pressure sensor port arrangements that induce a resonance during combustion measurement are a quarter wave cylinder and a Helmholtz chamber as shown in Figure 6.4.

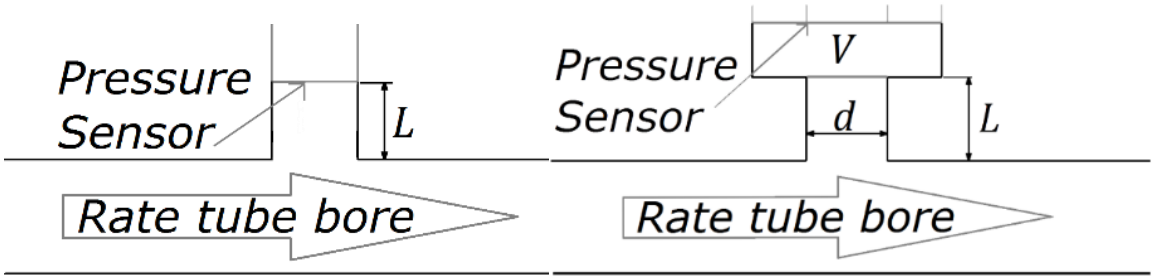


Figure 6.4: Section view of the (left) quarter wave cylinder and (right) Helmholtz chamber sensor port geometries.

The frequency components related to the resonant frequency of the quarter wave and Helmholtz port configuration are estimated using Equations [6.1] and [6.2], as provided by Walter (2004) in relation to dynamic air blast measurements.

Quarter wave cylinder:

$$f = \frac{c}{4L} \qquad [\,6.1\,]$$

Helmholtz chamber port:

$$f = \left[\frac{c}{(4\pi)}\right]\left[\frac{\pi d^2}{(V(L+0.85d))}\right]^{\frac{1}{2}} \qquad [\,6.2\,]$$

Where, f is the first resonant frequency of the port, c is the Speed Of Sound (SOS) in the medium present in the port, L is the length of the entrance tube, d is the diameter of the entrance tube, V is the volume of the lower cavity.

Initially, during experimental scheme four, the quarter wave port configuration was evaluated, as this was the standard port configuration used for the 2bar production measurement system. The spectrogram in Figure 6.3 shows a dominant frequency at 50kHz. Using estimated values for SOS in the fluid medium, at the injection temperature and system backpressure (Bazile *et al.*, 2012) within the tube and length of the cylindrical port, an equivalent frequency can be derived using the quarter wave Equation [6.1]. This suggests that the

dominant frequency observed in Figure 6.5 is caused by resonance of the sensor port.

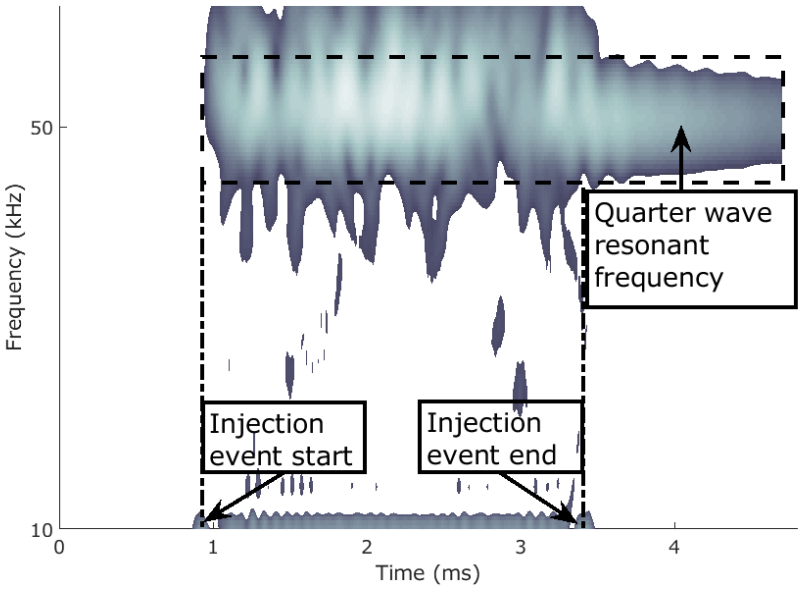


Figure 6.5: Spectrogram of frequency intensity vs time for the injection event measurement window with the resonance identified for the quarter wave cylinder port configuration.

The same sensor was mounted into an adapter to double its effective diameter. A port design typically specified for this width of sensor was then evaluated under the same high pressure condition. As shown in Figure 6.6, a new frequency three times lower than the previous quarter wave port resonant frequency was observed. Using the known geometry of the port and SOS in the fluid medium, a similar frequency can be derived using the Helmholtz chamber Equation [6.2]. A second frequency is observed at a similar level to the previous quarter wave frequency, but at a reduced intensity.

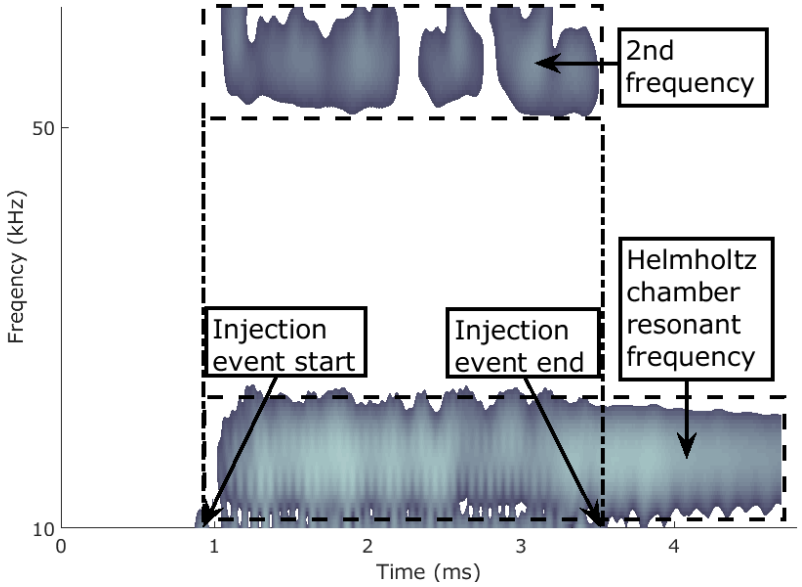


Figure 6.6: Spectrogram of frequency intensity vs time for the injection event measurement window with resonance identified for the Helmholtz port configuration.

The second lower intensity, higher frequency band on the Helmholtz spectrogram was investigated further, by observing how both frequencies changed at different injection pressures. Lower injection pressure results in lower temperatures in the fluid medium, caused by less cavitation related heat input to the system at lower injection pressures (Strotos *et al.*, 2015). A lower system fluid temperature for a fixed system backpressure is known to cause speed of sound to increase for ISO4113 oil (Bazile *et al.*, 2012).

This additional frequency maintained a fixed ratio with the primary Helmholtz resonant frequency across three pressure levels, 950, 1625 and 2400bar, as shown in Figure 6.7.

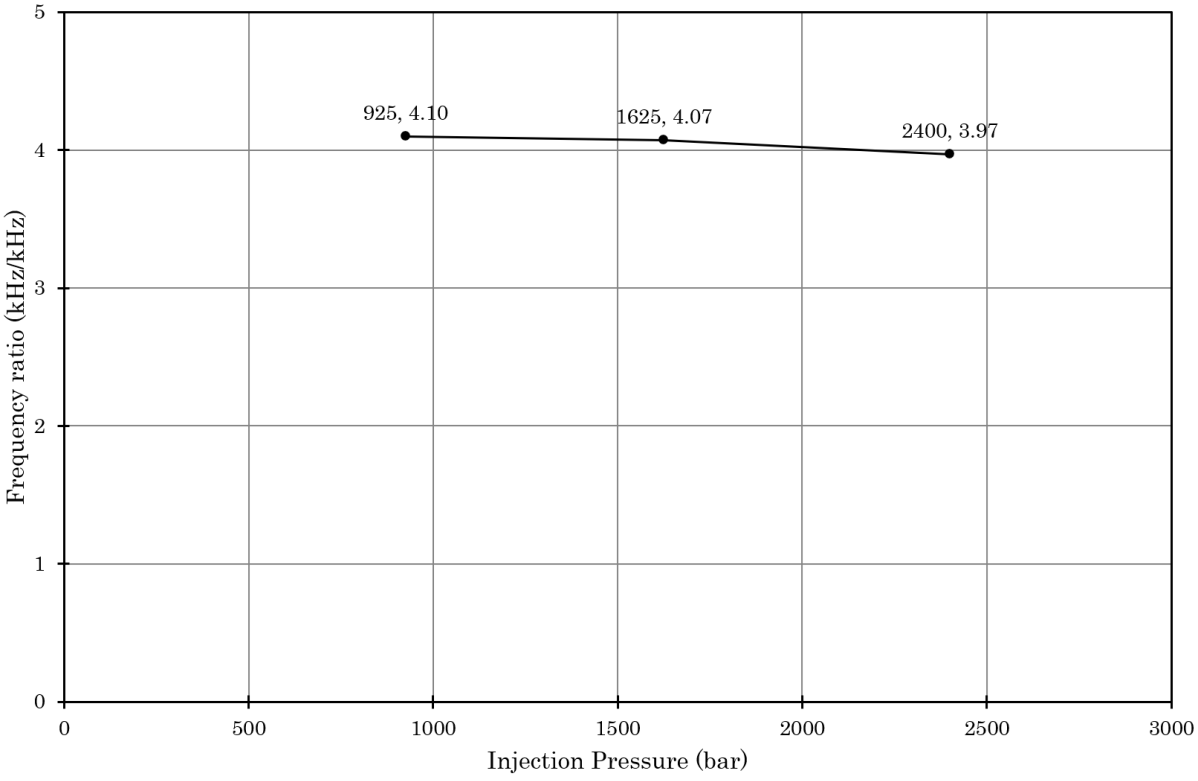


Figure 6.7: Ratio between primary and secondary Helmholtz frequencies across three pressure levels.

This constant relationship between pressure levels suggests that this second frequency is a higher modal order of the primary Helmholtz chamber resonant frequency.

The resonance intensity is linked to injection pressure, as shown in Figure 6.8, where frequency intensity of each pressure level has been normalised to the quarter wave frequency intensity at 2400bar. The intensity of the quarter wave resonance is significantly greater than the Helmholtz resonance. The Helmholtz frequency intensity was too low during injection to characterise at the lowest pressure 450bar condition.

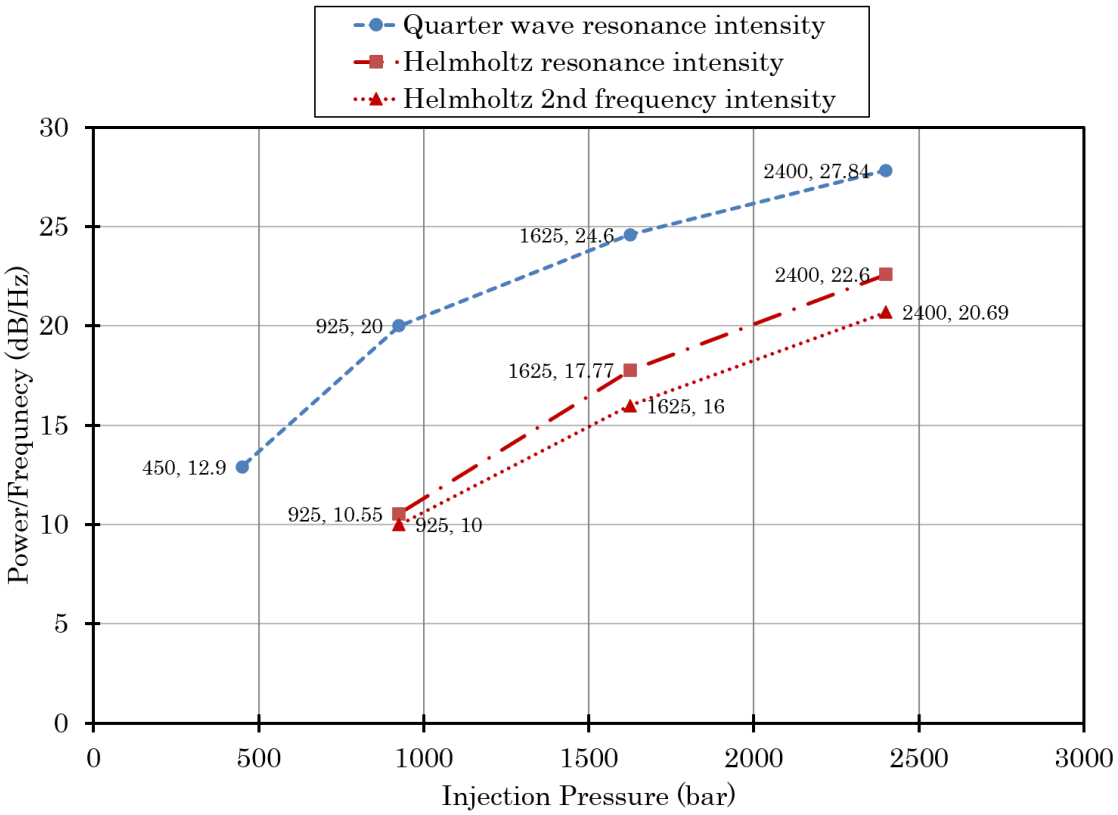


Figure 6.8: Injection pressure vs power spectral density for both port configurations.

A prediction for the frequency value of the resonance was performed, to see if the quarter wave resonant frequency followed SOS changes in the tube at different pressure levels. The median SOS for the whole rate tube length at each pressure level was measured using cepstrum analysis. A description of how cepstrum analysis is performed to extract SOS for the whole rate tube using frequency components and its use in de-noising is found in the Section 6.2.2.

The average SOS for the entire length of the tube will not be the same as SOS as at the sensor port, because of increased local heating effect from proximity to the injector nozzle (Strotos *et al.*, 2015). However, the relative difference in SOS between the whole tube length and SOS at the observation point, should remain consistent at stable temperature and backpressure conditions. This relative difference should remain stable for different rates of nozzle heat input into the measurement system for different injection pressures.

The resonant frequency at 2400bar was used to derive an exact value for SOS at the port, along with the known quarter wave port length. The same relative difference in SOS magnitude for the whole tube was applied to the 2400bar quarter wave port derived value. The results of predicted port resonance at the three lowest injection pressures, using this relative SOS change, follow the observed quarter wave frequency well, as shown in Figure 6.9.

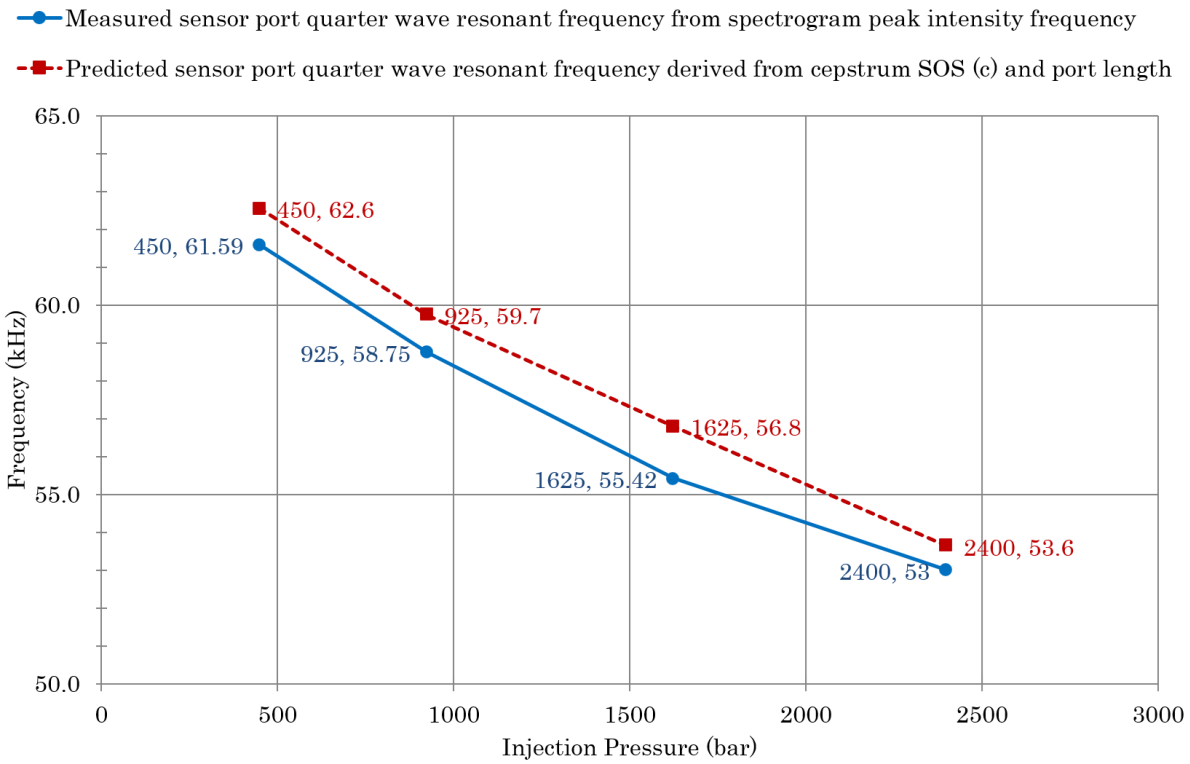


Figure 6.9: Quarter wave resonance vs normalised frequency at the three lowest pressure levels observed and predicted using relative SOS changes derived from the reflection period in the tube.

This provides further evidence that this frequency is caused by quarter wave resonance, that changes with SOS in the fluid medium, as predicted by the quarter wave Equation [6.1].

Further production application specific detail, showing how frequency intensity increases with nozzle seal fixture erosion, and how increased backpressure lessens their intensity at all injection pressures, is provided in Appendix 11.3.2.

6.2 Characterisation of electronic sources of high frequency variance

6.2.1 Effect of signal amplifier on high frequency variance

Using spectrogram analysis, it was possible to evaluate time resolved high frequency information and identify hydraulic resonances contained within. To perform spectrogram analysis, a high frequency 200kHz Kistler 5064c SCP slim laboratory piezo electric amplifier had to be used for the injection rate signal. However, the standard production measurement system used a 20kHz Kistler 5073 ICAM industrial piezo electric amplifier. A relic of the EU4 and EU5 measurement system designs, carried over to EU6 because of their robustness in an industrial environment.

When the signals from the two amplifiers were evaluated on experimental scheme four, there was a significant difference in the mean injection flow rate profile, as shown in Figure 6.10.

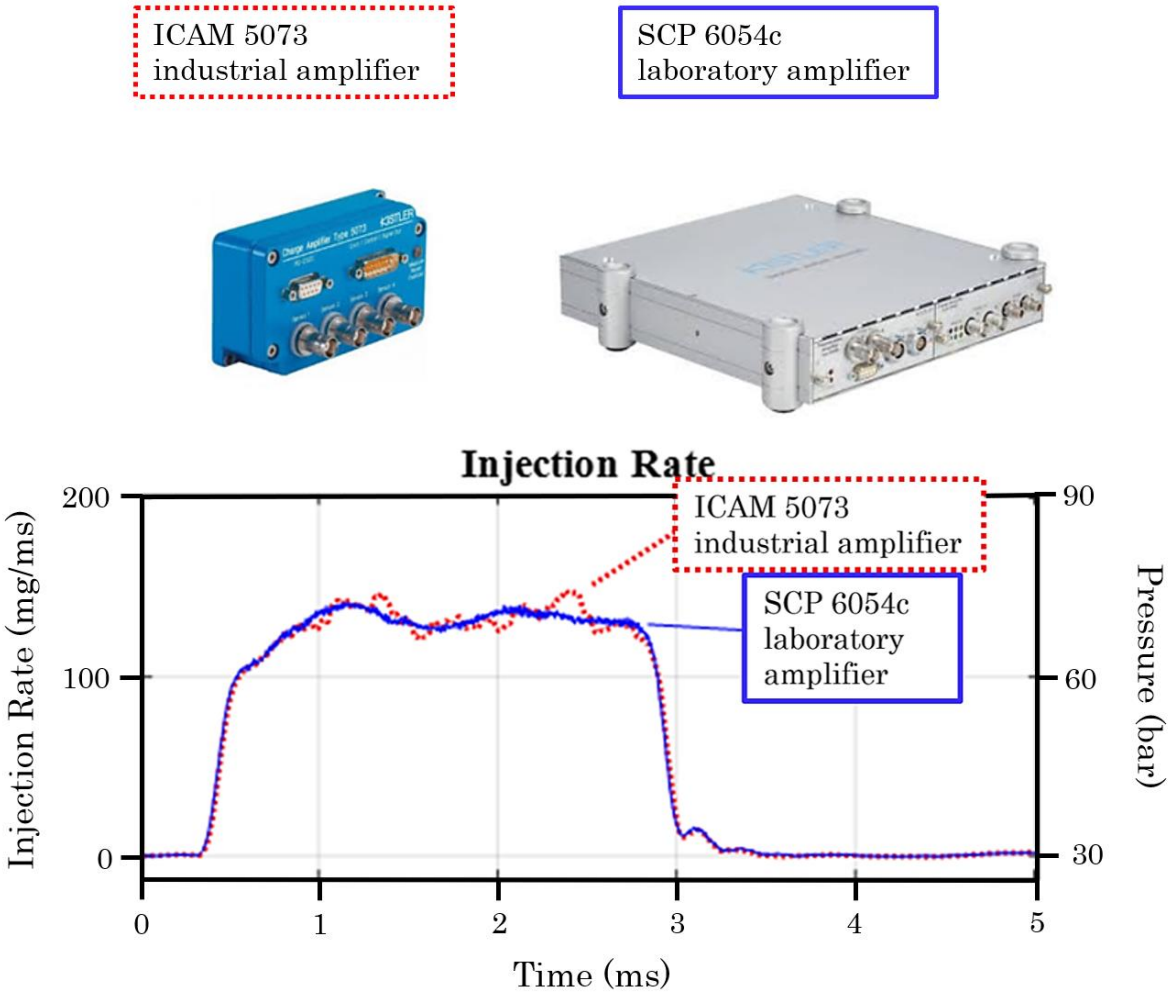


Figure 6.10: Comparison of 2400bar pressure 2300µs duration injection rate signals. Red: 20kHz 5073 ICAM industrial amplifier. Blue: 200kHz 5064C SCP slim laboratory amplifier employed during experimental scheme four.

To ascertain how the high frequency information differed between the two amplifiers, the spectrograms for both were evaluated at the 2400bar pressure 2300µs duration injection condition, as shown in Figure 6.11.

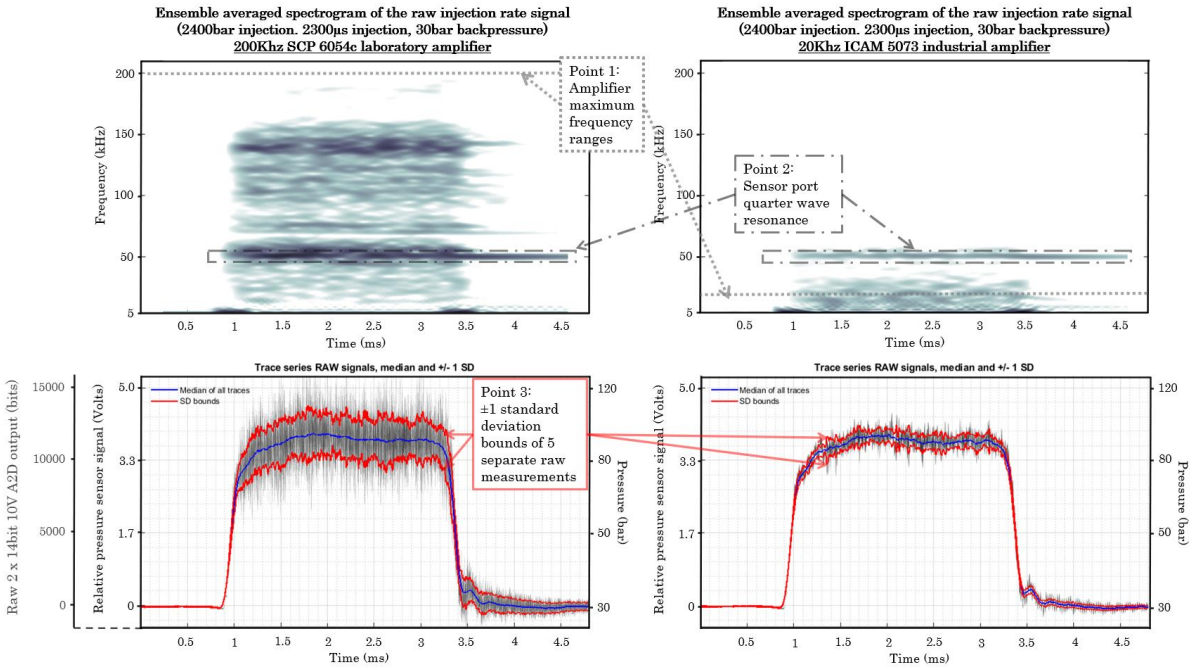


Figure 6.11: Comparison of injection rate signals for the different amplifiers. Left: 200kHz SCP slim laboratory amplifier employed during experimental scheme four. Right: 20kHz ICAM industrial amplifier. (An explanation of the Raw and voltage signals is provided in Section 3.3.1)

The ICAM 5073 amplifier is rated to 20kHz frequency range, as highlighted by point 1 of

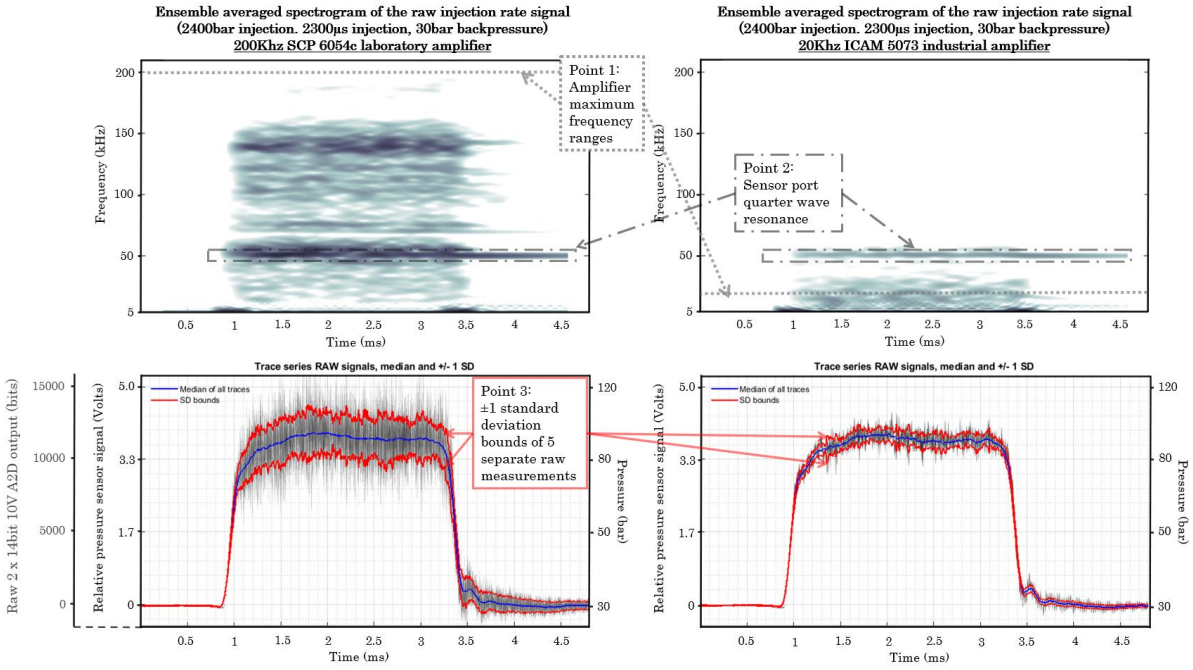


Figure 6.11. Despite this, there is still some high frequency information showing on its spectrogram for the sensor port resonance frequency band of 50kHz, as

shown by point 2 of

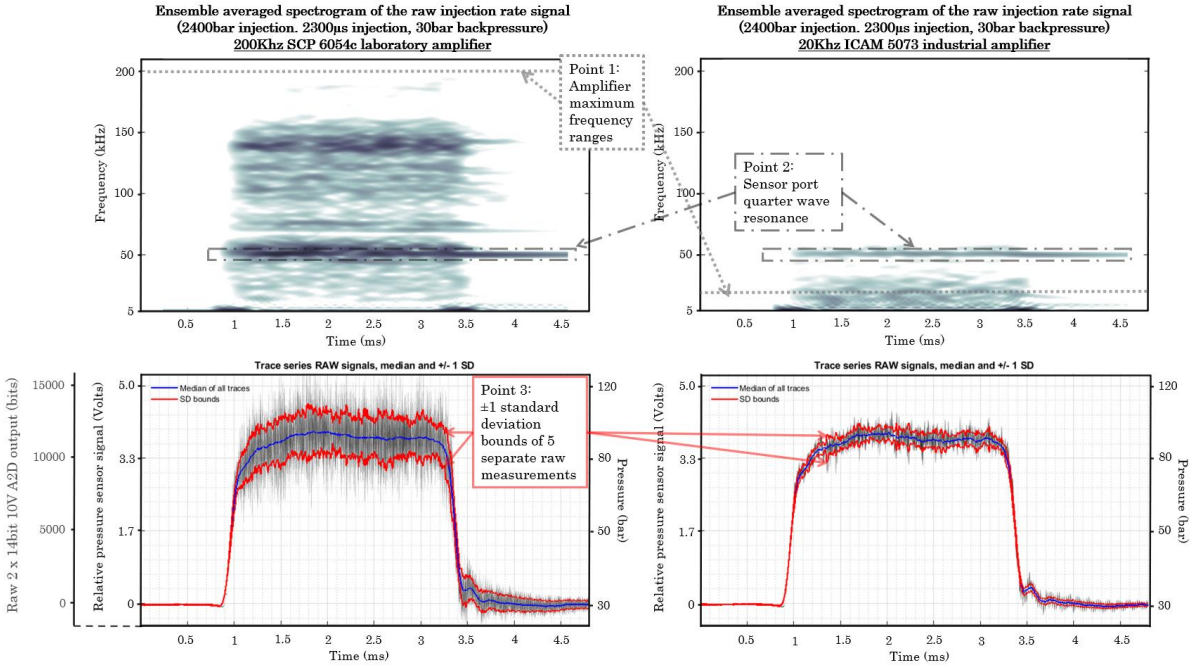


Figure 6.11. This could suggest that the response characteristic of the ICAM industrial amplifier means it is capable of representing these frequencies, but no higher than 55kHz.

There is a significant reduction in the SD bounds of the raw injection rate signal for the five separate measurements for the ICAM industrial amplifier, as shown by point 3 of

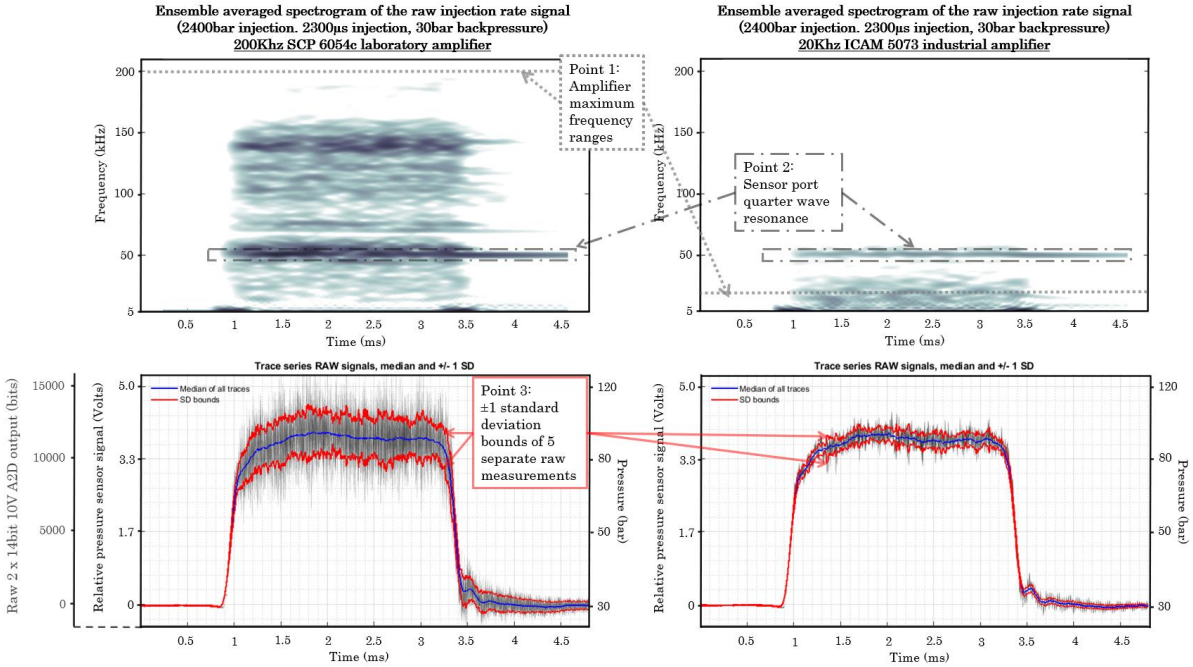


Figure 6.11. This indicates that, despite the port resonance being represented on the spectrogram, its characteristic and intensity are not the same as that observed for the SCP laboratory amplifier case. This reduction could also be caused by the fact that the ICAM industrial amplifier cannot perceive the sensor natural frequency excitation at 150kHz.

Klaus, Bruns and Volkers (2015) demonstrated that the phase and the magnitude responses can differ substantially from amplifier to amplifier, by evaluating the frequency transfer function of four different charge amplifiers with the same specified frequency range. They showed that as frequencies approach the upper limit of a charge amplifiers rated frequency range, significant deviations in phase delay and magnitude responses of the output signals are observed. They also demonstrated that non-linearity of the signal processing can cause distortions of the sinusoidal shape of the output signal. Hence, the true sinusoidal shapes of high frequency components near the limit of amplifiers frequency range will be distorted.

Therefore, it is of critical importance to characterise and amplifier's frequency response transfer function, which enables digital compensation for the dynamic influences of the amplifiers distortion within the measurement chain.

As the ICAM maximum frequency is rated at 20kHz, it stands that any frequency intensities between 20kHz and 55kHz will be distorted in phase and magnitude. It is concluded that this causes the loss of fidelity seen in the smoothed flow rate, shown in Figure 6.10, when using the ICAM amplifier.

This is one of the most significant contributions to knowledge and commercial outcomes from the present work. The knowledge that there is high frequency information contained within the injection rate signal and the amplifier characteristics can cause this frequency information content to be distorted if it is not rated to a high enough frequency range.

6.2.2 Cepstrum for periodic high frequency signal noise identification

When comparing the results for the same injection condition between experimental scheme one and four using the ICAM amplifier, it became apparent that there was more signal-to-noise ratio present on experimental scheme one.

Using spectrogram analysis, it was possible to observe time resolved frequency content for the injection rate measurement window. However, there was no apparent difference in the spectrograms between experimental scheme one and four, when using the ICAM amplifier.

Experimental scheme one was a production injector test machine fitted with four separate measurement system devices that test four injectors in parallel.

Whereas experimental scheme four was a custom apparatus with a single measurement system, setup for high signal fidelity and hardware flexibility. Whilst the rate tube measurement systems, injection condition and control of the injector test machines were the same, the overall supporting structure and electronics of the machine were not.

To gain another perspective, it was necessary to identify periodic frequency content in the signal. To achieve this goal, cepstrum analysis was applied to the entire 15Hz firing period, as shown in Figure 6.12.

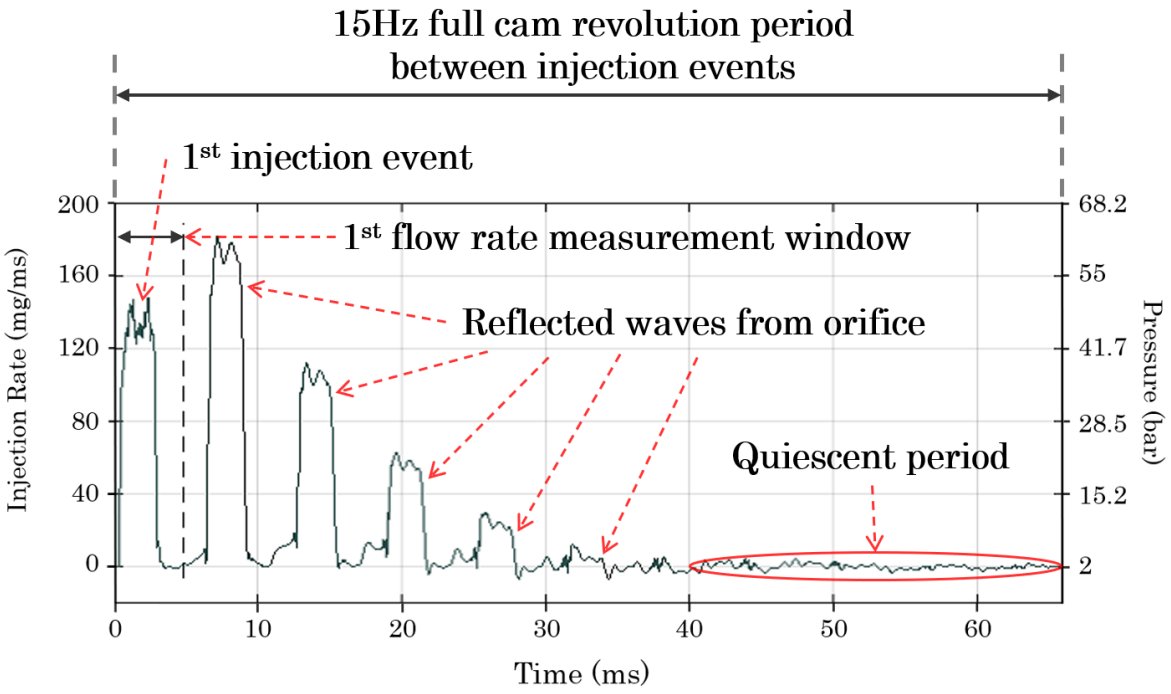


Figure 6.12: Injection rate signal for a full 15Hz period

Cepstrum is defined as "the power spectrum of the logarithm of the power spectrum". It was first defined as the "power cepstrum" by (Randall, 2017), where it was used for the analysis of seismic signals.

Terminology

To avoid confusion with the frequency domain and time domains, Bogert (1963) referred to values in the cepstrum as the *quefrency* domain, by reversing the first syllable of frequency. Similarly, the words *lifter* and *rahmonic* are commonly used.

Cepstrum Principle

It is important to note that quefrency domain is neither time nor frequency but rather a representation of additive periodic components in a signal. A useful

explanation of this process was given by Oppenheimer et al, for the mathematical representation of a signal and its echo:

$$x(t) = s(t) + \alpha s(t - \tau) \qquad [6.3]$$

The spectrum of such a signal is given by:

$$|X(f)|^2 = |S(f)|^2[1 + \alpha^2 + 2\alpha\cos(2\pi f\tau)] \qquad [6.4]$$

By taking the logarithm of the spectrum, the spectrum is converted to the sum of the two components.

$$C(f) = log|X(f)|^2$$

$$C(f) = log|S(f)|^2 + log[1 + \alpha^2 + 2\alpha\cos(2\pi f\tau)] \qquad [6.5]$$

"Thus, $C(f)$ viewed as a wave-form has an additive periodic component whose fundamental frequency is the echo delay τ." (Oppenheim and Schafer, 2004).

The use of the amplitude spectrum was demonstrated by Bogert (1963), for the identification of gearbox sideband families for fault identification. This is the method chosen for this study due to its ease of interpretation, defined as:

$$|C| = IFFT(\log|FFT(y)|) \qquad [6.6]$$

Where C is the cepstrum and y is the input signal.

The influence of components

Dominant cepstral peaks were identified in the Cepstrum for the full injection period on experimental scheme one. Their quefrency was compared with known measurement system characteristics, to identify what features they belong to. After evaluating the cepstrum in Figure 6.13, two dominant cepstral peaks were identified. The first peak was concentrated around 6.11-6.32ms quefrency, the second at 22.1ms quefrency.

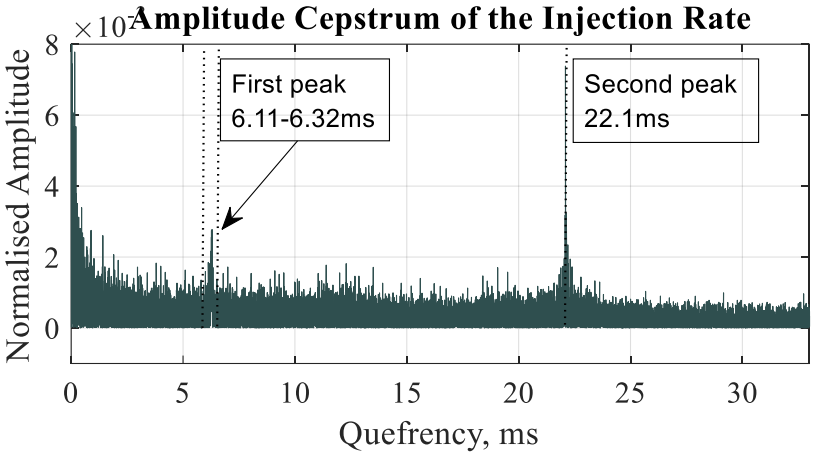


Figure 6.13: Injection rate real amplitude cepstrum on experimental scheme one.

The reflection period in a rate tube is a function of twice the length of the tube between the injection event and the termination orifice multiplied by the SOS of the fluid in the tube. The 6.11-6.32ms quefrency range corresponds to the separation period between the start of the injection event and its first reflection from the orifice, and the subsequent period between reflections in the rate time series shown in Figure 6.12. If we take the SOS of ISO 4113 oil (Bazile *et al.*, 2012) at the operating temperature and system backpressure of the fluid and estimate the wavelength, it corresponds to approximately twice the length of the tube. Hence, this quefrency may represent the SOS fluid property in the measurement device.

This suggests that cepstrum is a potential fluid property condition monitoring tool for pulsating hydraulic systems, as the location of the first cepstral peak would change if the termination orifice was repositioned, due to a different reflected wave travel distance and period. A potential replacement for the temperature to SOS algorithm discussed in chapter 7.

The influence of operating variables

Data was evaluated at different measurement system temperatures on experimental scheme one, to see if there was a corresponding difference in the cepstrum.

To evaluate if the first cepstral peak is a feature of the reflection period, data was captured at two-minute intervals whilst the apparatus was reaching the desired temperature on experimental scheme one. Figure 6.14 shows the injection rate signals for when the temperature delta was significant.

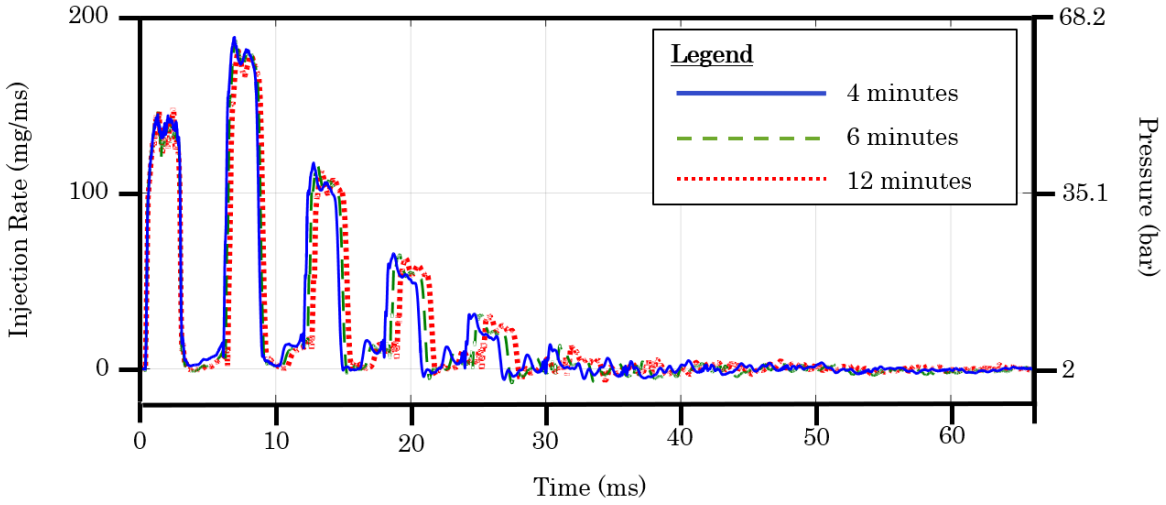


Figure 6.14: Full 15Hz period injection rate signal for 4, 6 and 12 minutes after beginning at ambient temperatures.
2400bar pressure 2300µs duration injection condition.

The time at which the first reflection is observed at the pressure sensor, changes with temperature, as seen in Figure 6.15.

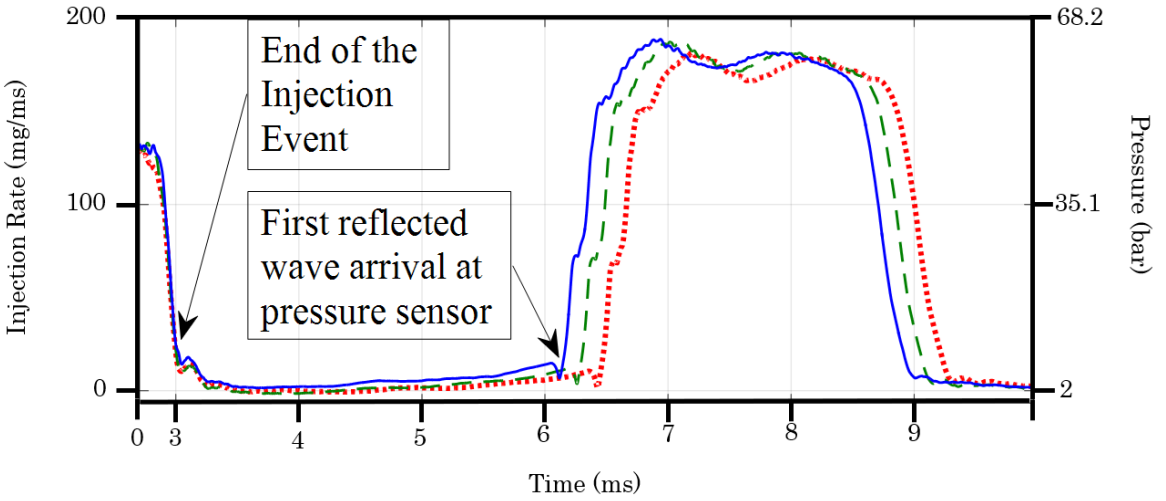


Figure 6.15: First reflected wave in rate signal at different temperatures

A corresponding shift in the position of the first cepstral peak is identified in Figure 6.16. If the system backpressure remains the same, as fluid temperature increases in the tube due to the heat input from the injection event, the SOS in the fluid decreases. Resulting in a longer travel time between the injection pulse hitting the termination orifice and returning to the observation point of the Kistler pressure transducer. As the cepstral peak changes with temperature, all other operating parameters remaining the same, suggests that this first cepstral

grouping of peaks represents the reflections of the initial wave induced by the mass injection event input.

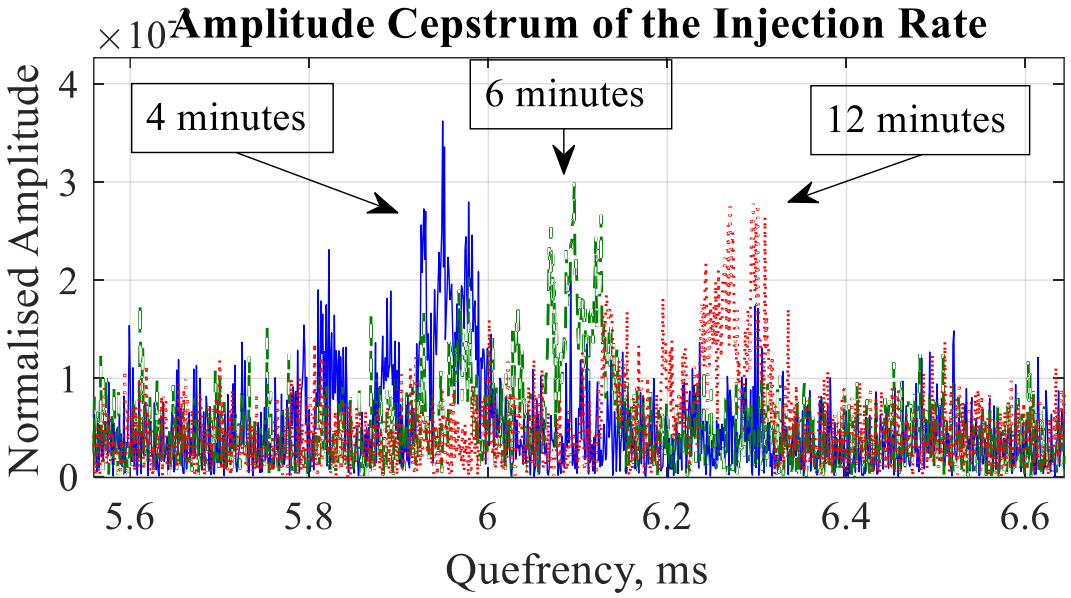


Figure 6.16: Zoomed view of the first cepstral peak with different tube temperatures.

This shows that cepstrum analysis can observe the influence of operating conditions on the fluid borne frequencies in pulsating hydraulic systems.

If the reflection period can be determined easily via the first cepstral peak, then the SOS in the fluid for the whole rate tube is known. This presents an alternative way of acquiring a SOS measurement, compared to the temperature measurement used on all known rate tube measurement systems. Theoretically, the SOS can be derived using Cepstrum from the existing rate tube pressure measurement signal, and the thermocouple could be removed. This would represent a significant commercial outcome, as the thermocouple temperature measurement is the most frequent source of hardware failure on Delphi Technologies EU6 injector test equipment.

A source of periodic signal noise

The second cepstral peak shown in Figure 6.13 was identified at 22.1ms quefrency, which corresponds to a frequency of 45.25Hz. This frequency is close to 3x the shaft rotation of the high-pressure pump cam. The high-pressure pump on experimental scheme one was programmed to generate pressure up to three times per revolution. However, the duration of pressure generation would depend on the load required at that instant to maintain a constant rail pressure from the ECU control. Therefore, the frequency of these events may not be constant.

To confirm whether this cepstral peak was a manifestation of the pumping frequency, the speed of the shaft driving the pump was swept at 50rpm intervals between 800 and 900rpm, whilst maintaining stable pressure in the rail so that injection settings would remain the same. Figure 6.17 shows that this cepstral peak moves with the shaft rotation.

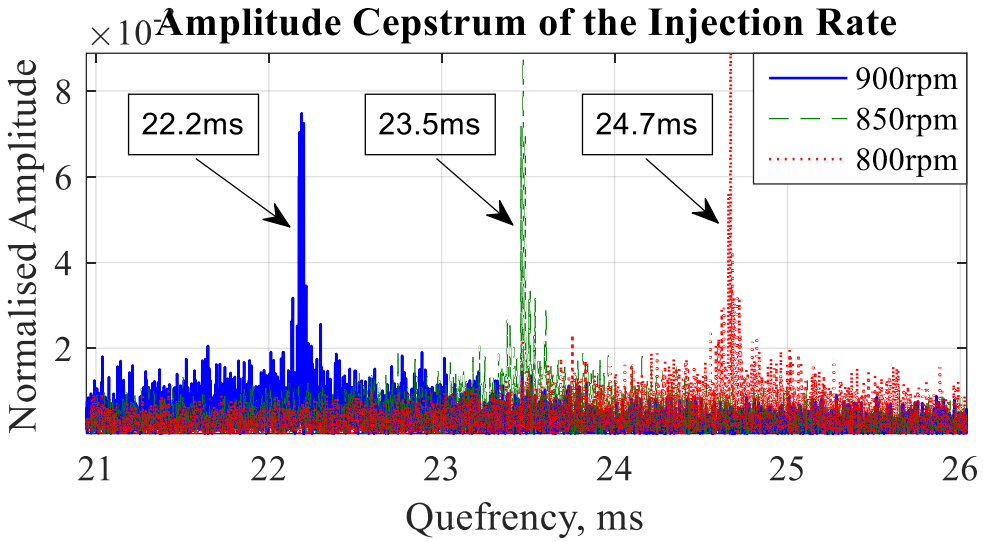


Figure 6.17: Location of second cepstral peak with pump driveshaft rotation

Identification of the pumping quefrency source

The equivalent drive shaft speed calculated from the quefrency in Table 6.1 suggests the cepstral peak location changes in line with pump driveshaft rpm. This demonstrates that cepstrum is a useful tool for evaluating what system features are the sources of periodic signal noise.

However, it is not clear from this data whether this quefrency is a product of fluid borne noise from the pump pulse in the high pressure fuel supply or electrical noise from the ECU pump drive pulse. Examining the rate time series does not clarify this, as the presence of the frequency corresponding to the quefrency seen in the cepstrum is not immediately obvious and is likely masked by the zero value resonant ripples present in the fluid medium of the rate tube.

Table 6.1: Location of second cepstral peak with pump driveshaft rotation

Shaft rotation speed setting (rpm)	Second cepstral peak quefrency (ms)	Corresponding frequency (fs=1/qf)	Equivalent rpm of cepstral peak
800	24.7	40.5	810
850	23.5	42.5	850
900	22.2	45	900

Therefore, cepstrum is a useful tool alongside other signal processing tools to highlight periodic signal noise in a time series where turbulence and signal processing of the true measurement act to mask it.

Influence of Instrumentation characteristics

Cepstrum analysis was carried out on the experimental scheme four for the same injector and injection conditions as previously used for the analysis on production equipment used in experimental scheme one. The primary rate tube reflection frequency was present as observed on experimental scheme one. However, a second pumping quefrency was not found on experimental scheme four. Experimental scheme one was a production test machine with standard wiring whereas experimental scheme four was a custom design optimised for original raw injection rate signal processing with an optimised signal measurement chain.

The same Kistler cylinder pressure piezoelectric transducer was used. A Kistler 5018 bench charge amplifier was used in place of the 5073 ICAM industrial charge amplifier. The power for this amplifier was taken from another source. The output of the laboratory amplifier was wired directly into the NI acquisition board, to ensure the injection rate signal was separated from the electrical hardware of the experimental apparatus, as shown in Figure 6.18.

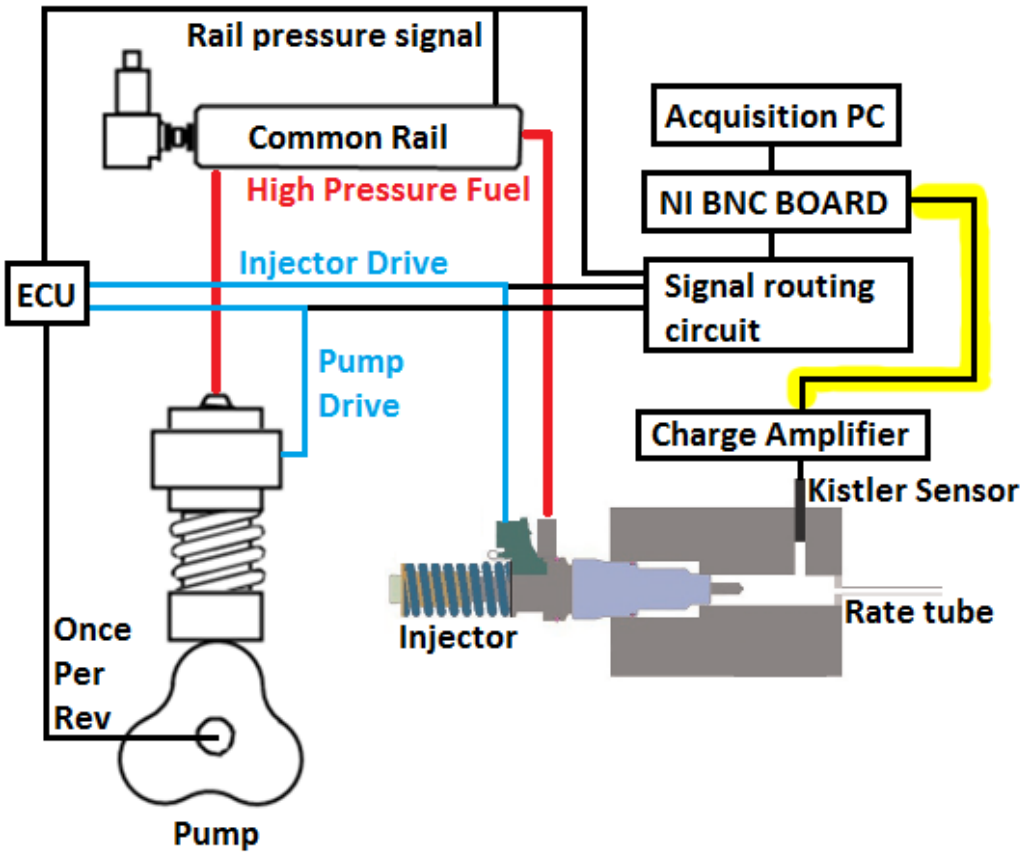


Figure 6.18: Alternative charge amplifier signal routing (highlighted in yellow).

As shown in Figure 6.19, the cepstral peak of the pump drive disappears. This confirms that the source of the noise is electrical pump drive noise from the high speed switches in the ECU, and is present in either the signal routing or power circuit of the experimental apparatus.

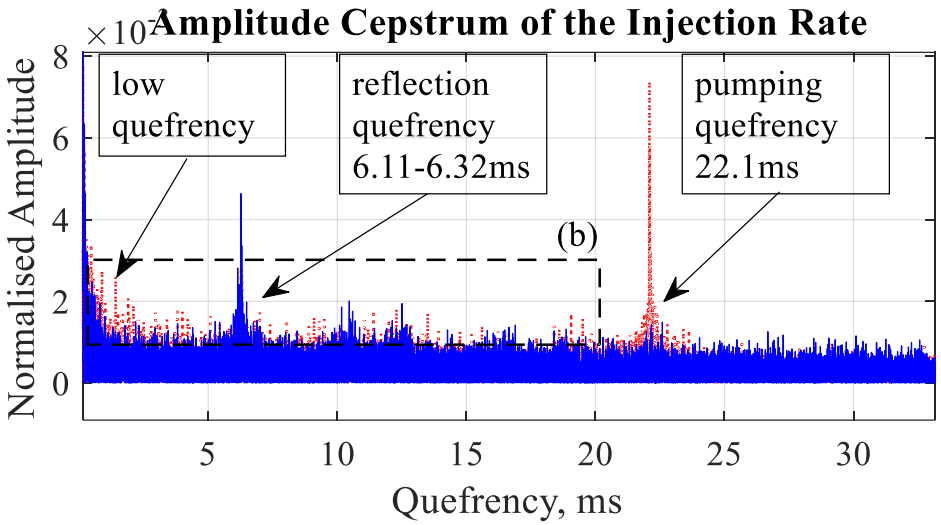


Figure 6.19: Difference in full cepstrum for alternative charge amplifiers.
Red dotted: Kistler 5073 ICAM industrial charge amplifier.
Blue: Kistler 5018 laboratory charge amplifier.

This demonstrates that cepstrum is useful for evaluating the differences in the representation of signals for different instrumentation characteristics. Hence if interpreted carefully can act as an instrumentation optimisation tool for busy signals.

An interesting aspect of the signal from the laboratory charge amplifier is that the 'thin' cepstral peaks that previously dominated the low quefrency part of the cepstrum have been significantly reduced in amplitude as shown in Figure 6.20.

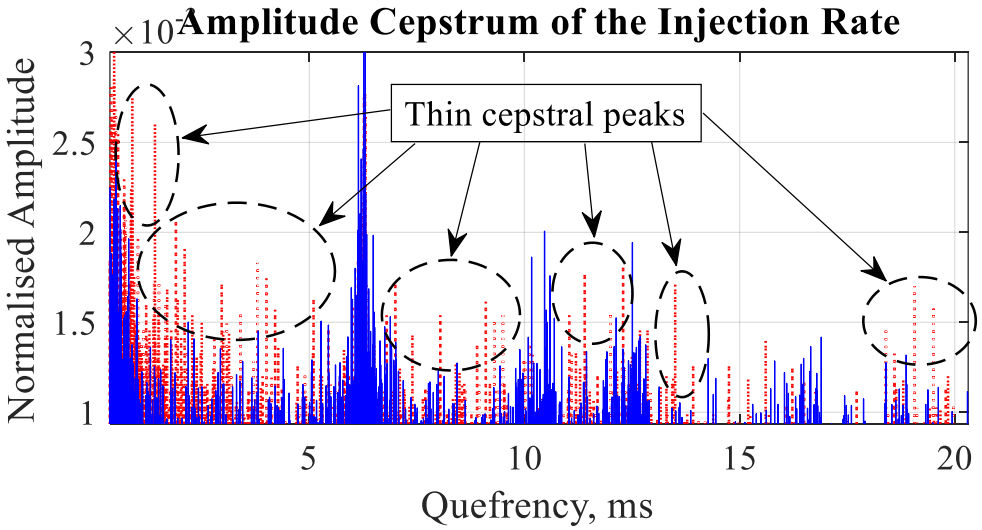


Figure 6.20: Zoom of low quefrency range of the cepstrum for alternative charge amplifiers to highlight thin cepstral peaks.
Red dotted: Kistler 5073 ICAM industrial charge amplifier.
Blue: Kistler 5018 laboratory charge amplifier.

This could indicate that the removal of high frequency harmonic signal noise, such as from the high speed electrical switches inside the ECU, are of great significance to the fidelity of cepstral peaks observed.

Ground loop signal noise

Whilst the result with the Kistler 5018 Bench amplifier demonstrated that there was high-pressure pump electrical drive signal noise present in the cepstrum of the injection rate signal, it did not indicate the exact transmission path by which the noise became superimposed on the signal. An investigation was carried out as to the signal noise transmission mechanism, so that a suitable retrofit could be devised for production injector test equipment to eliminate it.

A study of literature regarding the mechanisms by which signal noise can be superimposed onto piezoelectric pressure sensors was carried out (Asad *et al.*, 2011; Cassiolato, 2011; Bueno, Velásquez and Milanez, 2012; Dey, 2012; Hopkins and Lee, 2015; Knott and Robinson, 2020). A series of trials were devised where the signal measurement chain hardware was modified, to test for the presence of each potential source of signal noise identified separately. When the second

cepstral peak disappeared after a specific hardware change, the source of signal noise was confirmed. A ground loop was identified as the mechanism by which the signal noise is transmitted and is illustrated in Figure 6.21.

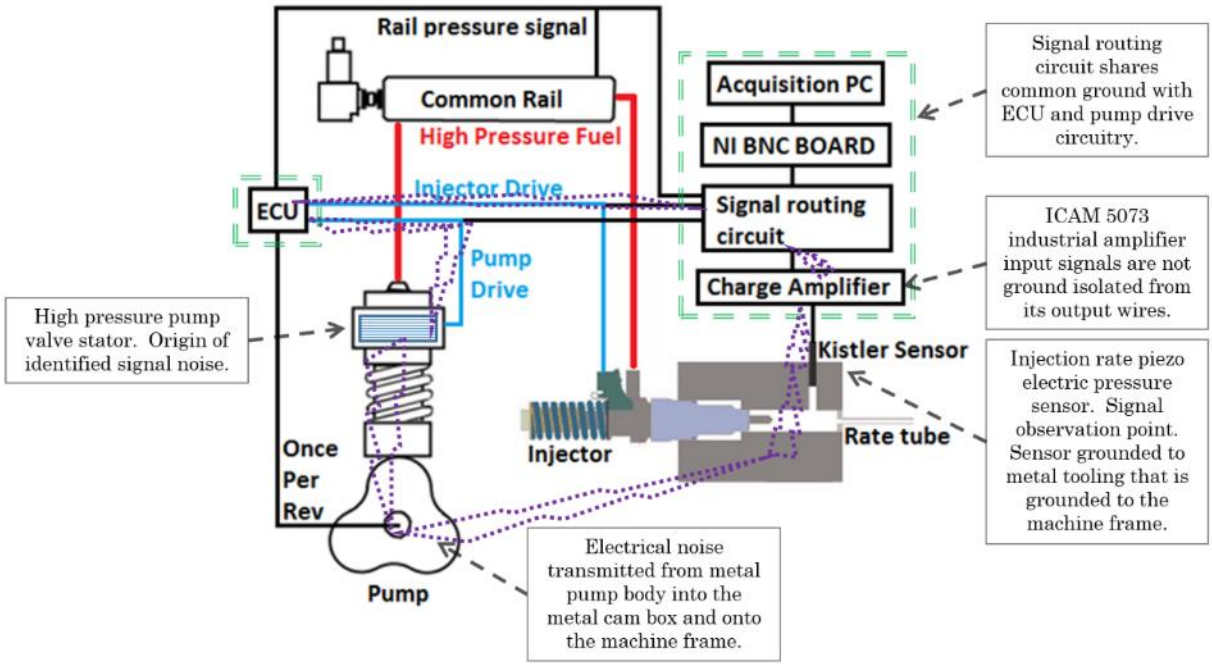


Figure 6.21: Schematic diagram detailing the ground loop source of measured injection rate signal noise identified using cepstrum.

This ground loop was eliminated by retrofitting an 5064c SCP slim amplifier with ground isolated signal inputs in place of the ICAM 5073, as illustrated in Figure 6.22.

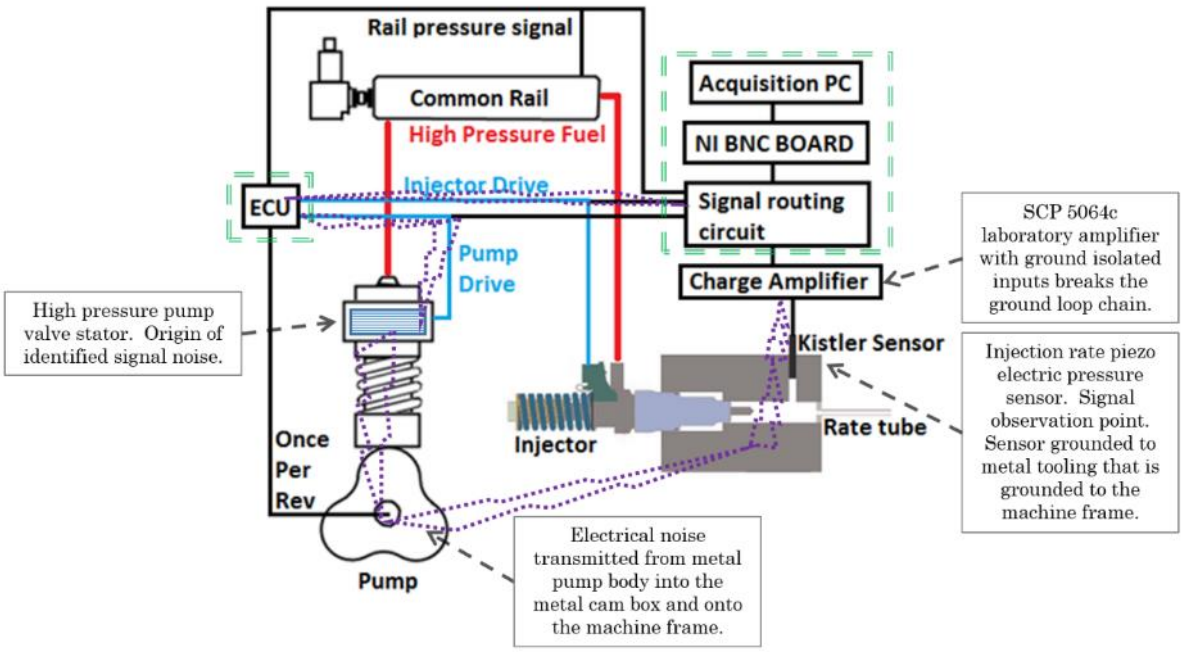


Figure 6.22: Schematic diagram detailing the ground loop source of measured injection rate signal noise identified using cepstrum.

This result demonstrates that cepstrum analysis of periodic frequency elements is a useful tool for identifying sources of electrical signal noise. In particular, signal noise that occurs at specific intervals, that would otherwise be hidden using time or frequency domain analysis techniques alone. A technical paper to share this novel contribution to knowledge was published as part of the present work (Stojanovic *et al.*, 2016).

7 Rate height

A concurrent secondary mass measurement is necessary to solve the rate tube mass injection rate Equation [2.6], by providing a calibrated reference mass value. Speed of Sound (SOS), cross sectional area of the tube and integral of the pressure wave at the observation point must be known to derive the total injected fuel mass value in a rate tube injection meter. The cross sectional rate tube area is known and fixed. The integral of the pressure wave is provided by the piezo electric pressure sensor at the observation point. However, SOS is not directly measured, but will dictate the signal magnitude, hence its precise estimation is crucial for estimating mass value. Direct measurement of SOS at the observation point is technically challenging on low cost production hardware. All known rate tube measurement systems derive a SOS value by instead relying on a temperature measurement local to the observation point, mapped to a secondary calibrated mass flow value.

Automating the SOS to mass calibration process of the EU6 rate tube production measurement equipment was a stated commercial objective of the present work. The knowledge gained during experimental schemes one and two allowed for a hydraulic circuit design to be derived to carry out experimental scheme three. Where a secondary measurement system in the form of a calibrated coriolis mass meter was added to production equipment to meet this objective. Data was collected over a three-month period in Q4 2017, for both shot-to-shot injected mass from the rate tube injection meter, and a reference average mass flow rate from the coriolis measurement system.

Current practice at Delphi Technologies is to use a 2nd order polynomial fitted transfer function, with a 1.5mm diameter insulated K-type thermocouple temperature measurement. To derive the polynomial terms, an additional calibrated mass flow measurement must be performed concurrently with the pressure wave and temperature measurement.

The equation used by Delphi Technologies is a second order polynomial as shown in Equation [7.1].

$$m = (a \times T^2 + b \times T + c) \times \int_{t_{start}}^{t_{end}} P dt \qquad [\ 7.1\ ]$$

Where m is the injected mass, T is the temperature at the pressure wave observation point and $\int_{t_{start}}^{t_{end}} P dt$ is the integration of the area under the raw pressure signal. t_{end} and t_{start} defines start and end of measurement window corresponding to start and end of the injection event.

7.1 Automating coriolis mass measurement

To solve for the unknown terms a, b and c, the temperature and pressure signal at the observation point must be recorded alongside a concurrent calibrated mass measurement. Once these terms are established, injected mass can be calculated from the pressure signal and a local temperature measurement alone.

At the start of EU6 injector testing in production, an initial mapping of the polynomial terms was carried out. The calibrated injected mass was captured using a precise weighing scales and a large beaker. The return to tank for the rate tube measurement system was redirected to this beaker. Using the mass change over time and a stopwatch, an average fuel delivery was ascertained and used to solve the polynomial, as illustrated in Figure 7.1.

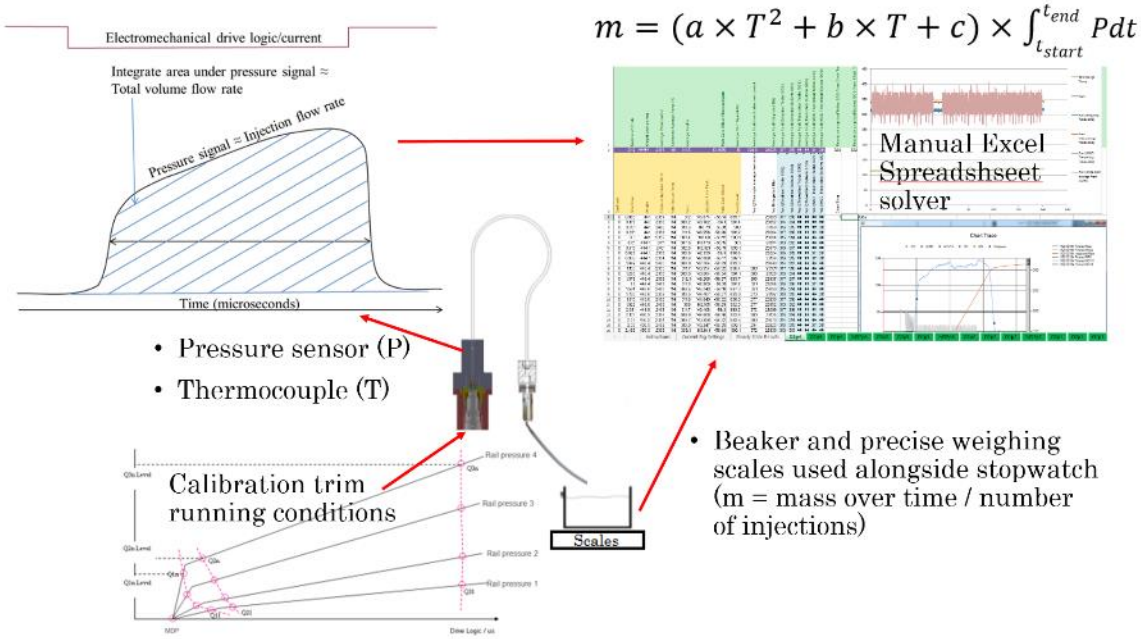


Figure 7.1: Existing manually operated weighing scales SOS to mass calibration technique.

Issues with this method include splatter outside of the beaker at high flow rates, resulting in loss of measured mass, evaporation and loss of measured mass to atmosphere as hot vapour, and manual intervention that disrupts the production output.

The regular checking of SOS to injected mass calibration is essential to maintaining the link between calculated injected mass from a rate tube and System International, via annual automotive manufacturing quality standard, external audit procedures (Ostadi, Aghdasi and Kazemzadeh, 2010). Therefore, an improved automated method was sought, to replace the flawed manual beaker and weighing scales technique.

If the accuracy of the derivation of polynomial terms can be improved, then it will improve the resultant temperature to SOS compensation. Which will improve the accuracy of the SOS estimation that dictates the signal magnitude and injected mass value. Greater calibration stability day-to-day could also be achieved if polynomial terms are automatically acquired, without production penalty, for each EU6 production measurement system.

Experimental scheme three achieved the commercial objective of automating this process whilst improving the precision of the SOS to mass calibration. Injected mass data from the calibrated coriolis mass meter was collected concurrently alongside the raw injection rate pressure signal in a continuous production environment. This was carried out using a specific set of known injectors with repeatable performance. Their performance was characterised once a day. A custom injector test program was developed to achieve steady state stable temperature conditions in the measurement system. This was required to capture a repeatable coriolis mass flow value that otherwise becomes distorted by fluid contraction effects under transient temperature injector test conditions. The test program ran through 16 steady state injector calibration trim conditions for the whole performance characterisation map. With a total daily cycle time of 20 minutes, the penalty to the daily production output was negligible and deemed acceptable for permanent implementation. An infographic outlining the calculation steps for this new procedure is shown in Figure 7.2.

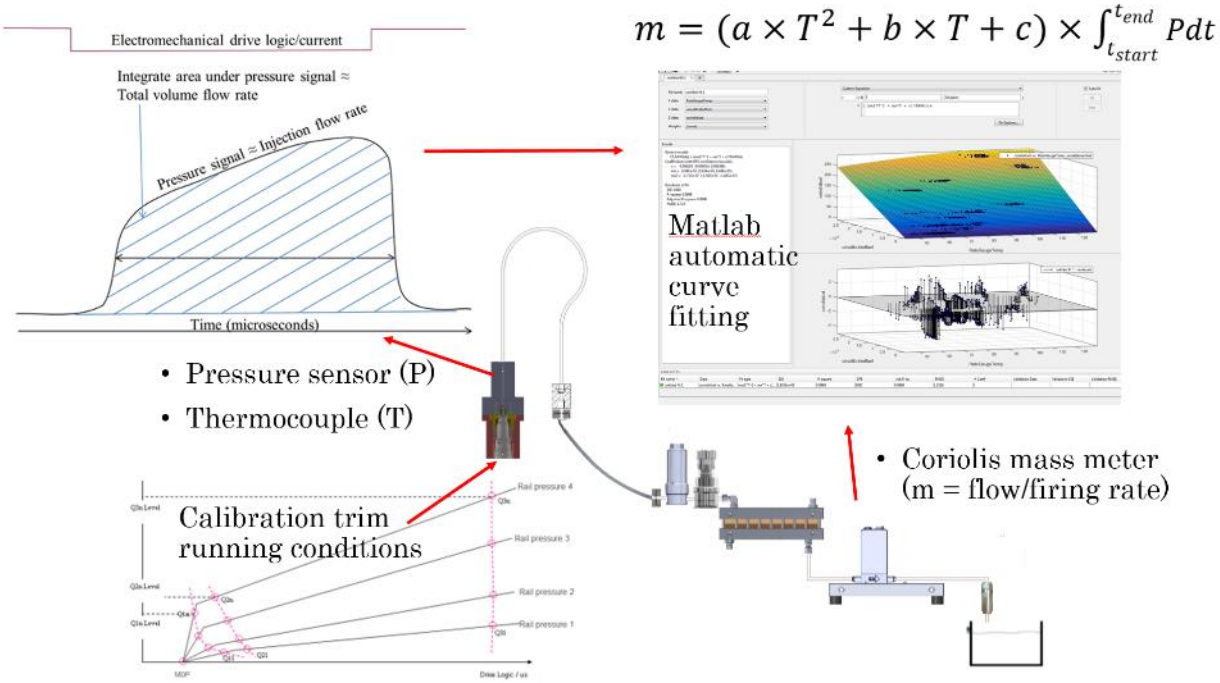


Figure 7.2: Newly developed automatic test cycle coriolis flow meter SOS to mass calibration technique.

7.2 Mass calibration curve fitting

The original technique involved acquiring a single data point from average volume over time collected in the beaker, which is converted to mass using density lookup tables for injector test fluid (Chorążewski *et al.*, 2013).

The automated test cycle used in experimental scheme three resulted in four large datasets for each of the four injectors studied. Each dataset contained data points for each of the 16 injector calibration test conditions. Resulting in over 1000 data points per test condition and injector over the three-month period of study.

With these new high-quality datasets in hand, two techniques were tried to improve the precision of the derivation of mass polynomial terms. First the traditional polynomial was fitted using the Matlab curve fitting toolbox and this large dataset, as seen in Figure 7.3.

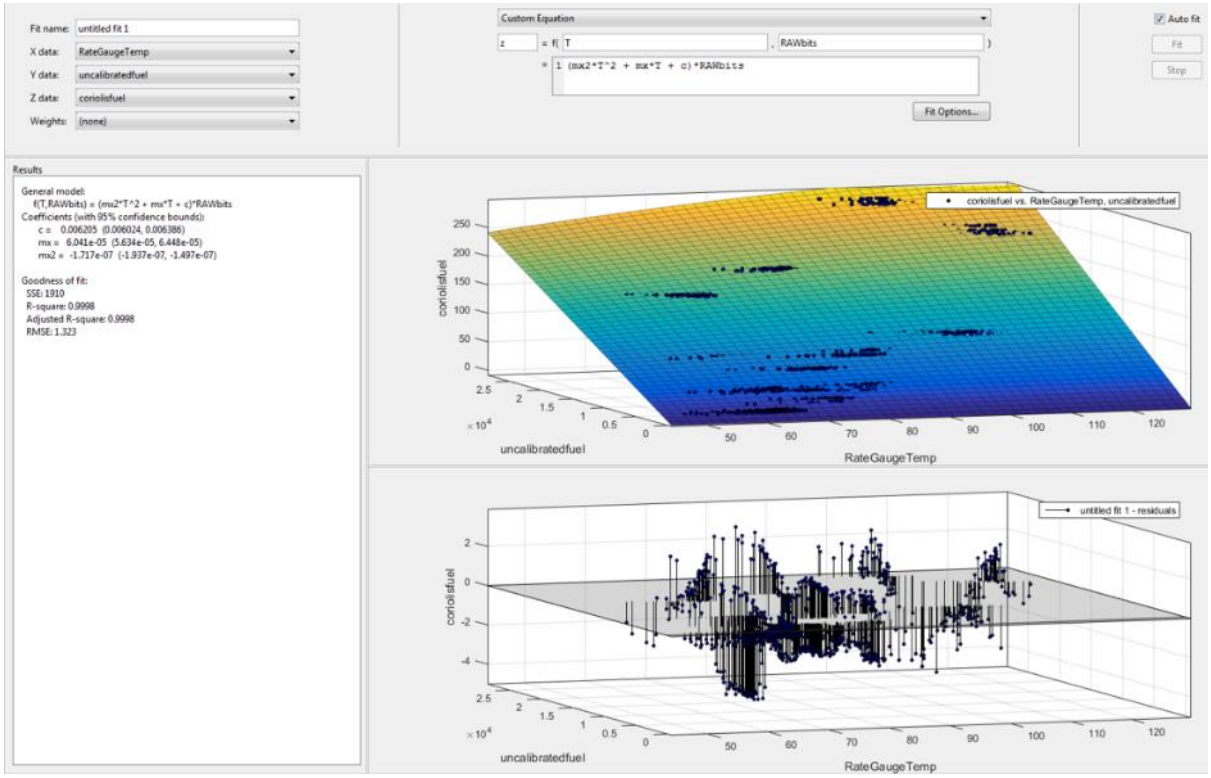


Figure 7.3: View of the Matlab curve fitting toolbox for 1 of the 4 datasets polynomial fit. uncalibrated fuel/RAWbits = Raw pressure signal at observation point; RateGuageTemp = Temperature of the thermocouple at the observation point; coriolisFuel = Average coriolis mass flow per second divided by the firing rate. Top: Surface map of polynomial fit. Bottom: Residual errors for the polynomial fit.

The datasets were manually pre filtered by removing data for test cycles where a fault was indicated on the measurement system. Which was identified by an abnormally high standard deviation of consecutive mass flow measurements.

Bi-square weights regression robustness method was used to minimise the influence of any remaining statistical outliers that could otherwise skew the polynomial derivation.

The second technique evaluated was using a simple single layer neural network comprising ten nodes. Trained using the Levenberg technique with 15% of the dataset used for validation. It was trained using default stopping parameters, as provided by Matlab neural network fitting app. An optimal solution is quickly found, and training completes the first ten training epochs as shown in Figure 7.4.

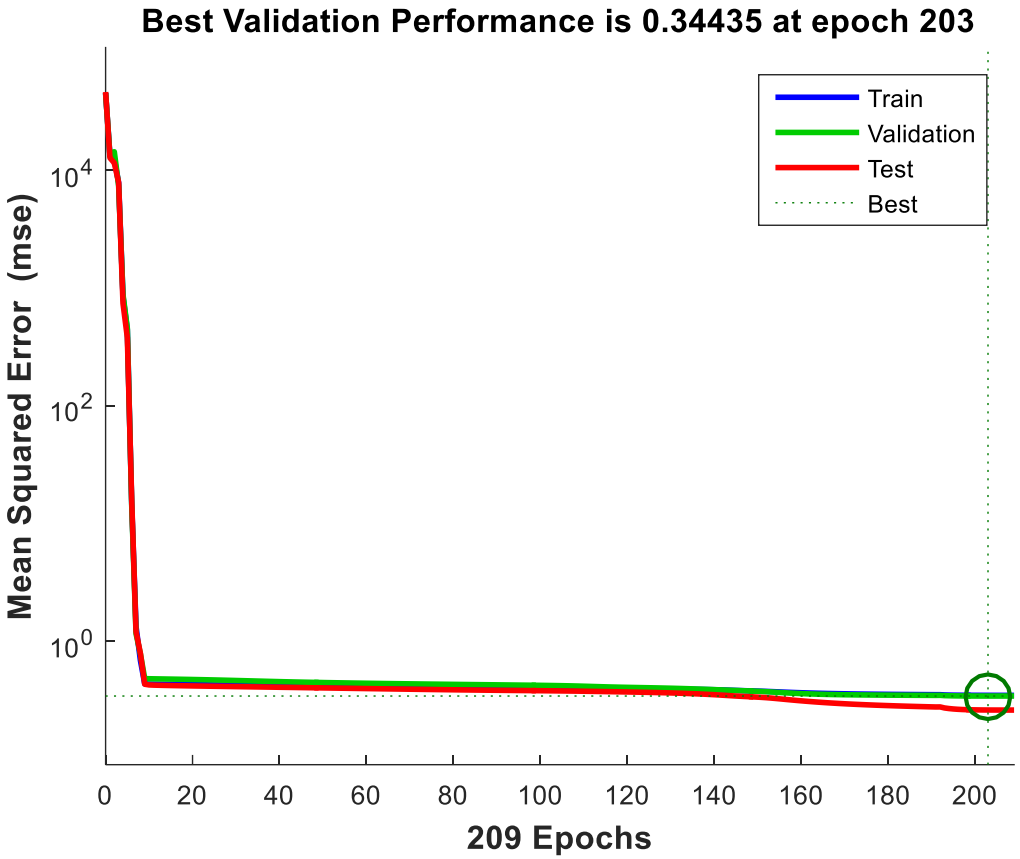


Figure 7.4: View of the Matlab neural network fitting app training epoch output for simple single layer network trained using 85%/15% training/validation dataset split and Levenberg technique for the 1000 data points.

A comparison of the Root Mean Square Error (RSME), representing quality of fit for the different techniques, is shown in Figure 7.5.

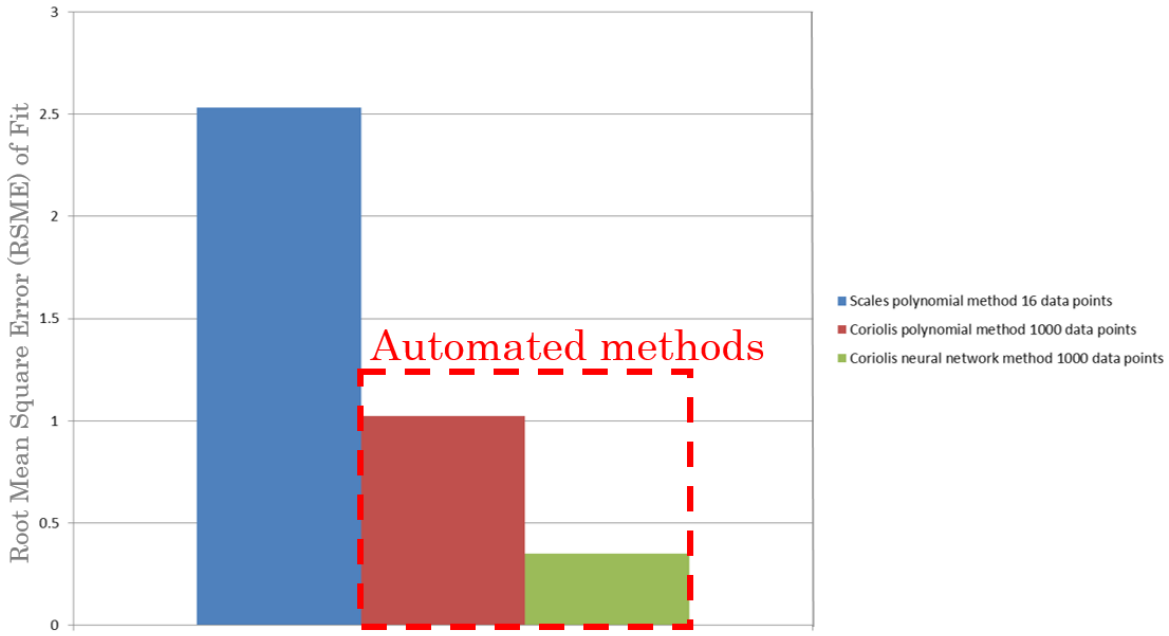


Figure 7.5: Root Mean Square Error of SOS to temperature compensation using different techniques.

The original technique, involving scales and only 16 data points in an excel solver, had an RMSE of 2.5mg. This calibration was manually undertaken by EU6 test development engineers over an extended period, so should represent the best result that can be achieved with that technique. Despite this, it shows significantly higher RMSE compared to the novel automated methods trialled.

When using a larger dataset and robust regression fitting techniques, an average RMSE of 1mg was achieved for all four datasets with a range of 0.7mg to 1.3mg. This significant improvement in error of fit demonstrates that large datasets automatically acquired, can provide a more accurate SOS calibration map, when compared to the original manual technique.

The Levenberg neural network fit (Gavin, 2011), was explored to see what is achievable when not constrained by a 2nd order polynomial based map. The RMSE result of 0.35mg is significantly improved on the polynomial fit RMSE error of 1mg when using the same dataset. Therefore, it is possible to produce a better SOS compensation map, using a Levenberg trained neural network, instead of polynomial curve fitting techniques.

The major risk with the neural network technique is over-fitting of the result, the 15% split for validation data goes some way to mitigate this. If the SOS calibration map is over fitted, it can produce an unstable result (Paluszek and Thomas, 2016), and hence requires further study before it can be used with confidence.

The original scope of this stage was to produce a new automated method for deriving polynomial fit constants. The production test equipment software already uses the polynomial, and the use of a neural network in its place would require significant software modification and validation. The effort to pursue the neural network implementation was deemed unnecessary, due to the level of improvement in RMSE seen for using a polynomial, fed with data points automatically captured over long time periods, instead of scales and a beaker.

The measurement system design used for experimental scheme three is known to have introduced a temperature dependant low frequency zero value variance as described in Section 5.3. Whilst this influenced the transient production test cycle, the stable steady state temperatures used in this datasets collection meant that this additional zero value variance was not present.

With the commercial objective met by demonstrating this automated technique, the work moved onto analysis of sources of variance present at the end of injection as discussed in the next Section.

8 End of injection variance

Once zero value variance, high frequency variance and rate height had been characterised and mitigated, the work moved onto studying the subtle sources of variance present at the end of the injection event. Summarised in in Figure 8.1.

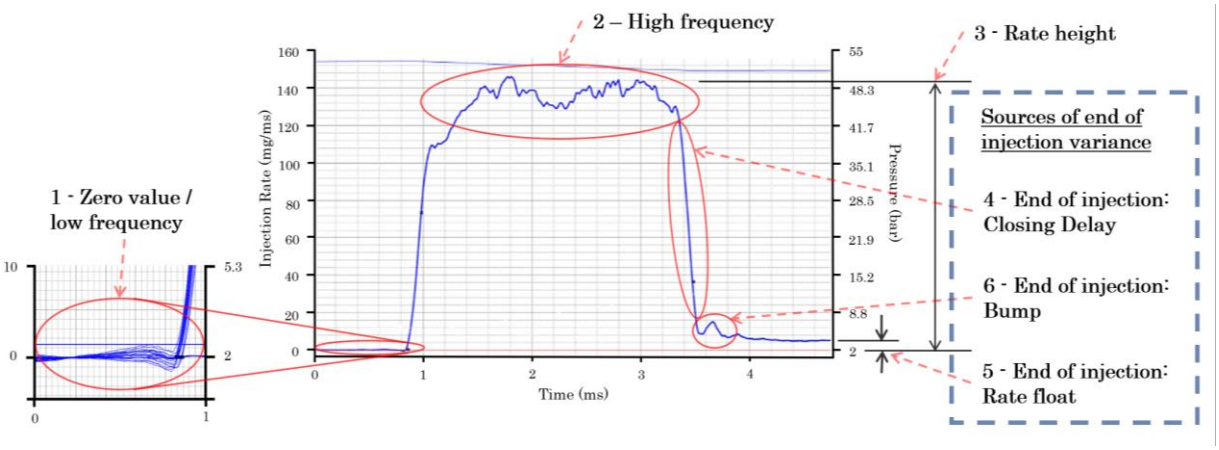


Figure 8.1: Sources of variance identified for an injection rate measurement device with the three sources of end of injection event variance highlighted in dashed box.

End of injection sources of measurement variance were previously masked by the magnitude of low frequency zero value and high frequency variances in the signal. Minimising zero value and high frequency variances enabled characterisation of end of injection variances for the first time in Delphi Technologies. This was achieved by revisiting datasets from experimental scheme four, that featured the optimised hydraulic circuit design and SCP slim ground isolated amplifier.

To derive the injected mass from a rate tube measurement, the integral of the pressure wave observed must be calculated for the duration of the injection event. The start and end of the integration is carried out between thresholds for the start and end of the injection event. The start of injection is easily identifiable using a first-order differential threshold approach. However, achieving a stable end of injection threshold is difficult on a rate tube injection meter, because of a bump artefact of variable height, present once the injection rate signal has fully decayed and the injection event has finished, as illustrated in Figure 8.2.

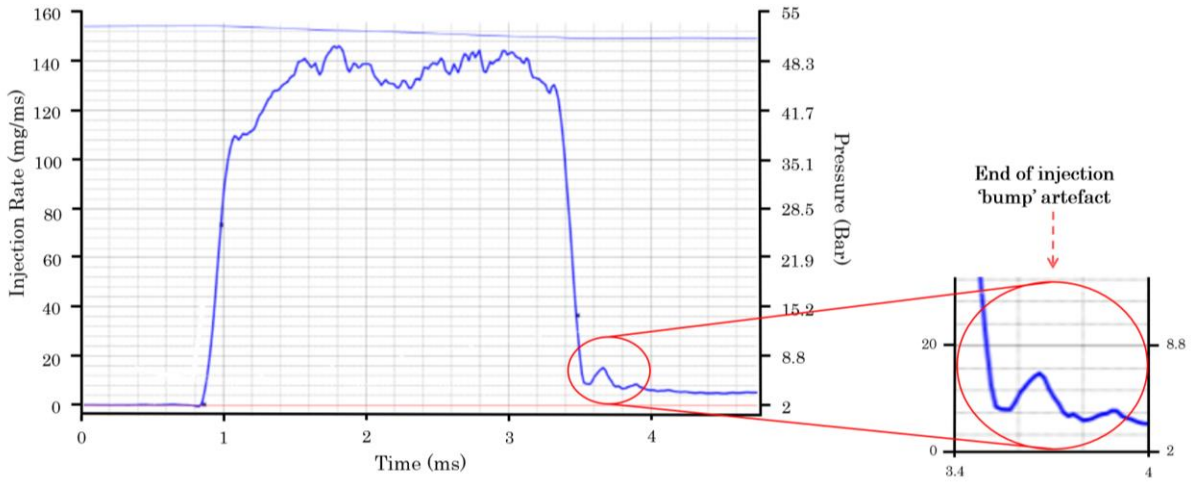


Figure 8.2: Post end of injection rate shape distortion in the form of a bump artefact.

The author is not aware of any experimental studies into the source of this specific artefact on a rate tube injection meter. It was observed during experimental scheme one that this artefact could indicate a wide range of potential fault conditions in the injector nozzle fixture. Caused by an application specific error in the nozzle fixture design, described in Appendix 11.4.1, that allowed a secondary sealed accumulation volume to form by accident. Once the design error had been removed, it was possible to characterise the inherent source of this artefact and is discussed in the following Section.

8.1 Influence of injection rate observation position

When end of injection distortion because of seal failure was interlocked, as described in Appendix 11.4.1, it was possible to study the root cause of the bump artefact at the end of injection for the first time. To achieve this during experimental scheme four, the injection rate sensor was installed as close to the injector nozzle as possible. The resulting injection rate signal was compared to the standard position. An illustration of the two sensor positions can be seen in Figure 8.3.

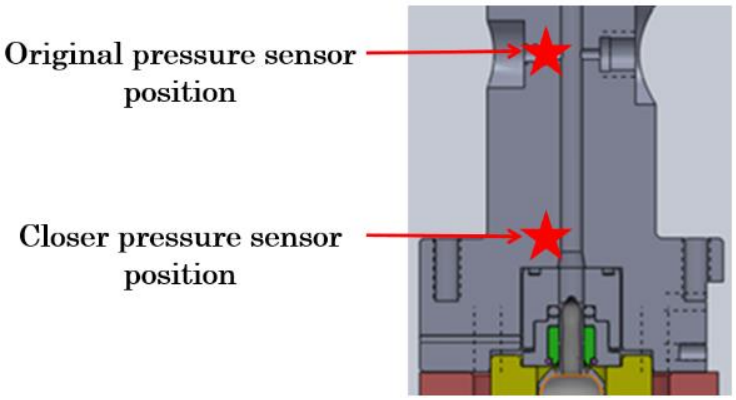


Figure 8.3: Original and closer pressure sensor position in the injector nozzle tooling fixture.

The injection rate for the 2400bar pressure 2300µs duration injection condition for both sensor positions is shown in Figure 8.4.

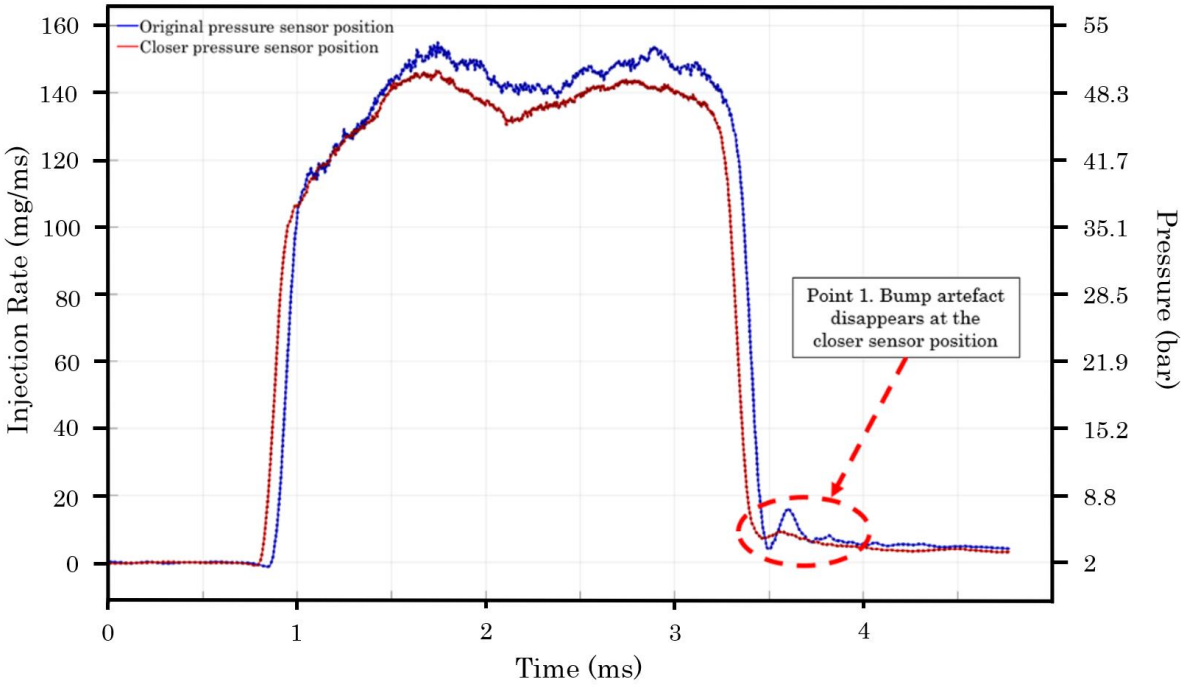


Figure 8.4: 2400bar pressure 2300µs duration injection rate shape comparison for the two pressure sensor positions.
Blue: Original position.
Red: Closer position.

The end of injection bump disappears for the closer sensor position case as shown by point 1 of Figure 8.4. Therefore, the bump artefact at end of injection is caused by the distance of the observation point from the injector nozzle and is not a characteristic of the true injection rate.

The Kistler 6054 piezo electric rate sensor failed after only a few hours of use at the closer observation point. The cause was identified as a significant increase in excitation of the sensors' 150kHz natural frequency. Evidenced by increased magnitude of the all the high frequency activity observed in spectrogram analysis discussed in Section 6.1.1. At the standard more distant observation point, this same sensor has an average lifespan of six months on production equipment. The additional frequency excitation at the closer position is caused by the sensor diaphragm being directly exposed to the injection event. Where shock waves produced by cavitation collapse in the injection event are at their greatest intensities. Hence, using the current hardware evaluated, the closer sensor position is not a practical solution in a production environment.

This result shows that to capture a mass injection rate signal with minimal distortion, the observation point should be as close to the injection event as

possible. However, to take advantage of this knowledge, a sensor with a much higher natural frequency between 300-500kHz could be used. Such as piezo electric sensors used for gas turbine applications that are optimised for high levels of structural vibration (Davulis, Kosinski and Da Cunha, 2006).

This result suggests that the bump artefact at end of injection is caused by the distance travelled up the rate tube bore by the high frequency pressure waves, generated due to the cavitation in the mass injection event. This demonstrates that the bump is an artefact that is formed by the pressure waves travelling up, shedding energy to, then partially reflecting off the rate the pipe bore. Therefore, the bump artefact contains high frequency pressure wave signal magnitudes that are required to calculate the true total injected mass.

Spectrogram content reduces in magnitude whilst introducing the bump artefact for the standard, more distant, injection rate observation point. Therefore, the loss of injection rate fidelity is in the high frequency domain. It is known that high frequencies will interact with the surface roughness of a tube's inner wall (Zielke, 1968). Therefore, the end of injection bump artefact must be a product of the high frequency content in the injection event shedding energy to the rate tube bore wall and partially reflecting off it in multiple directions. Causing a gradual distortion of the injection rate as the wave travels up the tube bore.

A similar but more exaggerated effect was observed by (ARAKI *et al.*, 2007) showing progressive distortion of the pressure wave along the rate tube length for a gas injector application, as illustrated in Figure 8.5.

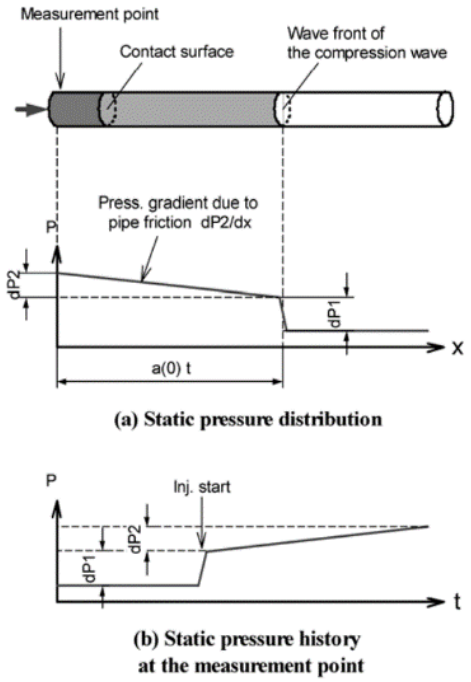


Figure 8.5: Effect of pipe friction on pressure gradient within a pipe. As demonstrated for a gas injector using the Bosch rate tube method by ARAKI et al. (2007).

Therefore, another way to mitigate this high frequency rate content distortion may be to polish the inner bore of the rate tube nozzle tooling's inner diameter to an ultra-fine mirror finish. This would only be necessary for the length of rate tube bore between the injector nozzle and rate observation point.

The knowledge gained from this work enabled the selection of an appropriate sensor for the EU7 F3 injection application on the Loccioni Mexus device. During its initial development, piezoelectric pressure sensors would fail within days of continuous use. Through a yearlong collaboration in 2018, a specialised sensor gas turbine sensor with a very high natural frequency of 500kHz was selected and proved robust in a production environment. Thus, this contribution to knowledge enabled EU7 injectors to be tested in a production environment in 2019.

8.2 Rate float

The primary weakness often quoted for rate tube injection meters (Gandhi, Meinhart and Ortiz, 2009) is that they suffer from what is known as rate float within Delphi Technologies, and referred to as the cumulative signal phenomenon in published literature (Payri *et al.*, 2008). It is a cumulative offset superimposed on the injection rate trace, characterised by the signal not returning to baseline backpressure at the end of the injection event and is illustrated in Figure 8.6.

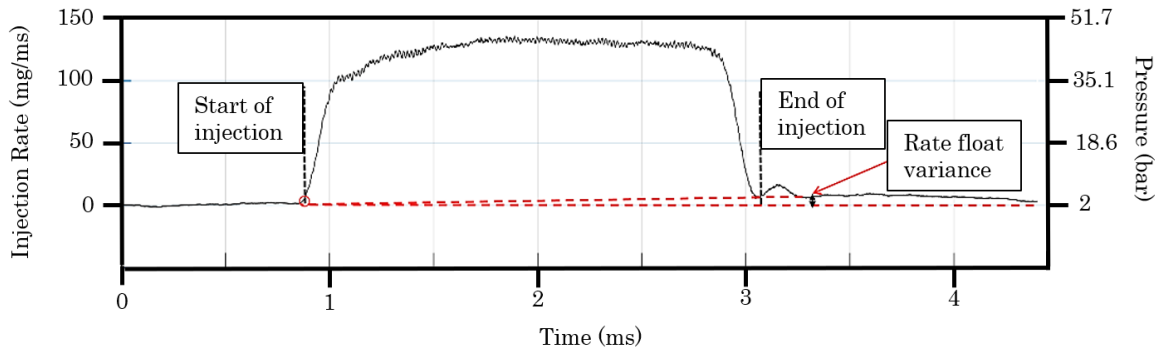


Figure 8.6: Illustration describing the Rate float / signal cumulative phenomenon effect 2300bar pressure 2300µs duration injection event.

It is caused by a temperature rise near the injection rate observation point that coincides with the start and end of the injection event. Attributed to heating of the fluid medium local to the injector nozzle by fluid shear and cavitation collapse induced by the injection event by van Bebber and Reuter (2017).

This fast transient rise in temperature in the fluid medium local to the injection rate observation point leads to an observed rise in pressure and injection rate. The rise in pressure begins with the injection event and ceases once injection has

finished. The pressure in the tube then decays back to baseline backpressure after a period of a millisecond or more. Therefore, the magnitude of this variance is linked to and increases with injection duration.

Previous attempts at Delphi Technologies to study this effect had been confounded by zero value variance and high frequency distortion. Those sources of variance are known to convolve on top of and hence will distort the true rate float characteristic at the end of injection. The optimisation carried out on experimental scheme four to minimise zero value variance and high frequency noise enabled a detailed study without distortion for the first time in Delphi Technologies.

Application specific investigations detailing how rate float specifically influences the F2 EU6 test can be found in Appendix 11.5.

8.2.1 Characterisation of rate float

The production rate tube measurement systems in Delphi Technologies allow for a small magnitude, less than 5mg, offset to be applied to the measurement. This offset is fixed and not linked to temperature. Therefore, variance in the injection rate float magnitude, driven by changing system temperatures test to test, will act as an error on top of the fixed offset.

Tuning criteria to stabilise the error were required for use during production injector test program development. To establish the necessary criteria, an experiment was devised to identify the effect of the localised nozzle event on fluid temperature.

Experimental scheme one was initialised to ambient temperatures, followed by a fixed 15Hz firing rate, 2400bar pressure 2300µs duration injection input for 20 minutes. This procedure was repeated ten times, to establish a range of temperature between tests. The range in temperature at different observation points local to the nozzle was then compared to the magnitude of rate float, at different time intervals. The acquisition had to be initialised for the first 60 seconds after a cold start, before automatic data logging could occur. During this period, images of the injection rate display were manually captured at ten-second intervals, as shown in Figure 8.7.

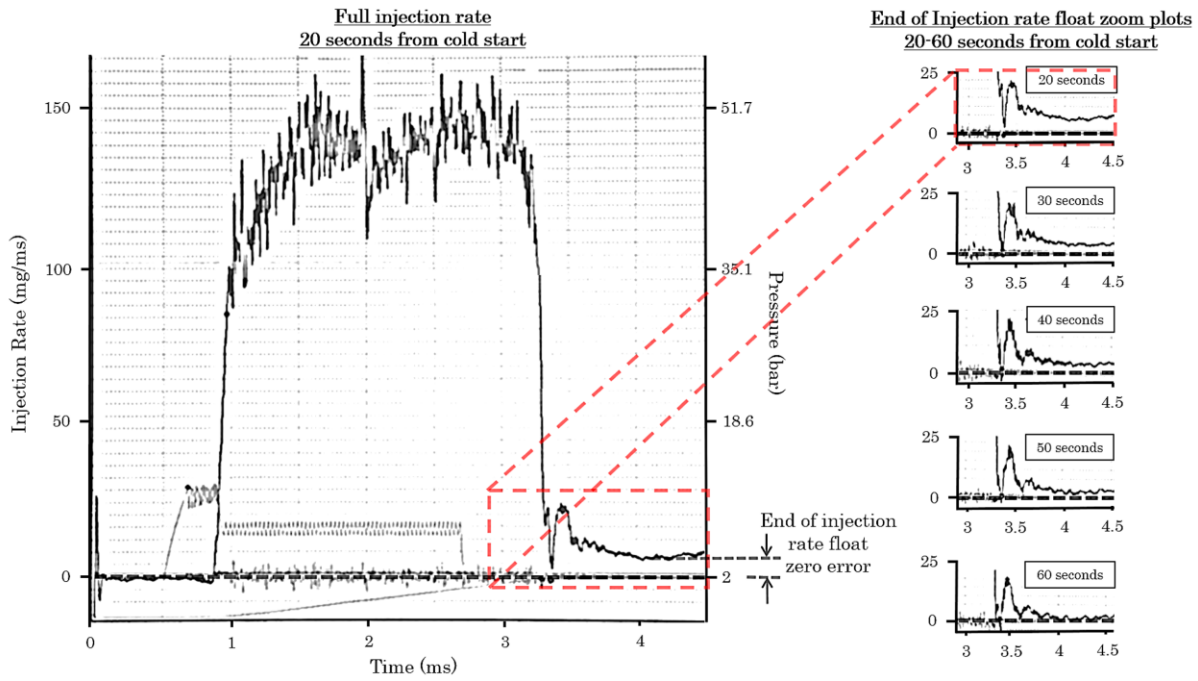


Figure 8.7: Photographic images of test machine console injection rate display for first 60 seconds after a cold start.
2400bar pressure 2300µs duration injection condition held for 15 minutes.

The first measurement trace could not be captured until after 20 seconds, because of entrained air in the rate tube, introduced into the fluid medium during clamping and un-clamping the injector for each test cycle. This entrained air at the start of each test cycle significantly distorts SOS until it is flushed out of the tube after 20 seconds.

The rate float is severe at 20 seconds and would introduce a large error to the measurement. After 40 seconds it stabilises to a consistent magnitude over time and the greatest change is observed between 20 and 30 seconds time period.

The range of temperature at the injection rate observation point was evaluated at 1-second intervals for the initial 60-second period as shown in Figure 8.8. The surface temperature of the nozzle tooling was examined for the same time period as shown in Figure 8.9.

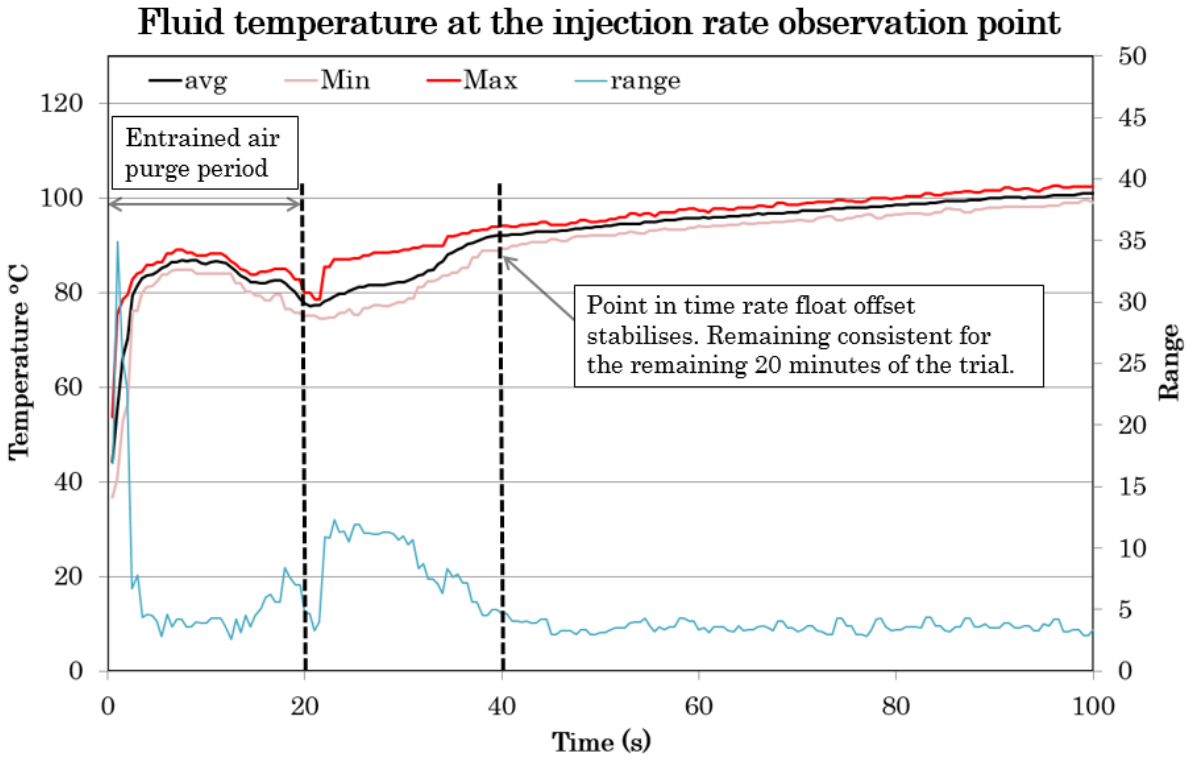


Figure 8.8: Temperature at the injection rate sensor during warmup from a cold start. 2400bar pressure 2300µs duration injection condition.

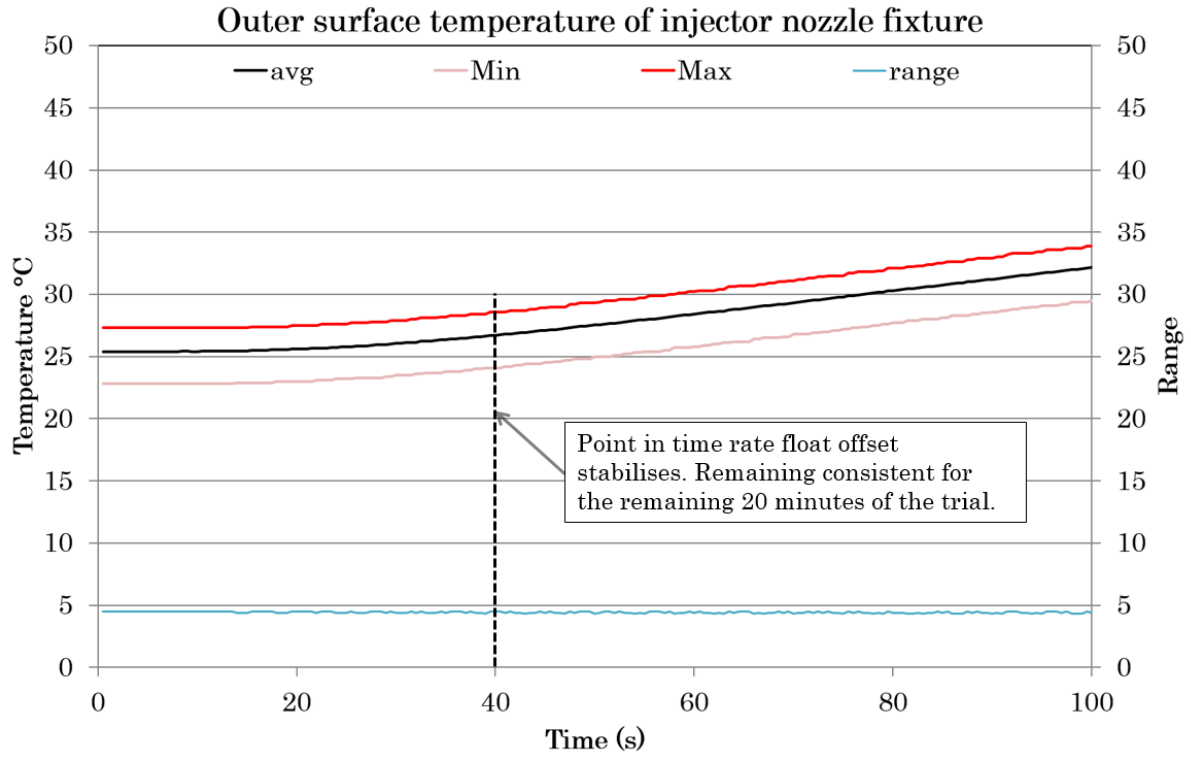


Figure 8.9: Temperature at the outer surface of the nozzle tooling during warmup from ambient temperatures.
2400bar pressure 2300µs duration injection condition.

After 40 seconds, the range in temperature at the injection rate sensor becomes consistent across the ten tests, maintaining a near constant time-series gradient. This matches the time when the measurement trace displays a minimal and stable rate float offset.

This coincides with the time when the surface temperature of the nozzle tooling also increases with a linear gradient. Representing the thermal transfer taking place between the hot fluid medium and the mass of the nozzle tooling. When the thermal mass of the nozzle tooling is changing with a linear trend over time, then its influence on the fluid medium temperature will be consistent test to test.

From this result, criteria for rate float error stabilisation was identified as a linear trend in temperature change over time being achieved, in the fluid medium, at the observation point.

This novel tuning criterion to minimise rate float variance enables the use of a fixed offset on the production injector test. Negating the need for compensation algorithms with thresholds that require the end of injection to be free from other sources of variance. Such as the popular method proposed by Payri *et al.* (2016).

This criterion was used to optimise EU6 production injector test cycles, reducing measurement stabilisation times by up to 50% in 2018. This was because of the previously conservative approach towards measurement stabilisation tuning necessary when there are no specific criteria to target.

8.3 Advanced data mining methods

At the end of experimental scheme four, all methods devised to minimise sources of measurement variance had been implemented. This was carried out to uncover any remaining unknown sources of measurement variance, using advanced data mining methodologies. With all other known sources of measurement variance addressed or characterised, hidden relationships can be revealed. Leading to novel sources of measurement variance being discovered for the first time.

Once the work on experimental scheme four concluded, a Matlab application was developed to allow advanced data mining functionality. Then applied to datasets from the variance optimised measurement system design.

A normalised matrix of all concurrently logged sensor data for any single test condition could be automatically constructed. Enabling various forms of correlation analysis available in the Matlab coding environment and user collaboration based FileExchange (Gulley, 2006).

Several techniques were used to explore relationships within these normalised datasets such as XY correlation charts of various forms (Joss and Müller, 2019), Principal component analysis of the first three most significant components (Richardson, 2009), stepwise regression feature selection with a ReliefF feature ranking layer (De Carli, Mejia and De Araújo, 2019) applied to its result. The fuel variance from the mean of each dataset of ten consecutive transient production tests was used as the response variable.

These analysis techniques were automated and applied to 159 separate transient production injector test conditions covering the entire F2 EU6 injector characterisation map.

Using this technique, unknown sources of variance were revealed, that were otherwise hidden, using traditional data analysis techniques. The most significant hidden feature revealed by this analysis was a link between measured fuel variance and Closing Delay (CD) variance. CD is a measure of the time between the injector electronic control signal ending and the measured end of the injection event using the injection rate signal. This strong correlation was observed at the 2400bar pressure 745µs duration injection condition as shown in Figure 8.10.

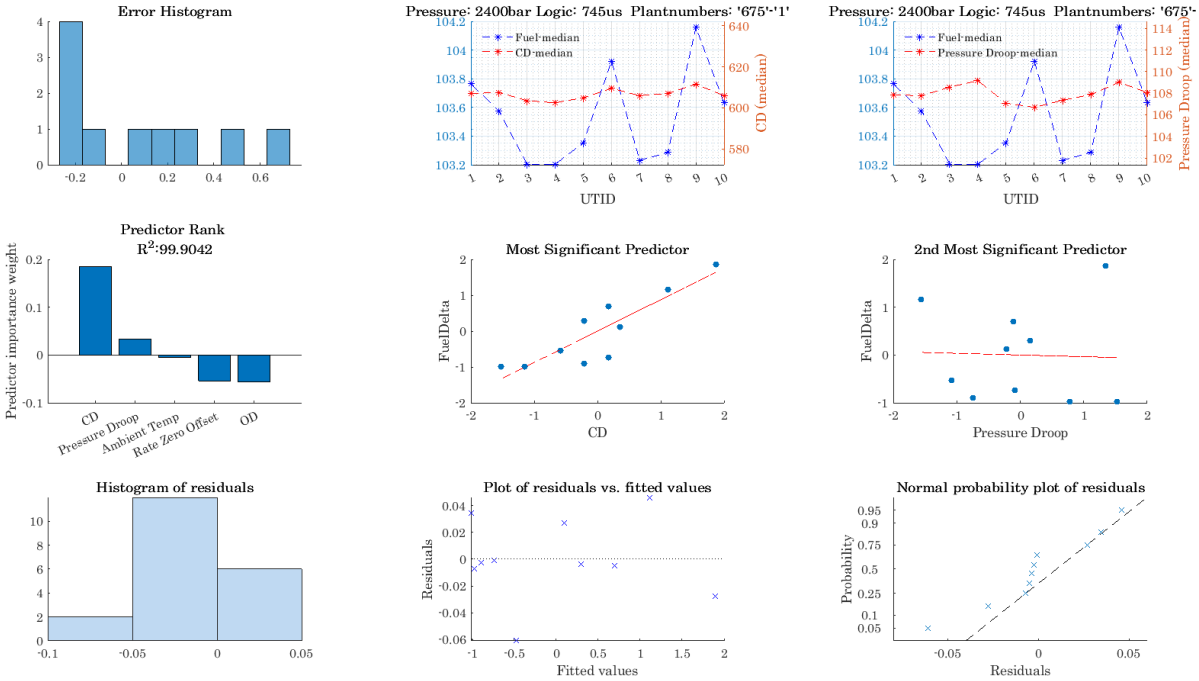


Figure 8.10: Stepwise feature selection with a ReliefF feature ranking layer applied to the result at the transient 2400bar pressure 745µs duration injection condition. Deviation in measured fuel value between injector test cycles as the target. CD and Supply pressure droop provide a combined predictor rank of 99% suggesting a strong relationship to fuel variance.

This relationship was is also apparent in the principal component domain. Where CD is strongly positively correlated with the variance of injected fuel

mass on the first most significant principal component axis, as highlighted in Figure 8.11.

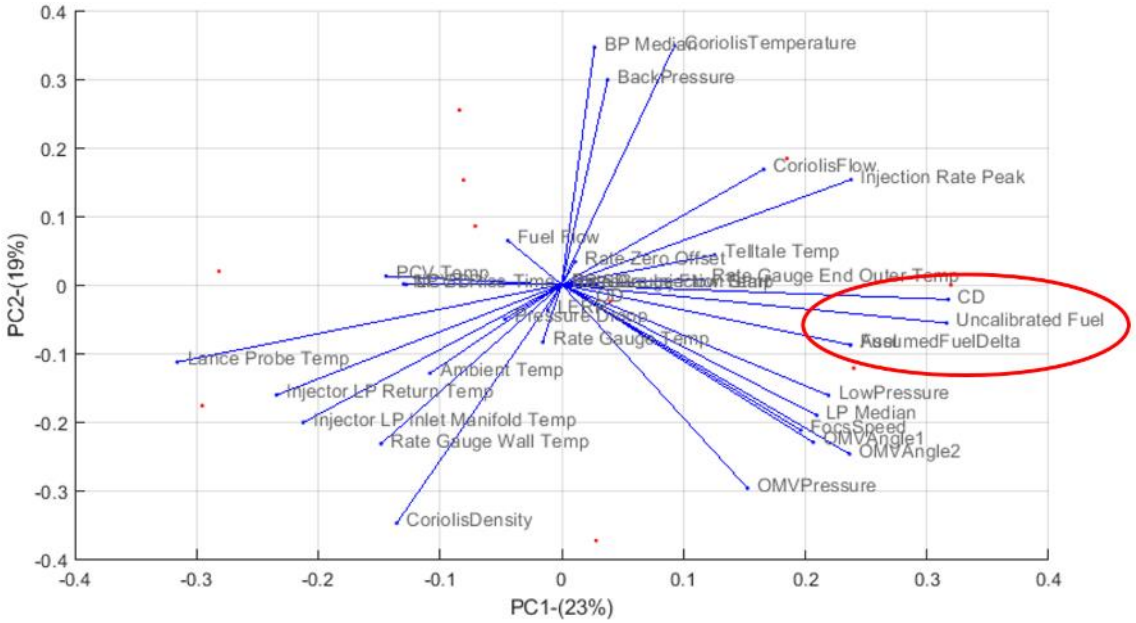


Figure 8.11: First two principal components for the 2400bar pressure 745µs duration injection condition with a strong positive correlation between CD and the Assumed fuel delta.

The secondary predictor of pressure drop in the injection pressure supply rail indicated an interaction between the injector supply pressure dynamics and variability in the end of the injection event timing.

These techniques can summarise large datasets into their primary relationships. The insight gained enables focussed investigations to uncover the causal nature of these relationships. Therefore, this result shows the power of advanced data mining analytics to reduce the time between data collection, evaluation and identification of novel sources of measurement variance.

8.4 Rail pressure influence on Closing Delay

The relationship between CD and variance in injected fuel mass was revealed by the mining. Knowledge of this hidden variance enabled a targeted experimental investigation to be carried out to identify the casual relationship driving it.

This was achieved by searching for this relationship at the 1625bar and 925bar injection pressure characterisation portions of the transient production injector test cycle. The same effect was observed but at different increasing injection durations, for decreasing injection pressures. The injection durations at which this effect appears is shown in Table 8.1.

Table 8.1: Injection pressure level in the transient production injector test and the corresponding injection duration at which peak closing delay variance is observed.

Injection Pressure (bar)	Peak Closing Delay standard deviation injection duration (μs)
2400	745
1625	900
925	1100

The injection durations where the relationship between CD and total injected mass variance occurs, increase as the injection pressure lowers. If this relationship was dictated by SOS decreasing isothermally (Bazile *et al.*, 2012), for lower injection pressures, it would decrease.

The temperature of the fluid will also affect SOS. On experimental scheme 3, the ISO4113 fluid is held at 40±3 degrees Celsius at the inlet to the high pressure pumps. The fluid is then heated during compression inside the pumps to reach the required injection pressure. This results in an injector high pressure supply fluid temperature that increases with increased compression required to reach higher injection pressures. It was observed on experimental scheme 3 that the injector supply pipe steady state temperature varied from 40-45 degrees for the lowest to highest injection pressures.

For a 5 degree Celsius temperature range, pressure related SOS changes will be dominant (Bazile *et al.*, 2012). Therefore, as injection pressure decreases, any quarter wave effects will elongate their wavelength with a decrease in SOS and occur at a longer injection duration. This confirms that this is a high pressure hydraulic resonance effect, as it changes as expected for typical SOS values in the fluid at different pressure levels.

It was theorised that if this is a real hydraulic effect, then it may be related to frequencies generated by resonant quarter wave effects. To understand what feature in the system is causing this resonant effect, a calculation for the quarter wavelength was carried out. The quarter wave resonance equation can be changed to solve for length of the feature, if SOS and frequency are known, as shown by the quarter wave Equation [8.1].

$$L = \frac{c}{4f} \qquad [\,8.1\,]$$

Where c is the speed of sound (SOS) and f is the frequency observed.

The SOS value for ISO 4113 oil at the injection supply pressures was obtained from the lookup tables at 318 K provided by Bazile *et al.* (2012) at three supply pressures. The SOS at 2400bar injection pressure was estimated to be 2000m/s

via extrapolation above the highest 2000bar pressure they characterised. Using the injection duration as the approximate wave travel time, the frequency and the length of the feature are estimated as 1342 Hz and 0.37m respectively.

In experimental scheme four, the high pressure pipe connecting the injector to the rail, has a length of 0.375m, which ties up closely with the estimated value as illustrated in Figure 8.12.

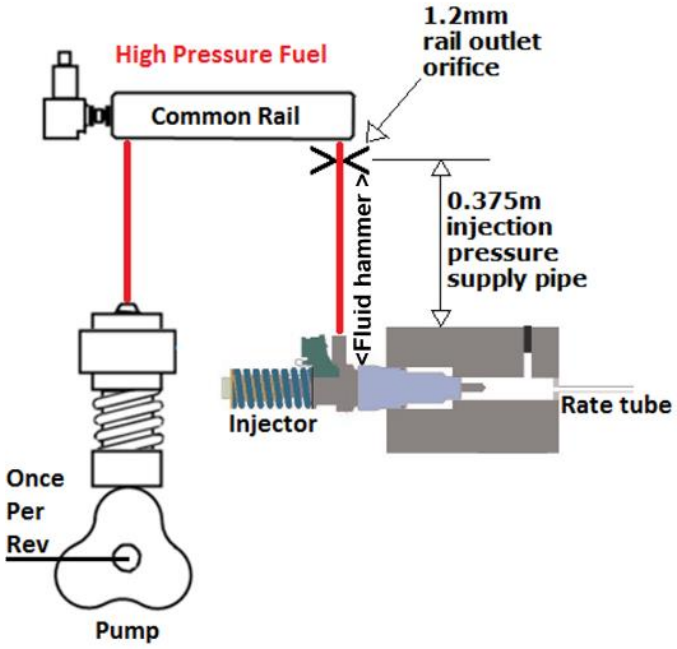


Figure 8.12: Illustration of the fluid hammer location in the high pressure supply pipe configuration of experimental scheme four.

This result confirmed that there is a hidden measurement variance, in the form of a fluid hammer within the high pressure supply pipe, that interacts with the nozzle closing event at the end of injection. Occurring at specific injection durations, that can be predicted by its resonant quarter wave frequency, that changes dependent on SOS.

This contribution to knowledge of an unknown source of measurement variance is one of many discovered using the advanced analytical techniques discussed. The use of which the author believes to be one of the most significant and lasting contributions to knowledge from this work. A novel automated method to identify unknown sources of measurement variance.

9 CONCLUSIONS

The research work outlined in previous chapters has been successful in characterising and minimising the primary sources of rate tube measurement variance in a production environment. This work was enabled by knowledge drawn from published work into the near future commercial vehicle injection rate measurement challenges, sources of measurement variance in a rate tube injection meter, methodologies for simulating hydraulic pressure wave activity and advanced data mining techniques available to extract novel knowledge from production data.

Informed by these reviews, experiments were devised and results analysed to fill the knowledge gap of the causal relationships driving measurement variance. This work then proposed, tested and implemented improvements to measurement system design and injector test methods. Required to minimise both known and novel sources of measurement variance, for transient injector calibration test cycles, in a production environment. The conclusions from the present work and their novel contribution to knowledge are as follows.

Referred to as zero value variance in the present work, low pressure waves in a rate tube measurement system, will become superimposed onto the injection rate signal, introducing significant error into the measurement of total injected mass. Literature had previously identified movement of the injector nozzle relative to the measurement system as a possible cause. But this effect was found not present when empirical trials were conducted on production equipment. Further empirical study of production equipment lead to the following contributions to knowledge, regarding novel sources of zero value variance:

i. The rate tube mass flow equation assumes a constant cross Section along its length. When cross-Sectional area of the rate tube is not uniform high frequency oscillations will appear at a period dictated by the rate tube resonant frequency.

ii. The frequencies of zero value variance are a combination of the primary rate tube resonant frequencies and its higher modal orders. Their magnitude is additionally influenced by convolved waves originating from the hydraulic configuration after the rate tube termination orifice. This work revealed empirical methods to reduce this influence:

    a. The volume of a flexible following (connecting) hose between the rate tube termination orifice and a flow impedance has a significant influence on zero value variance. Zero value variance magnitude is reduced by increasing the hose diameter and hence volume for a constant length, acting as a flexible hydraulic muffler connected at both ends.

b. If there is a flow impedance after the rate tube termination orifice, the increased backpressure will cause the magnitude of zero value frequency activity to increase. Installing a backpressure regulator positioned before any flow impedance was found to reduce the magnitude of this effect.

c. A back pressure regulator must have zero leakage at its inlet for mass flow rates of less than 0.15g/s to maintain stable backpressure at small injection rates.

A 1D hydraulic model of a rate tube was constructed, to identify the source of the causal relationship between hydraulic geometries and zero value variance. Meeting objective two of this work by using an advanced numerical technique. The following contributions to knowledge were derived from this simulation work:

i. Increased height of the first reflected wave in a rate tube injection meter is caused by an outward and returning reflected wave convolving at the injection rate observation point. An unexpected novel contribution to knowledge.

ii. The volume of a regulator following hose changes dependant on pressure pulsation acting on its flexible inner wall. This results in the hose quarter wave resonant frequency being distorted and superimposed on the injection rate signal. The following hose internal diameter, length and bulk modulus are critical parameters determining the magnitude and frequency content of zero value variance that will be observed.

iii. A leaking back pressure regulator acts as a fixed flow impedance, that causes a high magnitude low frequency wave artefact, synchronised to the injected mass flow input of the injector.

If low frequency activity is studied, damping techniques can be applied to the hydraulic configuration to eliminate this source of temperature dependant variance. This was achieved using an optimised hydraulic design with the following critical design features:

i. 1.2m aramid connection hose to minimise its quarter wave resonant excitation by the rate tube resonant frequency and it higher modes.

ii. Progressive orifice diaphragm regulators provide a flat pressure trend, responding proportionally to dynamic pressure wave inputs, without impeding flow.

iii. Accumulators before and after the rate tube orifice to damped both the rate tube, flexible hose resonant frequency magnitudes. Inlet restricted to

prevent Helmholtz resonance from their internal volumes. Enabling 25Hz firing rate capability on heavy-duty rate tube meters for the first time.

The source of variance found at peak injection rates was not known previous to this work. In Delphi Technologies it has been attributed to signal noise that must be filtered. To characterise this variance, unfiltered injection rate signals were assessed up to 200kHz, using an ensemble averaged spectrogram. The first time characterisation above 30kHz has been carried out on an injection rate meter. The following contributions to knowledge were attained with this technique:

i. The signal distortion present on the peak of a high pressure injection rate trace is caused by high frequency cavitation collapse, that starts and ends in time with the injection event.

ii. The injection rate sensor natural frequency is excited to a high magnitude. This was revealed to be the primary cause of sensor failure in rate tube measurement systems. A sensor with a high natural frequency, 150 kHz or greater is recommended for this application.

iii. Sensor port geometry will resonate because of excitation by this high frequency activity. Identified by its decaying ringing after injection ends. A quarter wave configuration is advised with a resonant frequency high enough, so it can be filtered whilst preserving the true mean injection rate signal.

iv. The sensor port resonant frequency is dominant in the injection rate signal and correlated with speed of sound (SOS) measured by other methods.

Cepstrum analysis was used for the first time on a rate tube injection meter to assess the periodic elements otherwise hidden in the injection rate signal. Meeting objective two, to use advanced numerical techniques. The following novel contributions to knowledge were revealed with this technique:

i. It can measure the rate tube resonant frequency and hence derive a SOS value for the rate tube.

ii. Its ability to separate periodic signal elements will highlight sources of periodic signal noise, such as periodic ECU drive signals superimposed on the injection rate by a ground loop. Leading to this loop being broken and the source of variance eliminated on production equipment.

The magnitude of the injection rate is dictated by SOS in the fluid which is not directly measured but inferred from a temperature reading. The precision of the temperature to SOS compensation was improved using large coriolis mass flow

datasets gained from trials on production equipment. A more accurate SOS value can be acquired using a Levenberg trained single layer neural network in place of the currently used second order polynomial function.

The elimination of low and high frequency variance was achieved on the final experimental setup. This made possible the characterisation of subtle sources of variance at the end of the injection event, for the first time at Delphi Technologies:

i. The bump artefact at the end of the injection event is a product of the distance of the observation point from the injection event.

ii. Some high frequency pressure wave magnitude is lost to frequency dependant friction of the rate tube inner wall. Leading to formation of the bump artefact. From literature it was thought this was a nozzle rebound at the end of injection. This is the first time frequency distortion caused by the observation point has been demonstrated on a heavy duty diesel rate tube meter, proving it is not a product of injector performance.

Injection rate float is a cumulative offset that starts and ends with the injection event, a product of temperature increases because of cavitation and fluid shear local to the rate observation point. A criteria to identify when the variance in rate float is minimised was revealed:

i. Rate float will be variable test to test if rate of change of temperature in the measurement system is not linear over time. Caused by thermal mass of the injector tooling, interacting with the fluid medium temperature near the injection rate observation point.

ii. Whenever there is a large change in injection temperature, a certain amount of time will be required for the thermal influence of the nozzle tooling to saturate and be negated. If this is not accounted for, injection rate float will have a variable magnitude test to test, for the same test starting conditions. A critical transient injector production test tuning parameter not previously understood.

To identify unknown and novel sources of measurement variance, normalised injector test data was used as inputs for advanced numerical data mining techniques. This enabled the use of Stepwise regression with a ReliefF importance ranking and visualisation of the dataset in Principal Component axis, satisfying objective two, to use advanced analytical techniques. These techniques identified a novel source of variance for the first time:

i. Closing delay variance increases significantly when quarter wave resonance of its high pressure supply pipe coincides with the end of the

injection event. Therefore hydraulic geometry of the high pressure supply system is a critical injector test equipment design consideration.

9.1 Commercial objective: Improve Overall Equipment Effectiveness (OEE)

The primary commercial objective of the present work was to improve OEE.

$$OEE = Availability \times Performance \times Quality$$

The OEE was improved from 70% to 80% by Q1 2019. A permanent 10% increase as a direct result of the following contributions from this work.

A Matlab application called Pythia was developed as part of the design of experiments for experimental scheme 4 and has been primary source of figures in this thesis. All the analysis techniques used in the course of the current work were adapted to be applied to production injector test data. This application enabled improved process *Availability* after its launch in production in 2018. Used as part of a 3 month machine evaluation by the author to identify sources of variance specific to each production measurement system. Using knowledge gained and normalised data-mining techniques, a checklist of critical parameters was devised and applied weekly. This methodology resulted in the identification of previously undetected faults having subtle influences on the measurement variance. The outcome of this analysis was a task list for operations engineers to carry out each week and is now standard procedure.

The process *Performance* was improved by developing a novel production injector test cycle that achieved a cycle time reduction of 40 seconds or 12.5% for all F2 EU6 production variants, enabled by the following research outcomes:

i. The ECU drive signal ground loop signal noise identified by Cepstrum was eliminated by fitting ground isolated amplifiers to all production measurement systems. Resulting in an order-of-magnitude reduction in shot to shot variance at peak injection loads, which enabled a reduced number of measurements per injection condition from 5 to 3.

ii. Minimal rate float variance was achieved by reducing measurement stabilisation times by up to 50%, using the stable rate float linear temperature trend criteria, identified in this work.

These cycle time reduction efforts raised the maximum daily output capability of each 4 head injector test machine from 900 injectors a day to 1300.

The product *Quality* was improved due to minimal distortion of the injection rate, that enabled targeted product performance investigations previously impossible with a high injection rate signal-to-noise ratio.

9.1.1 Secondary commercial objective: EU7 knowledge transfer

The stepwise regression method of highlighting relationships within large injector test datasets enabled sources of measurement to be identified for the EU7 application during its development in 2018, in collaboration with commercial measurement system manufacturers IAV and Loccioni. Leading to a successful product launch of EU7 injectors into series production in 2019.

9.2 Limitations of this present work

Using production hardware as the experimental schemes for this work limited hydraulic and geometric changes that could be trialled. The same 3m rate tube form had to be used throughout and changes limited to its termination and backpressure system attached after the termination orifice.

The spectrogram analysis was limited to 200kHz by the signal amplifier and logged at a 1MHz sampling rate. However, it is possible that frequency activity beyond 200kHz is also present. Hence, the ideal sensor natural frequency that would avoid excitation by cavitation is not known, but will be higher than the range studied in this work.

The frequencies observed in the injection rate using Spectrogram analysis include sensor and port resonant frequencies as well as cavitation. To delineate the frequency content accelerometers are needed on the injector tooling to cross compare their frequency domain content with the injection rate. This was not possible with the sensors and acquisition channels used in the experimental schemes.

The bump at the end of injection was found to disappear when injection rate was measured near the nozzle. However, this lead to early sensor failure after a matter of days, because of the excitation of its 150kHz natural frequency. Other sensors with higher natural frequencies are available commercially, but could not be sourced before experimental activities ceased. Hence the bump artefact at the end of injection remains present on production equipment.

9.3 Directions for future research

More exotic measurement system hydraulic configurations could be trialled if using a bespoke laboratory experimental setup. In future it is advised to develop a platform which would allow a wider range of configurations that are not constrained by the layout of existing production hardware. Such as the integration of fixed form passive acoustic attenuation features possible by additive manufacturing techniques (Suárez and del Mar Espinosa, 2020).

To further characterise higher frequency activity due to cavitation collapse any new experimental setup should aim to acquire injection rate at higher sampling rates than the 1Mhz acquisition system used for this work. To overcome the amplifier frequency limitation, it is possible to directly measure the small piezo electric charge directly into an acquisition system, such as a sensitive laboratory oscilloscope, to record high sampling rate datasets for spectrogram evaluation.

To capture concurrent accelerometer measurements to compare with the injection rate frequencies an accelerometer with high natural frequency is required. Most commercial accelerometers are limited to typically 10kHz which is insufficient for that analysis. The author recommends the use of the same miniaturised high frequency piezo electric accelerometer that has been developed for closed loop injection control on the Delphi Technologies EU7 product variants (Graham *et al.*, 2014).

To remove the end of injection bump artefact, a more robust injection rate sensor with the highest natural frequency should be fitted close to the injection event. Such as the Piezo-Cryst S Series sensors with a 400kHz natural frequency and identical outer geometry as the existing Kistler 6054 with a natural frequency of 150kHz used for this study. Alternatively, an optical sensor could be used with a fast dynamic response, as demonstrated in shock tubes, potentially enabling capture of both injection rate and temperature readings at higher sampling rates, with no electrical signal noise (Wang *et al.*, 2018).

With knowledge that fluid dependant friction and thermal mass of the injector nozzle seal fixture are sources of measurement variance, it is now possible to create the ideal rate tube meter nozzle tooling in the future, with the following characteristics:

i. Low thermal mass, high emissivity and surface area. E.g. cooling fin body design.

ii. Mirror polished internal bore using flow honing methods.

iii. Observation point next to the injection event using high natural frequency rate sensor.

iv. 2.3mm quarter wave sensor port, to allow SOS to be extracted from its resonant frequency, replacing the flawed thermocouple to SOS fluid property compensation method currently used.

10 REFERENCES

Alex Duggan, R. V. D. V., Bob Ransijn 2014. MULTI-ATTRIBUTE VEHICLE PERFORMANCE OPTIMIZATION: AMESIM AND MODEFRONTIER INTERFACE. *A Joint Webinar by ESTECO and SIEMENS.* SIEMENS: SIEMENS.

Andre, M. *et al.* (1995) 'Driving cycles for emission measurements under European conditions', *SAE transactions*, pp. 562-574.

Andriotis, A., Gavaises, M. and Arcoumanis, C. (2008) 'Vortex flow and cavitation in diesel injector nozzles', *Journal of Fluid Mechanics,* 610, pp. 195-215.

ARAKI, M. *et al.* (2007) 'A Measurement of Instantaneous Flow Rate of an Automotive Gaseous Fuel Injector': SAE Technical Paper (0148-7191.

Arcoumanis, C., Baniasad, M. and Banias, M. (1993) 'Analysis of consecutive fuel injection rate signals obtained by the Zeuch and Bosch methods', *SAE Transactions*, pp. 1371-1384.

Armas, O., Mata, C. and Martínez-Martínez, S. (2012) 'Effect of diesel injection parameters on instantaneous fuel delivery using a solenoid-operated injector with different fuels', *Revista Facultad de Ingeniería Universidad de Antioquia,* (64), pp. 9-21.

Asad, U. *et al.* (2011) 'Precise instrumentation of a diesel single-cylinder research engine', *Measurement,* 44(7), pp. 1261-1278.

AVL (2013) *Pressure Sensors for Combustion Analysis.* AVL Product Catalog— Edition. AVL.

Barree, R. D. 1989. Back pressure regulator. Google Patents.

Bazile, J.-P. *et al.* (2012) 'High pressure thermophysical characterization of fuel used for testing and calibrating diesel injection systems', *Fuel,* 98, pp. 288-294.

Binder, R. C. (1973) *Fluid mechanics.* Englewood Cliffs, N.J.: Prentice-Hall.

Bingqi, T. *et al.* (2015) 'Study of the fluctuation in the cycle fuel injection quantity in a common-rail system for a heavy-duty vehicle diesel engine', *Proceedings of the Institution of Mechanical Engineers, Part D: Journal of Automobile Engineering,* 229(7), pp. 819-834.

Bode, B. 'Verfahren zur Extrapolation wichtiger Stoffeigenschaften von Flüssigkeiten unter hohem Druck'.

Bogert, B. P. (1963) 'The quefrency alanysis of time series for echoes; Cepstrum, pseudo-autocovariance, cross-cepstrum and saphe cracking', *Time series analysis*, pp. 209-243.

Bosch, W. (1967) 'The fuel rate indicator: a new measuring instrument for display of the characteristics of individual injection', *SAE Transactions*, pp. 641-662.

Bueno, A. V., Velásquez, J. A. and Milanez, L. F. (2012) 'Internal combustion engine indicating measurements', *Applied measurement systems*, pp. 23.

Busch, S. and Miles, P. C. (2015) 'Parametric study of injection rates with solenoid injectors in an injection quantity and rate measuring device', *Journal of Engineering for Gas Turbines and Power,* 137(10).

Cassiolato, C. (2011) 'Tips on shielding and grounding in industrial automation', *SMAR Industrial Automation, Brazil, Tech. Rep*.

Catania, A., Ferrari, A. and Manno, M. 'Parametric study of hydraulic layout effects on common-rail multiple injections'. *Proceedings of the ASME ICED Fall Technical Conference, Ottawa, ON, Canada*, 11-14.

Catania, A. E. *et al.* (2008) 'Experimental investigation of dynamics effects on multiple-injection common rail system performance', *Journal of Engineering for Gas Turbines and Power,* 130(3).

Chaufour, P. *et al.* (2004) 'Advanced modeling of a heavy-truck unit-injector system and its applications in the engine design process': SAE Technical Paper (0148-7191.

Chorążewski, M. *et al.* (2013) 'Thermophysical properties of Normafluid (ISO 4113) over wide pressure and temperature ranges', *Fuel,* 105, pp. 440-450.

Choudhury, M. S., Thornhill, N. F. and Shah, S. L. (2005) 'Modelling valve stiction', *Control engineering practice,* 13(5), pp. 641-658.

Cori-Tech, B. (2014) 'Mini cori-flow', *Kompakte Coriolis-Massedurchflussmesser&-regler für Flüssigkeiten und Gase, Datenblatt*.

Crua, C. and Heikal, M. R. (2014) 'Time-resolved fuel injector flow characterisation based on 3D laser Doppler vibrometry', *Measurement Science and Technology,* 25(12), pp. 125301.

Currie, I. G. (2012) 'Fundamental Mechanics of Fluids, Fourth Edition'.

Dahlander, P., Iemmolo, D. and Tong, Y. (2015) 'Measurements of time-resolved mass injection rates for a multi-hole and an outward opening piezo GDI injector': SAE Technical Paper (0148-7191.

Davulis, P., Kosinski, J. and Da Cunha, M. P. 'GaPO4 stiffness and piezoelectric constants measurements using the combined thickness excitation and lateral field technique'. *2006 IEEE International Frequency Control Symposium and Exposition*: IEEE, 664-669.

De Carli, F., Mejia, R. and De Araújo, G. A. (2019) 'ADVANCED ANALYTICS APPLIED TO PROBLEM SOLVING TECHNIQUE ON A PULP MILL', *Latin American Applied Research-An international journal,* 49(3), pp. 175-180.

Delgado, O. and Lutsey, N. (2014) 'The US SuperTruck Program', *Washington DC*.

Delgado, O. *et al.* (2016) 'Estimating the fuel efficiency technology potential of heavy-duty trucks in major markets around the world', *Working Paper,* (14).

Delphi 2016. Worldwide emission standards: Heavy Duty and Off-Highway vehicles. Delphi Germany.

Dembinski, H., Angstrom, H. and Winklhofer, E. 'Injection pressure as a means to guide air utilization in Diesel engine combustion'. *Conference: Fuel Systems for IC Engines: Inject your Ideas, Fuel your Technology, IMechE, London*.

Dernotte, J. *et al.* (2012) 'Influence of physical fuel properties on the injection rate in a Diesel injector', *Fuel,* 96, pp. 153-160.

Dey, K. (2012) 'Characterization and rejection of noise from in-cylinder pressure traces in a diesel engine'.

Doebelin, E. 'System Dynamics: Modeling, Analysis, Simulation, Design'.

Drew, J., Longmore, D. and Johnston, D. N. (1997) 'Measurement of the longitudinal transmission characteristics of fluid-filled hoses', *Proceedings of the Institution of Mechanical Engineers, Part I: Journal of Systems and Control Engineering,* 211(3), pp. 219-228.

Du Tao, M. T. and Dazhuan, W. (2015) 'Study on a novel hydraulic muffler', *The 22nd International Congerss on Sound and Vibration*.

Emerson, R. S. 1977. Fuel injector testing apparatus. Google Patents.

Ferrari, A. *et al.* (2016) 'Hydraulic characterization of solenoid-actuated injectors for diesel engine Common Rail systems', *Energy Procedia,* 101, pp. 878-885.

Ferrari, A. *et al.* (2018) 'A new closed-loop control of the injected mass for a full exploitation of digital and continuous injection-rate shaping', *Energy Conversion and Management,* 177, pp. 629-639.

Ferrari, A. and Zhang, T. (2019) 'Benchmark between Bosch and Zeuch method–based flowmeters for the measurement of the fuel injection rate', *International Journal of Engine Research*, pp. 1468087419827732.

Franc, J.-P. and Michel, J.-M. (2006) *Fundamentals of cavitation.* Springer science & Business media.

Furno, F. and Gonard, R. (2011) 'Diesel Injection-System Simulation: Added Value of the Energy Conservation Equation', *SAE International Journal of Engines*.

Gandhi, A. H., Meinhart, M. and Ortiz, S. (2009) 'Summary of flow metering options for injector characterization': SAE Technical Paper (0148-7191.

Ganz, S. and Gutierrez, E. (2012) 'Cavitation: Causes, Effects, Mitigation and Application', *Rensselaer Polytechnic Institute*.

Gavin, H. (2011) 'The Levenberg-Marquardt method for nonlinear least squares curve-fitting problems', *Department of Civil and Environmental Engineering, Duke University,* 28, pp. 1-5.

Gholizadeh, H., Burton, R. and Schoenau, G. (2011) 'Fluid Bulk Modulus: A Literature Survey', *International Journal of Fluid Power,* 12(3), pp. 5-15. doi: 10.1080/14399776.2011.10781033.

Gibble, J. and Amar, P. (2013) 'Volvo SuperTruck powertrain technologies for efficiency improvement', *presentation at US Department of Energy Merit Review*.

Goris, N. H., Rauznitz, T. and Awad, J. K. 2006. Rate tube measurement system. Google Patents.

Graham, M. S. *et al.* (2014) 'Beyond Euro VI-development of a next generation fuel injector for commercial vehicles': SAE Technical Paper (0148-7191.

Grigg, H. and Heinz, R. (1989) 'The Lubricity of Diesel Fuel injection Equipment Calibration Fluid': SAE Technical Paper (0148-7191.

Gulley, N. 'Improving the quality of contributed software and the MATLAB file exchange'. *2nd Workshop on End User Software Engineering*, 8-9.

Hansen, C. (1951) 'Fundamentals of acoustics', *American Journal of Physics - AMER J PHYS,* 19.

Hardy, C. S. *et al.* (2012) 'Pressure is nothing without control: Evolution of control valve design', in ImechE (ed.) *Fuel Systems for IC Engines*: Woodhead Publishing, pp. 115-128.

Harris, F. J. (1978) 'On the use of windows for harmonic analysis with the discrete Fourier transform', *Proceedings of the IEEE,* 66(1), pp. 51-83. doi: 10.1109/PROC.1978.10837.

Herfatmanesh, M. R. *et al.* (2016) 'Characteristics of pressure wave in common rail fuel injection system of high-speed direct injection diesel engines', *Advances in Mechanical Engineering,* 8(5), pp. 1687814016648246.

Herrmann, O. *et al.* (2012) 'Ultra high pressure and enhanced multiple injection – potentials for the diesel engine and challenge for the fuel injection system', in ImechE (ed.) *Fuel Systems for IC Engines*: Woodhead Publishing, pp. 103-114.

Hixson, E., Kahlbau, J. and Galloway, D. (1962) 'Guide to the selection of acoustic filters for liquid-filled systems': TEXAS UNIV AT AUSTIN DEFENSE RESEARCH LAB.

Hogg, T. *et al.* (2020) 'A benchmark study on the flow metering systems for the characterisation of fuel injectors for future heavy duty commercial vehicles', *Measurement,* 153, pp. 107414.

Hopkins, M. B. and Lee, P. 'High frequency amplifiers for piezoelectric sensors noise analysis and reduction techniques'. *2015 IEEE International Instrumentation and Measurement Technology Conference (I2MTC) Proceedings*: IEEE, 893-898.

IAV 2019. IAV Cross - Injection Analyzer for Large Engine Applications.

Ijas, M. (2007) 'Damping of low frequency pressure oscillation'.

Ishikawa, S. *et al.* (2000) 'Measurement of rate of multiple-injection in CDI diesel engines': SAE Technical Paper (0148-7191.

Jeshani, M. (2013) *Optical characterisation of cavitating flows in diesel fuel injection equipment.* City University London.

Jia, T.-M. *et al.* (2016) 'Effects of ultra-high injection pressure on penetration characteristics of diesel spray and a two-mode leading edge shock wave', *Experimental Thermal and Fluid Science,* 79, pp. 126-133.

Johnson, T. V. (2015) 'Review of vehicular emissions trends', *SAE International Journal of Engines,* 8(3), pp. 1152-1167.

Joss, L. and Müller, E. A. (2019) 'Machine learning for fluid property correlations: Classroom examples with MATLAB', *Journal of Chemical Education,* 96(4), pp. 697-703.

Kagawa, T. (1983) 'High speed and accurate computing method of frequency-dependent friction in laminar pipe flow for characteristics method', *JSME Int. J., Ser. B,* 49(447), pp. 2638-2644.

Kaub, P. (1993) 'Selecting the proper fuel flow meter for engine testing', *SAE Transactions*, pp. 578-588.

Klaus, L., Bruns, T. and Volkers, H. (2015) 'Calibration of bridge-, charge-and voltage amplifiers for dynamic measurement applications', *Metrologia,* 52(1), pp. 72.

Knott, A. J. and Robinson, I. A. (2020) 'Dynamic characterisation of pressure transducers using shock tube methods', *Transactions of the Institute of Measurement and Control,* 42(4), pp. 743-748.

Komaroff, I. and Melcher, K. (1966) 'The Fuel Quantity Indicator-A New Measuring Device for Volumetric Evaluation of Individual Fuel Injection Quantities': SAE Technical Paper (0148-7191.

Kurt, E. 'Overview about emission regulation with a focus on RDE'. *AVL RDE Roadshow*. Italy 18.7.2015: AVL, 1-123.

LI, H.-c. and LI, J. (2006) 'Modeling and Simulation Software Amesim for Mechanical/Hydraulic System [J]', *Computer Simulation,* 12, pp. 075.

Lillington, R., Chetwynd, D. G. and Jones, R. P. (2015) 'Characterising heavy-duty fuel systems: a critique of industry practice and challenges', *Proceedings of the Institution of Mechanical Engineers, Part D: Journal of Automobile Engineering,* 229(3), pp. 391-403.

Luo, F., Cui, H. and Dong, S. (2014) 'Transient measuring method for injection rate of each nozzle hole based on spray momentum flux', *Fuel,* 125, pp. 20-29.

Manin, J., Kastengren, A. and Payri, R. (2012) 'Understanding the acoustic oscillations observed in the injection rate of a common-rail direct injection diesel injector', *Journal of engineering for gas turbines and power,* 134(12).

Manual, M. H. I. (2008) 'Injection Analysis Using the Method of Hydraulic Increase of Pressure'.

McKee, R. J. and Broerman, E. 'Acoustics in Pumping Systems'. *Proceedings of the 25th International Pump Users Symposium*: Texas A&M University. Turbomachinery Laboratories.

Meek, G. A. *et al.* (2014) 'F2E-ultra high pressure distributed pump common rail system': SAE Technical Paper (0148-7191.

Menucci, T. (2018) 'DEVELOPMENT OF BOSCH RATE OF INJECTION MEASUREMENT PROCEDURE AND RESULTS'.

Merritt, H. (1967) 'Hydraulic Control Systems, Wiley', *New York*.

Michel, J. (2001) 'Introduction to cavitation and supercavitation': CENTRE NATIONAL DE LA RECHERCHE SCIENTIFIQUE GRENOBLE (FRANCE) LAB DE ….

Minnetti, E. *et al.* (2017) 'Dynamic measurement of speed of sound in n-Heptane by ultrasonics during fuel injections', *Ultrasonics,* 81, pp. 39-49.

Morgan, R. *et al.* (2015) 'The benefits of high injection pressure on future heavy duty engine performance': SAE Technical Paper (0148-7191.

Mudway, I. S. *et al.* (2019) 'Impact of London's low emission zone on air quality and children's respiratory health: a sequential annual cross-sectional study', *The Lancet Public Health,* 4(1), pp. e28-e40.

Muncrief, R. and Sharpe, B. 2015. overview of the heavy-duty vehicle market and CO2 emissions in the european Union. international council on clean transportation. .

Nelles, M. (2019) 'New Engines at Volvo Trucks', *ATZheavy duty worldwide,* 12(3), pp. 12-17. doi: 10.1007/s41321-019-0033-7.

Neto, M. M. and Góes, L. C. S. 'Use of LMS Amesim® Model to Predict Behavior Impacts of Typical Failures in an Aircraft Hydraulic Brake System'. *Proceedings of 15: th Scandinavian International Conference on Fluid Power, June 7-9, 2017, Linköping, Sweden*: Linköping University Electronic Press, 29-43.

Nikuradse, J. (1932) 'Gesetzmassigkeiten der turbulenten Stromung in glatten Rohren', *Ver Deutsch. Ing. Forschungsheft,* 356.

Oppenheim, A. V. and Schafer, R. W. (2004) 'From frequency to quefrency: A history of the cepstrum', *IEEE signal processing Magazine,* 21(5), pp. 95-106.

Ostadi, B., Aghdasi, M. and Kazemzadeh, R. B. (2010) 'The impact of ISO/TS 16949 on automotive industries and created organizational capabilities from its implementation', *Journal of industrial engineering and management,* 3(3), pp. 494-511.

Paluszek, M. and Thomas, S. (2016) *MATLAB machine learning*. Apress.

Parrish, A. (2014) *Mechanical engineer's reference book.* Elsevier.

Payri, R. *et al.* (2016) 'On the rate of injection modeling applied to direct injection compression ignition engines', *International Journal of Engine Research,* 17(10), pp. 1015-1030.

Payri, R. *et al.* (2011) 'Effect of partial needle lift on the nozzle flow in diesel fuel injectors': SAE Technical Paper (0148-7191.

Payri, R. *et al.* (2008) 'A new methodology for correcting the signal cumulative phenomenon on injection rate measurements', *Experimental techniques,* 32(1), pp. 46-49.

Pearce, D. 2013. ESA progress report. Delphi Disel Systems Internal Document.

Pearce, D., Hardalupas, Y. and Taylor, A. (2015) 'Near nozzle field conditions in diesel fuel injector testing': SAE Technical Paper (0148-7191.

Pearce, D., Hardalupas, Y. and Taylor, A. (2016) 'Laser imaging of pressure waves and cavitation generated by diesel fuel injector jets in a model of an injection rate meter'.

Perna, A., Baraldi, E. and Gregori, G. (2012) 'Exploring the conditions for marketing an innovative and unique customized solution: Mexus case study', *The IMP Journal,* 6(1), pp. 1-16.

Phan, A. (2009) 'Development of a rate of injection bench and constant volume combustion chamber for diesel spray diagnostics'.

Postrioti, L. *et al.* (2014) 'Zeuch method-based injection rate analysis of a common-rail system operated with advanced injection strategies', *Fuel,* 128, pp. 188-198.

Randall, R. B. (2017) 'A history of cepstrum analysis and its application to mechanical problems', *Mechanical Systems and Signal Processing,* 97, pp. 3-19.

No 595/2009 of the European Parliament and of The Council of 18 June 2009 on type-approval of motor vehicles and engines with respect to emissions from heavy duty vehicles (Euro VI) and on access to vehicle repair and maintenance information and amending Regulation (EC) No 715/2007 and Directive 2007/46/EC and repealing Directives 80/1269 (EEC).

Richardson, M. (2009) 'Principal component analysis', *URL: http://people. maths. ox. ac. uk/richardsonm/SignalProcPCA. pdf (last access: 3.5. 2013). Aleš Hladnik Dr., Ass. Prof., Chair of Information and Graphic Arts Technology, Faculty of Natural Sciences and Engineering, University of Ljubljana, Slovenia ales. hladnik@ ntf. uni-lj. si,* 6, pp. 16.

Romano, R. A. and Garcia, C. (2008) 'Karnopp friction model identification for a real control valve', *IFAC Proceedings Volumes,* 41(2), pp. 14906-14911.

Rouse, H. 'Evaluation of boundary roughness'. *Proceedings Second Hydraulics Conference*.

Sadeghi Reineh, M. 2012. Physical modeling and simulation analysis of an advanced automotive racing shock absorber using the 1d simulation tool Amesim.

Samuel, S., Austin, L. and Morrey, D. (2002) 'Automotive test drive cycles for emission measurement and real-world emission levels-a review', *Proceedings of the Institution of Mechanical Engineers, Part D: Journal of Automobile Engineering,* 216(7), pp. 555-564.

Sewall, J. L., Wineman, D. A. and Herr, R. W. (1973) 'An investigation of hydraulic-line resonance and its attenuation'.

Sharp, C. *et al.* (2017) 'Achieving ultra low NOx emissions levels with a 2017 heavy-duty on-highway TC diesel engine and an advanced technology emissions system-thermal management strategies', *SAE International Journal of Engines,* 10(4), pp. 1697-1712.

Siemens, A. (2004) 'LMS Imagine. Lab. Amesim Manual', *Siemens AG*.

Siemens, A. (2013) 'LMS Imagine. Lab. Amesim Hydraulic Library User's Guide', *Siemens AG*.

Simms, V., Gandhi, A. and Sommer, C. (2009) 'Implementation and evaluation of a Coriolis flow meter': SAE Technical Paper (0148-7191.

Steven, H. (2001) 'Development of a Worldwide Harmonised Heavy-duty Engine Emissions Test Cycle. Final Report', *Geneva, Switzerland: UN/ECE-WP29 GRPE, WHDC Working Group, http://www. unece. org/trans*.

Stojanovic, S. *et al.* (2016) 'Cepstrum Analysis of a Rate Tube Injection Measurement Device': SAE Technical Paper (0148-7191.

Strotos, G. *et al.* (2015) 'Transient heating effects in high pressure Diesel injector nozzles', *International Journal of Heat and Fluid Flow,* 51, pp. 257-267.

Suárez, L. and del Mar Espinosa, M. (2020) 'Assessment on the use of additive manufacturing technologies for acoustic applications', *The International Journal of Advanced Manufacturing Technology*, pp. 1-15.

Sykes, D. *et al.* (2019) 'Visual Analyses of End of Injection Liquid Structures and the Behaviour of Nozzle Surface-Bound Fuel in a Direct Injection Diesel Engine': SAE Technical Paper (0148-7191.

T&E 2015. Europe's lost decade of fuel economy. *In:* Enviroment, T. (ed.).

Takamura, A. *et al.* (1989) 'Development of a new measurement tool for fuel injection rate in diesel engines', *SAE Transactions*, pp. 409-414.

Takamura, A. *et al.* (1992) 'A study on precise measurement of diesel fuel injection rate': SAE Technical Paper (0148-7191.

Tebbs, A. (2014) 'F4 and M8 commissioning tips': Delphi Technologies.

TfL, L., London, T.f. (2016) *New proposals to improve air quality. Consultation and information document*.

ToolBox, E. (2003) 'Roughness & Surface Coefficients.'.

van Bebber, D. and Reuter, U. (2017) '1D Model for Correcting the Rate of Injection Signal Based on Geometry and Temperature Influence': SAE Technical Paper (0148-7191.

Veggeberg, K. and Zhang, N. 'Advanced Signal Processing Algorithms for Sound and Vibration Beyond the FFT'.

Walter, P. L. (2004) 'Air-blast and the science of dynamic pressure measurements', *Sound and Vibration,* 38(12), pp. 10-17.

Wang, Z. *et al.* (2009) 'Extraction of Bistable-Percept-Related Features From Local Field Potential by Integration of Local Regression and Common Spatial Patterns', *Biomedical Engineering, IEEE Transactions on,* 56, pp. 2095-2103. doi: 10.1109/TBME.2009.2018630.

Wang, Z. *et al.* (2018) 'Fiber optic method for obtaining the peak reflected pressure of shock waves', *Optics express,* 26(12), pp. 15199-15210.

WIKA (2020) *60 bar WIKA Pressure guage technical datasheet.*

Yu, J. *et al.* (1999) 'Experimental evaluation for fluidborne noise attenuation in tuning cables and hoses of automotive power steering hydraulic systems', *SAE transactions*, pp. 2873-2878.

Zielke, W. (1968) 'Frequency-dependent friction in transient pipe flow'.

11 APPENDICIES

11.1 Additional photos of experimental hardware used for schemes one, three and four.

11.1.1 Experimental scheme one 'science mobile' data logger.



Figure 11.1: Picture of experimental scheme one 'science mobile' portable 1MHz four channels oscilloscope data logger.

11.1.2 Experimental scheme three coriolis mass flow meter installation.



Figure 11.2: Experimental scheme 3 coriolis mass meter installation on production equipment to enable 3 months of mass flow data collection in parallel with existing measurements.

11.1.3 Experimental scheme four custom work area.

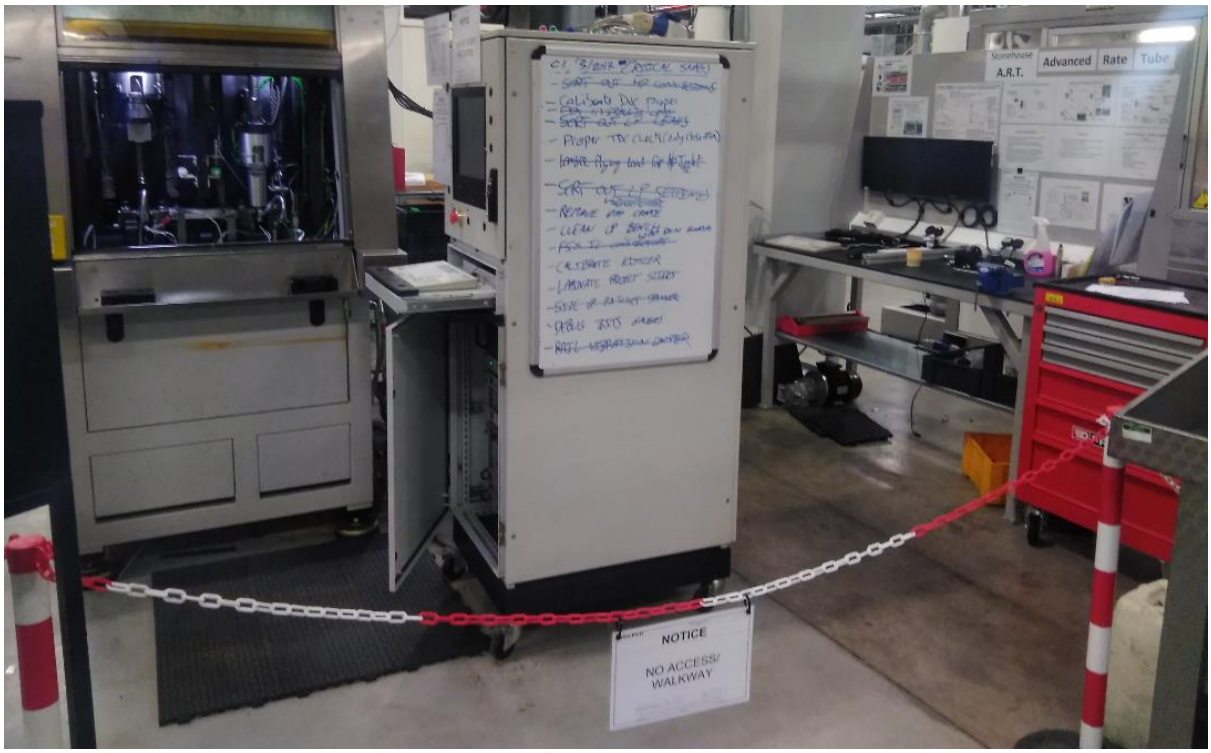




Figure 11.3: Experimental scheme 4 custom work area and experimental apparatus.

11.2 Injector calibration trim variance when using an ARO regulator

A short production run was carried out on one measurement system using the 30bar ARO® regulator configuration as shown in Figure 5.17 in Section 5.1.6. A manual dial pressure gauge was used on the regulator inlet in order to manually monitor backpressure level.

During this production run, the ARO® maintained a steady 30bar backpressure for the majority of the production test. However, a severe drop in backpressure was observed at low injected mass flow values of below 0.15g/s (10mg per injection at 15Hz firing rate). The production injector test program sweeps from high to fuel, such as the 2400bar injection pressure, 2300µs injection duration, down to zero fuel, for every calibration pressure level in the injector applications engine map. Therefore, the last few test conditions in a production test fuel injection level sweep produce little to no input of injected mass into the tube. This indicated that the ARO® regulator chosen was not capable of regulating the pressure under low or no flow conditions and would not be suitable for this application.

During the production trial, 18 injectors were tested on the ARO® backpressure Coriolis mass meter system and on the standard 2bar production measurement system. The standard deviation of injector fuel calibration trim spread in microseconds is shown in Table 11.1 and Figure 11.4.

Table 11.1: Difference in fuel calibration trim standard deviation in microseconds for the standard vs ARO® backpressure circuit configurations for a population of 18 injectors.

Injection pressure	400 bar	925 bar	1625 bar	2400 bar	400 bar	925 bar	1625 bar	2400 bar	400 bar	925 bar	1625 bar	2400 bar
Fuel demand	Small (25mg)	Small (25mg)	Small (15mg)	Small (35mg)	Medium (50 mg)	Medium (65 mg)	Medium (55 mg)	Medium (85 mg)	Large (155 mg)	Large (240 mg)	Large (310 mg)	Large (320 mg)
Standard 2 bar	20	11	7	11	18	14	13	14	23	21	13	16
30 bar ARO	25	17	15	10	38	20	20	11	41	39	24	19
SD Delta	5	6	8	-1	20	6	7	-3	18	18	11	3

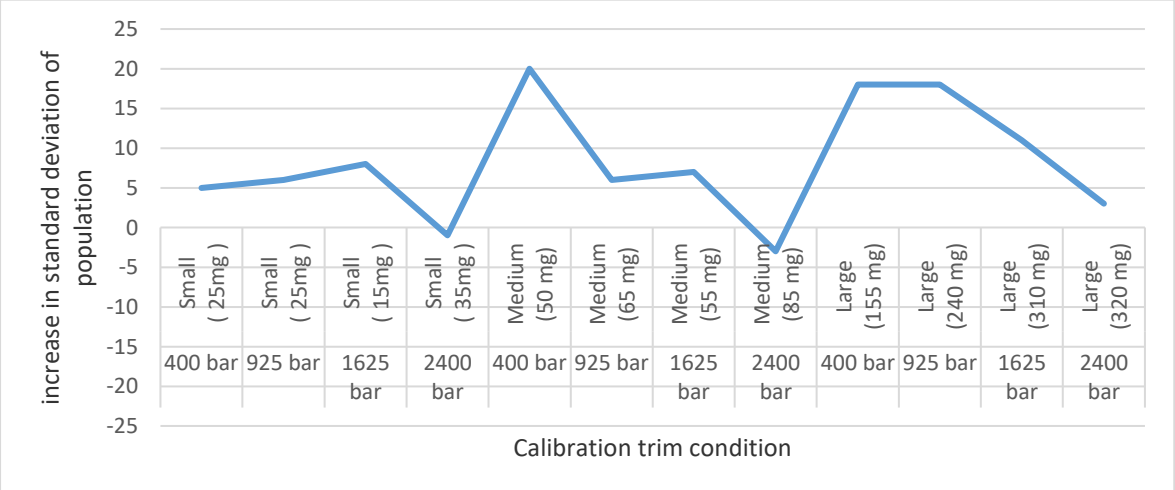


Figure 11.4: Increase in 1 standard deviation for the production test injector drive logic timing correction conditions as measured for a population of 18 injectors.

Standard vs ARO® backpressure circuit configurations.

There is an additional fuel calibration trim measured at 2mg injection load, known as the Minimum Drive Pulse (MDP) trim. However, it could not be measured due to the loss of stable backpressure at injected mass values of 10mg or 0.15g/s at 15Hz firing rate.

At the lower injection pressures for medium and high injected mass, there is a significant increase in calibration trim spread for the same injectors. It was believed that this was due to the backpressure instability, similar to that observed at low rates of injected mass >10mg per injection. A lower injection pressure would have a lower rate of injection. If there is a leak across the regulator seat, it will require a minimum level of flow to overcome the leak and lift the regulator poppet. Different ARO® regulators of the same model display this behaviour at different fuel flow levels. It was surmised that the large ARO® regulator poppet could not maintain a perfect seal at low flow rates. Resulting in a decay of the backpressure in the system when the injected mass is below a certain small injection quantity threshold specific to that regulator. Hence any regulator used for this application must have zero leakage characteristics, even when there is minimal or no flow through it.

The experimental scheme one was limited to the acquisition available for production injector tests only, so it was not possible to capture and observe the dynamic pressure characteristic at the backpressure regulator inlet. To understand the influence of backpressure regulator dynamics on the zero value variance in greater detail, the work moved to simulation space. The construction of a 1D rate tube model to study these dynamic effects is described in the following Section. With the aim to gain insight into the regulator's dynamic response to the pressure pulse input to the following hose. This insight was then used to define the criteria to select an appropriate backpressure regulator for use in experimental scheme three.

11.3 Production application specific cavitation frequency intensity studies

11.3.1 Rate tube bore surface finish

On EU6 production test equipment, when significant wear damage was found inside the injector nozzle 'Donut' seal carrier fixture, shown in point 1 of Figure 11.5, the calibration stability of the measurement system would degrade over time.

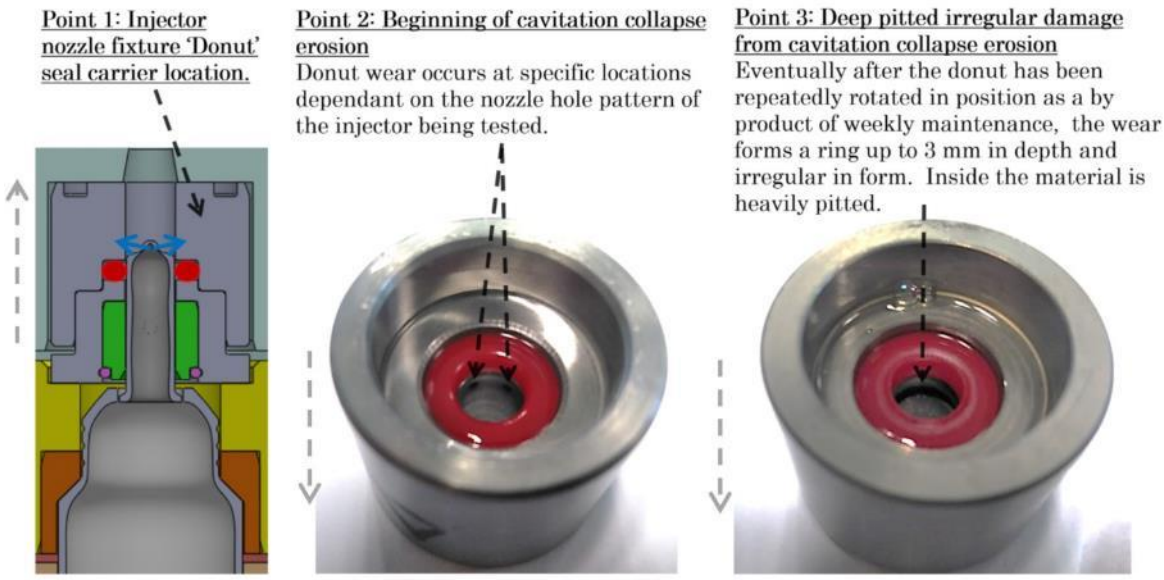


Figure 11.5: Location of nozzle 'Donut' seal carrier fixture.
With initial and heavy erosion damage after weeks and months of use in continuous production setting at pressures up to 3000bar.

The Donut can display initial signs of wear after a period of >500 hours of continuous use in a production environment, reached in approximately one month. The case hardened surface wears through as shown by point 2 of Figure 11.5. It has no rotational locating features, therefore the position of the fixed injector nozzle holes relative to the existing wear pattern will change. Eventually this leads to the erosion breaking through the case hardening around the entire circumference of the bore, creating an irregular, heavily pitted groove as shown by point 2 of Figure 11.5. This level of damage normally takes multiple months of continuous use and is when issues with calibration stability arise.

To characterise how the high frequency activity was influenced by this nozzle fixture erosion, a trial was carried out, comparing Donut fixtures of varying levels of wear, from new to heavily worn. Spectrograms for the new baseline Donut case and heavily eroded donut cases are shown in Figure 11.6.

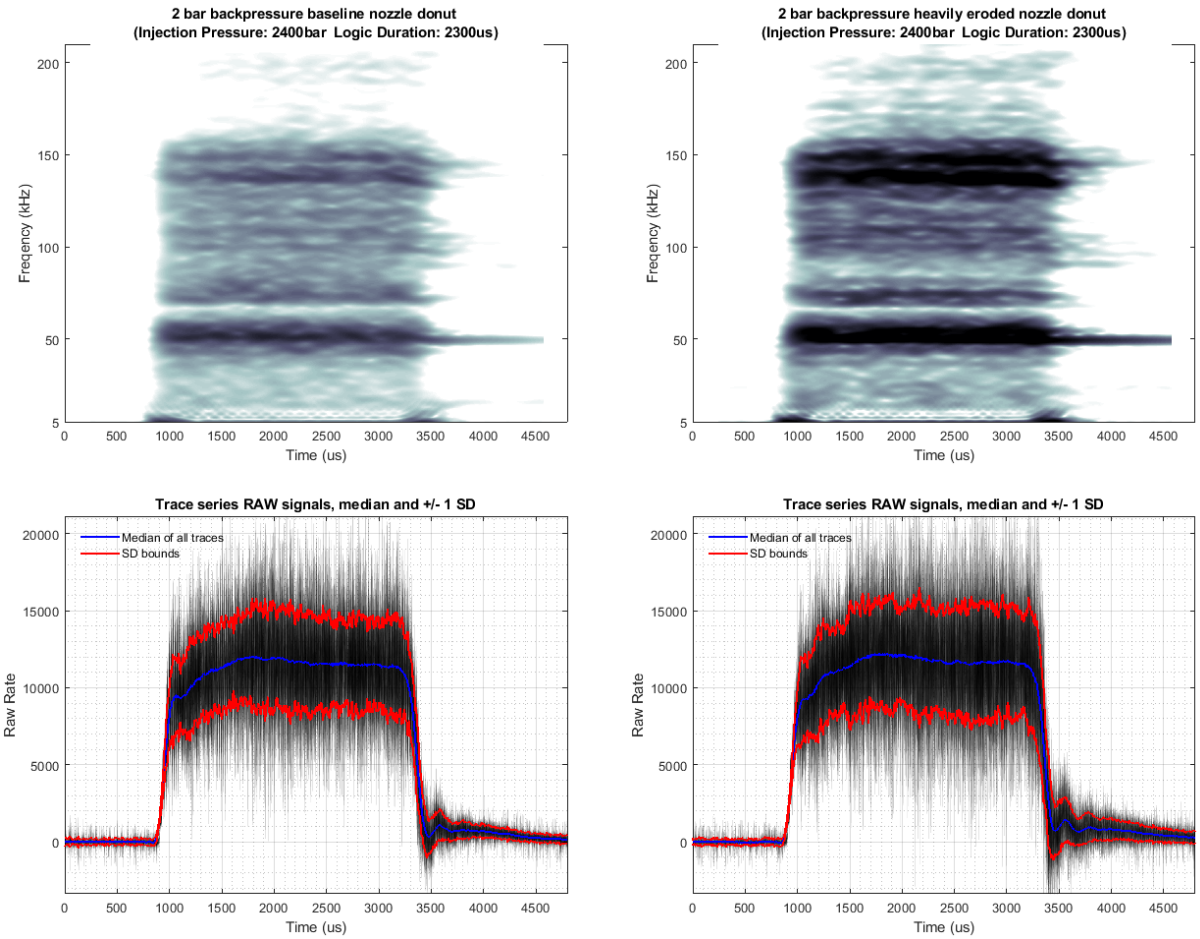


Figure 11.6: Spectrograms illustrating the effect of tooling erosion on frequency intensity.
Left: Baseline new smooth nozzle tooling donut.
Right: Heavily eroded rough nozzle Donut

The intensity of frequency activity observed for the heavily eroded Donut case is increased throughout the spectrogram. The specific frequency bands and overall characteristic remain the same. SD bounds of the raw signal for the eroded donut are larger than the baseline case, with a noticeable increase in the ringing after injection previously linked to sensor port resonance. Hence the rough surface of the Donut fixture significantly increases high frequency activity observed without changing its overall characteristic. This would explain why it was previously difficult for production technicians to spot signs of this issue in the calibration monitoring data. As the overall signal is similar in shape after filtering, it just has more overall variance shot to shot because of greater frequency intensities induced by the erosion.

It is known that a cavitation bubble does not have to collapse with a violent shock-wave, they can be reabsorbed into the fluid medium as vapour content when stable local pressure and flow conditions are achieved. With a rate tube injection meter, this would be further up the length of the rate tube bore away from the injector nozzle and the turbulence of the injection event.

If these cavitation bubbles impact a smooth Donut bore surface, they will rebound without potentially collapsing and sending out a destructive shock-wave. Ganz and Gutierrez (2012) concluded that when cavitation erosion mechanisms are present "the rate of erosion of the surface is accelerated over time as its deteriorated surface creates more turbulence thus creating more cavitation". Hence it is surmised that the rough surface area of the worn Donut fixtures encourages cavitation collapse events, which induces the increase in frequency intensity observed. This observation also shows that the frequency activity initially observed in Figure 6.3 is driven by cavitation present within or caused by the injection event.

It was also noted that if a statistically significant increase in temperature near the injection event was present with a worn donut, the standard deviation of mass injected between consecutive injection events would increase. Under production conditions, these changes would have been deemed as subtle and would not have been highlighted by the automatic calibration and machine health interlocks. As a result of this study, all EU6 injector test programs were updated to stop the machine if these subtle changes were observed, and call for a replacement part. This has led to significant improvement in calibration stability over time on EU6 production test equipment. As less regular intervention is required to maintain calibration stability if the Donut wear is monitored and not allowed to progress to a point where the measurement variance is negatively affected.

11.3.2 Effect of injection pressure and system backpressure

During experimental scheme four, both the standard 2bar backpressure and optimised 30bar production measurement system designs were trialled, as described in Section 5.4. The effect of injection pressure and measurement system back pressure on the high frequency activity for both systems was studied for four pressure levels, 450, 950 1625 and 2400 bar. The spectrograms for both system backpressure and the four different injection pressures are shown side by side in Figure 6.15.

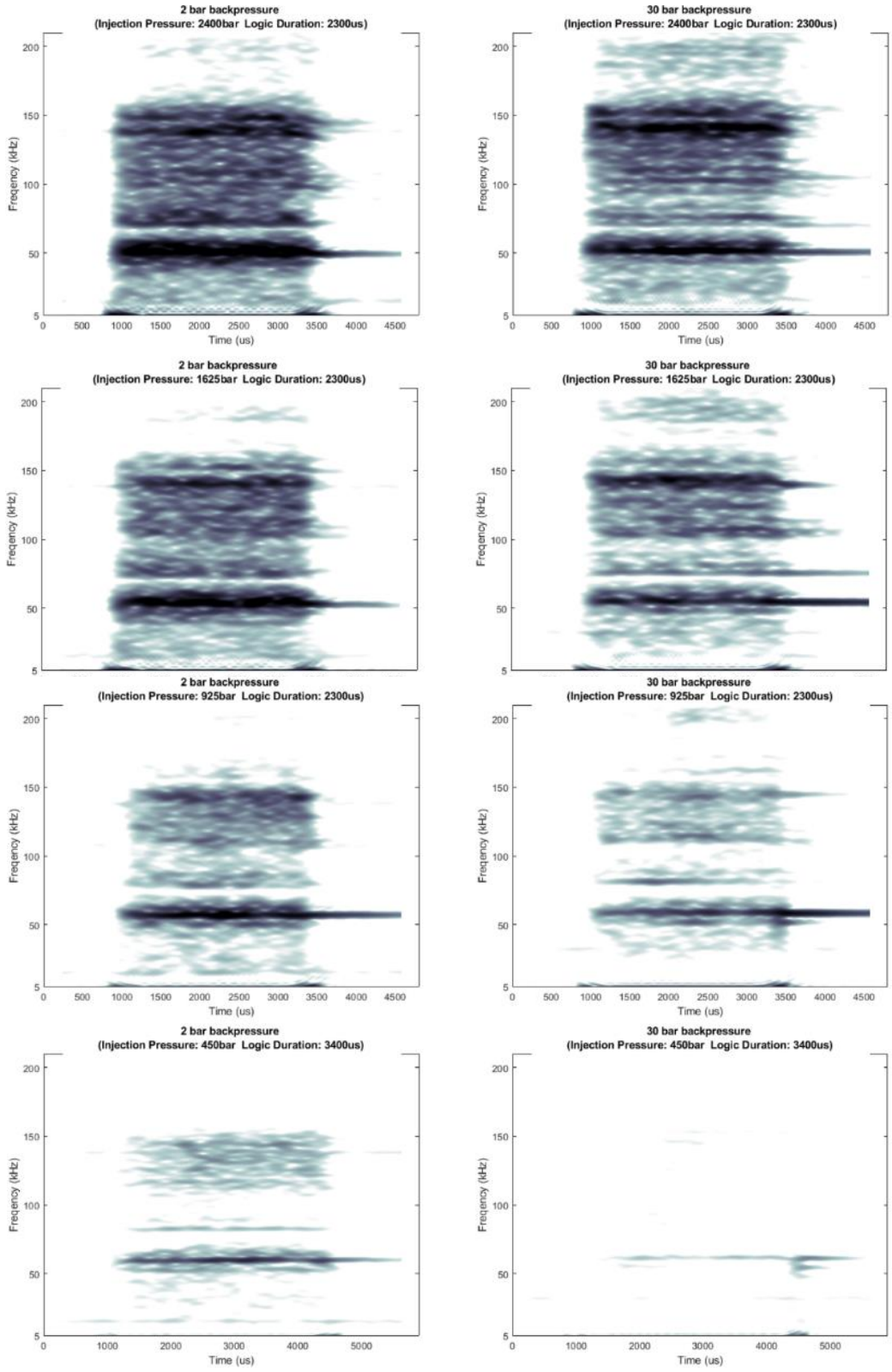


Figure 11.7: Effect of increasing pressure on frequency intensities.
X – Increasing back pressure.
Y – Increasing injection pressure.
Observed on the standard 2bar production measurement system and experimental scheme four optimised hydraulic design at 30bar backpressure.

Frequency intensity reduces for both system backpressures with decreasing injection pressure. Cavitation activity inside the injection event is known to increase with injection pressure (Dembinski, Angstrom and Winklhofer, 2014; Strotos *et al.*, 2015). This is further evidence that all of the high frequency activity observed in these spectrograms is caused, or excited by, cavitation activity present in the injection event.

The high frequency activity intensities are decreased when using an increased system backpressure of 30bar. With the greatest decrease in intensity observed at the 450bar injection pressure, and the lowest decrease in intensity at the 2400bar injection level. The local pressure must dynamically reach vacuum pressure at -0.6bar for vapour to coalesce into a cavitation bubble (Michel, 2001; Siemens, 2013). With measurement system backpressure increased by 28bar from 2bar to 30bar, it is harder for the -0.6bar threshold to be reached dynamically for cavitation bubbles to form. This effect explains why there would be reduced high frequency activity intensities when using increased system backpressure.

If increased measurement system backpressure suppresses cavitation activity, then it will also reduce high frequency variance. The optimised hydraulic design discussed in Section 5.4, addressed the issue of test to test zero value variance originating from changing system temperatures, and therefore SOS over long periods of time. This cavitation suppression effect explains why the optimised hydraulic design examined in Section 5.4 also has improved shot to shot consecutive injection variance over the standard 2bar production measurement system design.

Additionally, it was noted that throughout the use of the 30bar optimised hydraulic design on experimental scheme four, the Donut fixture examined in the previous Section did not suffer any identifiable wear, despite weeks of testing. If the cavitation bubble formation is suppressed by increased backpressure, then it would follow that the rate of nozzle Donut erosion would also significantly reduce. Therefore, by using increased measurement system backpressures on production equipment, less frequent maintenance of the nozzle tooling is required to maintain calibration stability over time.

11.4 Production application specific end of injection rate variance studies

11.4.1 Influence of additional connected volumes

A worn injector nozzle seal was discovered to be an application specific driver of the bump artefact characteristic, described at the start of Chapter 8. To investigate the influence of nozzle seal wear, a review of production data for time periods preceding nozzle seal replacement was carried out. A pattern emerged that indicates that calibration drift inception occurs over a period of a few hours as shown in Figure 11.8.

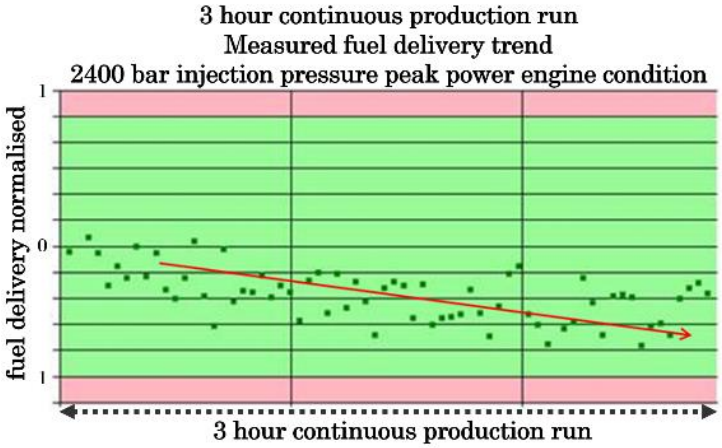


Figure 11.8: Measured fuel value drift caused by inception of seal degradation at wear level 2. A subtle fuel value drift of 0.6% (2-3mg) gradually trends over three hours, stabilising at a miss-calibrated position.

The measured fuel value stabilises at this drifted calibration position for multiple days. Only to drift again after an inconsistent and unpredictable amount of time. This subtle drift in measured fuel values was present on all production test hardware, to varying degrees, and was the most common cause of day-to-day calibration drift.

An experiment was planned to characterise the causal relationship between nozzle seal wear, the end of injection distortion and measured fuel value calibration drift. To achieve this characterisation, all failed nozzle seals were collected over a six-month period from 16 production rate tube measurement systems in 2016.

Five levels of wear were categorised from the collected sample. These categories were initially implemented in 2016, as a weekly maintenance visual inspection. With replacement of the seal triggered at level 3, as illustrated in figure 8.3. Despite the new inspection procedure implemented by the author, the smaller

calibration drift events were still occurring.

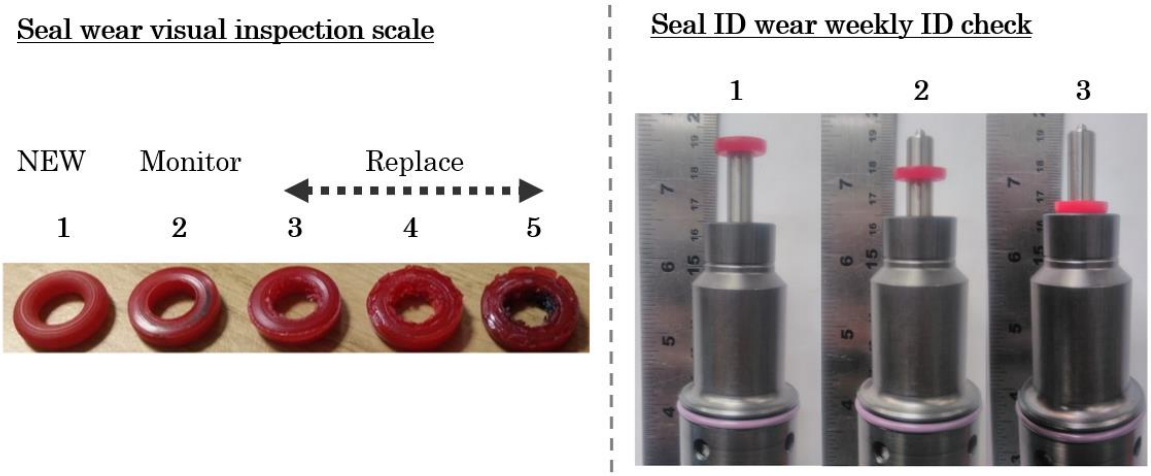


Figure 11.9: Injector nozzle seal 6 month dataset and wear scale devised. Left: Histogram of sear wear level categories over the six month period. Right: Visual scale for seal wear weekly inspection implemented in 2016.

A seal for each wear category was selected using the visual standard and tested on experimental scheme four. A case where the seal was removed entirely was also trialled. It was observed that the shape of the end start and end of injection would slowly drift over time as the seal became more heavily worn, as shown in figure 8.4.

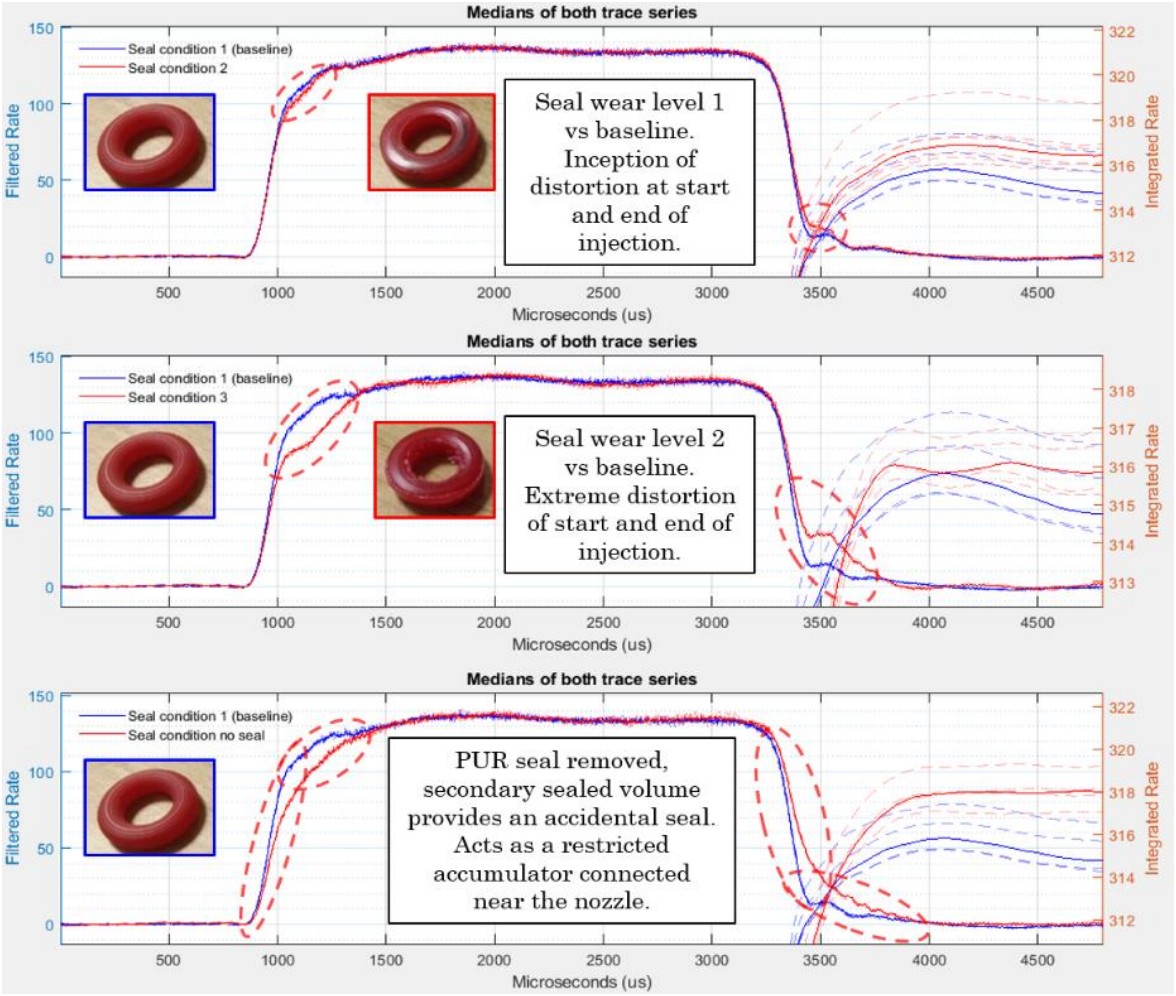


Figure 11.10: Injection rate shape comparison between seal wear condition levels 2, 3 and no seal compared to a new seal baseline.
Top: New seal baseline vs seal condition 2.
Middle: New seal baseline vs seal condition 3.
Bottom: New seal baseline vs no seal present in holder.

There is a high level of distortion of the injection rate for the no seal case, as highlighted by point 1 of Figure 11.10. It should not be possible to maintain pressure in the rate tube measurement system without a seal present. Despite this, the test completes as normal with a total fuel error of less than 3% at the peak power engine condition.

There is some shape distortion present for seal wear cases 1 and 2, when compared to the new seal baseline result. The injection rate distortion starts lower down the start of injection slope and higher up the end of injection slope for the seal wear level 2 case, as highlighted by point 2 of Figure 11.10. This result proved that energy in the form of pressure was being exchanged between the start and end of injection. It also demonstrated that the inception point and overall magnitude of distortion of the injection rate was primarily influenced by degradation of the nozzle seal.

This result explains why seal failure could not be easily detected on EU6 production equipment. The overall area under the pressure curve would be preserved, as shown by point 3 of Figure 11.10. Resulting in a minor but drifting injected fuel mass measurement error, if integration of the entire area under the injection rate signal in the measurement window is used to derive injected mass. As the seal wears, the rate shape distorts further, causing a subtle drift of less than a 1% of total fuel error.

The production injector test machine injector nozzle fixture design featured a telltale leak hole, visible to the operator, to indicate seal failure. However, fluid had never been observed at the port before changing a seal. Upon inspection of the tooling, it was discovered that the nozzle seal holder would form a metal to metal compression seal behind the nozzle as illustrated in Figure 11.11.

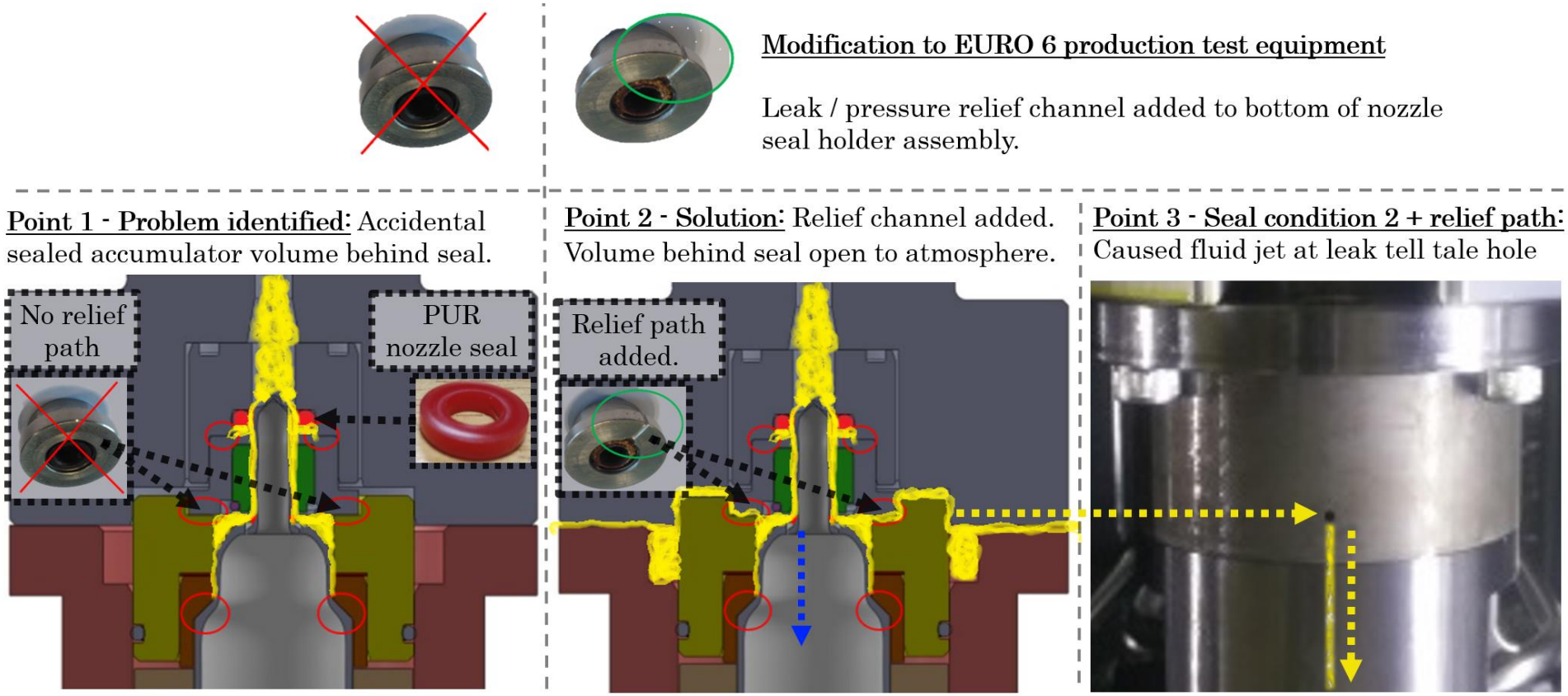


Figure 11.11: Illustration of additional accumulator volume behind the nozzle seal and the relief channel that removes it.
Top: Pressure relief channel added to bottom of nozzle seal holder assembly.
Left: Illustration of additional sealed accumulation volume behind the nozzle seal.
Middle: Illustration of trapped volume pressure being released through a relief channel in nozzle seal carrier.
Right: Image of the tell take leak path on the production equipment that indicates seal failure.

This secondary sealed volume acted like a fixed volume accumulator attached to the rate tube at the nozzle via a variable orifice. The orifice being formed by leakage past a worn nozzle seal inner diameter connecting to a secondary unintentional sealed accumulation volume. This secondary, restricted volume allowed energy in the form of pressure, and hence injection rate, to be exchange between started and end of injection. An affect exacerbated by the degree of nozzle seal inner diameter degradation.

With the addition of a relief channel to the bottom of the nozzle seal holder fixture, the original intention of the telltale leak path was restored. As soon as seal condition 2 was trialled with this relief channel present, a fluid jet was observed at the telltale. The injector test machine used for experimental scheme four automatically aborted the experiment within seconds because of a critical loss of pressure detected in the in the rate tube.

Previous to this addition of a relief channel, the error introduced by the trapped volume and seal degradation would unknowingly be compensated for by operations staff using time-consuming calibration procedures. Resulting in hundreds of hours a year of lost machine time trying to eliminate a moving calibration error. With the addition of the relief channel, seal failure was immediately detected at seal condition level 2. Before the calibration of the machine has drifted. Hence, seal replacement no longer affected the machine calibration.

This modification was immediately rolled out to all EU6 production injector test measurement systems in 2018, the result of which was a stable start and end of injection characteristic day to day. Which resulted in long-term calibration stability of production test equipment, for the first time in the history of F2 EU6 injector testing.

11.5 Application specific transient test conditions influence on rate float

It is known that temperature in the injection event increases with injection pressure, which in turn increases the magnitude of this effect. Hence, this source of variance is of greatest magnitude, at peak injection pressures and fuel deliveries, as shown in Figure 11.12.

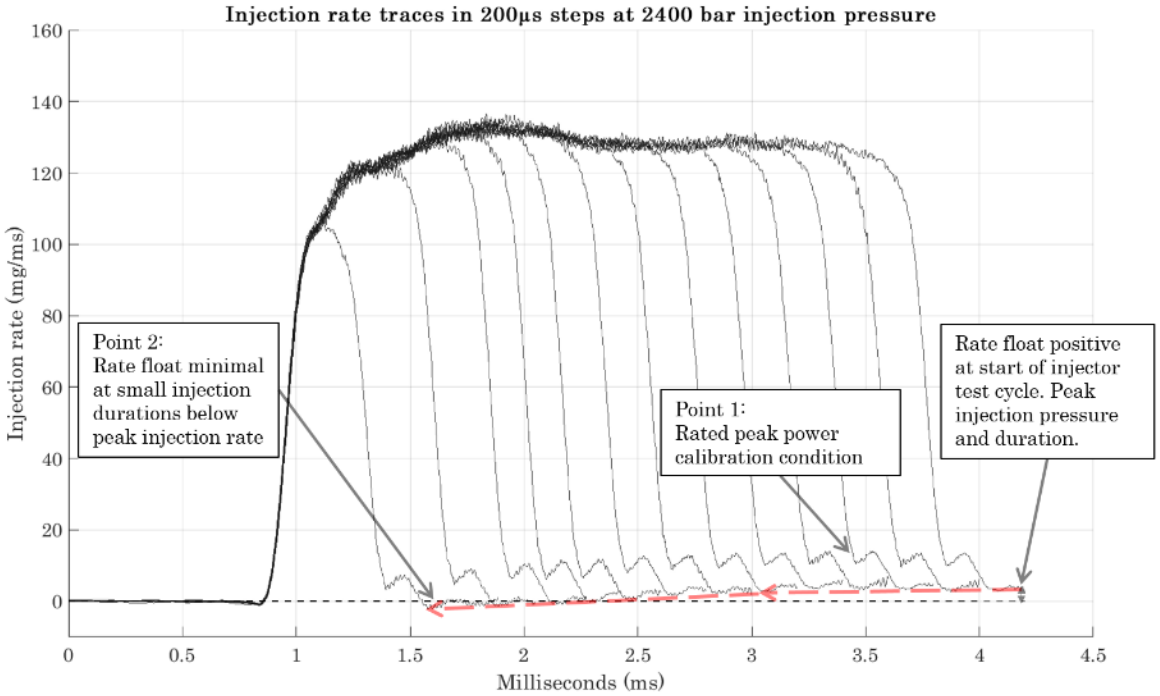


Figure 11.12: Start of calibration test high pressure injection duration sweep. Rate float shown for descending injection durations at 2400 bar injection pressure. High to low (right to left) duration as the test sequence.

Critical peak power rated engine load test conditions require high injection pressures and durations, where rate float is at its highest magnitude, as shown by point 1 of Figure 11.12. As expected, the effect is negligible for small injection durations, that do not achieve full injection rate, as shown by point 2 of Figure 11.12.

Once the highest pressure 2400 bar characterisation sweep completes, the transient production test steps down to 1625 bar and stabilises for 10 seconds. The first 1625 bar injection has a negative rate float magnitude, as highlighted by point 1 of Figure 11.13.

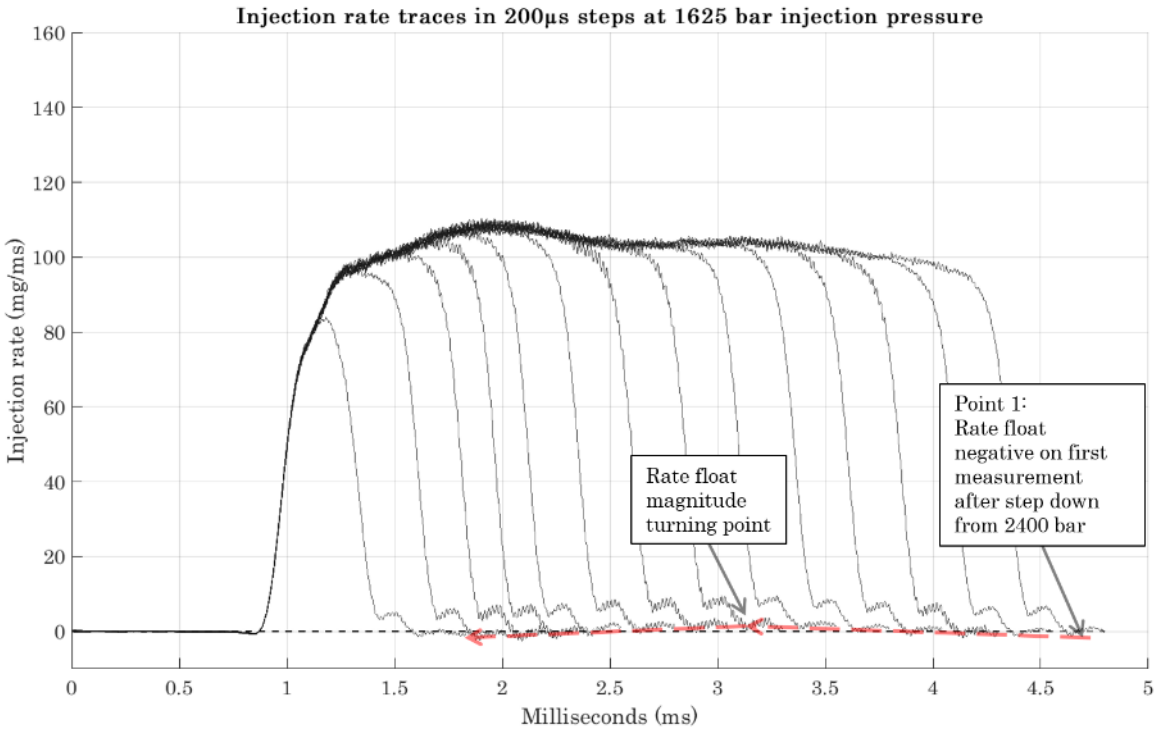


Figure 11.13: Negative rate float observed after pressure level step down from 2400 to 1625 bar injection pressure. Rate float shown for descending injection durations at 1625 bar injection pressure. High to low (right to left) duration as the test sequence.

This is due to the significantly lower injection temperatures at 1625 bar vs 2400 bar injection pressure. The fluid medium in the rate tube bore and the temperature of the rate tube wall are higher than would be achieved at 1625 bar. Hence, the lower pressure injection acts to cool the hot fluid medium and injector tooling, immediately after the injection pressure level change. This cooling effect will subsequently cause pressure in the fluid medium to drop, instead of rise, after the start of injection.

The change in rate float magnitude reverses direction half way through the injection duration characterisation sweep, as shown by point 2 of Figure 11.13. The characteristic of rate float effectively returns to the trend it would have had, if the characterisation test began at 1625 instead of 2400 bar.

The rate float characteristic is consistent when multiple injection rate traces are captured, for the five minutes under steady state tests conditions, on experimental scheme four, as shown in Figure 11.14.

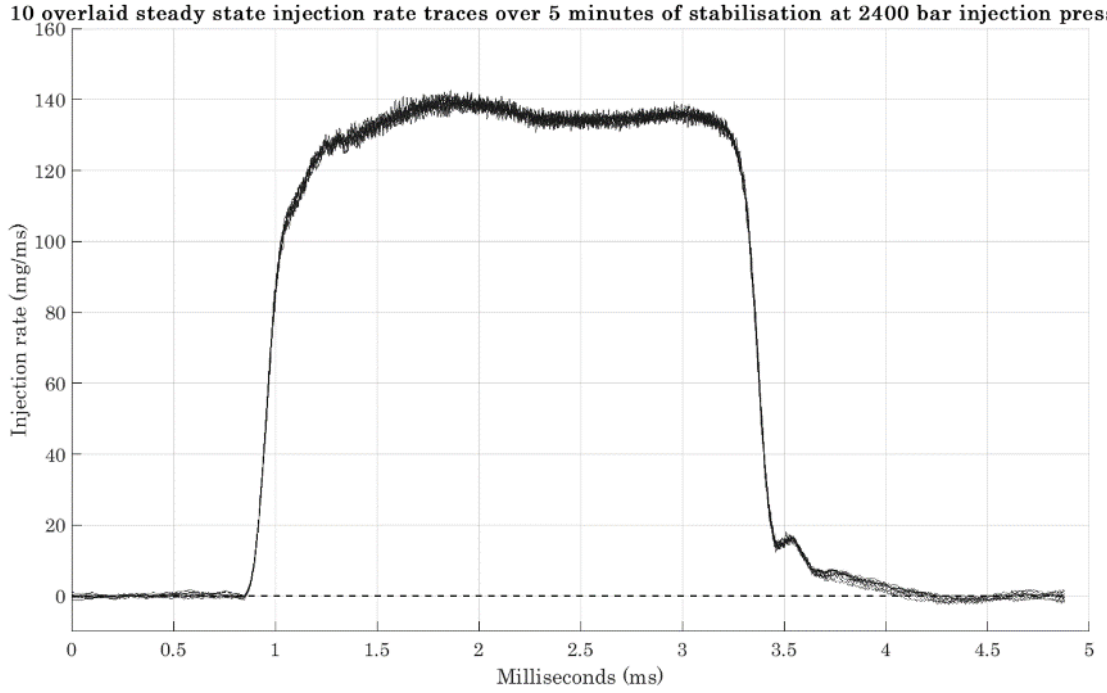


Figure 11.14: Difference in rate float magnitude between a fast transient production injector test cycle and a slow steady state temperature stabilised cycle for the 2400 bar 2300 µs test condition.

The implication of this analysis is that the signal magnitude can become significantly distorted, in either direction, under transient production injector test conditions. Which will be dependent on the delta in temperature between the injection event and the fluid medium of the rate tube measurement system. Hence, to minimise this source of measurement variance, it is desirable to spend a long time stabilising the system temperature at every single test condition, to reduce the delta between the fluid medium and the injection event. Stabilisation is required regardless of injection temperature, due to the bipolar nature of this variance.

This is acceptable for a laboratory environment, but not in a time critical production environment. The F2 EURO 6 transient production injector test cycle completes measurement of approximately 300 distinct injection pressure and duration test conditions, in less than 5 minutes. To perform the same test cycle under temperature stable steady state conditions takes an hour or more.

Hence, this primary driver of test to test measurement variance must be characterised, to minimise its influence on the day to day calibration of the transient production test cycle.

11.5.1 Rate float implications for multiple injection event measurement

This source of measurement variance also means rate tube measurement systems are currently unsuitable for measurement of close coupled multiple injection events. The measurement of a secondary injection event, as required for EURO 7 injector characterisation tests, will include this effect superimposed on their baselines. An injection rate measurement for a high pressure closed coupled injection event is shown in Figure 11.15 to illustrate this effect.

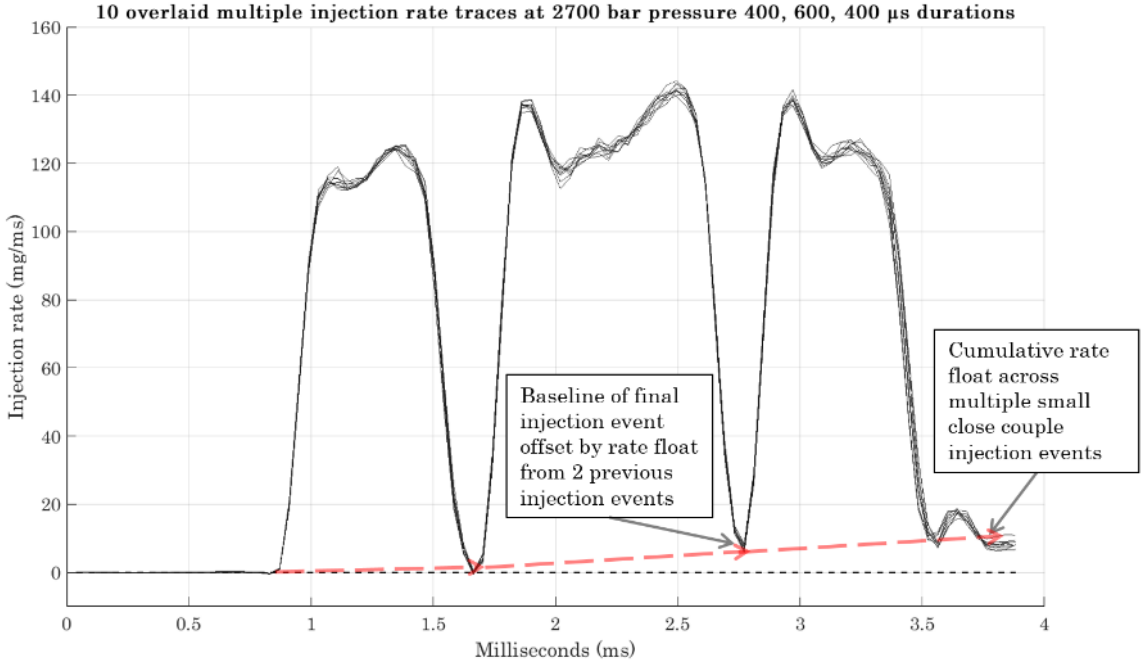


Figure 11.15: 2700 bar injection pressure, 3 x 750 µs duration with 500 µs separation between the injection events. Cumulative rate float magnitude increased highlighted in the time between injection events.

A mathematical correction can be applied and is used on the IAV commercially available rate tube injection meter. The transfer function to describe the effect was provided by Payri *et al.* (2008).

It was not possible to implement this correction on EURO 6 production test equipment previously due to other sources measurement variance that convolve on top of the end of injection characteristic. Which in turn leads to unstable thresholds for the exponential decay. With these additional sources of measurement variance minimised as demonstrated on experimental scheme 4 implementation of this correction should now be possible.

11.6 Amesim model details

11.6.1 Flexible hose model

HH06A - simple wave equation hydraulic pipe/hose + viscoelastic walls (C-IR-C)



Description

HH06A is a simple wave equation parameter submodel of a hydraulic hose in which the wall behavior is represented with a linear viscoelatic model.

The compressibility of the fluid and the static expansion of the hose wall with pressure are taken into account by using an effective bulk modulus. This can be calculated based on :

1. the wall thickness and Young's modulus of the wall material
2. a user supplied effective bulk modulus
3. a variable volumetric expansion ASCII table

A dynamic stiffness and damping are taken into account to represent the linear viscoelastic behavior of the hose wall.

Pipe friction is taken into account using a friction factor based on the Reynolds number and relative roughness.

The inertia of the fluid is taken into account by a flow rate state variable at the mid point of the pipe/hose. There are also state variables representing the pressures at the ends.

The submodel also computes a mean flow velocity in [m/s] and the Reynolds number.

Usage

HH06A is useful in general simulation of hydraulic systems where compressibility, friction and fluid inertia are important. One can use this submodel if pipe/hose wall stiffness cannot be neglected regarding the fluid stiffness and pressure excitations. Evaluating the wall bulk modulus could be a good way to decide whether you need this complexity or not.

External variables



	Title	Variable name	Unit	Type	In/Out	Default value
Port 1						
1	pressure at port 1	*p1*	bar	explicit state	→ output	0
2	flow rate at port 1	*q1*	L/min	basic variable	← input	-
Port 2						
1	pressure at port 2	*p2*	bar	explicit state	→ output	0
2	flow rate at port 2	*q2*	L/min	basic variable	← input	-

Internal variables

	Title	Variable name	Unit	Type	Default value
1	flow rate at center of pipe	*qmid*	L/min	explicit state	0
2	mean fluid velocity	*v*	m/s	basic variable	-
3	Reynolds number	*re*	null	basic variable	-
4	pipe volume	*hosevol*	cm**3	basic variable	-
5	wall bulk modulus	*hosebulk*	bar	basic variable	-
6	hydraulic stiffness	*khyd*	Pa/m**3	basic variable	-
7	hydraulic inertia	*ihyd*	kg*m**4	basic variable	-
8	dummy variable 1	*dumy1*	null	explicit state	0
9	dummy variable 2	*dumy2*	null	explicit state	0
10	dummy variable 3	*dumy3*	null	explicit state	0
11	dummy variable 4	*dumy4*	null	explicit state	0
12	activity of hydraulic capacitance (pipe)	*actCpipe*	J	explicit state for activity	0
13	power of hydraulic capacitance (pipe)	*powerCpipe*	W	power variable	-
14	energy of hydraulic capacitance (pipe)	*energyCpipe*	J	explicit state for energy	0
15	activity of hydraulic dissipation (frict)	*actRfrict*	J	explicit state for activity	0
16	power of hydraulic dissipation (frict)	*powerRfrict*	W	power variable	-
17	energy of hydraulic dissipation (frict)	*energyRfrict*	J	explicit state for energy	0
18	activity of hydraulic inertia (pipeinertia)	*actIpipeinertia*	J	explicit state for activity	0
19	power of hydraulic inertia (pipeinertia)	*powerIpipeinertia*	W	power variable	-
20	energy of hydraulic inertia (pipeinertia)	*energyIpipeinertia*	J	explicit state for energy	0
21	activity of hydraulic source (grav)	*actSgrav*	J	explicit state for activity	0
22	power of hydraulic source (grav)	*powerSgrav*	W	power variable	-
23	energy of hydraulic source (grav)	*energySgrav*	J	explicit state for energy	0

Real parameters

	Title	Variable name	Unit	Default value
1	diameter of pipe	*diam*	mm	25
2	pipe length	*length*	m	1
3	relative roughness	*rr*	null	1e-005
4	angle line makes with horizontal (+ve if port 2 above port 1)	*angle*	degree	0
5	wall thickness	*thick*	mm	10
6	Young's modulus for material	*emod*	bar	2.06e+006
7	user specified effective bulk modulus	*bmod*	bar	8000
8	bulk modulus of the fluid used for pipe expansion measurements	*bulkfluid*	bar	17000
9	dynamic stiffness of hose wall	*stiff2*	N/m	1.5e+009
10	dynamic damping of hose wall	*damp*	N/(m/s)	1e+006
11	time constant for differentiation	*tau*	s	1e-005

Integer parameters

	Title	Variable name	Default value
1	pipe bulk modulus	*bulkenum*	1: calculated bulk modulus
2	index of hydraulic fluid	*indexf*	0

Text parameters

	Title	Variable name	Default value
1	filename for volumetric expansion[cm**3/m] = f(P[bar])	*dvfile*	$AME/libhydr/data/dV_P.data

Parameter settings

LMS Imagine.Lab Amesim™ software provides three possibilities to users to evaluate the effective bulk modulus:

1. **calculated bulk modulus**

   The calculated bulk modulus value is determined from the bulk modulus of the fluid and the characteristics of the pipe/hose walls. If you use this option, you must specify the wall thickness of the pipe/hose and the Young's modulus of the material from which the walls are made. A wall thickness of zero is taken to mean that the bulk modulus from the hydraulic fluid properties will be used unmodified (i.e. the walls are infinitely stiff). Suitable values for Young's modulus of the wall material in [bar] are:

   - steel 2.06e6
   - aluminum 7.00e5
   - hose from 5.0e3 to 1.0e5

   For most purposes, it is better to choose this option to calculate the effective bulk modulus of the hydraulic fluid pipe/hose combination because its settings is the simplest.

2. **user specified bulk modulus : BEFF**

   Another solution is a direct specification of an effective bulk modulus at the working point and use a linear approximation around this point, i.e. elastic assumption. In this case pipe/hose volume is a linear function of the pressure:

   $$V_{wall(P)} = V_0 \times (1 + W_{comp} \times P)$$

   where Vo is the pipe/hose volume at zero pressure gauge and wcomp=1/BEFF-1/Bfluid(0) and Bfluid(0) is the pure fluid bulk modulus at zero pressure gauge. This effective bulk modulus should be under the reference conditions of zero bar gauge pressure and zero air content and should be less than the fluid bulk modulus under the same reference conditions.
   Remark: wall bulk modulus Bwall is defined as Vwall*DP/DVwall.
   By the linear approximation:

   $$B_{wall} = \frac{1 + w_{comp} \times P}{w_{comp}}$$

3. **volumetric expansion.**

   However, if good experimental values are available, you can specify a pipe/hose volumetric expansion. Volumetric expansion at pressure P is defined as the fluid volume measured at zero pressure gauge which enters in the pipe/hose when the pressure inside the pipe/hose increases from zero pressure gauge to P pressure gauge. This volume is normalized by line length. Obviously, for 0 pressure gauge, volumetric expansion is 0 [cm^3/m]. There are two important steps :

   i. Initialization. During the initialization, two linear spline functions are assessed for hose volume and hose bulk modulus estimation as function of pressure. Only experimental fluid bulk modulus is here used. To take into account experimental fluid characteristics a parameter has been added, i.e. bulk modulus of the experimental fluid which is assumed to be constant. If this parameter is set to zero, it is assumed that experimental fluid is infinitely stiff, i.e. volumetric expansion gives directly pipe/hose volume variation per unit length as function of pressure. See function **hosesinit** .
   ii. Running. Spline functions are used to estimate pipe/hose volume and bulk modulus at the current pressure. Simulation is done considering the fluid properties specified by the index of hydraulic fluid. See function **pcdyn3** .

   Pressure and volumetric expansion must be non decreasing sequences. Wall bulk modulus has been bounded to 1e6 [bar].
   Allowing the users the specification, at two different pressures, of the same volumetric expansion coefficient. In the latest case, experimental fluid bulk must be set to zero, i.e. a pressure increase do no only imply a volume increase only if the system (pipe/hose + experimental fluid) is infinitely stiff.

A mechanical dynamic stiffness and damping are used to represent a linear viscoelastic behavior of the wall. The dynamic stiffness is usually higher than the static stiffness.

The index of hydraulic fluid parameter refers to a fluid type defined by an icon put on the sketch.

A time constant is used for a differentiation for the calculation of the flow rate induced by the wall displacement. If the value of the time constant is too important, the system will be over damped.

The relative roughness (rr) is the ratio of the average height of asperities to the tube diameter:

$$rr = \frac{\Delta}{diam}$$

where:

Δ is the equivalent uniform roughness of the pipe;
$diam$ is the hydraulic diameter of the pipe.

A sampling of absolute pipe roughness Δ for new clean pipes is proposed by Binder [1] :

Pipe Material	Absolute roughness Δ
drawn brass	1.5 µm
drawn copper	1.5 µm
commercial steel	45 µm
wrought iron	45 µm
asphalted cast iron	120 µm
galvanized iron	150 µm
cast iron	260 µm
wood stave	0.2 to 0.9 mm
concrete	0.3 to 3 mm
riveted steel	0.9 to 9 mm

Remark: HH06A is based on HL06A, viscoelastic behavior of the wall is now taken into account.

Sketches and equations

The mode used to calculate the derivative of the pressure at port 1 is determined by the value of the integer parameter *bulkenum*. The basic formula is

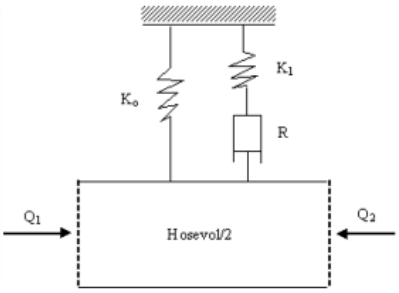
$$\frac{\partial P}{\partial t} = -\frac{B}{A} \times \frac{\partial Q}{\partial x}$$

where *A* is the cross-sectional area of the pipe and *B* is the effective bulk modulus of the pipe/fluid combination. Assuming *P* constant in the considered section of the line, the integration of the equation in the x-direction leads to

$$\frac{dP}{dt} = -\frac{B \times Q}{hose_{vol}}$$

which is the formula used in **pcdyn4** where $hose_{vol}$ is the volume of fluid and Q is the net flow rate into the volume.

The viscoelastic behavior of the wall is represented by a standard linear solid model. It consists on a combination of two springs (K_0 and K_1) and a dashpot (R). One half of a hose is presented in the following figure.



The mechanical stiffness of the hose K_0 is linked to the wall Bulk modulus $hose_{bulk}$:

$K_0 = \frac{hose_{bulk}}{0.5 \times hose_{vol}} \times A_2^2$ where A_2 is the transformer area $A_2 = \pi \times d \times \frac{l}{2}$ where d and l are respectively the diameter and the length of the hose.

Remark: Usually the dynamic stiffness K_1 is higher than the static one K_0 . A warning is displayed by the submodel otherwise.

Refer to the documentation of **pcdyn4** for full details of these calculations.

Depending on the value of the integer parameter *bulkenum*, the hose volume and the wall bulk modulus might be determined in three different ways:

1. Calculated bulk modulus
   If the calculated bulk modulus option is set, the function **compwc** is used to compute the wall volumetric compliance W_{comp} from the wall thickness and Young's modulus of the material. Refer to the documentation of **compwc** for full details of these calculations.

   Assuming a linear evolution of hose volume :

   $$hose_{vol} = V_0 \times (1 + W_{comp} \times P)$$

   where V_0 is the reference volume of the pipe at zero pressure gauge.

   Wall Bulk modulus is defined as:

   $$hose_{bulk} = \frac{(1.0 + W_{comp} \times P)}{W_{comp}}$$

2. User supplied effective bulk modulus
   If the option "user supplied effective bulk modulus" is set, the wall volumetric compliance W_{comp} is computed from the user supplied effective bulk modulus B_{eff} and the bulk modulus of the fluid under reference conditions B_{ref} using

   $$W_{comp} = \frac{1}{B_{eff}} - \frac{1}{B_{ref}}$$

   Assuming a linear evolution of hose volume :

   $$hose_{vol} = V_0 \times (1 + W_{comp} \times P)$$

   where V_0 is the reference volume of the pipe at zero pressure gauge.

   Wall Bulk modulus is defined as:

   $$hose_{bulk} = \frac{(1.0 + W_{comp} \times P)}{W_{comp}}$$

3. Volumetric expansion
   If the volumetric expansion option is set, the function **hosesinit** is used to assess two linear spline functions for hose volume ($hose_{vol}$) and hose bulk modulus ($hose_{bulk}$) estimation as function of pressure. During the initialization, only experimental fluid bulk modulus is used : *bulkfluid* .

   Hose volume is estimated by:

   $hose_{vol}$ = **getlspl** (*lspl2, P, disc*)

   Where *lspl2* is spline indicator for hose volume assessment and disc is used for discontinuity handling.

   Wall bulk modulus is given by:

   $hose_{bulk}$ = **getlspl** (*lspl1, P, disc*)

   Where *lspl1* is spline indicator for hose bulk modulus assessment and disc is used for discontinuity handling.

In all cases the function **pcdyn4** is used to compute the pressure derivative. Refer to the documentation of **pcdyn4** for full details of these calculations.

B_{eff} is the effective bulk modulus of the pipe/fluid combination. It is given by:

$$\frac{1}{B_{eff}} = \frac{1}{B_{fluid}} + \frac{1}{hose_{bulk}}$$

The global equivalent hydraulic stiffness of the pipe/fluid combination is defined as:

$$K_{hyd} = \frac{B_{eff}}{hose_{vol}}$$

where $hose_{vol}$ is the volume of the pipe at the current pressure.

Hydraulic inertia is defined as:

$$I_{hyd} = \rho \times \frac{l}{A}$$

where A is the cross-sectional area of the pipe (assumed constant) and l is the length of the pipe (assumed constant) and ρ is the fluid density.

The derivative of the flow rate in the hose is calculated using the utility **pipif3** . The basic formula used is

$$\frac{\partial Q}{\partial t} = \frac{A}{\rho} \times \frac{\partial P}{\partial x} - g \times A \times sin(\theta) - v \times \frac{\partial Q}{\partial x} - \frac{f_f \times Q^2 \times sign(Q)}{2 \times D \times A}$$

where ρ is the density, A the cross-sectional area of the pipe, D its diameter, θ its inclination, g is acceleration due to gravity and ff the friction factor. Since A is a function of pressure P , we need the radial compliance R_{comp} for **pipif3**.

1. Calculated bulk modulus
   If the calculated bulk modulus option is set, volumetric compliance V_{comp} and length compliance L_{comp} and radial compliance R_{comp} are related by

   $$V_{comp} = 2 \times R_{comp} + L_{comp}$$

   The radial compliance is calculated using the utility **compwr** .

   Cross-sectional area of the pipe is given by:

   $$A = A_0 \times \left(1 + R_{comp} \times P\right)^2$$

   Its diameter:

   $$D = D_0 \times \left(1 + R_{comp} \times P\right)$$

2. User specified bulk modulus
   If the option "user supplied effective bulk modulus" is set, the value of L_{comp} is assumed much smaller than R_{comp} and hence the following is used :

   $$R_{comp} = \frac{W_{comp}}{2}$$

   Cross-sectional area of the pipe is given by:

   $$A = A_0 \times \left(1 + R_{comp} \times P\right)^2$$

   Its diameter:

   $$D = D_0 \times \left(1 + R_{comp} \times P\right)$$

3. Volumetric expansion
   If the option "volumetric expansion" is set, cross-sectional area of the pipe is given by:

   $$A = \frac{hose_{vol}}{L}$$

   Its diameter:

   $$D = \sqrt{\frac{4 \times A}{\pi}}$$

   Where we assumed a constant pipe length during volumetric pipe expansion measurements.

Power, energy, activity

> For details concerning the calculation of power, energy and activity in this submodel, please refer to the definitions specific to this library.

11.6.2 Regulator poppet model

BAP28RT - poppet with conical seat (real time)



Description

BAP28RT represents the one-dimensional motion of a double cone poppet valve with conical seat. It is designed to avoid implicit loops when is used in the real time models.

The model of poppet valve with conical seat is used mainly in injection. See references [1] and [2] or look to the documentation of the utility **acon2sea** to have more details on the equations of the computed flow area.

The pressure at each hydraulic port is input in bar and the flow rate in L/min and a volume in cm^3 are computed and output at both these ports.

The velocity in m/s and the displacement in m of the piston are input at port 3 and passed without modification to port 4. A force in N is input at port 4 and an output force at port 3 is computed.

The net forces on the poppet and on the body are due to the pressure force and the external forces. These forces can optionally be corrected using a jet force. The jet angle is assumed to be constant (half angle of the poppet) and acts on spool and body.

The displacement and velocity of the spool are supplied by the submodel attached to port 4. There are no restriction on the displacement within BAP28RT but restrictions may be provided by an attached submodel employing end stops such as MAS005RT.

The opening is a variable related to this displacement by an offset.

Sometimes it is useful to restrict the orifice area with a minimum and/or maximum value. The minimum area can be used to simulate a leakage or a special orifice passing flow even when the spool is in an overlap position. The maximum area can be used to simulate the flow area adjacent to the orifice when the valve is wide open.

Note that the flow rates and volumes are corrected to take into account the movement of the poppet.

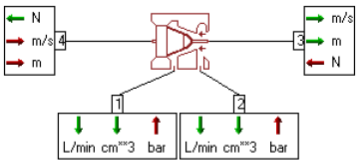
Usage

Use this submodel for any double conical poppet valve when there is a conical seat.

BAP28RT is a submodel dedicated to real-time applications. It allows removing implicit loops and is optimized for this specific usage. For general purpose, the user should use BAP28.

BAP28RT differs from BAP27RT only in that the variables associated with ports 3 and 4 are interchanged.

External variables



	Title	Variable name	Unit	Type	In/Out	Default value
Port 1						
1	flow rate port 1	*q1*	L/min	basic variable	→ output	-
2	volume port 1	*vol1*	cm**3	basic variable	→ output	-
3	pressure port 1	*p1*	bar	basic variable	← input	-
Port 2						
1	flow rate port 2	*q2*	L/min	basic variable	→ output	-
2	volume port 2	*vol2*	cm**3	basic variable	→ output	-
3	pressure port 2	*p2*	bar	basic variable	← input	-
Port 3						
1	duplicate of v4	*v3*	m/s	duplicate	→ output	-
2	duplicate of x4	*x3*	m	duplicate	→ output	-
3	force port 3	*f3*	N	basic variable	← input	-
Port 4						
1	force port 4	*f4*	N	multi-line macro	→ output	-
2	velocity port 4	*v4*	m/s	basic variable	← input	-
3	displacement port 4	*x4*	m	basic variable	← input	-

Internal variables

	Title	Variable name	Unit	Type	Default value
1	poppet lift	*xlap*	mm	basic variable	-
2	flow area	*area*	mm**2	basic variable	-
3	flow coefficient (Cq)	*cq*	null	basic variable	-
4	flow number (lambda)	*lambda*	null	basic variable	-
5	mean fluid velocity	*flv*	m/s	basic variable	-
6	flow force	*fjet*	N	basic variable	-
7	activity of hydraulic dissipation (orif)	*actRorif*	J	activity variable	-
8	average pressure	*averagep*	bar	basic variable	-

Parameter settings

The poppet diameter $dpop$, the cone diameter da, the hole diameter de and the rod diameter dr must be defined as:
$dpop \geq da \geq de \geq dr \geq 0$.

The half angle of the needle cone ($alpha = \alpha$) must be greater than the half angle of the seat ($sigma = \sigma$). The two angles must be defined in the range [0 ; 90 [degrees.

The maximum flow coefficient Cq_{max} and the critical flow number λ_c also influence the orifice flow rate/pressure drop characteristics. For most applications, the values can be left at their default setting.

The poppet lift needed for the setting of mean pressure $taux$ is used for the calculation of the average pressure.

The opening for minimum area x_{min} and opening for maximum area x_{max} are specified by the corresponding underlap positions. The default values imply that there is no restriction on the area. These restrictions are independent of any displacement restrictions applied by other submodels. In addition, irrespective of the upper restriction x_{max}, the flow area is not allowed to exceed the annular area defined by the hole and rod diameters. The minimum opening value must be greater than zero, so we are always in underlap mode even against the seat (leakages).
The maximum area will be given by the maximum opening value or the maximum flow area $\pi/4.(de^2 - dr^2)$. The minimum between these two values will be taken into account to limit the area.

There is a jet force coefficient k_{jet} which, when 0 (the default), disables the jet force and when 1 enables it. If experimental data are available, it can be set to other values to tune the submodel to the experimental data.
In this simple model, the jet angle is assumed to be constant. For most applications this value can be left at its original default setting. The jet angle is given relative to the valve axis.

The volumes at the ports corresponding to zero lift vol_{10} and vol_{20} are normally only of significance if the ports are connected to the HCD hydraulic chamber submodel **BHC11**. If this is the case, it is important to set volume at port 1 corresponding to zero lift and/or volume at port 2 corresponding to zero lift so that the two output volumes are never negative.

The '*index of hydraulic fluid*' parameter refers to a hydraulic fluid type defined by an icon put on the sketch.

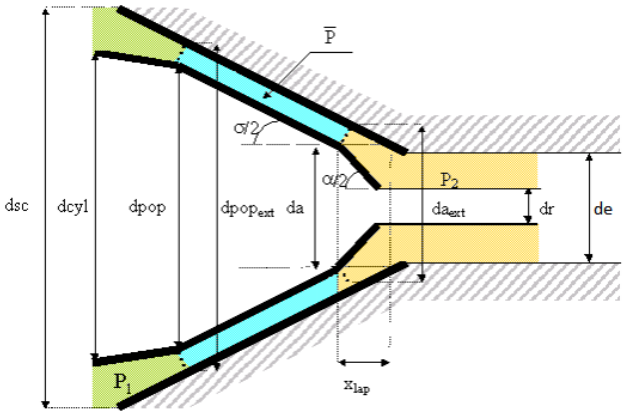
Sketches and equations



The poppet lift is

$$x_{lap} = x_0 - x_4$$

The flow area and the hydraulic diameter dh are computed using the utility **acon2sea**. The diameters are shown on the following figure:



The active area is the curved surface of a truncated cone and it is assumed that this surface divides the region occupied by the fluid into two. The region on port 2 side is subject to pressure p_2 and the region on port 1 side is subject to an average pressure $averagep$, function of p_1, p_2 and the poppet lift (exponential ratio with $taux$). These assumptions are reasonable if the poppet lift is small compared with the seat diameter (de). If the poppet lift is large, clearly at some point the smallest restriction is the hole area. The active area between $dcyl$ and $dpop$ has to be taken into account with a piston model **BAP11**.

The area returned by **acon2sea** is limited to the hole area:

$$\text{hole area} = \frac{\pi}{4}.\left(de^2 - dr^2\right)$$

The volume at port 2 is calculated as

$$vol_2 = vol_{20} + x_{lap}.\frac{\pi}{4}.\left(da^2 - dr^2\right)$$

and the volume at port 1 is

$$vol_1 = vol_{10} + x_{lap}.\frac{\pi}{4}.\left(dpop^2 - da^2\right)$$

The basic flow rate q_b is calculated using the utility **orif3f** and the flow rate at port 1 is this value with reversed sign. It also computes the flow coefficient (Cq), the flow number (λ) and the mean fluid velocity (flv).

The flow rate at port 2 is then

$$q_2 = q_b + \frac{\pi}{4}.\left(da^2 - dr^2\right).v_4.\frac{\rho(p_2)}{\rho(0)}$$

and the flow rate at port 1 is

$$q_1 = -q_b + \frac{\pi}{4}.\left(dpop^2 - da^2\right).v_4.\frac{\rho(p_1)}{\rho(0)}$$

The pressure ratio are given by the utility **q0top**.

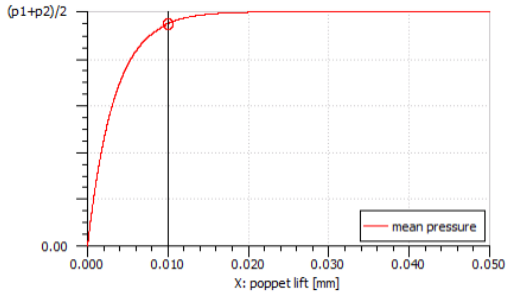
The flow or jet force f_{jet} is calculated by multiplying the value supplied by **jetforc** utility by :

$$k_{jet}.\frac{1}{2}\left[\tanh\left(2.\frac{x_{lap}-x_{min}}{x_{min}}\right)+1\right]$$

Then, you don't have any jet force in overlap.

The average pressure $averagep$ for the fluid in the region at port 1 side is assumed to act on the pressure forces if the poppet lift is greater than 10 microns (default value of $taux$) (the transition is assumed by an exponential function). The average pressure is given by:

$$averagep=\left(\frac{p_1+p_2}{2}\right).\left[1-\exp\left(-\frac{3.x_{lap}}{taux}\right)\right]$$



Evolution of the average pressure $averagep$ as function of the poppet lift

The force at port 4 is then:

- for $x_{lap}\geq 0$

$$f_4=f_3-f_{jet}+p_2.\frac{\pi}{4}.\left(da^2-dr^2\right)+averagep.\frac{\pi}{4}.\left(dpop^2-da^2\right)$$

- else

$$f_4=f_3-f_{jet}+p_2.\frac{\pi}{4}.\left(da^2-dr^2\right)$$

An example of use is given in the documentation of the utility **acon2sea**.

References

[1] Hardenberg H., "Die geometrischen Strömungsquerschnitte von Lochdüsen für Direkteinspritzmotoren", MTZ 45 (1984) 10, S. 427-429, 1984.

[2] DE GROEN O., KOK D. : "Rechenprogramm zur Simulation von Hochdruckeinspritzsystemen für Nutzfahrzeuge" - Motortechnische Zeitschrift MTZ - 57 (1996)

For more details concerning the calculation of power for activity analysis in this submodel, please refer to the definitions specific to this library.

11.6.3 Regulator moving mass model

MAS21 - mass with friction and configurable end stops (advanced)



Description

MAS21 represents the one-dimensional motion of a two ports mass under the action of two external forces in N, weight and frictional forces. The submodel returns the velocity in m/s, the displacement in m and the acceleration in m/s/s. The displacement is limited to a specified range by inclusion of configurable end stops (ideal, elastic or using a restitution coefficient). The friction force is modeled as Karnopp friction, stiction, Coulomb friction, viscous friction and windage.

Starting from a position where there is no frictional force, if the relative displacement changes, a stiction frictional force appears. This consists of two parts:

- a force which varies linearly with the change in relative displacement until the full user specified stiction force is reached. This occurs when the change in relative position reaches a user defined threshold.
- a viscous friction term that is included to prevent non-physical oscillations.

When the displacement exceeds the threshold, the friction force equals the dynamic friction force. It is possible to consider that this dynamic friction force is a function of the relative velocity. This effect is known as the Stribeck effect and the equation describing it is as follows :

$$F_{slip} + (F_{stick} - F_{slip})\, e^{-3\frac{|V_{rel}|}{astrib}}$$

with positive 'astrib' value.

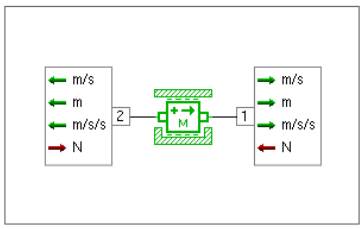
The user can select or not the Stribeck effect. If it is not selected, the transition from static force to dynamic force is instantaneous. If the Stribeck effect is selected, the modulation of the slope during Stribeck effect (positive or negative slope) is only due to the change in static friction force.

When the displacement enters the end stops (in case of elastic endstops), an additional contact force is applied. This consists of a spring and damping force. To give continuity to this force, the damping coefficient is modified so that it is zero at contact beginning and then approaches its full value asymptotically, achieving 95% of its full value at three times the penetration in mm specified by the user.

Usage

Use MAS21 for one-dimensional motion of a mass with two forces applied on it when there is friction and restrictions on displacement with (optional) elastic effects during contact. Typical applications are for moving parts in valves or pistons in jacks.

External variables



	Title	Variable name	Unit	Type	In/Out	Default value
Port 1						
1	velocity at port 1	*v1*	m/s	explicit state	→ output	0
2	displacement at port 1	*x1*	m	explicit state	→ output	0
3	acceleration at port 1	*acc1*	m/s/s	basic variable	→ output	-
4	force at port 1	*fext1*	N	basic variable	← input	-
Port 2						
1	duplicate of v1	*v1dup*	m/s	sign reversed duplicate	→ output	-
2	duplicate of x1	*x1dup*	m	sign reversed duplicate	→ output	-
3	duplicate of acc1	*acc1dup*	m/s/s	sign reversed duplicate	→ output	-
4	force at port 2	*fext2*	N	basic variable	← input	-

Internal variables

	Title	Variable name	Unit	Type	Default value
1	contact force at lower limit	*fmin*	N	basic variable	-
2	contact force at higher limit	*fmax*	N	basic variable	-
3	viscous friction force	*Fvisc*	N	basic variable	-
4	dry friction (stiction/dynamic)	*ffric*	N	basic variable	-
5	stick flag (1:stick;0:slip)	*stick*	null	basic variable	-
6	activity of mechanical dissipation (frict)	*actRfrict*	J	explicit state for activity	0
7	power of mechanical dissipation (frict)	*powerRfrict*	W	power variable	-
8	energy of mechanical dissipation (frict)	*energyRfrict*	J	explicit state for energy	0
9	activity of mechanical inertia (mass)	*actImass*	J	explicit state for activity	0
10	power of mechanical inertia (mass)	*powerImass*	W	power variable	-
11	energy of mechanical inertia (mass)	*energyImass*	J	explicit state for energy	0
12	activity of mechanical capacitance (endstop)	*actCendstop*	J	explicit state for activity	0
13	power of mechanical capacitance (endstop)	*powerCendstop*	W	power variable	-
14	energy of mechanical capacitance (endstop)	*energyCendstop*	J	explicit state for energy	0
15	activity of mechanical source (grav)	*actSgrav*	J	explicit state for activity	0
16	power of mechanical source (grav)	*powerSgrav*	W	power variable	-
17	energy of mechanical source (grav)	*energySgrav*	J	explicit state for energy	0

Real parameters

	Title	Variable name	Unit	Default value
1	mass	*mass*	kg	1
2	stiction force	*fstick*	N	0
3	Coulomb friction force	*fcoul*	N	0
4	coefficient of viscous friction	*rvisc*	N/(m/s)	0
5	coefficient of windage	*wind*	N/(m/s)**2	0
6	stick velocity threshold	*dvel*	m/s	1e-06
7	velocity threshold	*restdvel*	m/s	1e-06
8	restitution coefficient	*restcoeff*	null	0.65
9	Stribeck constant	*astrib*	m/s	0.001
10	lower displacement limit	*xmin*	m	-1
11	lower limit stiffness	*Kbmin*	N/mm	1e+06
12	lower limit contact damping coefficient	*Dbmin*	N/(mm/s)	10
13	lower limit penetration for full damping	*Pdmin*	mm	0.1
14	higher displacement limit	*xmax*	m	1
15	higher limit stiffness	*Kbmax*	N/mm	1e+06
16	higher limit contact damping coefficient	*Dbmax*	N/(mm/s)	10
17	higher limit penetration for full damping	*Pdmax*	mm	0.1
18	inclination (+90 port 1 lowest, -90 port 1 highest)	*theta*	degree	0

Integer parameters

	Title	Variable name	Default value
1	endstop type	*stoptype*	1: ideal
2	Stribeck effect	*strib*	1: no

Parameter settings

Friction

The friction characteristics are to be defined as follows :

- the coefficient of viscous friction in N/(m/s)
- the coefficient of windage in N/(m/s)**2
- the Coulomb friction force in N
- the stiction force in N

None of these quantities may be negative. The stiction force is the maximum friction force when the mass is at rest and the Coulomb friction force is the friction force (assumed constant) when the mass is in motion. Note that the stiction level cannot be less than the Coulomb friction. If the stiction force is a lot bigger than the Coulomb friction force, the motion can be very `jerky' but such motion does often occur.

Both viscous friction (proportional to speed) and windage (proportional to speed squared) add damping resulting in a steady speed being reached quicker.

It can be difficult to know the value to set for the viscous friction. It is often necessary to start with zero viscous friction and raise the level progressively if motion appears to be under damped.

If you use the Stribeck effect, for most applications the default value of the Stribeck constant is acceptable.

End stops

The initial position of the mass should be between lower and upper end stop positions. If there is a limit on the displacement in one direction only, set the other end stop parameter to a very high (10^{30} m) or very low (-10^{30} m) value as appropriate.

Several approaches to collision modeling are available:

- ideal end stop (or plastic collision)
- elastic end stop
- restitution coefficient

Ideal end stop

The ideal end stop approach requires only end stop positions (or displacement limits) as parameters.

Details are given in the Mechanical libray user's guide at the plastic collision section.

Elastic end stop

This example of use can help you for the parameter setting of the end stop positions; MAS21 is similar to MAS30 if you assume that the position of mass M2 is fixed.

For most applications, the parameters for the elastic end stops (stiffness, damping coefficient, limit penetration) can be left at their default values.

The lower the contact damping coefficient is, the more likely the contact at the end stop will result in a bounce. For a damping ratio of z, the contact damping coefficient Db [N/(mm/s)] in terms of the stiffness K and mass M is given by:

$$Db = \frac{2.z}{1000} \cdot \sqrt{K.M}$$

K [N/m] is the equivalent rate or spring constant of all the springs generating the oscillations.
M [kg] is the equivalent mass of all the masses generating the oscillations.
The factor 1000 converts N/(m/s) into N/(mm/s).
For steel parts, the damping ratio z is typically between 0.01 and 0.05.

The limit *penetration for full damping* (strictly speaking 63% of full damping) parameter must be positive. The effective contact damping coefficient *reff* used in the contact force computation is at least 95% of the constant value *Db* when the deformation is greater than three times the *penetration for full damping*.

Details are given in the Mechanical libray user's guide at the elastic collision section.

If undesirable peak occurs on a contact force at the beginning of the simulation, the mass is probably in contact with one of the elastic endstops. Set the displacement limits *xmin*, *xmax* and the initial mass displacement *x1* so that *xmin* ≤ *x1* ≤ *xmax*.

Sketches and equations



The non-frictionnal force is computed as

$$F_{ext} = F_{ext2} - F_{ext1} + 9.81 * mass * sin(theta)$$

The 2 elastic end stop contact forces are

$$F_{min} = \begin{cases} Kb_{min} \cdot (X_{min} - X_1) - Db_{min} \cdot \left(1 - e^{\frac{-(X_{min} - X_1)}{Pd_{min}}}\right) \cdot V_1 & \text{if } X_1 < X_{min} \\ 0 & \text{if } X_1 \geq X_{min} \end{cases}$$

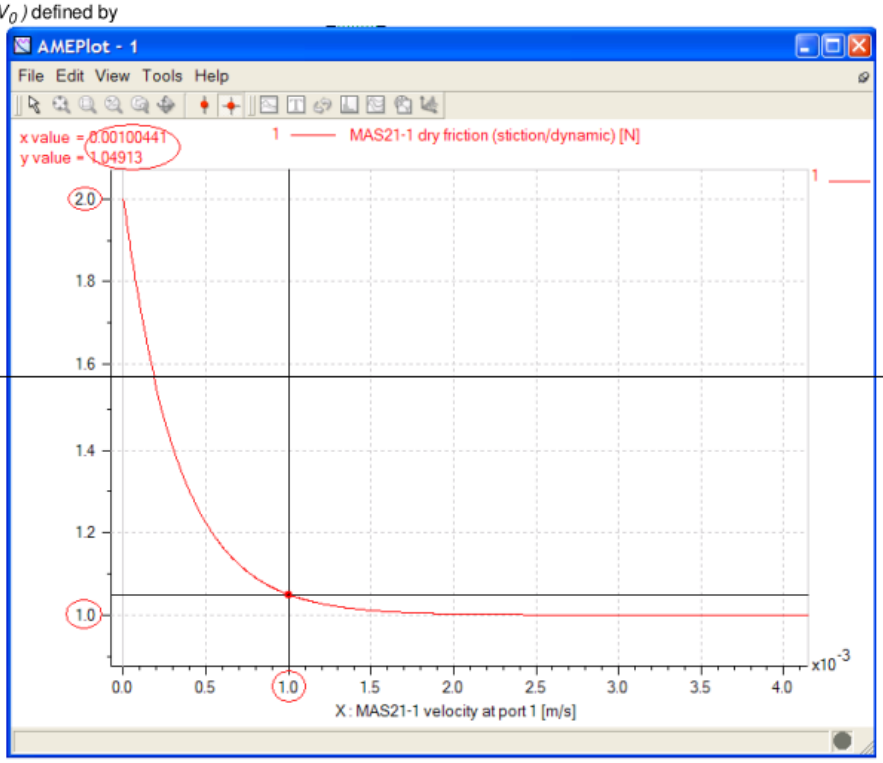
$$F_{max} = \begin{cases} Kb_{max} \cdot (X_1 - X_{max}) + Db_{max} \cdot \left(1 - e^{\frac{-(X_1 - X_{max})}{Pd_{max}}}\right) \cdot V_1 & \text{if } X_1 > X_{max} \\ 0 & \text{if } X_1 \leq X_{max} \end{cases}$$

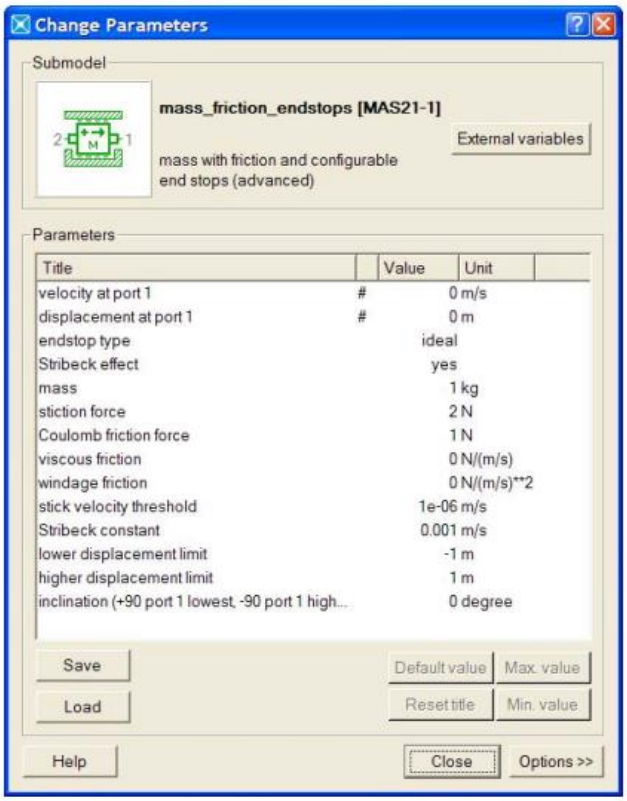
These are computed by the utility function endst1b . In case of ideal end stops or end stops using restitution coefficient the utilities endst2 and endstrc are respectively used.

The friction force developed at the contact has the value :

$$F_{fric} = \left(F_{dyn} + (F_{stat} - F_{dyn}) e^{\frac{|V_{rel}|}{dV_0}}\right) * sign(V_{rel})$$

where F_{dyn} is the Coulomb friction force and F_{stat} is the static friction force, both modulated by the command input and V_0 the velocity threshold $(d=1/V_0)$ defined by





The V_0 value (Stribeck constant) given by the user defines the velocity threshold at which the dynamic friction is more or less alone. This effect is the friction force variation due to relative velocity and is known as the Stribeck effect [1]. This effect generates a damping due to variations i.e.

$$R_{frot} = \frac{\partial F_{frot}}{\partial V_{rel}}$$

This damping can be either positive or negative depending on the shape of the curve. To take this into account, the user simply has to change the static friction force with a greater value than the Coulomb friction force. In fact, most of the time, the static friction is greater than the Coulomb friction. It is too specific to have the opposite phenomenon.

Here the model is the well known Karnopp friction model [2]. This model requires the knowledge of the inertia values, that is the reason why the icon has this aspect. Basically the model calculates the stiction force as a result of inertia acceleration equalities. When sliding, the calculated torque depends on the relative velocity (see before). In this case, the reference has an infinite inertia and a zero velocity.

Adding the friction terms, the acceleration is then

$$Acc_1 = \frac{F_{ext} + F_{min} - F_{max} - F_{fric} * sign(V_1) - R_{visc} * V_1 - Wind * V_1 * |V_1|}{mass}$$

The derivatives of the state variables V_1 and X_1 are then set as

$$\frac{dV_1}{dt} = Acc_1 \text{ and } \frac{dX_1}{dt} = V_1$$

The utility function linert1c is used to perform these computations.

Power, energy, activity

For details concerning the calculation of power, energy and activity in this submodel, please refer to the definitions specific to this library.

References

[1] ARMSTRONG-HELOUVRY B., "Control of Machines with Friction", Norwell, Massachussets: Kluwer Academic Publishers, 1991.

[2] KARNOPP D., "computer simulation of stick slip friction in mechanical dynamic systems", Transactions ASME, Journal of Dynamic Systems, Measurement and Control, vol. 107, March 1985, pp. 100-103.

11.6.4 Regulator setting spring model

BAP016 - piston with spring



Description

BAP016 represents part of a jack (or a valve) where a pressure and a spring force act on a piston (or a spool). The body of the jack (or the valve) is fixed.

The pressure at port 1 is input and the flow rate and a volume are computed and output at this port.

The velocity and the displacement of the piston are input at port 3 and passed without modification to port 2. External force is input at port 2 and output force at port 3 is computed from the pressure, the spring force and the external force.

The volume of the chamber formed by the body and the piston is computed from the displacement at port 3. Port 1 is normally connected to a pressure source, a conventional hydraulic line submodel or an HCD hydraulic chamber submodel.

There is no restriction on the displacement but restrictions may be provided by a connected submodel of mass having end stops (like MAS21 or MAS005).

Note that the flow at port 1 is assumed never to be blocked by the piston.

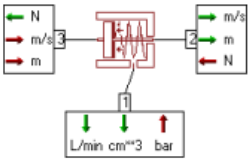
This submodel is Real Time compatible.

Usage

Use this submodel to construct hydraulic jacks and spool valves where there is a spring return. For example, in hydraulics parts of brake systems and automatic gearboxes.

BAP016 differs from BAP015 only in that the variables associated with ports 2 and 3 are interchanged.

External variables



	Title	Variable name	Unit	Type	In/Out	Default value
Port 1						
1	flow rate at port 1	*q1*	L/min	basic variable	→ output	-
2	volume at port 1	*vol1*	cm**3	basic variable	→ output	-
3	pressure at port 1	*p1*	bar	basic variable	← input	-
Port 2						
1	duplicate of v3	*v2*	m/s	duplicate [hidden]	→ output	-
2	duplicate of x3	*x2*	m	duplicate [hidden]	→ output	-
3	force at port 2	*f2*	N	basic variable	← input	-
Port 3						
1	force at port 3	*f3*	N	multi-line macro	→ output	-
2	velocity at port 3	*v3*	m/s	basic variable	← input	-
3	displacement at port 3	*x3*	m	basic variable	← input	-

Internal variables

	Title	Variable name	Unit	Type	Default value
1	length of chamber	*length*	mm	basic variable	-
2	spring stiffness	*kval*	N/mm	basic variable	-
3	spring force	*fspr*	N	multi-line macro	-
4	activity of mechanical capacitance (spring)	*actCspring*	J	explicit state for activity	0
5	power of mechanical capacitance (spring)	*powerCspring*	W	power variable	-
6	energy of mechanical capacitance (spring)	*energyCspring*	J	explicit state for energy	0

Real parameters

	Title	Variable name	Unit	Default value
1	piston diameter	*dp*	mm	10
2	rod diameter	*dr*	mm	5
3	spring stiffness	*k*	N/mm	1
4	spring force at zero compression	*f0*	N	1
5	chamber length at zero displacement	*x0*	mm	0
6	material shear modulus	*G*	N/m**2	8.57e+010
7	spring diameter	*sdiam*	mm	8
8	wire diameter	*wdiam*	mm	2
9	spring compression at zero displacement	*xs0*	mm	0

Integer parameters

	Title	Variable name	Default value
1	index of hydraulic fluid	*indexf*	0
2	stiffness mode	*stiffmode*	1: constant
3	number of active coils	*ncoils*	10
4	discontinuity handling	*disc*	2: active

Text parameters

	Title	Variable name	Default value
1	filename or expression for spring force[N] = f(x[m])	*springtable*	1*x

Parameter settings

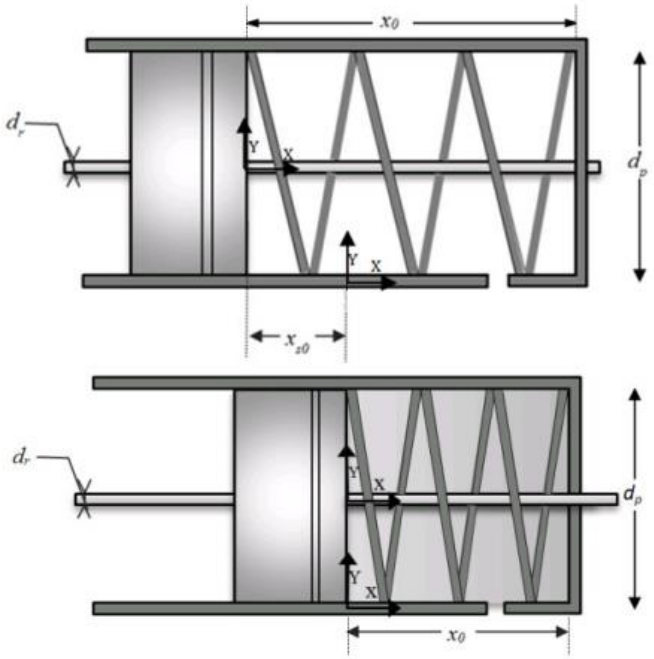
Following figures show parameters associated with the spring piston model. Two reference frames are defined in order to characterize the piston movement:

- one reference frame is attached to the pisotn body
- one reference frame is attached to the piston rod

The relative axial position between these 2 frames depends on the input displacements at ports.
When all the port displacements are assumed to be 0, the axial position of the piston rod into the piston body frame can be defined by the parameter "spring compression at zero displacement" (*xs0*).

Both figures correspond to the "zero displacement" condition. In the first figure (*xs0*) is not equal to zero.

$x_{s0} = 0$ means that the two frames are aligned as shown in the second figure. In this case only the spring force at zero compression(f_0) is applied.



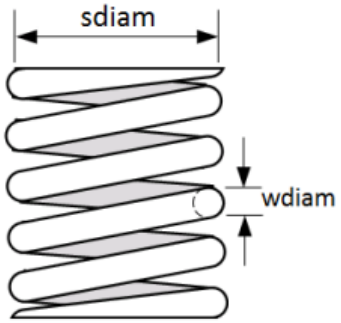
Parameters are defined below:

x_{s0} : spring compression at zero displacement of the piston, positive for compression [mm]
f_0 : spring force at zero compression, positive for compressive force on spring [N]
x_0 : chamber length at zero displacement of the piston [mm]
dp : piston diameter [mm]
dr : piston rod diameter [mm]

Parameters are defined below:

x_{s0} : spring compression at zero displacement of the piston, positive for compression [mm]
f_0 : spring force at zero compression, positive for compressive force on spring [N]
x_0 : chamber length at zero displacement of the piston [mm]
dp : piston diameter [mm]
dr : piston rod diameter [mm]

Spring parameters are defined below:



Where:

s_{diam} : spring diameter [mm]
w_{diam} : spring wire diameter [mm]
G : material shear modulus [N/m^2]
n_{coils} : number of active coils
Note that it is possible to have the *spring diameter* greater than the *piston diameter*. In this case the spring is located outside the piston body.

If there is no rod, set the *rod diameter* to zero.

Spring preload (f_0) and spring compression (x_{s0}) at zero displacement can be set independently.

There are 3 methods to define the spring stiffness:

- ***constant stiffness***
- ***geometrical parameters***, shear modulus of material, spring diameter, wire diameter and number of active coils must be defined.
- ***file or expression***, the spring force must be defined as a function of the spring displacement. It is done through a 1D Format table or an expression. Spring force must be in [N] and displacement (x) in [m].

In the first two cases the spring stiffness is constant.

The ' *index of hydraulic fluid* ' parameter refers to a fluid index defined by the fluid properties component.

Sketches and equations



The current chamber length and volume are calculated as

$$length = x_0 - x_3$$

$$vol_1 = length \frac{\pi}{4} \left(dp^2 - dr^2 \right)$$

The flow rate at port 1 is

$$q_1 = v_3 \frac{\pi}{4} \left(dp^2 - dr^2 \right) \frac{\rho(p_1)}{\rho(p_0)}$$

The force at port 3 is calculated from the force at port 2, the pressure force and the spring force as

$$f_3 = f_2 + p1. \frac{\pi}{4} \left(dp^2 - dr^2 \right) + f_{spr}$$

When *constant stiffness* or *geometrical parameters* method is used, the *spring force*, f_{spr} is given as

$$f_{spr} = K. (x_3 + x_{S0}) + f_0$$

For the *geometrical parameters* method, the stiffness is computed using the expression for a helical spring:

$$K = \frac{G \times w_{diam}^4}{8 \times s_{diam}^3 \times n_{coils}}$$

When *file or expression* method is used f_{spr} is calculated as

$$f_{spr} = Ft(x_3 + x_{s0}) + f_0$$

where Ft is the user table or expression defined by the parameter "springtable".

Power, energy, activity

For more details concerning the calculation of power for activity analysis in this submodel, please refer to the definitions specific to this library.